



N°d'ordre NNT : xxx (créé ultérieurement)

THESE de DOCTORAT DE L'UNIVERSITE DE LYON

opérée au sein de
Laboratoire Hubert Curien

Ecole Doctorale N° 488
Science Ingénierie Santé

Spécialité de doctorat : Optique, Photonique
Discipline : Matériaux pour l'optique et traitement d'images

Soutenue publiquement le 14/12/2016, par :
Zeming LIU

Self-organization of metallic nanoparticles in waveguides by laser: Mechanisms modelling and new approaches

Auto-organisation de nanoparticules métalliques dans des guide-ondes sous flux laser :
Modélisation des mécanismes et nouvelles approches

Devant le jury composé de :

SZUNERITS Sabine
CANIONI Lionel
SIEGEL Jan
EPICIER Thierry

Professeur des Universités, Université Lille 1
Professeur des Universités, Université de Bordeaux
Faculty Research Scientist, Instituto de Óptica, CSIC
Directeur de recherche CNRS, INSA Lyon

Rapporteuse
Rapporteur
Examineur
Examineur

DESTOUCHES Nathalie
VITRANT Guy

Professeur des Universités, Université Jean Monnet
Directeur de recherche CNRS, Grenoble INP - Minatec

Directrice de thèse
Co-directeur de thèse

Contents

Contents	I
Chapter I. Introduction	1
References	5
Chapter II. Experimental techniques	9
1. Sample preparation	10
2. Laser processing setup	11
2.1 continuous-wave laser setup	11
2.2 Pulsed laser setup	12
3. Electron microscopy	13
3.1 Scanning Electron Microscopy	14
3.2 Transmission Electron Microscopy	16
3.2.1 TEM sample preparation	17
3.2.2 Morphological feature characterization	18
3.2.3 Crystalline structure characterization	22
3.2.4 Chemical composition characterization	23
4. Raman microspectroscopy	24
4.1 Crystal phase characterization	24
4.2 Temperature rise estimation	26
5. Atomic Force Microscopy	27
6. Optical spectroscopy	29
References	29
Chapter III. Threshold behavior of NP growth	31
1. Introduction	32
2. Experimentally observed speed threshold	33
2.1 Studied laser intensity range	33
2.2 Speed threshold of laser scan	34
2.3 Temperature rise during NP growth	36
3. Modeling with mono-size approximation	38
3.1 Photo-oxidation	39
3.2 Reduction	41
3.3 Ostwald ripening growth	42
3.4 Temperature rise and NP volume concentration	43
3.5 Coupling of Equations	45
3.6 Simulation Parameters	46

4. Comparison of numerical and experimental results	49
4.1 Origin of the speed threshold	49
4.2 Dependence of the threshold value on other parameters	51
4.2.1 Incident Power	52
4.2.2 Laser Beam width	52
4.2.3 Initial Ag NP size distribution	53
5. Conclusion	54
References	55
Chapter IV. Growth kinetics above the threshold	59
1. Experimental characterization of the NP growth	60
1.1 Grown NP size	60
1.2 Laser-induced temperature rise	62
1.2.1 <i>Post mortem</i> characterization	62
1.2.2 Real-time <i>in situ</i> characterization	67
1.3 Evolution of the NP growth	68
2. Modeling with particle size distribution	69
2.1 State of the art	69
2.2 Developed numerical scheme	70
2.2.1 Nanoparticle coalescence	70
2.2.2 Nanoparticle growth by Ostwald ripening	74
2.2.3 Nanoparticle photo-oxidation and silver ion reduction	76
2.2.4 Final equation set	77
2.2.5 Simulation parameters	78
2.3 Validation of the model	80
3. Origins of growth kinetic variation	82
3.1 A two-step activation of growth	82
3.1.1 Growth of the average size of the NP distribution	83
3.1.2 Growth of the total volume fraction of Ag in NPs	85
3.2 Influence of scan duration at higher speeds	86
4. Conclusion	89
References	90
Chapter V. Pulsed laser induced NP self-organization and anisotropic growth	93
1. Introduction	94
2. Self-organization of NPs versus LIPSS formation	96
2.1 Self-organization of NP related to the LIPSS formation	96
2.1.1 Surface structure	97
2.1.2 Volume structure	97
2.1.3 Crystallization state	98
2.1.4 Origin of NP self-organization	100
2.2 NP self-organization perpendicular to LIPSS	101
2.2.1 Surface structure	101
2.2.2 Volume structure	102
2.2.3 Origin of NP self-organization	103

3. NP growth in anisotropic shape	105
3.1 Anisotropic Ag NPs in surface structured TiO ₂ Layer	105
3.2 Anisotropic Ag NPs in mesoporous TiO ₂ Layer	106
3.3 Possible origin of NP anisotropic growth	107
4. Optical properties of fs laser irradiated Ag:TiO₂ and their potential applications	108
4.1 Guided mode excitation	108
4.2 Diffractive and dichroic color upon transparent support	110
5. Thermal effect of fs and CW laser processes	112
6. Conclusion	114
References	114
General conclusion	119
Perspectives	123
Modeling of NP growth – Towards a Monte-Carlo approach	123
Laser experimentation – Better control of thermal effect	125
References	125
 Annex I. Segmentation of Ag NPs in heterogeneous matrix	 127
1. NP segmentation method	127
2. Filtering segmented NPs from quantitative analysis of the HAADF STEM signal	128
References	131
 Annex II. Evaluation the robustness of the image processing technique and HAADF STEM images synthesis	 133
1. HAADF STEM image synthesis of Ag:TiO ₂ composite	133
2. Reliability of the NP segmentation technique at different image magnifications	135
References	136
 Annex III. Curve fitting of real-time in situ raw Raman spectra	 137
1. Preprocessing of raw spectra	137
2. Curve fitting of Raman peaks	137
2.1. Models of spectral line shape	137
2.2. Curve fitting and error evaluation	140
3. Temperature rise estimations by different numerical processes	140
 Scientific productions in relation with the thesis	 143

Chapter I. Introduction

During the past decades, nanotechnology was of growing interest and new nanomaterials have unconsciously changed our lives in domains like biology, optics, electronics, medicine, cosmetics, design etc. [Liz-Marzan 2004, Zhang 2013, De 2008, Hong 2009, Moriarty 2001]. High-efficiency photovoltaic cells, cancer therapy, self-cleaning materials, photochromic coatings, long-life rechargeable batteries are just few examples. Nanotechnology aims at fabricating and manipulating matter on nanometer (1-100 nm, *i.e.* 1×10^{-9} - 1×10^{-7} m) or molecular scales. The potentiality of nanomaterials in different applications can be straightly linked to their small sizes which usually offer astonishing properties as compared to their bulk state.

Metallic nanoparticles (NP) are a typical example. Bulk metals are characterized by their free electrons that are responsible for their high electrical conductivity. In the case of a metallic NP, these free electrons can interact with the electric field of an external light excitation and redistribute around the NP. Under the periodic oscillation of the electric field of the incident light at certain frequencies, such redistribution of the negative charges exhibits a resonance behavior, represented by a collective excitation of the free electrons of the NP, known as the Localized Surface Plasmon Resonance (LSPR). Collective excitations of electrons can exist in different modes and each LSPR mode corresponds to a natural frequency of the NP, which is defined by the NP characteristics such as its chemical nature, size, shape and also on the surrounding material of NP. The LSPR results in high absorption and scattering of light at resonance frequencies and tailors the optical response of the metallic NP based material. In the case of several noble metals like gold or silver, this LSPR band falls into the visible range and opens the possibility to color NP based materials. Actually, our ancestors have already enjoyed this property to color their glass or ceramic from thousands years ago [Freestone 2007, Caseri 2000], even if the origins of these colors were not known at this period. In 1908, G. Mie gives a first theoretical analysis of the optical response of metallic NPs by solving the Maxwell's equations for the interaction between a plane electromagnetic wave and a spherical particle [Mie 1908].

Variations of Mie theory and other models have then been developed during more than one hundred years for NPs of different shapes and spatial arrangements. These models give better predictions of LSPR and deeper understandings of other LSPR-induced phenomena. Thanks to the coherent excitation of electrons at LSPR frequency, a local electromagnetic field can be generated. This extremely intense local field is very useful to

amplify weak signals or provide non-linear optical responses for applications such as Surface Enhanced Raman Scattering (SERS) and non-linear optical devices [Hou 2013, Haus 1989, Kauranen 2012, Nie 1997]. The plasmon field then decays at a femtosecond time scale through either radiative relaxation, like emission of photons, or non-radiative relaxation by transferring the energy to conduction electrons of metallic NPs. These high energetic electrons which are not in thermal equilibrium with the atom are also called “hot electrons” [Knight 2013]. Relaxation of hot electrons can generate a local heating around the NP via electron-phonon coupling [Inagaki 1985], which can increase the reaction rate of some chemical processes [Christopher 2011]. By incorporating metallic NPs into a semi-conductor matrix, hot electrons can also easily escape from the NP and flow into the conduction band of semi-conductors through the Schottky junction formed at the metal/semi-conductor interface [Tian 2005]. This innovative platform of charge transfer and electron-hole separation gives rise to breakthroughs in the design of photocatalytic and photovoltaic devices [Clavero 2014]. Moreover, in the case of noble metal NPs in semiconductor, for instance Au or Ag in TiO_2 (band gap ≈ 3.2 eV), the LSPR of NPs can enlarge the absorption band of the composite into the visible and near-infrared range, which makes this platform efficient for solar energy harvesting [Zhou 2014, Atar 2013].

As we explained before, the performances of LSPR-based applications strongly depend on the characteristics of metallic NPs and their environment. It then becomes a permanent goal for researchers to find new NP synthesis methods that give a better control of the NP morphologies and their spatial arrangements within different host materials over large surfaces and at low cost. Two classes of NP synthesis strategies can be found in the literature: Top-down and bottom-up approaches. Top-down techniques, like electron-beam lithography, fabricate NPs by removing matter from bulk material. These techniques offer a precise control of NP characteristics and spatial distributions but they are time-consuming, expensive and not suited to produce NPs over large areas [Griffith 2002]. Bottom-up approaches form NPs through a growth process by either deposition of metallic atoms, or reduction of metallic ions. These techniques can provide well-controlled features of NPs but not necessarily organized patterns, especially when the NPs are grown in a solid host matrix [Farrell 2013, Kagnanovskii 2007, Martinez 2014, Sudeep 2005, Hulteen 1995]. Recently, different self-organization mechanisms have been implemented to grow organized NP patterns; the related processes have the advantage to be cost-effective, easy to implement and well-suited for large surface patterning [Destouches 2013, Bris 2014, Watanabe 2012, Öktem 2013]. However, these processes often result from complex interactions and various physicochemical mechanisms promoted by photons or heat. Then it appears critical for researchers to investigate experimentally and theoretically the different mechanisms involved in the NP formation for a better control of their morphology and organization, in order to improve the efficiency of plasmonic applications.

The “NANOPARTICULE” team of Laboratoire Hubert Curien has solid experience in the control of metal NP size within oxide matrix and in the study of light interactions with NP composite systems. They have successfully developed several reversible growth processes of Ag NPs in oxide matrix like TiO_2 and SiO_2 , using either light energy of different wavelengths [Crespo-Monteiro 2010, Tricot 2015] or electric energy delivered by an Atomic Force Microscope (AFM) probe [Bakhti 2014]. Using electromagnetic simulations, they also revealed and interpreted certain special plasmon resonance modes of metallic NP structures [Bakhti 2016].

Recently, the team demonstrated that 1D periodic self-organized growth of silver NPs could be produced within TiO_2 thin films in a versatile and stable process, where a single visible continuous-wave (CW) laser beam scans the film surface [Destouches 2014]. Apart from the plasmon absorption of Ag NPs, the resulting structures exhibit a waveguide behavior that traps additional light into the TiO_2 films, which in turn increases hot electrons generation efficiency. Besides, the self-organization of NPs gives rise to singular dichroic colors on transparent support, which provides original printing solutions for applications like active color displays, security, or polarization imaging. The origin of the self-organized structure was then explained by the interference between the incident light and the scattered light trapped in guided modes of the TiO_2 thin layer. This interference pattern initiates a spatial periodic modulation of the light energy and Ag NPs grow at positions where light intensity is enhanced.

However several counter-intuitive behaviors concerning the growth of Ag NPs have drawn our attention. For a fixed pair of laser power and beam width, the speed at which the laser scans the sample surface appears to be a crucial parameter to control the final NP size and organization: Ag NPs shrink at low scanning speed with no sign of heating, whereas growth and self-organization occur above a speed threshold where high temperatures are reached. At speed where Ag NPs grow, the final average size of Ag NPs firstly increases then decreases with speed. Interpretation of these phenomena and optimization of the Ag NP structures required a thorough understanding of the mechanisms involved in the growth of Ag NPs, and gave rise to the initial objective of this thesis performed at Laboratoire Hubert Curien in collaboration with IMEP-LAHC in Grenoble.

In this work, the counter-intuitive behaviors of NP growth were firstly investigated by different experimental characterization techniques. Transmission Electron Microscopy (TEM, CLYM of Lyon, France) and Scanning Electron Microscopy (SEM) were used for measuring the Ag NP size distributions by coupling with a dedicated image processing algorithm developed during the thesis. Thermal effects were estimated using techniques like *post mortem* Raman spectroscopy, High Resolution TEM (HR TEM), Electron Energy-Loss Spectroscopy (EELS). Evaluation of the temperature rise during CW laser writing was also performed using a real-

time *in situ* Raman setup specially developed by Lucien Saviot and Maria-Del-Carmen Marco-de-Lucas of Laboratoire Interdisciplinaire Carnot de Bourgogne in Dijon, France.

Interpretations of growth phenomena of Ag NPs were based on the numerical models developed to simulate changes in the size distribution of silver NPs induced by visible light. These models take into account the collective contribution of various physico-chemical processes that are involved during the NP size variations that occur upon CW laser scan. These processes are driven by the number of absorbed photons and by the temperature reached in the film. Therefore, theoretical modeling also includes the calculation of the film optical absorption through plasmonic absorptions of the NP distribution, thermal heating, conduction phenomena, and atomic diffusion.

Finally, tailoring the optical response of NP composite films by pulsed laser has also drawn our attention [Ruiz de la Cruz 2014, Nicolas Filippin 2013, Fort 2003]. The large variability of pulsed laser induced structures can be strongly related to the confinement of light within a short pulse leading to both highly intense light pulse, and the possibility to control the transient response of light-composite interaction through exposure conditions such as pulse length, repetition rate etc. However, most of the reported structures in literature were based on pre-deposited NPs or thin films. The studied Ag:TiO₂ samples exhibit a growth behavior of NP during CW laser exposure and a good ability to organize NPs. This encouraged us to exploit new Ag NP structures on the studied samples produced by pulsed laser and to optimize them. The first tests of pulsed laser irradiations were performed at the Laser Processing Group (LPG) of the Instituto de Óptica (IO) of Consejo Superior de Investigaciones Científicas (CSIC) in Madrid, Spain under the supervision of Jan Siegel. Experimental characterizations of the obtained NP structures were then performed at both Laboratoire Hubert Curien and CLYM of Lyon.

The thesis was financed by the Region Rhône-Alpes of France during the three first years from October 2013 to September 2016. A prolongation of this thesis until the end of 2016 was then supported by the Photoflex project (ANR-12-NANO-0006, ANR-11-IDEX-0007) of Agence Nationale de Recherche (ANR) of France, where the thesis was also involved for theoretical studies. Several experiments and missions were assisted by LABEX MANUTECHSISE (ANR-10-LABX-0075) of the University of Lyon.

This manuscript is organized in five chapters, including this first chapter of introduction. Chapter II gives firstly an overview of the experimental techniques that were used during this work. The objective of the chapter is to give only the basic principles of each characterization technique and its specific advantages and drawbacks for our studies compared with similar techniques.

Chapter III and Chapter IV focus on the studies of CW laser induced growth of Ag NPs within TiO₂ films. Chapter III presents the experimentally observed threshold behavior of the Ag NP growth. Using a first simulation model considering mono-disperse NP sizes, a tunable competition between the physicochemical processes involved in the Ag NP evolution is put to the fore. In Chapter IV, the NP growth phenomena and thermal effects at speeds above the growth threshold are presented. These phenomena are then interpreted by a more sophisticated numerical model that has been improved compared to the one of Chapter III, to take into account poly-disperse NP distributions.

Chapter V is devoted to the experimental results obtained using fs laser irradiations. Surface and volume characterizations of the fs laser processed samples are presented in this chapter for a better understanding of the resulting structures. Possible origins of these structures were proposed. The thermal effect produced on the fs laser processed samples is compared with the one produced by CW laser. Possible applications in optics of the fs laser induced structures are also proposed.

The manuscript finishes by a general conclusion of the main results and perspectives of the experimental and simulation works. Several numerical processes developed during this work, such as TEM image processing algorithm, are presented in form of annex, for interested readers.

References

- Atar, F. B.; Battal, E.; Aygun, L. E.; Daglar, B.; Bayindir, M.; Okay, A. K. Plasmonically Enhanced Hot Electron Based Photovoltaic Device. *Optics Express* **2013**, *21* (6), 7196.
- Bakhti, S.; Biswas, S.; Hubert, C.; Reynaud, S.; Vocanson, F.; Destouches, N. Switchable Silver Nanostructures Controlled with an Atomic Force Microscope. *J. Phys. Chem. C* **2014**, *118* (14), 7494–7500.
- Bakhti, S.; Destouches, N.; Tishchenko, A. V. Modeling and Interpretation of Hybridization in Coupled Plasmonic Systems. In *Reviews in Plasmonics 2015*; Geddes, C. D., Ed.; Reviews in Plasmonics; Springer International Publishing, 2016; pp 19–49.
- Bris, A. L.; Maloum, F.; Teisseire, J.; Sorin, F. Self-Organized Ordered Silver Nanoparticle Arrays Obtained by Solid State Dewetting. *Applied Physics Letters* **2014**, *105* (20), 203102.
- Casari, W. Nanocomposites of Polymers and Metals or Semiconductors: Historical Background and Optical Properties. *Macromol. Rapid Commun.* **2000**, *21* (11), 705–722.
- Christopher, P.; Xin, H.; Linic, S. Visible-Light-Enhanced Catalytic Oxidation Reactions on Plasmonic Silver Nanostructures. *Nat Chem* **2011**, *3* (6), 467–472.
- Clavero, C. Plasmon-Induced Hot-Electron Generation at Nanoparticle/metal-Oxide Interfaces for Photovoltaic and Photocatalytic Devices. *Nat Photon* **2014**, *8* (2), 95–103.

- Crespo-Monteiro, N.; Destouches, N.; Bois, L.; Chassagneux, F.; Reynaud, S.; Fournel, T. Reversible and Irreversible Laser Microinscription on Silver-Containing Mesoporous Titania Films. *Adv. Mater.* **2010**, *22* (29), 3166–3170.
- De, M.; Ghosh, P. S.; Rotello, V. M. Applications of Nanoparticles in Biology. *Adv. Mater.* **2008**, *20* (22), 4225–4241.
- Destouches, N.; Battie, Y.; Crespo-Monteiro, N.; Chassagneux, F.; Bois, L.; Bakhti, S.; Vocanson, F.; Toulhoat, N.; Moncoffre, N.; Epicier, T. Photo-Directed Organization of Silver Nanoparticles in Mesostructured Silica and Titania Films. *J Nanopart Res* **2013**, *15* (1), 1–10.
- Destouches, N.; Crespo-Monteiro, N.; Vitrant, G.; Lefkir, Y.; Reynaud, S.; Epicier, T.; Liu, Y.; Vocanson, F.; Pigeon, F. Self-Organized Growth of Metallic Nanoparticles in a Thin Film under Homogeneous and Continuous-Wave Light Excitation. *J. Mater. Chem. C* **2014**, *2* (31), 6256–6263.
- Farrell, Z.; Shelton, C.; Dunn, C.; Green, D. Straightforward, One-Step Synthesis of Alkanethiol-Capped Silver Nanoparticles from an Aggregative Model of Growth. *Langmuir* **2013**, *29* (30), 9291–9300.
- Fort, E.; Ricolleau, C.; Sau-Pueyo, J. Dichroic Thin Films of Silver Nanoparticle Chain Arrays on Facetted Alumina Templates. *Nano Lett.* **2003**, *3* (1), 65–67.
- Freestone, I.; Meeks, N.; Sax, M.; Higgitt, C. The Lycurgus Cup — A Roman Nanotechnology. *Gold Bull* **2007**, *40* (4), 270–277.
- Griffith, S.; Mondol, M.; Kong, D. S.; Jacobson, J. M. Nanostructure Fabrication by Direct Electron-Beam Writing of Nanoparticles. *Journal of Vacuum Science & Technology B* **2002**, *20* (6), 2768–2772.
- Haus, J. W.; Kalyaniwalla, N.; Inguva, R.; Bowden, C. M. Optical Bistability in Small Metallic Particle Composites. *Journal of Applied Physics* **1989**, *65* (4), 1420–1423.
- Hong, H.; Zhang, Y.; Sun, J.; Cai, W. Molecular Imaging and Therapy of Cancer with Radiolabeled Nanoparticles. *Nano Today* **2009**, *4* (5), 399–413.
- Hou, W.; Cronin, S. B. A Review of Surface Plasmon Resonance-Enhanced Photocatalysis. *Adv. Funct. Mater.* **2013**, *23* (13), 1612–1619.
- Hulsteen, J. C.; Duyne, R. P. V. Nanosphere Lithography: A Materials General Fabrication Process for Periodic Particle Array Surfaces. *Journal of Vacuum Science & Technology A* **1995**, *13* (3), 1553–1558.
- Inagaki, T.; Goudonnet, J. P.; Little, J. W.; Arakawa, E. T. Photoacoustic Study of Plasmon-Resonance Absorption in a Bigrating. *J. Opt. Soc. Am. B* **1985**, *2* (3), 433–439.
- Kaganovskii, Y.; Lipovskii, A.; Rosenbluh, M.; Zhurikhina, V. Formation of Nanoclusters through Silver Reduction in Glasses: The Model. *Journal of non-crystalline solids* **2007**, *353* (22–23), 2263–2271.
- Kauranen, M.; Zayats, A. V. Nonlinear Plasmonics. *Nat Photon* **2012**, *6* (11), 737–748.
- Knight, M. W.; Wang, Y.; Urban, A. S.; Sobhani, A.; Zheng, B. Y.; Nordlander, P.; Halas, N. J. Embedding Plasmonic Nanostructure Diodes Enhances Hot Electron Emission. *Nano Lett.* **2013**, *13* (4), 1687–1692.
- Liz-Marzán, L. M. Nanometals: Formation and Color. *Materials Today* **2004**, *7* (2), 26–31.
- Martínez, E. D.; Boissière, C.; Grosso, D.; Sanchez, C.; Troiani, H.; Soler-Illia, G. J. A. A. Confinement-Induced Growth of Au Nanoparticles Entrapped in Mesoporous TiO₂ Thin Films Evidenced by in Situ Thermo-Ellipsometry. *J. Phys. Chem. C* **2014**, *118* (24), 13137–13151.
- Mie, G. Beiträge Zur Optik Trüber Medien, Speziell Kolloidaler Metallösungen. *Annalen der Physik* **1908**, *330*, 377–445.
- Moriarty, P. Nanostructured Materials. *Rep. Prog. Phys.* **2001**, *64* (3), 297.

- Nicolas Filippin, A.; Borrás, A.; Rico, V. J.; Frutos, F.; González-Elípe, A. R. Laser Induced Enhancement of Dichroism in Supported Silver Nanoparticles Deposited by Evaporation at Glancing Angles. *Nanotechnology* **2013**, 24 (4), 45301.
- Nie, null; Emory, null. Probing Single Molecules and Single Nanoparticles by Surface-Enhanced Raman Scattering. *Science* **1997**, 275 (5303), 1102–1106.
- Öktem, B.; Pavlov, I.; Ilday, S.; Kalaycıoğlu, H.; Rybak, A.; Yavaş, S.; Erdoğan, M.; Ilday, F. Ö. Nonlinear Laser Lithography for Indefinitely Large-Area Nanostructuring with Femtosecond Pulses. *Nat Photon* **2013**, 7 (11), 897–901.
- Pileni, M. P. Nanosized Particles Made in Colloidal Assemblies. *Langmuir* **1997**, 13 (13), 3266–3276.
- Ruiz de la Cruz, A.; Lahoz, R.; Siegel, J.; de la Fuente, G. F.; Solis, J. High Speed Inscription of Uniform, Large-Area Laser-Induced Periodic Surface Structures in Cr Films Using a High Repetition Rate Fs Laser. *Opt. Lett.* **2014**, 39 (8), 2491–2494.
- Sudeep, P. K.; Kamat, P. V. Photosensitized Growth of Silver Nanoparticles under Visible Light Irradiation: A Mechanistic Investigation. *Chem. Mater.* **2005**, 17 (22), 5404–5410.
- Tian, Y.; Tatsuma, T. Mechanisms and Applications of Plasmon-Induced Charge Separation at TiO₂ Films Loaded with Gold Nanoparticles. *J. Am. Chem. Soc.* **2005**, 127 (20), 7632–7637.
- Tricot, F.; Vocanson, F.; Chaussy, D.; Beneventi, D.; Party, M.; Destouches, N. Flexible Photochromic Ag:TiO₂ Thin Films Fabricated by Ink-Jet and Flexography Printing Processes. *RSC Adv.* **2015**, 5 (103), 84560–84564.
- Watanabe, S.; Mino, Y.; Ichikawa, Y.; Miyahara, M. T. Spontaneous Formation of Cluster Array of Gold Particles by Convective Self-Assembly. *Langmuir* **2012**, 28 (36), 12982–12988.
- Zhang, X.; Chen, Y. L.; Liu, R.-S.; Tsai, D. P. Plasmonic Photocatalysis. *Rep. Prog. Phys.* **2013**, 76 (4), 46401.
- Zhou, W.; Li, T.; Wang, J.; Qu, Y.; Pan, K.; Xie, Y.; Tian, G.; Wang, L.; Ren, Z.; Jiang, B.; et al. Composites of Small Ag Clusters Confined in the Channels of Well-Ordered Mesoporous Anatase TiO₂ and Their Excellent Solar-Light-Driven Photocatalytic Performance. *Nano Res.* **2014**, 7 (5), 731–742.

Chapter II. Experimental techniques

Experimental techniques used in this thesis concern Ag:TiO₂ sample preparation, laser processing and different kinds of characterization tools. Only the basic principles of each characterization technique, which are helpful to interpret the experimental results of the thesis, will be presented in this chapter. For a given studied phenomenon, different characterization techniques are often used to get complementary information. Each technique has advantages and drawbacks and is selected relative to the targeted objectives. We do not describe all of them extensively but rather give the main features that allow the user to choose the most appropriate technique depending on the studied sample. The outlines of certain complex numerical processes, like STEM image processing, developed during the PhD work are explained with the description of the implemented experimental methods. Numerical details of these developments are presented in annex, to not overload this part.

1. Sample preparation

The PhD work deals with composite Ag:TiO₂ samples that are prepared according to a well mastered technique used in the team for several years [Destouches 2014, Crespo-Monteiro 2014]. Firstly, mesoporous amorphous TiO₂ films are elaborated by a sol-gel process. A titania solution containing Pluronic P123 copolymer ((PEO)₂₀(PPO)₇₀(PEO)₂₀, Aldrich; MW: 5000) is deposited on a glass slide by a dip-coating technique. The deposited film is then calcined at 340°C for 3 hours to remove the P123 copolymer, which frees the nanopores inside the TiO₂ layer. The thickness of the TiO₂ layer is measured at 200±50 nm and pore size varies from 5 nm to 20 nm typically (Figure II.1.a).

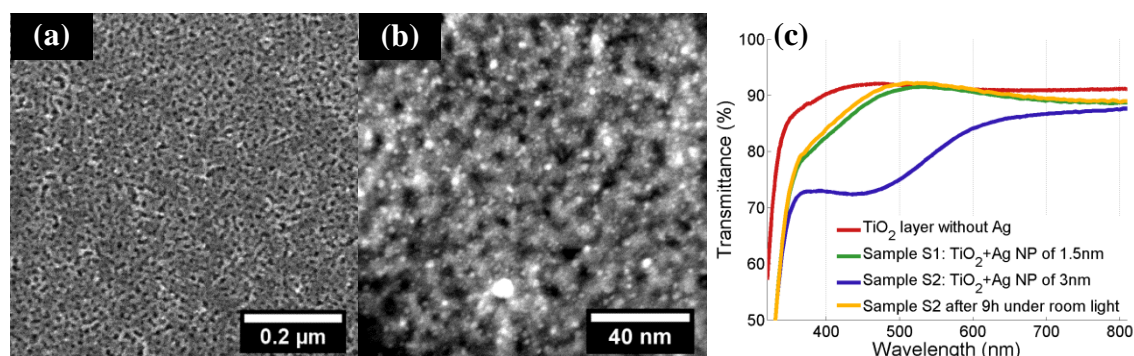


Figure II.1 (a) Top view SEM image of a mesoporous thin layer of amorphous TiO₂. (b) STEM image of a specimen of sample S1. The brighter points in the image correspond to small silver NPs and the non-uniform background is produced by the mesostructure of TiO₂. (c) Transmittance of a TiO₂ mesoporous layer, sample S1 and sample S2.

Secondly, a silver precursor is loaded into the TiO₂ matrix by impregnating the TiO₂ thin layer with a silver nitrate solution. After rinsing with deionized water and drying for 12h in dark at room temperature, small silver NPs with an average size of 1.5 nm are spontaneously formed in the TiO₂ matrix as revealed by STEM measurements (Figure II.1.b). These NPs induce a broad but not high absorption band that appears on the film transmittance spectrum (see sample S1 in Figure II.1.c). However, at this stage the sample is still transparent and nearly colorless at macroscopic scale. Let us name this sample as S1. For most of the works in this thesis, a sample with higher absorbance is appreciated. Hence, sample S1 is often additionally exposed to UV light (254 nm, 400 μW.cm⁻²) for 1 hour to form a sample named S2. In sample S2, the average size of silver NPs is increased to 3 nm thanks to the photocatalytic behavior of TiO₂. Indeed, under UV light, TiO₂ can generate free electrons, which reduce silver ions into silver atoms and increase the silver NP size and density [Nadar et al. 2013, Naoi et al. 2004]. Sample S2 exhibits a brown color and its optical transmittance spectrum (blue curve in figure II.1.c) shows clearly an increase of the absorption in the visible range. In the following part of the thesis, without special precision, the term “initial sample” corresponds to sample S2.

Silver NPs in contact with TiO_2 are known to be photosensitive [Ohko 2003, Crespo 2014], and to shrink under visible light. If the initial sample is left under normal room light condition for about 9 hours, the NP size and the corresponding film absorbance can be significantly decreased (figure II.1.c). In order to avoid an important evolution of the initial sample state in a short time, Ag: TiO_2 samples are stored in a dark box between experiments. It must be noted that due to non-perfectly reproducible processes, especially the step when silver is loaded into the porous film, one may observe slight differences in the NP size distribution from one sample to another. The importance of such a non-reproducibility on the laser-induced nanostructures will be discussed for each studied phenomena in the following chapters.

2. Laser processing setup

2.1 continuous-wave laser setup

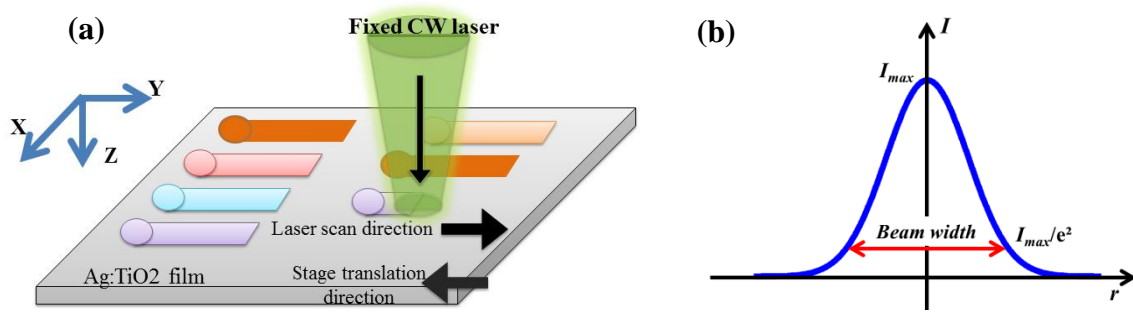


Figure II.2 (a) A simplified illustration of the CW laser setup. A CW Gaussian laser beam is focused on the sample surface under normal incidence. The sample is fixed on a 3-axis translation stage for performing laser scans at constant speed. (b) Spatial intensity profile of a Gaussian beam with the definition of the beam width at $1/e^2$ in intensity.

A continuous-wave (CW) laser, as its name means, is a laser delivering a constant light power in continuous. In this work, the CW laser setup works in the following manner (Figure II.2.a): a laser beam is delivered by an Ar-Kr ion laser (Coherent Innova i70), which is slightly focused by an optical microscope with a 10x objective (Olympus MPlan N, N.A. 0.25) to illuminate the Ag: TiO_2 sample fixed on a 3-axis translation stage. The Ar-Kr ion laser can provide a large choice of wavelengths in the visible range from 457nm to 647nm and a stable output power that reaches 1 W at 488nm. The cross-section of the beam intensity has a Gaussian form and the Gaussian beam width ($1/e^2$ intensity, i.e. Figure II.2.b) in the focal plane is measured at around 12 μm for different incident wavelengths. Under normal incidence, the laser beam arrives from the negative Z direction (Figure II.2.a) and forms a circular spot on the sample surface. The beam width at sample surface can then be modified

by moving the stage along the Z axis and the laser scan is performed by moving the sample along the X or Y directions at constant speed from 0.3 $\mu\text{m/s}$ to 3 mm/s.

2.2 Pulsed laser setup

Unlike CW laser, the energy of a pulsed laser is not delivered in continuous but only within certain temporal lengths called “pulses” (Figure II.3.a). The pulse duration varies typically from the nanosecond to the femtosecond and the same laser pulse is periodically repeated in time. Compared with CW lasers, pulsed lasers have a temporal power profile (Figure II.3.a) in addition to a spatial energy profile (Figure II.3.b) and different parameters are used to characterize them.

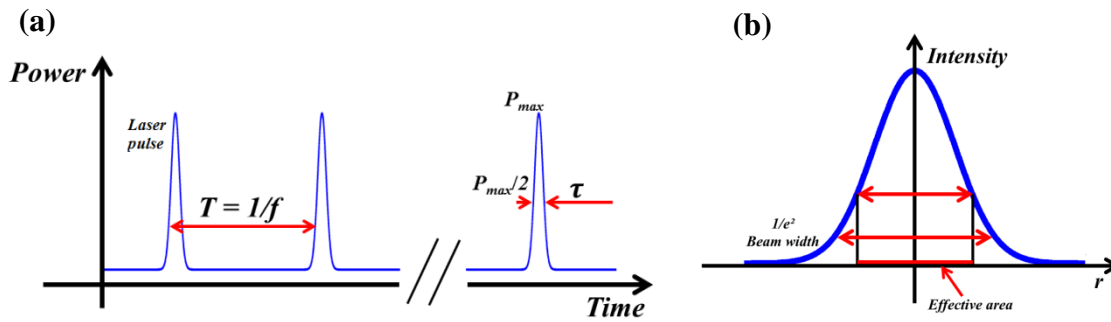


Figure II.3 Temporal profile (a) of a pulse series and Gaussian spatial profile (b) of one laser pulse.

Laser pulses are characterized by two durations: the pulse width τ and the pulse period T . The pulse width is usually expressed by the FWHM (Full Width at Half Maximum) of the pulse temporal profile. The pulse period is the temporal length between two successive pulses and yields the laser repetition rate f by $1/T$. In terms of the temporal evolution of energy flow, two different powers can be defined using τ and T : Peak power and average power. For a given laser pulse energy (Eq. II.1), the peak power is defined as the evolution of energy flow within one pulse as shown by (Eq. II.2). However, the average power corresponds to the evolution of energy flow over the full period T .

In the spatial scale, laser pulses are measured by their Fluence (J/cm^2), which is defined by the pulse energy per area or effective area (Eq II.3). In the case of Gaussian spatial profile, the effective area corresponds to the half of the beam area calculated at $1/e^2$ intensity and the Fluence can be written as (Eq II.4).

$$\text{Pulse Energy (J)} = \frac{\text{Average Power (W)}}{\text{Repetition rate (Hz)}} \quad (\text{II.1})$$

$$\text{Peak Power (W)} = \frac{\text{Pulse Energy(J)}}{\text{Pulse width (s)}} \quad (\text{II.2})$$

$$\text{Fluence (J/cm}^2\text{)} = \frac{\text{Pulse Energy(J)}}{\text{Effective area(cm}^2\text{)}} \quad (\text{II.3})$$

$$(\text{Fluence})_{\text{gaussian}} = \frac{(\text{Average Power}) \times 2}{(\text{Repetition Rate}) \times (\text{Beam area at } 1/e^2)} \quad (\text{II.4})$$

The pulsed laser system used in this thesis is a fiber-based laser (Tangerine, Amplitude Systems) delivering femtosecond pulses at a wavelength of 1030 nm with a pulse width of 300 fs and a repetition rate of 500 kHz. Optionally, the wavelength can be converted to 515 nm by a double frequency crystal placed on the light path. A F-Theta lens (focus length 88 mm) focuses the laser beam that arrives on the sample under normal incidence. During laser irradiation, the sample is fixed in the focal plane where the beam width is measured at about 35 μm . The laser scan is performed by a galvanometer scanner (Figure II.4) composed of two rotating mirrors, which reflect and sweep the laser beam on the fixed sample. Used in conjunction with the F-Theta lens, galvanometer mirrors provide high scan speeds up to several meters per second over a large flat field in the focal plane.

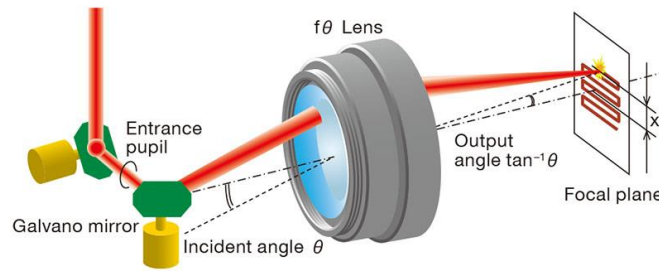


Figure II.4 Schematic of a galvanometer scanner completed by a F-theta lens to perform laser scans over a large area. Image source: OptoSigma.

3. Electron microscopy

Electron microscopy is used to perform observations of samples at the nanometer scale. According to the Abbe's theory (Eq. II.5),

$$d \approx \frac{\lambda}{2} \times N.A. \quad (\text{II.5})$$

the minimum resolvable distance, d , in the image plane of a microscope depends on the incident wavelength λ and numerical aperture N.A. of the imaging system. Limited by the shortest wavelength of a visible photon (~ 400 nm), the minimum resolvable distance of an optical microscope is only about 200 nm, which is much larger than the Ag NP size studied in

this work. In the case of an electron microscope, photon beam is replaced by an electron beam accelerated to a precise kinetic energy. As revealed by the De Broglie's theory, the wavelength of the electron is inversely proportional to the electron kinetic energy, which increases with the acceleration voltage of electrons. In a modern electron microscope, the wavelength of an electron can reach several pm, which decreases the resolvable spatial distance down to the angstrom or sub-angstrom scale [Crewe 1970].

When a high energy electron beam interacts with the probed material, various signals are produced and give rise to different imaging modes of electron microscopes. During this work, Scanning Electron Microscopy (SEM) was used as an efficient and simple tool for a first study of the morphology features over an important quantity of samples. A deeper and more precise study of the selected samples was then performed by Scanning Transmission Electron Microscopy (STEM) under different modes to characterize various features such as the nanoparticle morphology, atomic structure or chemical composition.

3.1 Scanning Electron Microscopy

A simplified diagram of a Scanning Electron Microscopy (SEM) is shown in figure II.5.a. An electron beam generated by an electron gun and accelerated is focused by an electromagnetic lenses system and deflected by a scan unit before impinging on the sample located in a vacuum chamber. Different signals resulted from the probe beam/matter interaction can be recorded by detecting electrons or photons above the sample surface. SEM imaging is performed by a raster scan: the selected signal and the spatial position of the probe are simultaneously recorded to plot, pixel by pixel, the SEM image.

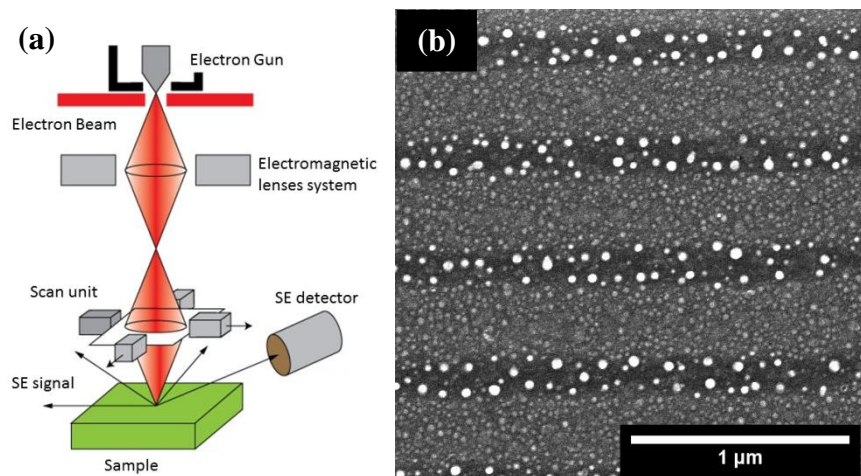


Figure II.5. (a) Simplified schematic of SEM. (b) A SEM image of fs laser irradiated Ag:TiO₂ sample containing embedded and surface Ag NPs (bright spheres) together with periodic surface structure of TiO₂.

When the probe beam interacts with sample, signals are generated from a volume around the point where the probe hits the sample. Depending on the nature and energy of the measured signals, different imaging modes of SEM can be obtained. Electrons encountered elastic and inelastic interactions with the probed volume. Secondary Electrons (SE) are those that result from inelastic scattering. They are emitted from excited atoms and have low energy. Hence, only SE coming from the near surface of the sample (typically a few tens of nanometers) can successfully be detected. SEM images formed under SE mode are useful to get information about sample surface topography [Seiler 1983]. Backscattered Electrons (BSE) are high energy electrons resulting from elastically scattering that are mainly scattered in the direction opposite to the incident one [Goldstein 2003]. The quantity of BSE strongly depends on the atomic number of the probed matter and BSE images have thus a chemical contrast. In BSE images, regions with higher atomic number scatter more BSE and exhibit brighter colors. Thanks to their high energy, BSE produced from deeper volumes can be detected. For the same reason, the intensity of one pixel under BSE mode is generated from a larger volume than the one under SE mode, so BSE images have usually a lower spatial resolution than SE images.

The scattered electrons can be easily deflected if the probed sample is charged. This produces distortions such as large bright regions in the image. The direct measurement of dielectric samples is therefore impossible in standard conditions except if a conductive (Au-Pd or carbon) layer is deposited on the sample surface. Another solution is to use a gaseous detector. In this case, a residual pressure of gas in the chamber helps to evacuate extra charges on the sample surface. This solution is implemented on the Nova nanoSEM available in the lab.

Besides, SEM can be also used for elemental analysis by stimulation of EDX (Energy-Dispersive X-ray) signal from the studied sample. When an electron beam of sufficient high energy hits the sample, excited electrons can relax by emission of X-rays at characteristic wavelengths defined by the atomic structure of the probed chemical element. Each chemical element emits X-ray at its unique set of characteristic wavelengths and the quantity of characteristic X-ray photons is proportional to the atomic concentration of the chemical element. Qualitative and quantitative elemental analysis can therefore be achieved by interpreting emitted X-ray spectra. The accuracy of EDX analysis is often affected by factors as surface topography, overlapping between close characteristic peaks, sample inhomogeneity, etc. The EDX signal is emitted from a larger volume than the case of BSE and SE and its spatial resolution is of the order of one μm .

During this thesis, SEM images were recorded by a SEM-FEI Nova nanoSEM 200 with an electron beam of 15 kV. During measurements, the Ag:TiO₂ composite samples are placed in a chamber under partial vacuum. This configuration allows a direct and non-destructive

characterization of our samples without deposition of a conductive layer. The studied sample is fixed upon a translation stage and any interesting zone over cm^2 area can be placed under the probe for local features investigation. The SE mode is preferred during this thesis thanks to its short acquisition time for one image (less than 1 minute) and its better spatial resolution (around 1 nm). For these reasons, SEM is a useful tool for a first rapid investigation of the sample morphological features, such as NP grating orientation, period, surface morphology, shape of the porosity (Figure II.5.b) or crystal form, over an important quantity of samples. But, as SEM probes only the near surface volume under SE mode, the embedded objects in the probed volume cannot be precisely imaged at the right size and form (Figure II.6.b-c). For a deeper investigation, like the reconstruction of the size distribution of embedded Ag NPs, a more precise but time-consuming method, Transmission Electron Microscopy, is preferred.

3.2 Transmission Electron Microscopy

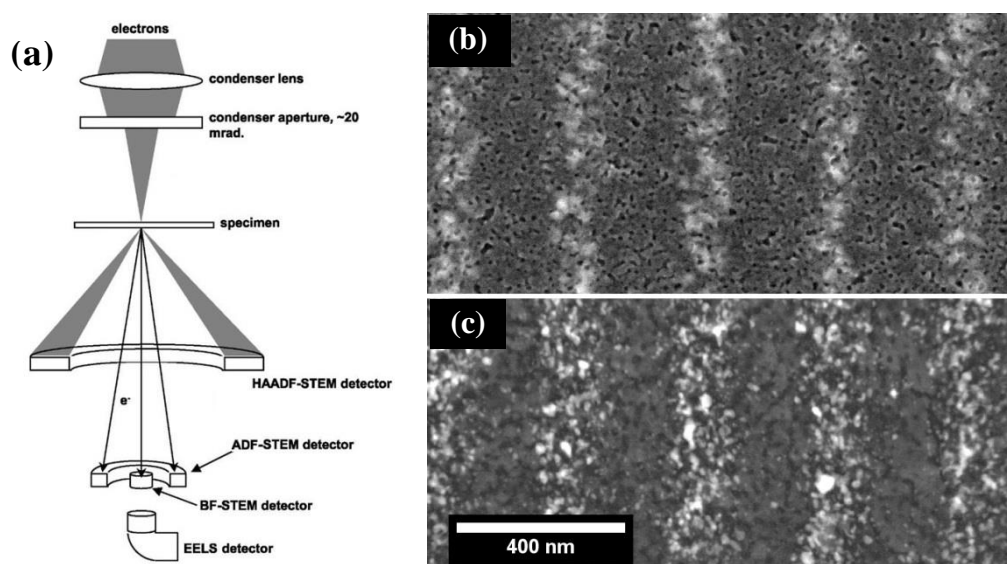


Figure II.6 (a) Schematic of STEM (JEOL 2010) with different signals generated by electron-matter interactions. (b-c) Comparison of SEM (b: SE mode) and TEM (c: HAADF STEM) images of small Ag NPs embedded in TiO_2 matrix. Ag NPs correspond to the bright zones in images.

A Transmission Electron Microscope (TEM) records signals transmitted through samples whose thickness must be less than 100 nm. During TEM imaging, the electron probe interacts with a thin layer instead of a large volume within the bulk sample. The spatial resolution of TEM images is thus significantly improved compared to the one of SEM images, especially for embedded objects. This makes TEM very useful for the characterization of the small Ag NP embedded in a TiO_2 matrix used in this studied (Figure II.6.b-c). TEM usually works with a voltage of several hundred kV, with which a direct observation at atomic scale [Qiao 2011, Akita 2008] becomes possible. In this thesis, TEM characterizations were performed with a FEI-TITAN ETEM (300kV) and a JEOL 2010 FEG (200kV).

TEM uses a collimated electron beam to probe the sample and the transmitted beam is then focalized to form the image, so all the pixels of an image are formed simultaneously. TEM works under different imaging modes by recording the direct transmitted electrons or diffracted electrons. Another largely used type of imaging mode in TEM is Scanning Transmission Electron Microscope (STEM, Figure II.6.a). It works in a similar manner as SEM. Images are formed pixel by pixel under a focused electron beam. But, instead of detecting the signals from sample surface, different type of transmitted signals are recorded for diverse characterizations. In the following subsections, we present firstly the techniques for TEM sample preparation. Then, the TEM and STEM modes used in this thesis are successively presented according to the types of characterization.

3.2.1 TEM sample preparation

In this work, the TEM specimens can be prepared by two methods. In the first method, Ag:TiO₂ films are manually scrapped into micrometer-size chips, which are then embedded, with non-controlled random orientations, in a resin (Epothin epoxy resin). The resin is then polymerized under room condition for 12 hours before cutting with an ultramicrotome (Leica MTXL) to get slices of thickness around 40-80 nm. These slices are deposited on a copper grid and the whole grid is observed by TEM. This preparation method is relatively cheap but finding the area of interest is often like a needle in a haystack. Besides, it is impossible to know the precise spatial position and orientation of the measured zone in the original Ag:TiO₂ film. The specimens are also rarely observed in a plane-view from the top. In order to observe the periodicity of the NP grating from the top view of samples, we use directly the manually cut chips. In this case, only the chips with good thickness and orientation for imaging can be useful.

Another technique is to use Focused Ion Beam (Dual beam FIB FEI Helios 600i) to prepare well-defined film cross-sections. A FIB machine is often coupled with a SEM: Instead of focusing an electron beam, an ion beam is used to sculpt the sample surface. The studied sample is firstly covered by a protective layer to avoid the sample contamination induced by a direct contact with the ion beam. During the sample preparation, FIB removes some parts of sample by milling the sample surface. A rough milling is first performed to obtain a cross section which is perpendicular to the sample surface (Figure II.7.a) at a precise position. This cross section is then extracted from the sample and placed on a TEM grid before thinning to a thickness of about 100 nm for TEM measurement (Figure II.7.b). FIB is an efficient tool to obtain a cross section of precise orientation, spatial position and size. By combining with different kinds of measurement, such as STEM HAADF, STEM EELS and EDX, the analysis of the in-depth structure of samples becomes feasible. However, the preparation of FIB cross sections requires a long time and the process is more expensive than manual cut. Hence,

during this work, FIB cross sections are only prepared for a limited quantity of well-chosen samples.

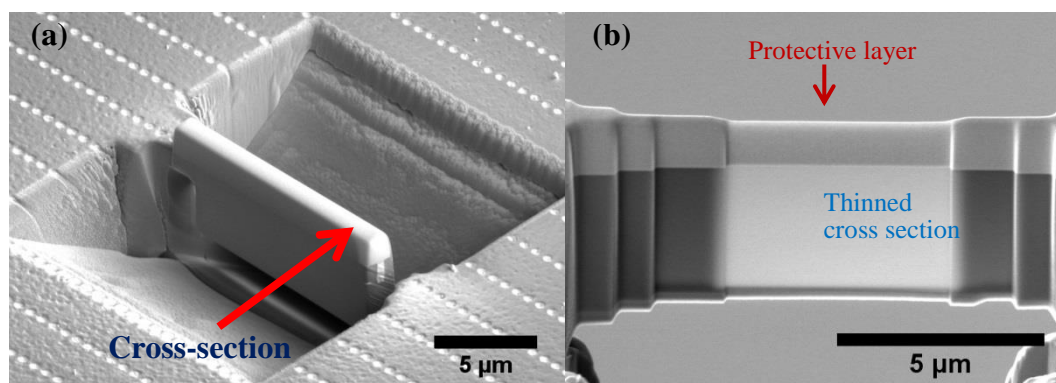


Figure II.7. a. Cross section left on the sample after the sculpture by FIB. b. Cross section is thinned to about 100 nm before TEM measurement. (Source FEI)

3.2.2 Morphological feature characterization

In order to perform a thorough analysis of the morphological features of nanostructures produced in our Ag:TiO₂ composite films, Annular Dark Field STEM (ADF STEM) imaging mode is often chosen in this thesis for its chemical sensibility. More precisely, High Angle Annular Dark Field STEM (HAADF STEM) images are preferred as they allow the selection of nanoparticles of specific chemical nature among heterogeneous ensembles [Akita 2008, Epicier 2012, Young 2008]. This Z-contrast is not only usefully for identification of Ag NPs within the TiO₂ film, but is also an important tool to validate the accuracy of the NP size distribution segmented by automatic TEM image processing algorithm as described in Annex I and II.

Advantages of HAADF STEM imaging mode

ADF STEM and HAADF STEM images are formed by an annular detector which collects the scattered electrons at different angles with respect to the incident beam (Figure II.6.a). The intensity of these scattered electrons depends on both the atomic number of the probed matter and the Bragg scattering efficiency of the crystalline structure within the probed volume. The latter only occurs at low angles with respect to the incident beam. As a consequence, at high angles, the electron intensity is only defined by the atomic number of the probed matter and HAADF STEM images have a pure chemical sensitivity compared to classical ADF STEM images.

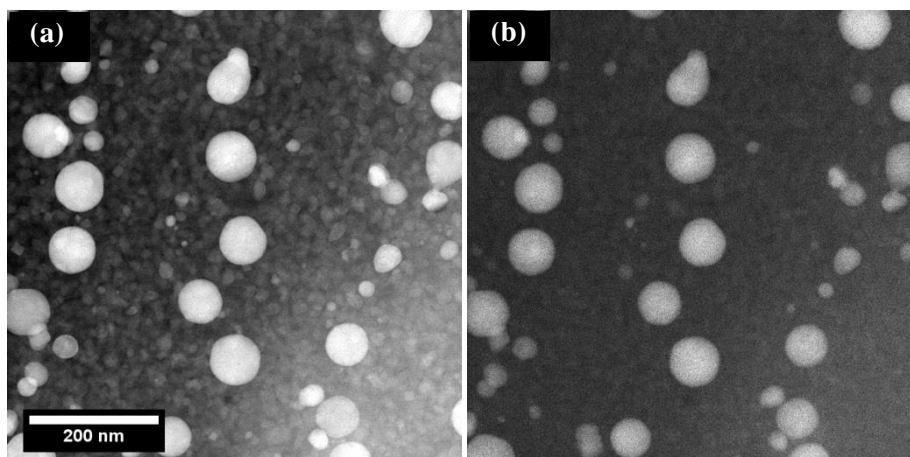


Figure II.8. Comparison of ADF and HAADF images of the same zone containing both Ag NP and TiO_2 crystal. ADF imaging (a) is sensitive to the atomic number and crystalline structure. TiO_2 crystal exhibits therefore a similar gray level as some small Ag NPs on ADF images. HAADF imaging (b) is only sensitive to the atomic number, which helps to distinguish Ag from TiO_2 crystals.

For the studied Ag: TiO_2 samples, this pure chemical sensitivity of HAADF STEM is useful to improve the reliability of the NP identification. Figure II.8 gives a comparison of STEM ADF and HAADF images of a laser processed Ag: TiO_2 sample where TiO_2 is partially crystallized in small nanocrystals and coexists with Ag NPs whose size and shape are sometimes similar. Since Ag has a higher atomic number (47) than TiO_2 (Ti: 22, O: 8), spherical Ag NPs are generally brighter than the surrounding TiO_2 . However, in the ADF image, some TiO_2 crystal can appear with a similar gray level as the Ag NP, because the Bragg scattering efficiency of their crystalline structure can increase the pixel intensity. It is therefore difficult to distinguish with a great certitude TiO_2 crystals from Ag NPs on an ADF image. Under HAADF mode, thanks to the absence of Bragg scattering, TiO_2 crystals have a lower gray level and Ag NPs can be thus easily identified.

Quantitative characterization of the NP size distribution from HAADF STEM images

The chemical sensitivity is also an important tool to select the right population of NPs and warrant the accuracy of automatically reconstructed NP size distributions. In the HAADF STEM images of the initial state of Ag: TiO_2 samples (Figure II.9.a), the mesoporosity of TiO_2 matrix induces a non-uniform background upon which Ag NPs of average size of 3 nm are randomly distributed. Straightforward image processing methods, such as global thresholding for instance, are not sufficient to correctly segment Ag NPs as their gray levels are influenced by the surrounding mesoporous TiO_2 . Moreover, the presence of a white Gaussian noise induced by the camera and the small size of NPs also brought rapidly the automatic segmentation methods to their precision limit. In this context, it was required to measure a huge quantity of NPs in order to have an accurate statistical view of the size evolution during the light excitation process, which consequently led us to prohibit the use

of manual segmentation procedures. We thus developed, a semi-automatic segmentation method dedicated to the HAADF STEM characterization of small NPs embedded in a heterogeneous matrix of a nature different than that of the NPs themselves. Numerical details of this method are given in Annex I.

HAADF signals are formed by the electrons undergo Rutherford scattering whose intensity at high angle relative to incident beam can be approximated by a simple equation depending on the atomic number Z of the probed matter [Treacy 1989, Jesson 1995]:

$$I_{HAADF} = k \sum n_i Z_i^\alpha \quad (II.6)$$

where n_i is the quantity of atoms of nature i within the probed volume, Z_i their atomic number and k a constant which depends on the STEM configuration. For a modern HAADF detector, α is a coefficient estimated to be close to 2 for high angle detectors [Jesson 1995]. Enjoying this simple intensity formulation of HAADF signal, the developed image processing method was improved and validated in the two following ways:

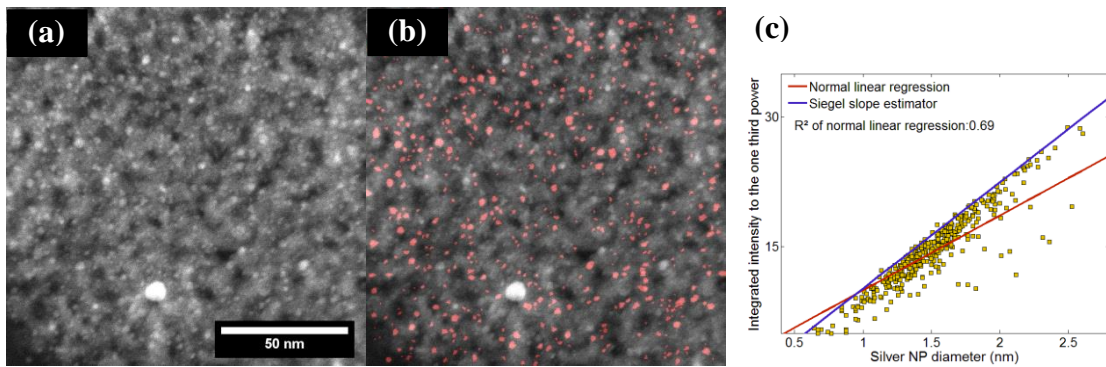


Figure II.9. a. STEM-HAADF image of initial state Ag:TiO₂ sample. b. Candidate Ag NP zone detected by automatic image processing method (red zones). c. HAADF Quantitative Analysis of the candidate zone: the non-Ag NP zone or Ag NP segmented at wrong size are presented as the outliers to be filtered

Firstly, a HAADF quantitative analysis has been applied on the automatic segmentation results to eliminate the false positive error. A false positive error is a false segmented zone which does not correspond to Ag NP. As shown by Epicier et al. [Epicier 2012], for a spherical NP, the integrated intensity I_{NP} of its HAADF pixels is directly related to the particle's volume as $I_{NP} \propto \frac{4}{3}\pi(\frac{D_{NP}}{2})^3$, where D_{NP} is the NP diameter. According to Eq.II.6, one can yield a linear relation between D_{NP} and $I^{1/3}$ for NPs of same chemical nature. For a given set of segmented NPs (Figure II.9.b), the correctly segmented Ag NP zones draw a straight line in the D_{NP} - $I^{1/3}$ space, and the non-Ag NP zones or the Ag NP segmented at a wrong size appear as the outliers far from this line (Figure II.9.c). The accuracy of the size histogram can be improved by eliminating these outliers. A D_{NP} - $I^{1/3}$ line passes through the origin point. The slope of this line can be given by a median slope estimator such as Siegel

estimator [Siegel 1982] which calculates an accurate slope of point distribution with the presence of outliers. The outliers can be then easily detected by calculating their Euclidean distance with the $D_{NP}-l^{1/3}$ line given by Siegel estimator.

Secondly, the robustness of the developed image processing algorithm has been validated by the generation of “virtual” STEM images. Using the geometrical features of pores within the TiO_2 matrix and the estimated Ag NP size distribution, realistic HAADF STEM images (Figure II.10.a) can be generated by Eq.II.6. These synthesized images are then used to evaluate the false negative errors resulting from the Ag NP segmentation, which correspond to the Ag NP lost by the segmentation algorithm. As the real Ag NP size distribution in a synthesized image is known, by comparing with the automatically segmented NP size distribution, one can estimate the quantity of false negative errors and their importance on the size distribution (Figure II.10.b). The synthesis technique ensures the quantitative-precision of results. Besides, synthesized images also help to find the most efficient image magnification for the reconstruction NP size distributions. In order to have an important NP quantity to represent the NP distribution, images are preferred to be obtained under low magnifications to increase the NP quantity per image. However, the latter induces a low pixel resolution, which decreases the accuracy of the segmented NP size. An efficient image magnification can be then found by testing the segmentation algorithm on synthesized images at a series of magnifications and evaluating the shape and height of the segmented NP size histogram compared with the synthesized ones.

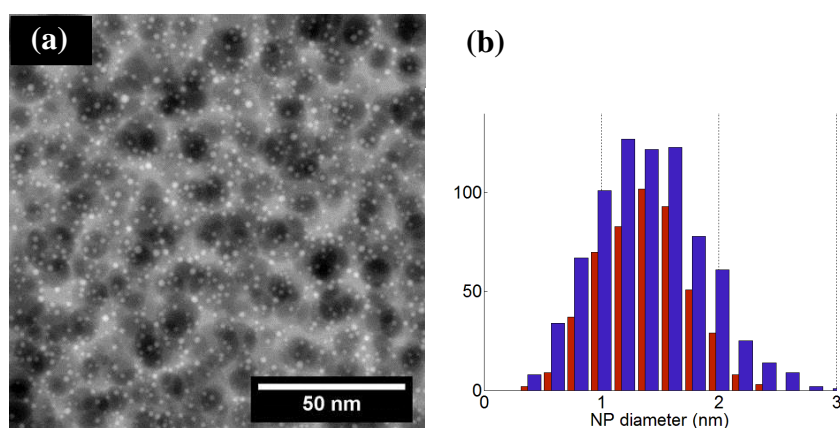


Figure II.10. (a) Synthesized STEM-HAADF image of initial state Ag:TiO₂ sample. (b) Comparison of the distribution used for image synthesis (bleu bar) and distribution obtained after segmentation by the automatic image processing algorithm developed.

For the numerical details of the developed automatic segmentation image processing algorithm and the quantitative analysis, the readers are referred to Annex I. HAADF STEM Image synthesis is presented in Annex II.

3.2.3 Crystalline structure characterization

When using a STEM mode in a TEM, as the probe beam width can be decreased to the angstrom scale, a direct visualization of single atoms and atomic structures of crystals is possible under High Resolution STEM (HR STEM) [Akita 2008, Crewe 1970], as shown in Figure II.11.a. The lattice motif in an HR STEM image can be interpreted as the atomic plane of the probed crystal and their gray levels depend on the atomic number of the probed matter. HR images can be also achieved in a bright field mode in a TEM (HR TEM). From the appearance, a HR TEM image is similar to HR STEM image, whereas the gray level contrast in a HR TEM cannot be simply interpreted as the atomic plane of probed matter. Indeed, under HR TEM mode, both directly transmitted beam and scattered beam are used to form the image. The gray level contrast under HR TEM mode is principally raised from the interference of the transmitted beam and Bragg scattered electrons induced by the atom column. So the HR TEM is also named as phase-contrast image. The gray level of a crystal in HR TEM image is defined by the experimental configuration of the microscope instead of the chemical nature of the crystal. During this thesis, the choice between HR TEM and HR STEM was only dependent on the availability of the TEM machine.

Anyway, if the spatial resolution of the microscope is sufficiently high and a zone axis of a crystal is suitably oriented along the incident beam, an exploitable lattice image can be obtained (Figure II.11.a). The identification of a crystal relies then on the analysis of the diffraction pattern of the HR lattice image, usually obtained by a Fast Fourier Transform (FFT) of the HR image (Figure II.11.b). The peak positions in the diffraction pattern identify the nature and the phase of the crystal by comparison with data reported in literature. The fitting in the work is performed by a semi-automatic program provided by Thierry Epicier (INSA Lyon, CLYM) names diffraction workshop software.

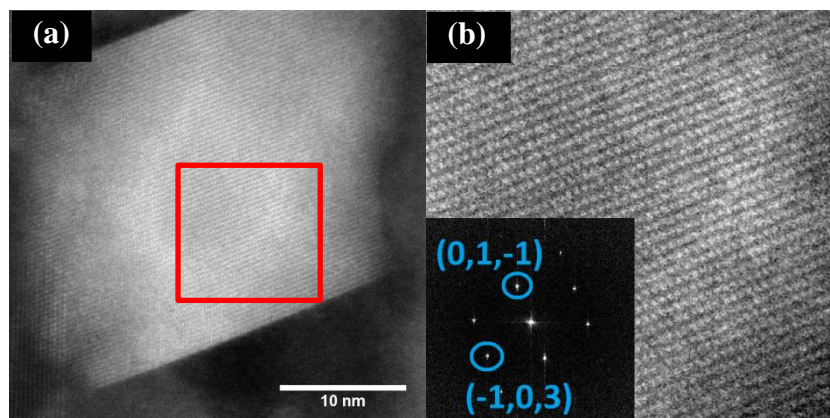


Figure II.11. (a) HR STEM HAADF image of an anatase nanocrystal. (b) Identification of the anatase phase by indexing the zone axis in diffraction pattern of the red square zone in (a).

HR (S)TEM images provide a direct analysis of specific crystals at well identified locations, for instance around one Ag NP. However, one need to find a suitable crystal with a zone axis oriented along the incident beam to form the lattice image. Moreover, an important quantity of exploitable HR images needs to be recorded to reconstruct the global crystalline structure information, which appears as a long process.

3.2.4 Chemical composition characterization

Electron Energy-Loss Spectroscopy (EELS) is used in this work to investigate the chemical composition of laser processed Ag:TiO₂ samples, usually upon a FIB cross section. When an electron beam probes a sample, certain electrons undergo inelastic interactions with matter, which means that they lose one part of their energy after passing through the sample. The quantity of lost energy directly depends on the chemical nature of the atom with which the electron has interacted. By recording the distribution of the lost-energy within a certain energy range, one can obtain an EELS spectrum which characterizes the atomic signature of the probed matter. The spatial distribution of one chemical component can be therefore mapped with the EELS signal by scanning over an interesting zone (Figure II.12). As EELS works with the main transmitted beam (Figure 6.a), ADF image is usually formed in parallel with EELS spectrum to have morphological features of the investigated zone.

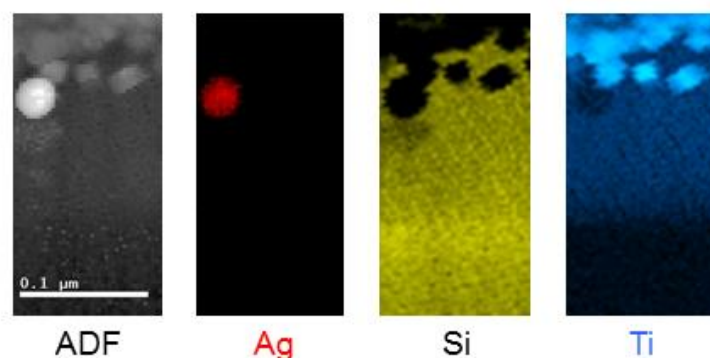


Figure II.12. ADF image (left) and EELS maps (the others) on the cross section of a Ag:TiO₂ sample. The spatial distribution of one chemical component can be revealed by EELS.

HAADF images have a similar chemical sensitivity as EELS mapping but they have non-negligible differences. EELS data can directly identify the chemical nature of matter. With HAADF imaging mode, a quantitative analysis of the probed matter is only possible after a complex calibration process to find an accurate value of k in Eq.II.6 for a given microscope configuration and requires *a priori* knowledge about the sample composition.

In terms of acquisition time, a 1024*1024 pixel HAADF image can be formed in less than one minute. However the typical acquisition time of EELS maps varies from several

minutes to few hours depending on the number of pixels and the acquisition time per pixel. Limited by this long acquisition duration, EELS maps are usually limited to only few hundreds of pixels, which limit the size of the studied areas. EELS signal is often much less resolved spatially than HAADF signal. For these reasons, HAADF is more suitable for the morphology characterization over large areas.

An alternative technique for chemical composition characterization used in this work is Energy-Dispersive X-ray Spectroscopy (EDS). Different from EELS, EDS relies on the X-ray signal generated from the electron beam interaction with the studied sample. Similarly to EELS, the chemical nature of the studied material is identified by its set of signature peaks on the X-ray emission spectrum. EELS data provide more information than EDX, such as the surface properties, chemical bonding etc. [Egerton 2009]. However, as the generated X-ray is recorded from the sample surface, EDS is also feasible in a SEM whose experimental configuration and sample preparation are much simple than STEM.

4. Raman microspectroscopy

Raman microspectroscopy is used in this work for TiO₂ crystalline phase identification and for the estimation of the laser-induced temperature rise with an *in situ* experimental configuration. Raman microspectroscopy is a non-destructive analysis technique. It uses a focused laser beam to probe the sample surface and detects the scattered photons that undergo inelastic interaction with the sample. Inelastic scattered photons are identified by their shift in wavenumber relative to the wavenumber of the probe laser beam, and are usually written in cm⁻¹. For a given wavelength λ , the wavenumber ν is given by $\nu = 1/\lambda$. The Raman spectrum is the distribution of these inelastic scattered photons with respect to the wavenumber shift. If inelastic scattered photons have a lower energy than the incident one, the difference of $\nu_{\text{incident}} - \nu_{\text{scatter}}$ is positive and these photons form the Stokes spectrum. Contrarily, if scattered photons have higher energy, the wavenumber difference becomes negative and these photons form the anti-stokes spectrum.

4.1 Crystal phase characterization

The crystalline phase of probed matter is characterized by feature peaks in Raman spectrum that form a signature. The peaks in Stokes and Anti-stokes spectra are at the same wavenumbers in absolute value. However, the emission probability of Stokes photons is usually higher and the latter spectrum is more commonly used for characterizations. In our experiments, Raman spectra were principally recorded with a LabRam ARAMIS. As our samples are sensitive to visible wavelength, the probe beam was chosen at 633 nm (as far as

possible from the plasmon resonance of Ag NP) and used with relatively low intensity to avoid any change in the sample when probing. The probe laser was focalized by a $\times 100$ objective, which forms a $1\text{ }\mu\text{m}$ spot upon the sample surface. The spatial resolution is thus limited by this spot size. The probed depth is typically around $10\text{ }\mu\text{m}$. The TiO_2 crystals are formed within a thin layer less than 100 nm thick and the probed volume contains also a large part of the film substrate, which is usually glass from microscope slides in our experiments. The signal-to-noise ratio for one single acquisition is therefore very low and a single spectrum is usually recorded by averaging about 100 acquisitions.

In this work TiO_2 can be crystallized in anatase or rutile phase. According to the literature [Zhang 2000 ,Ma 2007], the signature peaks of anatase are 144 , 196 , 396 , 515 and 639 cm^{-1} (Figure II.13.a) whereas the rutile phase raises Raman peaks at 140 , 235 , 446 , 610 and 826 cm^{-1} (Figure II.13.b). The amplitude and the form of Raman peaks is not considered in this study as they depend on various factors such as the environmental temperature [Oshaka 1980, Maher 2008]. The positions of the peaks can also be slightly shifted by few cm^{-1} by the presence of defects in the crystals or the presence of Ag NP for instance. These small shifts will be neglected most of the time in this study.

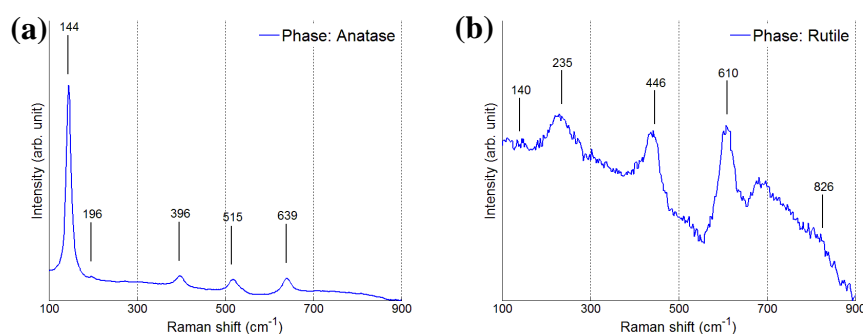


Figure II.13. Raman spectra of Ag: TiO_2 samples after different laser exposures. TiO_2 appears to be crystallized in anatase phase (a) or rutile phase (b).

Compared with the identification of crystal phases by HR (S)TEM image, Raman spectrum gives the average crystallization state of the sample instead of individual information on nanocrystals. Note that in our samples, Ag NPs with an average size around 100 nm , which lie in the samples along with TiO_2 crystals, produce a significant Surface-enhanced Raman Scattering (SERS) effect [Rycenga 2010]. The latter amplifies the TiO_2 Raman signal and makes identification easy despite the low thickness of the film. Such identification is however much more difficult when only small Ag NPs are present, since the Raman peaks become less pronounced or even non-interpretable. In this case, the identification of crystal phases can only rely on HR (S)TEM images. In terms of sample preparation, Raman measurements need no specific sample preparation and the acquisition time per spectrum is less than 20 minutes. For HR (S)TEM characterizations, one needs few days to prepare the sample, perform the measurements and process the HR micrographs.

4.2 Temperature rise estimation

Raman spectra recorded *in situ* during dynamic laser exposure performed at a constant scanning speed were also used in this work to estimate the temperature rise during CW-laser scan. These experiments were carried out by Lucien Saviot and Maria-Del-Carmen Marco-De-Lucas at Université de Bourgogne Franche-comté with a Renishaw Invia Raman microspectrometer equipped by a translation stage of Jobin-Yvon T64000. A single laser is used to growth Ag NPs and to excite the Raman signal. As the laser-induced temperature rise evolves in time during exposure, measurements cannot be performed in static mode, nor once the NPs have been grown at their maximum size. The wavelength used for such experiments must lie in the plasmon absorption band of silver NPs; it is chosen at 532 nm and focalized by a $\times 50$ objective. Both Stokes and anti-Stokes spectra are recorded from -200 cm^{-1} to 200 cm^{-1} to include the anatase peak at $\pm 144\text{ cm}^{-1}$ (Figure II.14). The minimum time required to record one spectrum is about 10s. According to the limited sample size and the accuracy with which the right focus could be maintained during the sample translation, only lines of about 1 cm long could be drawn. This constraints limited the speed at which measurements could be performed at $1000\text{ }\mu\text{m/s}$. The minimum value of the scanning speed was fixed by the translation stage specifications. The temperature rise that occurs during the laser scan is then estimated from the ratio of Stokes and anti-Stokes peaks at $\pm 144\text{ cm}^{-1}$ or from the shift of the Stokes peak at 144 cm^{-1} . The position of these peaks is temperature dependent and shifts slightly during *in situ* characterizations.

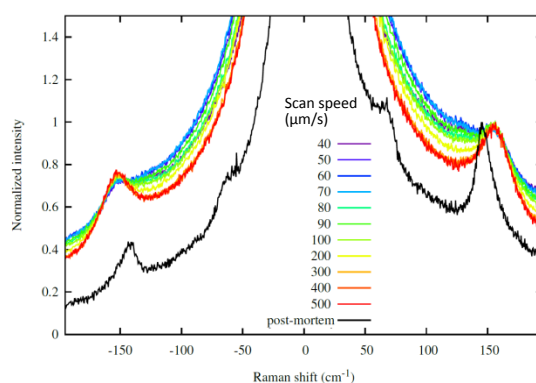


Figure II.14. Raman spectra measured *in situ* during the NP growth when scanning the sample with the laser at different constant scan speeds. All the spectra are normalized so that the amplitude of the 144 cm^{-1} is the same.

It is well known that a temperature rise induces an amplitude difference in the Stokes and anti-stokes spectra (Figure II.14) as described by Eq.II.7 [Maher 2008], where I_s and I_{as} are the maximum intensities of the anatase mode at $\pm 144\text{ cm}^{-1}$ in Stokes and anti-Stokes spectra, respectively.

$$\frac{I_{as}}{I_s} = \alpha \frac{(w_i + w_r)^4}{(w_i - w_r)^4} \exp(-hw_r/2\pi k_B T) \quad (II.7)$$

Here, T is the absolute temperature in Kelvin, α is an instrument depend parameter which can be calibrated by a Raman spectrum under a known temperature, for instance the *post mortem* spectrum measured with low laser intensity and assumed to be at room temperature. w_i and w_r are the frequency of the probe laser and the studied Raman mode, respectively. h is the Planck constant. k_B is the Boltzmann constant. The temperature rise can be estimated by properly measuring I_{as} and I_s . The numerical processes used to determine these values from the raw Raman spectra are detailed in Annex III. Note that slight changes in the way we calculate I_{as} and I_s can lead to large changes in the estimated temperature rise, typically several tens of degrees. It is therefore useful to compare the results with those obtained with other methods.

The temperature rise can also be deduced from the shift of a Raman peak relative to its position at room temperature. In order to evaluate the accuracy of the first temperature estimation method, we also used the peak shift data reported by Oshaka et al. in [Oshaka 2003]. The position of the Raman peak of anatase TiO_2 at 144cm^{-1} is deduced from raw spectra using the numerical processes described in Annex III and the corresponding temperature rise is reported in the abacus given by Oshaka et al.

Other factors can change both the ratio I_{as}/I_s ratio and the peak shift, they will be discussed in chapter IV, as well as the accuracy of such estimates.

5. Atomic Force Microscopy

Atomic Force Microscopy (AFM, Agilent 5500) is used in this work to quantitatively characterize the surface topography of samples with nanometer resolution. The simplified schematic of an atomic force microscope is illustrated in figure II.15.a. The probe of an AFM is a small tip integrated at the end of a cantilever. During AFM image acquisition, the probe follows a raster scan over the investigated zone and is quasi-contacted on the sample surface. When the probe encounters a topographic variation, the attractive force and the repulsive force, raised from the interaction between the probe and sample surface, can slightly deflect the probe. In order to detect this tiny deflection, a laser beam is directed on probe. The probe reflects the light intensity to a photodiode sensor and the tiny deflection is thus amplified and interpreted by the light intensity variation in the four quadrants of the sensor.

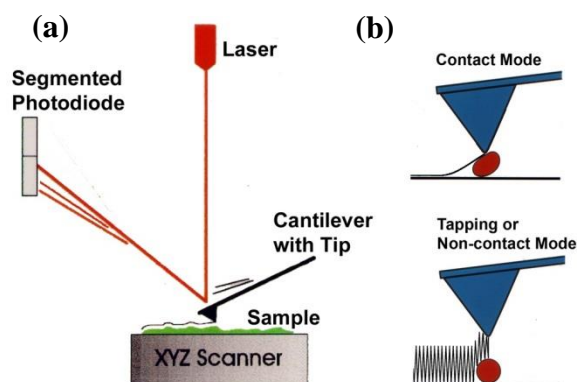


Figure II.15. (a) Schematic of an AFM: Laser beam is reflected to a four-quadrant photo sensor by a metallic probe. The latter is deflected by the surface topography which induces a variation of laser intensity at the sensor. (b) Contact mode and Tapping mode of AFM

In our experiments, we mainly used two modes of the AFM: contact mode and tapping mode (Figure II.15.b). Interested readers could refer to the cited reviews [Giessibl 2003, Jalili 2004] for further information about these modes and the way AFM works. The choice of the mode depends on the characteristics of the probed matter. The tapping mode is often preferred thanks to its negligible mechanic interaction with the sample with prevent from modifying the sample surface with the probe scan.

In this study, AFM is a useful tool to characterize the laser induced periodic surface structure on our sample (Figure II.16). AFM doesn't need specific sample preparation. Compared with SEM, AFM gives more precise quantitative information of the surface topography such as the surface profile (Figure II.16.b). Besides, the high resolution helps to reveal the tiny surface structures, which are not perceivable by SEM (Figure II.16.a). However, the duration of an AFM imaging is usually very long. In our case, about 1 hour is needed to obtain a topography map of 512×512 pixel over a zone of 3×3 μm^2 .

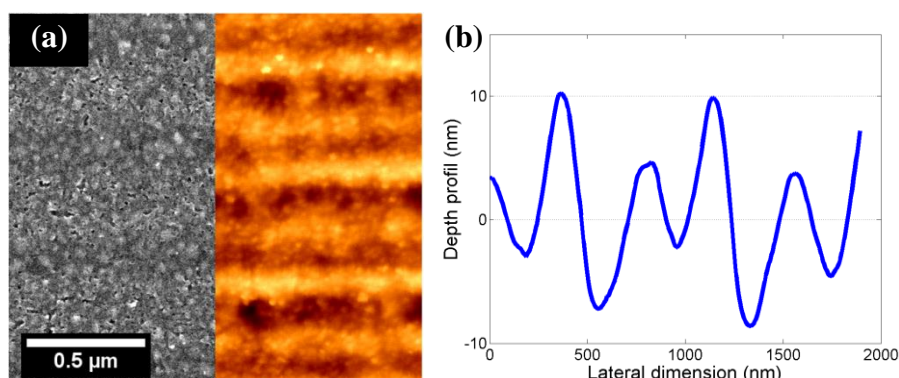


Figure II.16. (a) Comparison of SEM (left) and AFM (right) images on a sample with laser-induced periodic surface structures. (b) AFM topography profile of the sample surface. AFM gives the surface profile with a high accuracy, which is not measurable with SEM.

6. Optical spectroscopy

Optical spectroscopy is an analytical tool which characterizes the optical response of samples, which consists of reflectance (R), absorptance (A) and transmittance (T). R, A, T are usually expressed in percentage (%) whose values respectively correspond to the portion of the incident light energy reflected, absorbed and transmitted by the studied sample. It is worth remarking that there is a difference between the absorbance and previously defined absorptance. The Absorbance, which can be directly deduced by the transmittance (Eq. II.8), represents the importance of the non-transmitted energy.

$$\text{Absorbance} = \log_{10}(1/T) \quad (\text{II.8})$$

The optical responses are usually studied in a given wavelength range. By plotting R, A and T as a function of the incident wavelength, one obtains the corresponding spectra of reflectance, absorptance and transmittance. Modern spectroscopy tools can easily record T and R spectra. In this work, the diffusion of the Ag:TiO₂ sample is negligible. The absorptance spectrum (A) is then calculated by 1-R-T, as deduced by the conservation of energy.

In this thesis, transmittance spectra are recorded with a conventional spectrophotometer based on a double-beam configuration (Perkin Elmer Lambda 900). The incident beam coming from the light sources, covering both ultraviolet (UV), visible and near infrared (NIR) ranges, is split into two beams which are respectively orientated to the sample chamber and the reference port to overcome the fluctuation of source intensity during measurement. The spectral resolution is about 1nm.

References

- Bosch, E. G. T.; Lazić, I. Analysis of HR-STEM Theory for Thin Specimen. *Ultramicroscopy* **2015**, *156*, 59–72.
- Treacy, M. M. J.; Rice, S. B. Catalyst Particle Sizes from Rutherford Scattered Intensities. *Journal of Microscopy* **1989**, *156* (2), 211–234.
- Crespo-Monteiro, N.; Destouches, N.; Epicier, T.; Balan, L.; Vocanson, F.; Lefkir, Y.; Michalon, J.-Y. Changes in the Chemical and Structural Properties of Nanocomposite Ag:TiO₂ Films during Photochromic Transitions. *J. Phys. Chem. C* **2014**.
- Epicier, T.; Sato, K.; Tournus, F.; Konno, T. Chemical Composition Dispersion in Bi-Metallic Nanoparticles: Semi-Automated Analysis Using HAADF-STEM. *J Nanopart Res* **2012**, *14* (9), 1–10.
- Egerton, R. F. Electron Energy-Loss Spectroscopy in the TEM. *Rep. Prog. Phys.* **2009**, *72* (1), 016502.
- Akita, T.; Tanaka, K.; Kohyama, M.; Haruta, M. HAADF-STEM Observation of Au Nanoparticles on TiO₂. *Surf. Interface Anal.* **2008**, *40* (13), 1760–1763.
- Garcia-Gutierrez, D.; Gutierrez-Wing, C.; Miki-Yoshida, M.; Jose-Yacaman, M. HAADF Study of Au-Pt Core-Shell Bimetallic Nanoparticles. *Appl Phys A* **2004**, *79* (3), 481–487.
- Giessibl, F. J. Advances in Atomic Force Microscopy. *Rev. Mod. Phys.* **2003**, *75* (3), 949–983.

- Jalili, N.; Laxminarayana, K. A Review of Atomic Force Microscopy Imaging Systems: Application to Molecular Metrology and Biological Sciences. *Mechatronics* **2004**, *14* (8), 907–945.
- Jesson, D. E.; Pennycook, S. J. Incoherent Imaging of Crystals Using Thermally Scattered Electrons. *Proceedings of the Royal Society of London A: Mathematical, Physical and Engineering Sciences* **1995**, *449* (1936), 273–293.
- Nadar, L.; Destouches, N.; Crespo-Monteiro, N.; Sayah, R.; Vocanson, F.; Reynaud, S.; Lefkir, Y.; Capoen, B. Multicolor Photochromism of Silver-Containing Mesoporous Films of Amorphous or Anatase TiO₂. *J Nanopart Res* **2013**, *15* (11), 1–10.
- Ohko, Y.; Tatsuma, T.; Fujii, T.; Naoi, K.; Niwa, C.; Kubota, Y.; Fujishima, A. Multicolour Photochromism of TiO₂ Films Loaded with Silver Nanoparticles. *Nat Mater* **2003**, *2* (1), 29–31.
- Zhang, W. F.; He, Y. L.; Zhang, M. S.; Yin, Z.; Chen, Q. Raman Scattering Study on Anatase TiO₂ Nanocrystals. *J. Phys. D: Appl. Phys.* **2000**, *33* (8), 912.
- Maher, R. C.; Cohen, L. F.; Lohsoontorn, P.; Brett, D. J. L.; Brandon, N. P. Raman Spectroscopy as a Probe of Temperature and Oxidation State for Gadolinium-Doped Ceria Used in Solid Oxide Fuel Cells. *J. Phys. Chem. A* **2008**, *112* (7), 1497–1501.
- Ma, H. L.; Yang, J. Y.; Dai, Y.; Zhang, Y. B.; Lu, B.; Ma, G. H. Raman Study of Phase Transformation of TiO₂ Rutile Single Crystal Irradiated by Infrared Femtosecond Laser. *Applied Surface Science* **2007**, *253* (18), 7497–7500.
- Seiler, H. Secondary Electron Emission in the Scanning Electron Microscope. *Journal of Applied Physics* **1983**, *54* (11), R1–R18.
- Destouches, N.; Crespo-Monteiro, N.; Vitrant, G.; Lefkir, Y.; Reynaud, S.; Epicier, T.; Liu, Y.; Vocanson, F.; Pigeon, F. Self-Organized Growth of Metallic Nanoparticles in a Thin Film under Homogeneous and Continuous-Wave Light Excitation. *J. Mater. Chem. C* **2014**, *2* (31), 6256–6263.
- Qiao, B.; Wang, A.; Yang, X.; Allard, L. F.; Jiang, Z.; Cui, Y.; Liu, J.; Li, J.; Zhang, T. Single-Atom Catalysis of CO Oxidation Using Pt₁/FeO_x. *Nat Chem* **2011**, *3* (8), 634–641.
- Ohsaka, T. Temperature Dependence of the Raman Spectrum in Anatase TiO₂. *J. Phys. Soc. Jpn.* **1980**, *48* (5), 1661–1668.
- Naoi, K.; Ohko, Y.; Tatsuma, T. TiO₂ Films Loaded with Silver Nanoparticles: Control of Multicolor Photochromic Behavior. *J. Am. Chem. Soc.* **2004**, *126* (11), 3664–3668.
- Rycenga, M.; Camargo, P. H. C.; Li, W.; Moran, C. H.; Xia, Y. Understanding the SERS Effects of Single Silver Nanoparticles and Their Dimers, One at a Time. *J. Phys. Chem. Lett.* **2010**, *1* (4), 696–703.
- Crewe, A. V.; Wall, J.; Langmore, J. Visibility of Single Atoms. *Science* **1970**, *168* (3937), 1338–1340.
- Young, N. P.; Li, Z. Y.; Chen, Y.; Palomba, S.; Di Vece, M.; Palmer, R. E. Weighing Supported Nanoparticles: Size-Selected Clusters as Mass Standards in Nanometrology. *Phys. Rev. Lett.* **2008**, *101* (24), 246103.

Chapter III. Threshold behavior of NP growth

Under visible CW laser scan, the Ag:TiO₂ film can undergoes spectacular structural modifications. We show here that depending on the laser parameters, either the shrinkage or growth of NPs can occur. Both NP's behaviors are due to different physicochemical mechanisms which are in competition and which are induced by the excitation of localized surface plasmon resonance (LSPR) in Ag NPs. In particular, we provide evidence that, for a given laser parameter set, the growth of Ag NPs only occurs if the writing laser scan speed is fast enough, *i.e.* above a speed threshold. On the contrary, Ag NPs shrink at speeds below this threshold. This phenomenon appears counter-intuitive as growth of NPs requires sufficient energy that is usually obtained by accumulating the irradiation time, *i.e.* when using low scan speed. In order to explain this counter-intuitive behavior, we propose here a phenomenological theoretical model based on a set of coupled differential equations describing the matter transformations between the Ag⁰, Ag⁺ and Ag NP states under laser excitation. Numerical results are found in good agreement with the experimental ones, both for the prediction of speed threshold and its dependence to various parameters. This study constitutes a deep understanding of NP growth-shrinkage processes involved during laser exposure.

1. Introduction

Plasmon-induced charger transfer [Tian 2004, Tian 2005] via hot electrons generations is of great important in the design of highly efficient photocatalysis [Clavero 2014, Zhou 2014, Kowalska 2010] and photovoltaic devices [Tian 2005, Sakai 2010, Valverde-Aguilar 2011]. Such devices rely on the electron-hole separation that occurs at the interface of noble metal NP and semiconductor, such as Ag:TiO₂ composite. Localized Surface Plasmon Resonance (LSPR) of noble metal NP leads to a strong light absorption at visible range, which not only extends the optical responses of TiO₂ but also generates hot electrons that are formed by the decay of the localized surface plasmon, which transfers and accumulate its energy to electrons of metallic NP. These highly energetic electrons can then emit from the NPs and the Schottky junction [Tian 2005] formed at the interface with semiconductor can act as an efficient platform to collect this electron emission.

Periodically arranged metallic NPs can also be used to improve the efficiency of the optical absorption of NP composites by trapping light into photonic modes propagating in the semiconductor layer and consecutively increase the hot electron generation [Atwater 2010]. Combining both processes give rise to the formation of periodic arrays of metallic NPs in TiO₂ films, that was reported by the NANOPARTICULE group of Laboratoire Hubert Curien [Destouches, Crespo-Monteiro et al. 2014]. They showed that self-organized growth of Ag NPs could be produced in TiO₂ thin film by single visible CW laser beam scans. The resulting structures were demonstrated to act as resonators trapping various wavelengths into the Ag:TiO₂ thin film. The periodic growth was explained as originating from the interference of the guided waves with the incident one. The spectral responses and the hot electrons generation of these structures, is strongly related to the morphological properties of this well-ordered Ag NPs, such as the size, shape and density. It is of paramount importance to study the physicochemical reactions that are at the origin of the self-organization process and to understand the formation of Ag NPs.

Under visible light, excitation of LSPR of Ag NPs promises an efficient means to convert photons into plasmons. The latter decays in the femtosecond timescale, either through a radiative path by photon re-emission [Sönnichsen 2002] or a non-radiative path by generation of hot electrons [Lehmann 2000]. Having energies higher than the Schottky barrier at Ag/TiO₂ interface, hot electrons can be injected into the TiO₂ matrix with a certain probability. This process leading to positively charged atoms around NPs, which are unstable and have a tendency to dissolve into Ag⁺ ions, is widely known to give rise to multicolor photochromism by selective oxidation of certain sizes of NPs under monochromatic light [Crespo-Monteiro 2011, Nadar 2013, Ohko 2003]. The other hot electrons relax through both electron–electron and electron–phonon collisions, which finally transforms into heat [Inagaki 1985]. It has been experimentally observed that when sufficient heating impacts the

Ag:TiO₂ matrix, Ag ion reduction and NP coarsening also occur, resulting in the growth of Ag NPs [Destouches, Crespo-Monteiro et al. 2014, Crespo-Monteiro 2012]. Plasmon-induced light absorption of Ag NPs therefore produces two opposite processes whose competition controls the temporal evolution of the NP size distribution during CW laser exposure.

Here, we demonstrate that for a fixed pair of laser power and beam width, the speed at which the laser scans the sample surface is a crucial parameter to control the final NP size and organization: Ag NPs shrink at a low scanning speed, whereas growth and self-organization occur above a speed threshold. This phenomenon is counter-intuitive, as higher scan speed corresponds to shorter exposure time which may prohibit the growth of Ag NPs. In order to explain this phenomenon, we have developed a numerical model describing the temporal evolution of the NP size during the beam passage. This model links the transformations among silver atoms (Ag⁰), silver ions (Ag⁺) and silver NPs (Ag NP) in the composite system through the analysis of the involved physico-chemical mechanisms. The theoretical simulations have been compared with experimental observations and the origin of this threshold has been interpreted.

2. Experimentally observed speed threshold

2.1 Studied laser intensity range

A minimum intensity is required to induce the Ag NP growth in TiO₂ matrix. It is widely reported that Ag NPs can be easily oxidized in TiO₂ matrix under visible light exposure due to the Schottky junction formed at the Ag/TiO₂ interface [White 2012]. Indeed, hot electrons of Ag NPs excited by visible light [Clavero 2014] exhibit a higher potential than the conduction band of TiO₂, so that a certain portion of the hot electrons can flow to the conduction band of TiO₂ matrix which results in the oxidation of Ag atoms into Ag⁺ ions at the NP surface, and then in the shrinkage of NPs. The rate of the generated hot electrons is proportional to the incident laser intensity. When the incident intensity is high enough, many hot electrons are generated. But as only one part of them goes to the TiO₂ structure and the others relax through the electron-electron or phonon-electron collisions, an important temperature rise can be finally induced if the incident intensity is high enough, which leads to the growth of Ag NPs.

We remark this intensity threshold by a set of static exposure upon the initial sample. We focus the beam at the 488 nm wavelength on the sample surface to form a spot of 12 μm diameter, and perform 1 s long exposures. We vary only the laser power and a dramatic color change is observed on the sample above a certain threshold (Figure III.1.a). Above this

power threshold, the color change is sharp. Below this threshold, no significant effect occurs. SEM image of one bright dot confirms the emergence of large Ag NPs at the dot center and self-organized Ag NP within a ring out of the center.

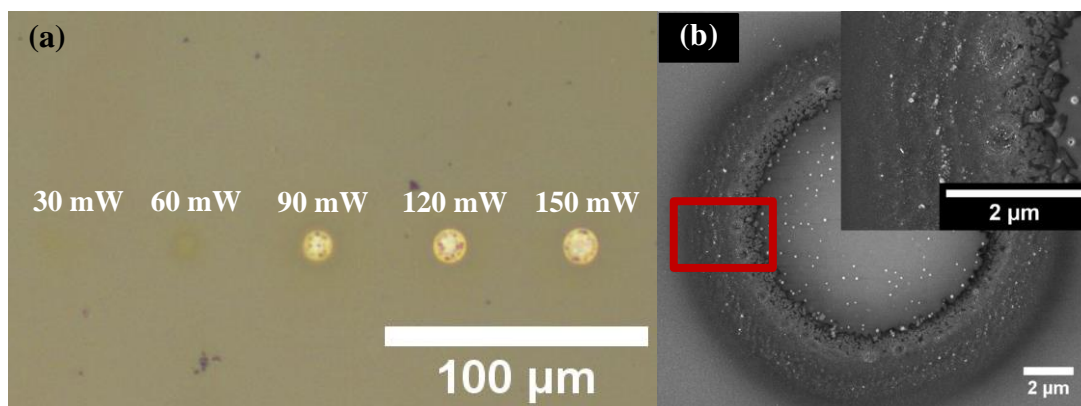


Figure III.1. a. Optical image (in reflection) of laser induced dots under static exposure at different powers and fixed beam width. b. SEM image of one bright dot in (a). Inset figure: zoom at the red rectangular zone.

The exposure time is also tested from 10 ms to 1 min for each power. However, it has no influence on the measured intensity threshold. This implies that the NP growth occurs on a timescale shorter than 10 ms and the NP growth is not an accumulative process under CW laser. The value of the minimum intensity strongly depends on the initial state of the sample and particularly on the volume concentration and size of Ag NPs. For example, at beam width of 12 μm , this threshold is between 60 mW and 90 mW for sample S2 defined in Chapter II. This value is often shifted to around 180 mW upon sample S1. The experiments reported below were carried out with intensities greater than the minimum value leading to the NP growth.

2.2 Speed threshold of laser scan

Using a constant incident power and beam width, both resulting in NP growth, we performed a series of laser scans at different speeds and observed the following surprising behavior: Ag NPs grow only at higher speed and oxidize at low speed. Figure III.2 shows an optical microscopy image of lines drawn on the initial sample S2 at various speeds for different laser powers but same beam width. Each line is 100 μm long and starts with a dot exposure on its left-hand side similar to the case of static exposure. At lower speeds (0.1 mm.s^{-1} for 120 mW and 0.1 mm.s^{-1} , 0.2 mm.s^{-1} for 90 mW), the drawn line only begin with a bright dot and Ag NPs appears to be oxidized in the rest of the line, as no significant color change is observed compared to the initial brown color of the sample. Contrarily, Ag NPs grow and the sample color turns bright at higher speeds (above 0.2 mm.s^{-1} for 120 mW and

above 0.3 mm.s^{-1} for 90 mW). This bright color change can be observed until the scan speeds increase to 30 mm.s^{-1} , which is the maximum speed of our translation stage.

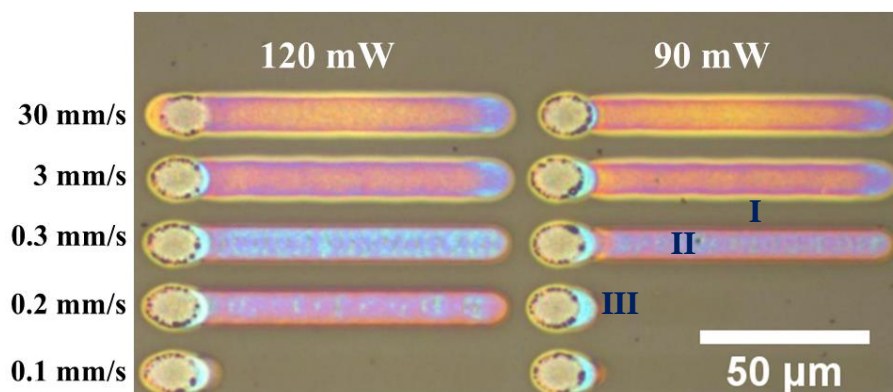


Figure III.2 Optical image (in reflection) of scanning laser-induced micro-inscriptions on a Ag:TiO₂ film. One can identify a speed threshold for a fixed power and beam width.

NP size distributions (Figure III.3) before and after laser scans were then measured by HAADF STEM imaging of the zone marked by I, II and III in figure III.2, which respectively correspond to the initial sample (I), the laser scanned zone at speed above the threshold (II) and below the threshold (III). Size histograms of the NPs distributions constructed by automatic image processing algorithm are plotted on the lower-left part of each figure. They result from measurements of an important quantity of NPs (around 15000 NPs for zone I and II, 2000 NPs for zone 3) in several HAADF STEM micrographs. The accuracy of the distribution center is around $\pm 0.2 \text{ nm}$ in diameter. For the details of the image processing technique and size distribution accuracy, the readers are referred to the section 2.3 of Chapter II and annex I and II of the thesis.

In Figure III.3, the NP size distributions were fitted by a single Gaussian function or superposition of two Gaussian components. In the case of initial sample S2, one peak is centered at 3 nm and corresponds to nanoparticles located near the film top surface (left-hand side of the grey area in Figure III.3.a), and the other is centered at 1.5 nm and corresponds to particles located in the rest of the film. This peak of 1.5 nm corresponds to what was found on initial sample S1, without UV exposure. The larger NPs near the film top surface were principally due to the photocatalytic behavior of TiO₂ in the UV range [Crespo-Monteiro 2014, Destouches 2013].

The NP size histogram confirms the conclusion of the optical images. After exposure, at lower speed (Figure III.3.b, zone I in figure III.2), the average NP size decreases to about 1 nm, whereas a spectacular growth to around 80 nm can be achieved only above the speed threshold, as illustrated in Figure III.3.c (zone II in figure III.2). HAADF-STEM micrograph clearly shows that Ag NPs keep a nearly spherical shape once grown. These grown NPs can self-organize along well-defined 1D gratings under certain exposure conditions (detailed in

Chapter IV) as demonstrated by a previous study of the team [Destouches, Crespo-Monteiro et al. 2014, Destouches, Martinez-Garcia et al. 2014]. The works reported here focus more on the NP growth mechanisms and not on the self-organization.

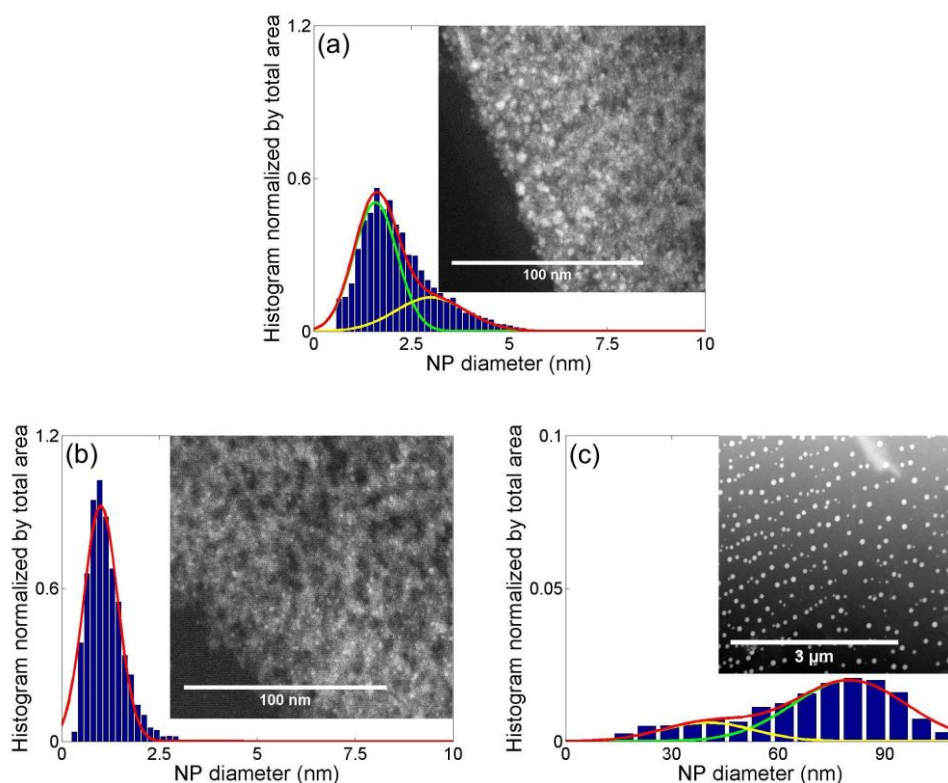


Figure III.3 Size histograms deduced from the HAADF-STEM micrographs of sample S2 before and after laser processing. a: initial state (sectional view of zone I in figure III.2). b: Laser processed zone at scan speed below the threshold (sectional view of zone III in figure III.2). c: Laser processed zone at scan speed above the threshold (top view of zone II in figure III.2).

One can therefore deduce a speed threshold of laser induced Ag NP growth. Below the threshold, NPs only oxidize during the beam passage and film color has not change. Above this threshold, NPs growth can be observed. In the case of figure III.2, the threshold locates between 0.1 mm.s^{-1} and 0.2 mm.s^{-1} for 120 mW and it shifts between 0.2 mm.s^{-1} and 0.3 mm.s^{-1} for 90 mW. The initial dot starting each line still appears even if the shutter is open after the translation stage reaches a constant speed. The opening of the shutter delivers instantaneously the maximum local intensity on the sample surface which creates this dot similar to the case of static exposure. However, below the speed threshold, NP growth only occurs in the initial dot but cannot hold when scanning the film.

2.3 Temperature rise during NP growth

According to the theory described in section 2.1, the growth of Ag NP is assisted by the temperature rise due to the plasmon absorption of Ag NPs in TiO_2 film. Here we

experimentally demonstrate this temperature rise, by the collapse of the TiO_2 meso-structure and crystallization of TiO_2 layer after the growth of Ag NPs.

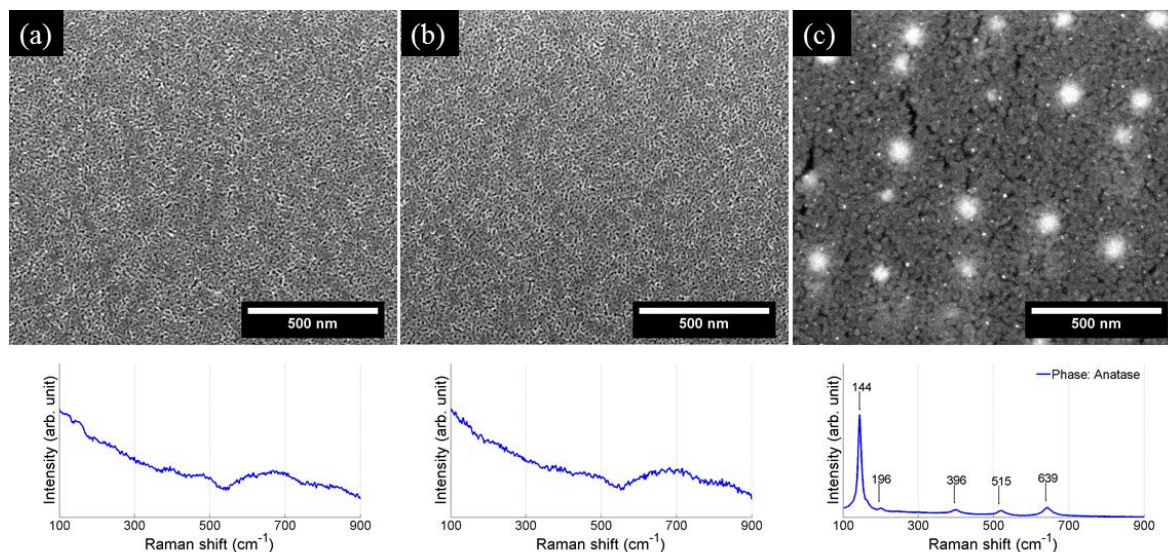


Figure III.4 SEM images (top) and Raman spectrums (bottom) of initial sample S2 (a), laser-scanned zone at speed below (b) and above (c) the speed threshold. Collapse of the TiO_2 meso-structure and crystallization of the TiO_2 only occurs at speed above the threshold.

Figure III.4 reports the SEM images and Raman spectra upon the initial sample S2 and the laser scanned zone at speed above and below the threshold. As presented in Chapter II, the initial TiO_2 film is amorphous and mesoporous. Below the threshold, the film remains mesoporous whereas above the threshold the mesostructure totally disappears and large spherical Ag NPs (brighter spherical zones in SEM images) emerge, buried in the film (they appear blurred on SEM micrographs).

The crystallization of the TiO_2 layer also occurs above the speed threshold. Below the threshold (Figure III.4.b), the Raman spectrum is the same as the one of the initial amorphous sample, where no significant peaks can be observed on the spectra. Above the speed threshold (Figure III.4.c), signature peaks of TiO_2 anatase at 144, 196, 396, 515, 639 cm^{-1} appear. This crystallization reveals an important temperature rise induced by the laser scan. According to the literature [Cheng 1995, Ocana 1992, Kholmanov 2003], amorphous TiO_2 turns into anatase phase at a high temperature usually around 400°C, which gives the minimum temperature rise achieved during laser scans.

ADF STEM image (Figure III.5.a) of a zone between two self-organized Ag NP lines confirms also the crystallization of the film in small nano-crystals. These crystals can be also assigned to the anatase phase of TiO_2 according to the indexing of the diffraction pattern of HR HAADF STEM images (Figure III.5.b). Besides, figure III.5.a shows also the small spherical Ag NP particles of around 3 nm between self-organized Ag NP lines.

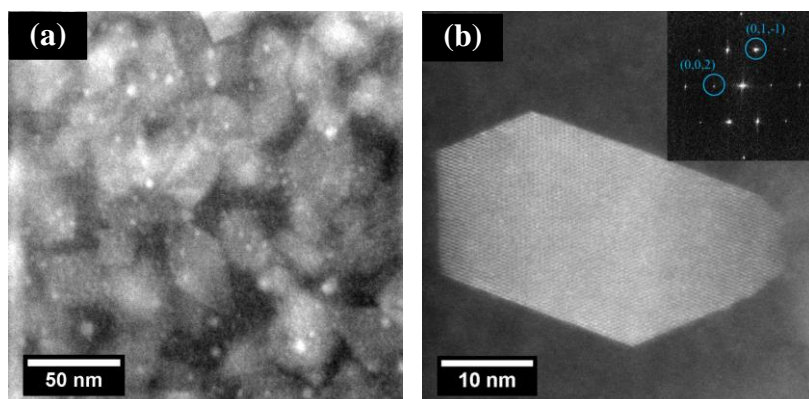


Figure III.5. a: ADF STEM image of a zone between two self-organized Ag NP lines after laser scan at speed above the threshold. b: HR HAADF STEM image of one crystal in the same sample of a. Inset figure: Diffraction pattern of b. The circled peak can be assigned to the (0,1,-1) and (0,0,2) zone axis of TiO_2 anatase.

3. Modeling with mono-size approximation

In order to explain this counter-intuitive behavior of NP growth, we propose a relatively simple model that predicts the temporal size variation of Ag NPs under CW laser scan. Three main reactions are coupled in the model, which influences NP size as well as temporal evolution of silver atoms between its three forms: Ag^0 , Ag^+ and Ag NPs (Figure III.6). We consider an oxidation reaction that decreases the Ag NPs size and increases the number of Ag^+ ions, a reduction reaction which converts Ag^+ to Ag^0 , and an Ostwald Ripening growth reaction that increases the NP size by adsorption of Ag^0 atoms to NPs. All these reactions are controlled by laser light and plasmon-induced temperature rise. The oxidation rate is proportional to the number of absorbed photons per unit time, whereas reduction and growth depend on the film temperature rise during laser exposure. The model therefore also includes the calculation of the film optical absorption through the plasmon resonance of Ag NPs, thermal heating and atomic diffusion.

The model is developed under mono-size approximation of the NP distribution. One can follow the global Ag NP size variation by only considering one Ag NP, which largely simplifies the involved equations. The NP volume concentration is experimentally found to decrease with the growth of NP. This feature is also taken into account through an additional empirical equation which describes the NP volume concentration as a function of the NP size. Parameters of this equation were fitted with experimental data. The mathematical and numerical details for each involved reactions is presented in the sub-sections below. It gives rise to a set of Ordinary Differential Equations (ODEs). They are numerically integrated by

considering a time dependent intensity distribution with a Gaussian shape, whose temporal width depends on the beam diameter and the scan speed.

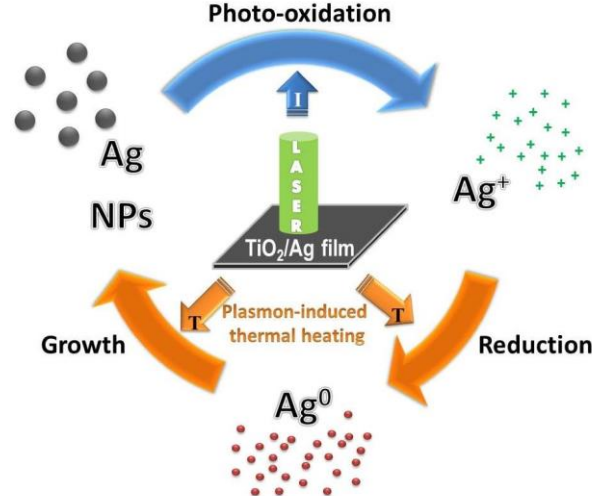


Figure III.6. Illustration of the three main chemical reactions that control the distribution of silver between its three possible forms activated either directly by the laser intensity or by the plasmon-induced temperature increase.

3.1 Photo-oxidation

For one NP of radius R_{NP} , the number of silver atoms oxidized per unit time is proportional to the number of photons it absorbs:

$$Oxy(R_{NP}, t) = \frac{\eta I(t) \sigma_{abs}(R_{NP})}{h f_{inc}} \quad (III.1)$$

where h is the Planck constant, f_{inc} is the incident frequency, $I(t)$ the instantaneous incident laser intensity within the Ag:TiO₂ film at the position of the considered NP, $\sigma_{abs}(R_{NP})$ the absorption cross-section of the considered NP and η the ionization quantum efficiency of silver in TiO₂.

The absorption cross-section σ_{abs} corresponds to the effective projected area of an NP in the direction of incident light, within which light is fully harvested and absorbed by the NP. It is calculated for each NP size using the Mie theory [Mie 1908] for spherical particles (codes proposed by Scott Prahl). The absorption cross-section can be expressed as a complex function of incident wavelength, NP size, refractive index of the NP and its surrounding medium (TiO₂ matrix). In particular, Localized Surface Plasmon Resonance (LSPR) of Ag NPs was also taken into account by considering a corrected refractive index of Ag NP, n_{NP} . The latter is calculated from the expression of the dielectric function of bulk silver corrected in size according to the classical free path effect [Kreibig et Vollmer 1995]. The incident wavelength (488nm) and refractive index of TiO₂ matrix ($\cong 1.7$) are treated as constants in

this study. Finally, the absorption cross-section of Ag NP can be expressed as $\sigma_{abs}(R_{NP}, n_{NP}(R_{NP}))$ or even simplified as $\sigma_{abs}(R_{NP})$ in the following text. In figure III.7, the absorption cross-section σ_{abs} is plotted as a function of the Ag NP radius R_{NP} under light excitation at 488nm. One observes clearly that the LSPR induces a strong increase in the absorption for NPs of radius between 18nm and 23nm.

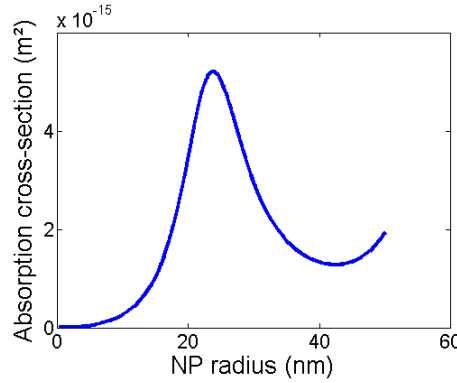


Figure III.7. Absorption cross section of Ag NP embedded in TiO₂ matrix calculated by Mie theory under incident excitation at 488 nm.

$I(t)$ can be written as $I(t) = I_0(t)(1 - R_{tot}(t))$ where $I_0(t)$ is the instantaneous incident intensity whose analytic form will be discussed in section 3.6 of this chapter and $R_{tot}(t)$ the total reflectivity of the sample considering multiple wave interferences within the TiO₂ film [Born 1999]. To calculate $R_{tot}(t)$, the film is divided into two layers of equal thickness. The top layer contains NPs with a fixed size (the initial one) and the bottom one contains the studied NPs whose size varies in time. This two-layer model is in line with previous results of the team, which show that the final samples consist of a plane of grown NPs buried within the TiO₂ film near the film/substrate interface [Destouches, Crespo-Monteiro et al. 2014]. This plane is covered with a thin layer of TiO₂ that may contain very small silver NPs as those shown in Figure III.5.a. Experimental characterizations of films suggest a thickness of 100 nm for each layer. The refractive index of the glass substrate was estimated as 1.35. The refractive index of Ag NP:TiO₂ layer were deduced using the Maxwell-Garnett theory [Garnett 1904] in which Ag NPs were considered as inclusions of mono-size within TiO₂ matrix. The volume concentration of Ag NPs in the bottom layer varies also with the NP size, which will be discussed later in section 3.5.

The term $I(t)\sigma_{abs}(R_{NP})$ gives therefore the power absorbed by one NP of radius R_{NP} . The term hf_{inc} corresponds to the energy of one photon at frequency f_{inc} . One can deduce that $I(t)\sigma_{abs}(R_{NP})/hf_{inc}$ gives the number of incident photons absorbed by the NP per unit time. As we previously described in section 2.1, only a few part of these absorbed photons can flow into the conduction band of TiO₂ matrix and thus lead to the oxidation of Ag NPs. We use therefore, the ionization quantum efficiency, η , to estimate the percentage of hot electrons that contribute to the NP oxidation. In the studied Ag:TiO₂ system, η can depend

on the geometric feature of the TiO_2 matrix and is estimated from experimental results where only oxidation occurs. This was performed by working with a laser power below the power threshold and measuring time variations of the sample transmittance [Crespo-Monteiro 2010].

3.2 Reduction

The growth of silver NPs is described by a two-step model adapted from reference [Kaganoskii 2007] where silver ions are firstly reduced to silver atoms, which diffuse to be adsorbed on silver NPs.

In this earlier work, the reduction reaction was limited by the diffusion of the reducing agent in the film that must be caught by the “trap-type” silver ions for their reduction. The film thickness was higher than 1 μm and a depth-dependent silver ions concentration was used in this reference work. Our layers, in contrast, are only 100 nm thick. As a consequence, with the assumption that the silver ions mobility is sufficiently high, we consider an homogeneous distribution of silver ions at any time. We therefore write the number of Ag^+ ions reduced per unit time and per unit volume as:

$$\text{Red}(t) = K \times C_{\text{Ag}^+} \times C_{\text{red}} \quad (\text{III.2})$$

where, C_{red} and C_{Ag^+} are respectively the volume concentration of the reducing agent and silver ions within the $\text{Ag}:\text{TiO}_2$ film. K is the capture coefficient of the reducing agent. The physical meaning of the term $K C_{\text{Ag}^+}$ can be explained as the average frequency at which a reducing agent is caught by a silver ion and then reduced into Ag^0 . This frequency is estimated by $p D_{\text{red}} / l^2$, where D_{red} is the diffusion coefficient of the reducing agent, l is the average distance between two Ag^+ given by $C_{\text{Ag}^+}^{-1/3}$ and p is the probability of Ag^+ ion reduction once a reducing agent is trapped. The diffusion coefficient D_{red} has a unit of $\text{m}^2 \cdot \text{s}^{-1}$ which can be interpreted as the mean squared displacement of one particle under stochastic process per unit time. The term D_{red} / l^2 corresponds to the average frequency at which a reducing agent is caught by one of the Ag^+ in the film and $p D_{\text{red}} / l^2$ is therefore the average frequency at which an Ag^+ is successfully reduced. One can rewrite the Eq.III.2 as:

$$\text{Red}(t) = p(t) D_{\text{red}}(t) C_{\text{red}} C_{\text{Ag}^+}^{2/3}(t) = e^{\frac{-E_p}{k_B T(t)}} \cdot D_r e^{\frac{-E_D}{k_B T(t)}} C_{\text{red}} C_{\text{Ag}^+}^{2/3}(t) \quad (\text{III.3})$$

As noted in the right-hand side of Eq.III.3, $p(t)$ and $D_{\text{red}}(t)$ are actually not direct functions of time but functions of the absolute film temperature $T(t)$ that varies in time. The temperature dependence of p and D_{red} can be reasonably described by the Arrhenius law, as written in the right-hand side of Eq.III.3 where E_p and E_D are activation energies and k_B is the Boltzmann constant.

The reducing agent is not clearly identified in our system yet, it may be atmospheric H_2 , CO , NO_3^- the counter ion from the initial silver nitrate solution, TiO_2 itself at high temperature or even other chemical compounds in the glass substrate. In any case its concentration can reasonably be assumed to be constant. Specific experiments need to be carried out in the future to identify chemical species that contribute to the reduction of silver ions during laser exposure under high intensity. However, whatever the reducing agents involved in this reaction, the analytical form of Eq.III.3 will remain the same. To run numerical calculations, we will consider D_r values close to the diffusion coefficient of H_2 in mesoporous systems at room temperature and for E_D the activation energy of the reduction reaction of silver ions by H_2 .

3.3 Ostwald ripening growth

The Ag NP growth process is considered here as an Ostwald Ripening process in which two phases are distinguished: the cluster and the monomer. The cluster is Ag NP in our case. The monomer is the Ag^0 that is initially present in the film and whose concentration then increases with the previous reduction step. In an Ostwald Ripening process, the growth of one Ag NP relies on the adsorption of single atom Ag^0 which is diffused by a force raised from the difference in Ag^0 volume concentration at macroscopic scale and at Ag NP surface. Let's denote the Ag^0 flow, coming from macroscopic scale toward one NP, as J_{Ag^0} . The number of absorbed Ag^0 atom on one Ag NP of radius R_{NP} per unit time by Ostwald Ripening process, grw , can be written as the product between the flow $J_{Ag^0}(R_{NP})$ at NP surface and the surface area of the Ag NP:

$$grw = J_{Ag^0}(R_{NP}) \times 4\pi R_{NP}^2 \quad (III.4)$$

In order to give the analytical formulation of J_{Ag^0} , one needs to defined the Ag^0 volume concentration at the Ag NP surface and at macroscopy scale. The classical formulation of Ostwald Ripening is given by the Lifshitz-Slyozov-Wagner (LSW) theory [Lifshitz et Slyozov 1961, Wagner 1961] where the Ag^0 volume concentration at the Ag NP surface of R_{NP} radius can be written as:

$$C_{R_{NP}} = S + 2\gamma\omega S/k_B T R_{NP} \quad (III.5)$$

where, S is the solubility of Ag^0 , γ is the interface tension between the Ag NP and the matrix and ω is the atomic volume of Ag in a NP. For FCC crystals, $\omega = a^3/4$, where the lattice parameter of silver a equal to 0.4086 nm. k_B is the Boltzmann constant. T is the absolute temperature. At macroscopic scale the Ag^0 volume concentration C_{Ag^0} is increased by the reduction reaction of the previous section. One can then formulate the steady state solution of appropriate diffusion equation for Ag^0 volume concentration c_{Ag} as [Kaganovskii 2007]:

$$c_{Ag}(r) = C_{Ag^0} - (C_{Ag^0} - C_{RNP}) \frac{R_{NP}}{r} \quad (III.6)$$

where, r is the distance between the considered point and the center of the Ag NP of radius R_{NP} . One deduces easily that Eq.III.6 satisfies the boundary conditions that at Ag NP surface, $r = R_{NP}$, we have $c_{Ag}(R_{NP}) = C_{RNP}$ and at macroscopy scale $c_{Ag}(\infty) = C_{Ag^0}$. The Ag^0 flow towards Ag NP can be yielded by the Fick's first law using the gradient of $c_{Ag}(r)$ at Ag NP surface and D_{Ag^0} diffusion coefficient of Ag^0 :

$$J_{Ag^0}(R_{NP}) = D_{Ag^0} \frac{\partial c_{Ag}}{\partial r} \Big|_{r=R_{NP}} = D_{Ag^0} \frac{C_{Ag^0} - C_{RNP}}{R_{NP}} = D_0 e^{\frac{-E_{D_0}}{k_B T(t)}} \frac{C_{Ag^0} - C_{RNP}}{R_{NP}} \quad (III.7)$$

Eq.III.7 shows that for NPs whose radius satisfies $C_{Ag^0} > C_{RNP}$, the NP will grow by atomic adsorption. As the diffusion coefficient in the previous section, D_{Ag^0} also depends on the temperature rise within the film and follows the Arrhenius' law. One can rewrite $D_{Ag^0} = D_0 e^{\frac{-E_{D_0}}{k_B T(t)}}$ where E_{D_0} is the activation energy of D_{Ag^0} and D_0 is the diffusion coefficient at infinitely high temperature. In conclusion, J_{Ag^0} is a function of absolute temperature $T(t)$ varying in time and R_{NP} also depends on time. Finally we can simplify Eq.III.4 as:

$$grw(t) = J_{Ag^0}(t) \times 4\pi R_{NP}^2(t) \quad (III.8)$$

3.4 Temperature rise and NP volume concentration

The Ag^+ reduction and Ag NP growth are both assisted by the temperature of the Ag:TiO₂ film. The latter is calculated using the model developed by I. D. Calder et R. Sue [Calder 1982] to determine the CW laser annealing for a general multilayer structure. This model is adapted here to our two-layer system deposited on glass substrate, as described in section 3.1. In this model, the absorption coefficient is supposed to be homogenous under the Gaussian laser beam and an analytical expression is proposed for the laser induced temperature rise at steady state. We esteemed that using the steady state solution is well suited in our case. Temperature is known to stabilize in the picosecond regime [Von der Linde 1997] and the scan speeds used in these experiments are sufficiently slow ($\mu m.s^{-1}$ order) so that the time step to solve the differential equations is larger than picosecond. In this model, the temperature rise upon laser exposure depends on the incident power, the beam width, the distance between the considered point and the beam center, the reflection coefficient of the sample, and the layer thicknesses; it also depends on the thermal conductivity of the different layers and their absorption coefficients. Thermal conductivities are assumed to be constant and are chosen in reasonable ranges of values for the nanocomposite layers (from 10 W/(m·K) to 30 W/(m·K)) or for the glass substrate (2

W/(m·K)). TiO₂ is fully transparent at the visible wavelength used to grow Ag NPs and does not contribute to the film absorption. The film absorption is only due to the presence of silver NPs and its absorption coefficient α is then deduced by

$$\alpha = \sigma_{abs}(R_{NP}) \times C_{NP} \quad (\text{III.9})$$

where C_{NP} is the NP volume concentration and $\sigma_{abs}(R_{NP})$ is the absorption cross-section calculated from the Mie Theory for one NP, as already explained in section 3.1.

The NP volume concentration decreases strongly with the growth of NPs, as shown by the HAADF STEM micrographs in the section 2. Table III.1 gives experimental values obtained after different treatments on initial samples S1 and S2 where the NP volume concentration can vary up to four orders of magnitude after the CW laser scan. This suggests that the NP volume concentration should not be considered as constant during the size variations of NPs. An empirical law is proposed to fit the experimental data. This law corresponds to a linear variation of the interparticle distance with the NP size. It leads to the following relation between the NP volume concentration C_{NP} and the NP radius R_{NP} :

$$C_{NP}(t) = 1/(mR_{NP}(t) + n)^3 \quad (\text{III.10})$$

where coefficients m and n are fitted from values of Table III.1 to 2.6 and 8.7×10^{-9} , with R_{NP} and C_{NP} expressed respectively in m and m⁻³ (Figure III.8).

Sample	Measured Average NP diameter (nm)	Measured Average NP radius (nm)	Measured NP volume concentration (m ⁻³)	Fitted NP volume concentration (m ⁻³)
S2 after NP oxidation	1	0.5	$13.2 \times 10^{23} \pm 5.5 \times 10^{23}$	10×10^{23}
S1 initial state	1.5	0.75	$10.8 \times 10^{23} \pm 6.5 \times 10^{23}$	8.2×10^{23}
S2 initial state	3	1.5	$9.8 \times 10^{23} \pm 7.2 \times 10^{23}$	5.0×10^{23}
S2 after NP growth	80	40	$3.0 \times 10^{20} \pm 2.1 \times 10^{20}$	6.9×10^{20}

Table III.1. Average NP volume concentration and diameter measured on samples after different treatments and the NP volume concentration fitted by relation in Eq.III.10

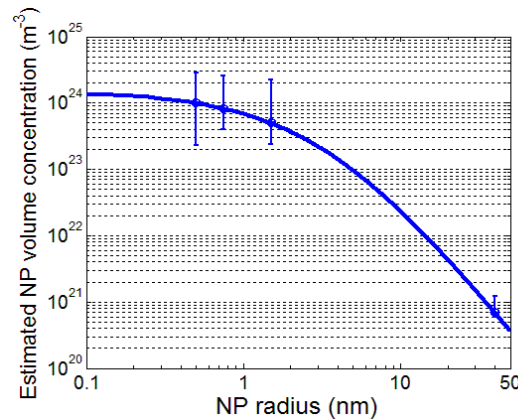


Figure III.8. Volume concentration of NPs versus NP radius plotted using Eq.III.10. Error bars are plotted according to the data reported in Table III.1

We introduced Eq.III.10 in the model, which consists in taking the coalescence phenomenon into account and to force the theoretical volume concentration of NPs to decrease when the NP size increases. According to results reported on similar systems [Martinez 2014, Kim 2008, Sun 2006], coalescence is indeed expected to occur at high temperature during the laser scan. In our sample, we have already mentioned that the increase of temperature during the laser scan is higher than the crystallization temperature of TiO_2 in the anatase (>700 K). This temperature is much higher than the Tammann temperature of Ag NPs. The latter is considered as the threshold temperature above which bulk atoms tend to move, leading to NP coalescence. The Tammann temperature is usually estimated by the half of the melting point [Sun 2006], which is 1233 K for bulk silver. However, in the case of Ag NPs, this temperature significantly decreases when the NP size decreases [Castro 1990, Luo 2008]. The melting point of Ag NPs only 3 nm in diameter is less than 850K, and this temperature decreases to 680K for 2 nm NPs, which is lower than the crystallization temperature of TiO_2 anatase. Note however that liquid silver remains in the film.

3.5 Coupling of Equations

We can now deduce the final Ordinary Differential Equations (ODEs) set for our system containing Ag^+ , Ag^0 and Ag NP. Let's firstly focus on the size variation of Ag NPs. The quantity of silver atoms, $N_{\text{Ag}_{1\text{NP}}}$, in one NP of radius R_{NP} is varied by the Ostwald Ripening (Eq.III.8) and Photo-oxidation(Eq.III.1):

$$\frac{dN_{\text{Ag}_{1\text{NP}}}(t)}{dt} = (\text{grw}(t) - \text{oxy}(t)) \quad (\text{III.11})$$

Under the assumption of spherical NPs, one finds also $N_{\text{Ag}_{1\text{NP}}}(t) = 4\pi R_{\text{NP}}^3(t)/3\omega$, where ω is the atomic volume of Ag, as already defined. The variation of the NP radius with respect to time can be written as:

$$\frac{dR_{\text{NP}}(t)}{dt} = \frac{\omega}{4\pi R_{\text{NP}}^2(t)} (\text{grw}(t) - \text{oxy}(t)) \quad (\text{III.12})$$

If we consider all the NPs within unit volume, the total number of Ag atoms in phase Ag NP can be written as $C_{\text{Ag}_{\text{NP}}}(t) = C_{\text{NP}}(t)N_{\text{Ag}_{1\text{NP}}}(t)$, where the two terms in the right hand side of the equation are both functions of time. The temporal variation of $C_{\text{Ag}_{\text{NP}}}(t)$ is then:

$$\frac{dC_{\text{Ag}_{\text{NP}}}(t)}{dt} = C_{\text{NP}}(t) \frac{dN_{\text{Ag}_{1\text{NP}}}(t)}{dt} + N_{\text{Ag}_{1\text{NP}}}(t) \frac{dC_{\text{NP}}(t)}{dt} \quad (\text{III.13})$$

One can then simplify the second term in the right hand part of Eq.III.13 as follows:

$$N_{Ag_{1NP}}(t) \frac{dC_{NP}(t)}{dt} = N_{Ag_{1NP}}(t) \frac{dC_{NP}(t)}{dR_{NP}(t)} \frac{dR_{NP}(t)}{dt} \quad (III.14)$$

Substituting the Eq.III.12, we have:

$$N_{Ag_{1NP}}(t) \frac{dC_{NP}(t)}{dt} = \frac{R_{NP}(t)}{3} \frac{dC_{NP}(t)}{dR_{NP}(t)} (grw(t) - oxy(t)) \quad (III.15)$$

substituting also Eq.III.11 in the first term of the right hand part of Eq.III.13, we rewrite Eq.III.13 as follow:

$$\frac{dC_{Ag_{NP}}(t)}{dt} = (C_{NP}(t) + \frac{R_{NP}(t)}{3} \frac{dC_{NP}(t)}{dR_{NP}(t)}) (grw(t) - oxy(t)) \quad (III.16)$$

One can then deduce from Eq.III.16 that the number of Ag atoms consumed per unit volume by Ostwald Ripening is $(C_{NP}(t) + \frac{R_{NP}(t)}{3} \frac{dC_{NP}(t)}{dR_{NP}(t)}) grw(t)$. And the number of Ag ions produced per unit volume by Photo-oxidation is $(C_{NP}(t) + \frac{R_{NP}(t)}{3} \frac{dC_{NP}(t)}{dR_{NP}(t)}) oxy(t)$.

Now, it becomes easy to write the temporal change of Ag^+ and Ag^0 volume concentration. Oxidation turns the silver atoms in NPs into Ag^+ ions, and the reduction transforms Ag^+ into free silver atoms Ag^0 . So the variation in the Ag^+ ions volume concentration is:

$$\frac{d}{dt} C_{Ag^+}(t) = -red(t) + oxy(t) \left(C_{NP}(t) + \frac{R_{NP}(t)}{3} \frac{dC_{NP}(t)}{dR_{NP}(t)} \right) \quad (III.17)$$

Similarly, the temporal variation of free silver atoms Ag^0 volume concentration is given by:

$$\frac{d}{dt} C_{Ag^0}(t) = red(t) - grw(t) \left(C_{NP}(t) + \frac{R_{NP}(t)}{3} \frac{dC_{NP}(t)}{dR_{NP}(t)} \right) \quad (III.18)$$

The final ODE set is given by Eq.III.12, Eq.III.17 and Eq.III.18. We notice that the sum of Eq.III.16, Eq.III.17 and Eq.III.18 yields zero, which corresponds to the conservation of matter in the system. This three dimension ODE set is solved by Matlab using ode15s solver which gives the best time/accuracy compromise.

3.6 Simulation Parameters

The incident wavelength is 488nm and the cross section of the incident beam intensity has a Gaussian shape. The time range for simulation is defined by the beam width and scan speed of laser. Let us consider a XY space where the simulated NP locates at its origin point (Figure III.9). The laser beam scans along the positive X-axis direction. Therefore, the simulation begins when the beam center arrives at position $(-2\omega_r, 0)$ and finishes when

the beam center arrives at $(2\omega_r, 0)$, where ω_r is the laser beam radius at $1/e$ of the maximum intensity. The time range for simulation is then $[0, 4\omega_r/v]$, where v is the laser scan speed. One can write the analytical expression of instantaneous light intensity, for a given laser power P , as:

$$I_0(t) = \frac{P}{\pi\omega_r^2} \exp\left(-\left(\frac{tv-2\omega_r}{\omega_r}\right)^2\right) \quad (\text{III.19})$$

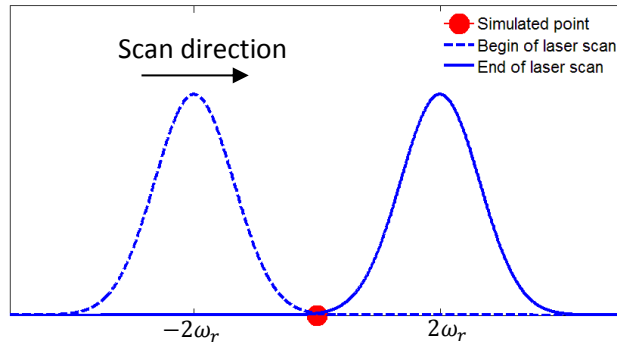


Figure III.9 Illustration of simulated Gaussian laser scan on a considered point of Ag:TiO₂ composite.

Not all of the parameters involved in the ODE system have an important influence on the simulation results. So, for instance, changing the value of the Ag⁰ solubility S or of the element $2\gamma\omega/Tk_B R_{NP}$ in Eq.III.5, in a reasonable range that we can deduce from the literature does not change significantly the final results. According to Kaganovskii et al [Kaganovskii 2007], the solubility S is small and we estimated its value in between 1×10^{-24} and 1×10^{-25} [Prudenziati 2004, von Goetz 2013]. $\gamma\omega/Tk_B$ at 500 K is in the range from 0.5 nm to 5 nm [Kaganovskii 2007], *i.e.* γ in the range from 0.2 J/m² to 2 J/m². Also, the diffusion coefficient D_{red} of H₂ and its concentration C_{red} do not significantly influence the simulated results (see Table III.2 for their variation range). In the literature [Shang 2009, Torresi 1987, Battisti 2011, Haran 1998, George 1985, Korn 1970, Vykhodets 2005], the activation energy E_D of H₂ diffusion is found to vary from 0.01 eV to 0.1 eV and the diffusion coefficient at infinitely high temperature D_0 is estimated to vary from 1×10^{-15} to 1×10^{-10} m².s⁻¹. The activation energy E_p of the reduction reaction probability is chosen at about 0.7×10^{-19} J, *i.e.* 0.4 eV, as in the work of Kaganovskii et al.[Kaganovskii 2007], it has however, as all these parameters, no significant influence on the simulation results.

On the contrary, the diffusion coefficient D_{Ag0} of free silver atom Ag⁰ and the metallic ionization quantum efficiency η have an important influence on the simulation results as they directly influence the NP size. It is difficult to evaluate the precise value of the activation energies of different diffusion processes in mesoporous TiO₂ film, as they strongly depend on the characteristic of the film for instance the film porosity or the crystallization state. But a reasonable value range can be estimated from the activation energy of similar materials. We chose therefore the activation energy of Ag⁰ diffusion within the value range

from 0.5 eV to 1.5 eV. The diffusion coefficient of Ag^0 at 500K can vary from 5×10^{-17} to $1 \times 10^{-14} \text{ m}^2 \cdot \text{s}^{-1}$ [McBrayer 1986, Butrymowicz 1974, Miotello 2000]. As explained in the section 3.1, the ionization quantum efficiency of Ag in TiO_2 , η , can depend on the geometric feature of the TiO_2 matrix and is estimated from experimental results where only NP shrinkage occurs [Crespo-Monteiro 2010]. The value of this η is chosen in the range from 6×10^{-5} to 1×10^{-7} .

These parameters are resumed in the table below.

η	E_p (eV)	D_{red} (m^2/s)	E_D (eV)	D_{Ag0} (m^2/s)	E_{Ag0} (eV)	C_{red} (m^{-3})	γ (J/m^2)	S (m^{-3})
6×10^{-7} - 6×10^{-5}	0.4	1×10^{-10} - 1×10^{-15}	0.01-0.1	5×10^{-17} - 1×10^{-14}	0.5-1.5	1.5×10^{20} - 1.5×10^{21}	0.2 - 2	1×10^{24} - 1×10^{25}

Table III.2. Values of parameters used in simulation. The values of the diffusion coefficients of reducing agent D_{red} and silver atom D_{Ag0} are presented for the case of $T=500\text{K}$.

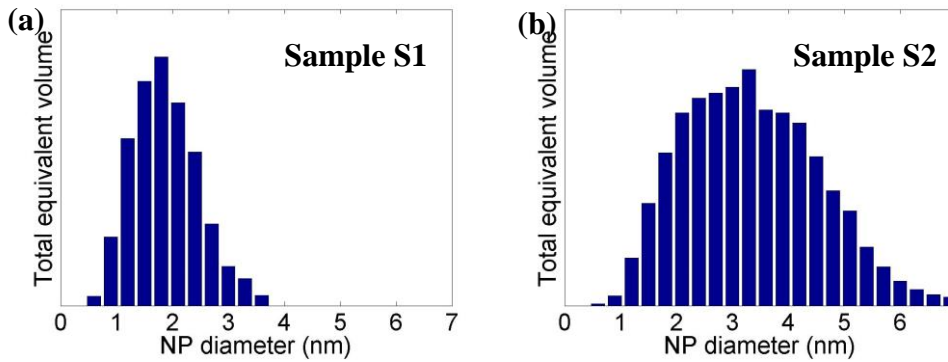


Figure III.10. Histograms of total equivalent volume versus NP size for initial sample S1 (a) and S2 (b). The initial NP size used in simulated is then respectively chosen at 1.8 nm and 3 nm for S1 and S2.

Assuming that all silver can be reduced into Ag NPs at the end of the laser scans in growth regime (speeds above the threshold), the total quantity of silver presented in the initial sample can be estimated according to the quantity and average size of grown Ag NPs estimated from its HAADF STEM micrographs. The latter suggests a total Ag quantity varying from $3 \times 10^{27} \text{ m}^{-3}$ to $3 \times 10^{28} \text{ m}^{-3}$. We consider the higher one for the simulations. In this work, Ag^0 , Ag^+ concentration is respectively chosen at $1.2 \times 10^{28} \text{ m}^{-3}$ and $0.6 \times 10^{28} \text{ m}^{-3}$, which is one possible parameter set that allows to obtain the experimentally observed phenomena. Considering the initial NP size, sample S2 exhibits two size distributions centered on 1.5 and 3 nm respectively (Figure III.3). The growth processes (Reduction and Ostwald Ripening) are both activated by the temperature rise within the film which depends on the absorption of NPs for a given incident light intensity. Since the model works under mono-size approximation, it is more appropriate to consider as the initial NP size, the one that imposes the temperature rise but not the average NP size. For very small NPs, the absorption cross-section of NPs given by the Mie theory is found to be proportional to the NP volume, after a simplification under the quasi-static approximation [Born 1999]. The initial sizes of NP used in the simulations are chosen as the size whose total volume is more representative than

others. Figure.III.10 shows the histograms of the total volume of NPs of each size per unit volume with respect to the NP size for initial sample S1 and S2. The height of each bar in histogram is calculated by the product between the volume of one NP and its volume concentration. Average initial diameter of 1.8 nm and 3 nm are respectively used for simulations of sample S1 and S2.

4. Comparison of numerical and experimental results

4.1 Origin of the speed threshold

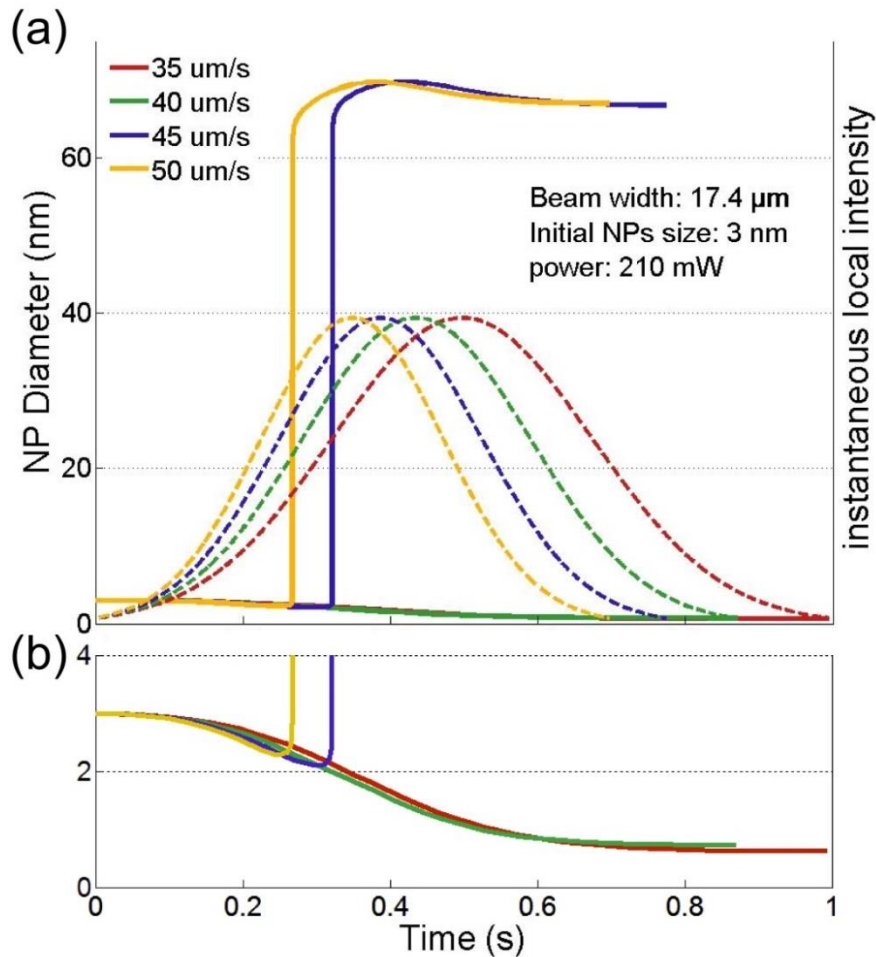


Figure III.11 Temporal profile of NP size under laser scans at different speeds. The dotted lines are the instantaneous incident intensities and the continuous lines are the NP size variation.

The resolution of the ODE set gives the temporal variations of the NP size during the laser scan. The experimentally observed threshold behavior of NP growth is also found in

simulation results. As shown in Eq.III.19, the temporal width of the Gaussian beam recorded from a fixed point is defined by the spatial width of the beam and its scan speed. By only decreasing the scan speed, one enlarges the temporal width of the Gaussian beam, which is shown as the dotted lines in Figure III.11. We notice that the scan speed greatly influences the NP size variation (continuous lines in Figure III.11). The experimentally observed speed threshold is found here between 40 and 45 $\mu\text{m.s}^{-1}$. Similar to the experimental results shown in Figure III.3, the final NP size is smaller than the initial one at speeds below the threshold and is much larger than the initial size above the threshold. The kinetics of oxidation and growth process are also given by the simulations. Above the threshold, the growth kinetic (grw in Eq.III.12) leads to a sharp increase in the NPs size. The latter then tends to saturate before the end of laser scan.

The origin of the speed threshold can be explained in the following manner:

1- The NP growth phenomenon depends on the temperature rise within the film. For one NP, the quantity of oxidized atoms is proportional to the number of absorbed photons (Eq.III.1). It increases linearly with the instantaneous local intensity and with the absorption cross-section of Ag NPs. However, for the growth process, the quantity of absorbed free silver atom Ag^0 (Eq.III.7 and Eq.III.8) doesn't directly depends on the instantaneous local intensity and Ag NP absorption but on the temperature rise within the film. Moreover, this quantity increases exponentially, but not linearly, with the temperature rise. So, one gets the same conclusion as shown in section 2.1: for a given size of NP (a given Ag NP absorption), only if the incident intensity is sufficient high, the growth process can get over the oxidation process, thanks to the exponential growth laws.

2- In the case of Gaussian scan beam, the temporal profile of the intensity needs to be taken into consideration as it influences the film absorption. At the beginning of laser scan, as the low intensity arrives firstly on the considered point, oxidation predominates over the growth process and starts decreasing the NPs size. At lower speeds, this oxidation lasts longer and decreases the NP size and the related absorption at a value small enough to inhibit any significant temperature increase during the laser beam passage. In this case, even at the highest laser intensity (at beam center), oxidation always predominates over growth. On the contrary, at higher speeds, oxidation last shorter and the laser encounters less oxidized NPs, *i.e.* larger NPs. The laser intensity increases rapidly enough and the absorption of NPs is still sufficient to create a significant temperature rise leading to the growth process.

The surprising fast jump of NP growth comes from the nonlinear feature and the feedback mechanisms of the equations. Once NPs begin to grow (from around 2-3 nm), the absorption of the film (Figure III.12) increases and leads to a higher temperature rise within the film. The latter then enhances again the NP growth. This positive feedback loop results in the fast jump observed on the NP growth. The self-stabilization of this fast jump then results

from the lower film absorption at larger sizes of NPs. Once the absorption coefficient starts decreasing, from a NP radius of around 22 nm, the temperature rise rapidly decreases and the growth kinetic slows down to about the same level of oxidation kinetic.

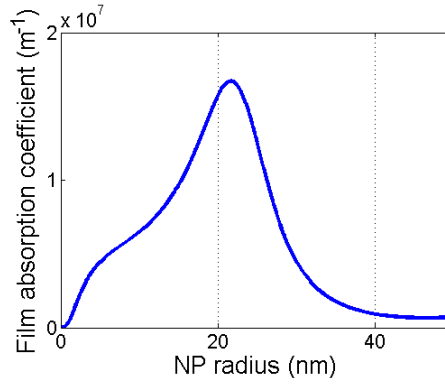


Figure III.12. The Ag:TiO₂ film absorption coefficient plotted as a function of Ag NP radius by considering the Ag NP volume concentration law defined in Eq.III.10

4.2 Dependence of the threshold value on other parameters

The experimental parameters that have a major influence on the threshold are studied numerically. By comparing with experimental results, the relevance of the model is again validated. These parameters are both intrinsic and extrinsic: the initial Ag NP size distribution of the Ag:TiO₂ sample, the incident laser power and the beam width of the CW laser. Experimental and simulation results of the variations in the speed threshold induced by these parameters are shown in Figure III.13. The simulation parameters used to calculate the speed curves in figure III.13 c and d are also shown in Table III.3 and 4. The same trends that are present in the experimental and simulated curves can be understood from physical interpretations of the model.

η	E_p (eV)	D_{red} (m ² /s)	E_D (eV)	D_{Ag0} (m ² /s)	E_{Ag0} (eV)	C_{red} (m ⁻³)	γ (J/m ²)	S (m ⁻³)
1.3×10^{-6}	0.4	2.5×10^{-14}	0.1	1×10^{-14}	1.04	1.36×10^{20}	1	1×10^{24}

Table III.3. Values of parameters used in simulation for figure III.13.c. The values of the diffusion coefficients of reducing agent D_{red} and silver atom D_{Ag0} are presented for the case of T=500K.

η	E_p (eV)	D_{red} (m ² /s)	E_D (eV)	D_{Ag0} (m ² /s)	E_{Ag0} (eV)	C_{red} (m ⁻³)	γ (J/m ²)	S (m ⁻³)
2.3×10^{-6}	0.4	2.5×10^{-14}	0.1	1×10^{-14}	1.38	1.36×10^{20}	1	1×10^{24}

Table III.4. Values of parameters used in simulation for figure III.13.d. The values of the diffusion coefficients of reducing agent D_{red} and silver atom D_{Ag0} are presented for the case of T=500K.

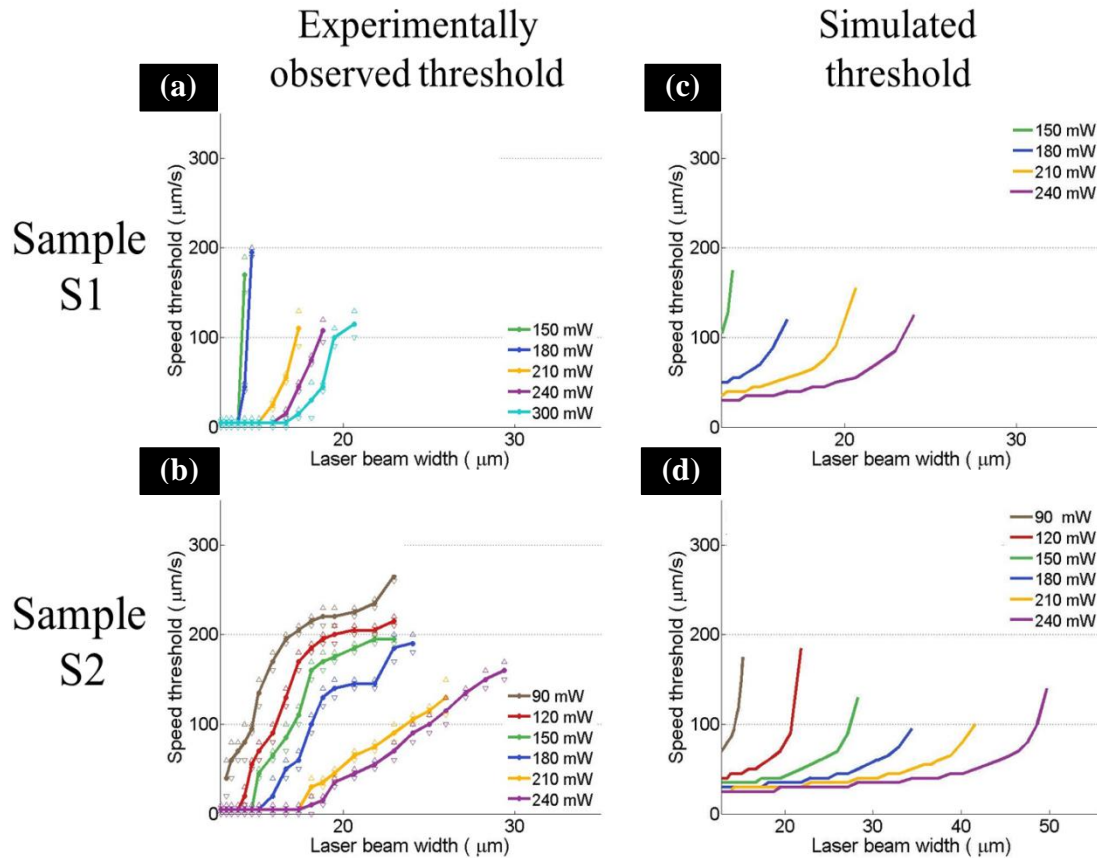


Figure III.13 Experimental (a, b) and simulated (c, d) speed threshold versus laser beam width for several incident powers and two initial NPs sizes. Subfigure a and c correspond to initial sample S1. Subfigure b and d correspond to initial sample S2. The Open triangles in experimental curve show the measurement uncertainty. The initial Ag NP sizes used in simulation are respective 1.8 and 3 nm for S1 and S2.

4.2.1 Incident Power

For a given beam width, the speed threshold increases with the decrease of the incident laser power. This can be easily understood from the interpretation in section 4.1 that sufficient temperature rise of the film is the key condition to observe the NP growth. With a lower laser power, the temperature rise within the film becomes lower. In order to have sufficient temperature rise to activate the growth process, this lower power should be compensated by a higher absorption of the composite film, *i.e.* larger Ag NP size. For this reason, one should increase the scan speed to shorten oxidation time and get larger NP size at the beginning of the NP growth.

4.2.2 Laser Beam width

For a fixed power, the speed threshold increases when the incident laser beam width increases. Larger beam width corresponds to a decrease in incident intensity. Just as the

previous case, lower intensity produces lower temperature rise, so one needs to increase the scan speed to observe the NP growth. Moreover, it is worth to remark that, according to the reference [Calder 1982], the temperature rise does not vary proportionally with the incident intensity. Indeed, Temperature rise is proportional to the incident power but changes as a complex function of the beam width. Two different pairs of incident power and beam width, which gives the same intensity, do not produce the same temperature rise and hence do not lead to the same speed threshold.

Simulated curves exhibit an exponential-type growth with the increase of laser beam width, especially when the latter approaches the maximum value that leads to the NP growth. The same trends can be also found for the experimental case of sample S1, where the Ag NP size distribution locates within a very narrow range (Figure III.3.a). This exponential-type growth of threshold can come from two effects. When the beam width is enlarged, oxidation duration is enlarged and increases the value of speed threshold. At the same time, enlarged beam width reduces the laser intensity and disfavors the thermal growth. The laser scan must be sped up to counteract this double-fact to achieve the NP growth, which leads to the exponential-type growth of threshold. However, the experimental growth of the speed threshold versus the laser beam width is less sharp for the experimental case of S2. This difference can be attributed to the broader size distribution of sample S2 (Figure III.3.b), which is not taken into account in this model. The experimental observed NPs that are much larger than 3 nm can activate the growth process even at larger beam width than the ones predicted by the simulated curve in figure III.13.d. A useful improvement of the model that considers size distributions of Ag NPs will be presented in the next chapter.

4.2.3 Initial Ag NP size distribution

For a fixed power and beam width, the speed threshold is lower for a larger initial NP size. Larger initial NP size provides higher absorption, *i.e.* higher temperature rise. The latter helps to activate the NP growth even if the oxidation time is slightly extended by reducing the speed. Besides, compared with smaller initial NPs size, larger initial NPs size also permits growth of NPs at lower power (90mW and 120 mW in figure III.13 b and d) or larger beam width (above $\sim 25 \mu\text{m}$ in figure III.13 b and d). The phenomenon can be also observed in the simulated speed threshold curves in figure III.13.

Finally, we note that the calculated speed threshold ranges are in very good agreement with the experimental ones for the same values of varying parameters. All the fitted parameters are close to values found in the literature. This model appears therefore to

be quite relevant for the study of the threshold behavior of NP growth resulted from plasmon-induced charge transfers in Ag:TiO₂ systems despite several approximations were done. The main one is to consider monodisperse NPs. We also know that crystalline phase changes of TiO₂ and a collapse of the matrix mesoporosity occur during the NP growth, due to the high temperature rise [Crespo-Monteiro 2012, Destouches, Crespo-Monteiro et al. 2014]. These major events influence the thermal, optical and chemical properties of the material and could change the final predicted NP size when growth becomes predominant. However, they will not change the way both mechanisms compete at the initiation of the chemical reaction.

5. Conclusion

In this chapter, the threshold behavior of NP growth in TiO₂ matrices loaded with Ag⁺, Ag⁰ and Ag NPs, under visible light exposure is investigated both experimentally and numerically. The Ag NPs growth only occurs above a speed threshold, and is accompanied by a strong temperature rise. The origin of this counter-intuitive threshold behavior is interpreted by characterization and modeling of the main physicochemical mechanisms that influence the size of Ag NPs when exposed to visible light. According to this model, NP oxidation competes with NP growth for sufficiently high incident laser intensity. Oxidation linearly depends on the number of photons absorbed by silver NPs due to their LSPR. The thermal growth of the NPs, modeled by a two-step process, is activated by the plasmon-induced temperature rise of the film and varies in a strong non-linear manner with the incident laser intensity. For a given couple of incident power and beam width, the relative importance of both reactions can be tuned by the scan speed of the laser beam whose intensity has a Gaussian profile. Oxidation occurs whatever the intensity and increases linearly with it, with a relatively slow kinetics. On the contrary, growth only becomes significant above a certain temperature rise produced by a combination of a high incident intensity and suitable NP size (high enough absorption cross-section) and it increases rapidly with the temperature rise. This gives rise to the two distinct regimes and a threshold value which separates these two regimes: At lower speed, oxidation outweighs over growth and the final NP size is smaller than the initial one after the beam passage. Above certain speed (*i.e.* shorter oxidation time), growth outweighs over oxidation and the final NP size is larger than the initial one.

The speed threshold is experimentally observed to increase with the beam width and to decrease when the incident power and the initial NP size increase, and these variations can be well interpreted by the numerical model. The relevance of the model can be thus established. The proposed phenomenological model is relatively simple to understand

thanks to the mono-size approximation of the Ag NP size distribution. This model, as well as the laser process presented to control the NPs size would be useful to design and produce devices for photocatalysis and photovoltaic applications. Besides, it provides also a starting point to investigate more precisely the growth kinetics at speed above the threshold.

References

- Atwater, H. A.; Polman, A. Plasmonics for Improved Photovoltaic Devices. *Nat Mater* **2010**, 9 (3), 205–213.
- Battisti, A.; Taioli, S.; Garberoglio, G. Zeolitic Imidazolate Frameworks for Separation of Binary Mixtures of CO₂, CH₄, N₂ and H₂: A Computer Simulation Investigation. *Microporous and Mesoporous Materials* **2011**, 143 (1), 46–53.
- Born, M.; Wolf, E.; Bhatia, A. B.; Clemmow, P. C.; Gabor, D.; Stokes, A. R.; Taylor, A. M.; Wayman, P. A.; Wilcock, W. L. *Principles of Optics: Electromagnetic Theory of Propagation, Interference and Diffraction of Light*, Édition : 7.; Cambridge University Press: Cambridge ; New York, 1999.
- Butrymowicz, D. B.; Manning, J. R.; Read, M. E. Diffusion in Copper and Copper Alloys, Part II. Copper-Silver and Copper-Gold Systems. *Journal of Physical and Chemical Reference Data* **1974**, 3 (2), 527–602.
- Calder, I. D.; Sue, R. Modeling of CW Laser Annealing of Multilayer Structures. *Journal of Applied Physics* **1982**, 53 (11), 7545–7550.
- Castro, T.; Reifengerger, R.; Choi, E.; Andres, R. P. Size-Dependent Melting Temperature of Individual Nanometer-Sized Metallic Clusters. *Phys. Rev. B* **1990**, 42 (13), 8548–8556.
- Cheng, H.; Ma, J.; Zhao, Z.; Qi, L. Hydrothermal Preparation of Uniform Nanosize Rutile and Anatase Particles. *Chem. Mater.* **1995**, 7 (4), 663–671.
- Clavero, C. Plasmon-Induced Hot-Electron Generation at Nanoparticle/metal-Oxide Interfaces for Photovoltaic and Photocatalytic Devices. *Nat Photon* **2014**, 8 (2), 95–103.
- Crespo-Monteiro, N.; Destouches, N.; Nadar, L.; Reynaud, S.; Vocanson, F.; Michalon, J. Y. Irradiance Influence on the Multicolor Photochromism of Mesoporous TiO₂ Films Loaded with Silver Nanoparticles. *Applied Physics Letters* **2011**, 99 (17), 173106.
- Crespo-Monteiro, N.; Destouches, N.; Saviot, L.; Reynaud, S.; Epicier, T.; Gamet, E.; Bois, L.; Boukenter, A. One-Step Microstructuring of TiO₂ and Ag-TiO₂ Films by Continuous Wave Laser Processing in the UV and Visible Ranges. *J. Phys. Chem. C* **2012**, 116 (51), 26857–26864.
- Crespo-Monteiro, N.; Destouches, N.; Bois, L.; Chassagneux, F.; Reynaud, S.; Fournel, T. Reversible and Irreversible Laser Microinscription on Silver-Containing Mesoporous Titania Films. *Adv. Mater.* **2010**, 22 (29), 3166–3170.
- Crespo-Monteiro, N.; Destouches, N.; Epicier, T.; Balan, L.; Vocanson, F.; Lefkir, Y.; Michalon, J.-Y. Changes in the Chemical and Structural Properties of Nanocomposite Ag:TiO₂ Films during Photochromic Transitions. *J. Phys. Chem. C* **2014**.
- Destouches, N.; Battie, Y.; Crespo-Monteiro, N.; Chassagneux, F.; Bois, L.; Bakhti, S.; Vocanson, F.; Toulhoat, N.; Moncoffre, N.; Epicier, T. Photo-Directed Organization of Silver Nanoparticles in Mesostructured Silica and Titania Films. *J Nanopart Res* **2013**, 15 (1), 1–10.
- Destouches, N.; Crespo-Monteiro, N.; Vitrant, G.; Lefkir, Y.; Reynaud, S.; Epicier, T.; Liu, Y.; Vocanson, F.; Pigeon, F. Self-Organized Growth of Metallic Nanoparticles in a Thin Film under Homogeneous and Continuous-Wave Light Excitation. *J. Mater. Chem. C* **2014**, 2 (31), 6256–6263.

- Destouches, N.; Martínez-García, J.; Hébert, M.; Crespo-Monteiro, N.; Vitrant, G.; Liu, Z.; Trémeau, A.; Vocanson, F.; Pigeon, F.; Reynaud, S.; et al. Dichroic Colored Luster of Laser-Induced Silver Nanoparticle Gratings Buried in Dense Inorganic Films. *J. Opt. Soc. Am. B* **2014**, *31* (11), C1–C7.
- Garnett, J. C. M. Colours in Metal Glasses and in Metallic Films. *Phil. Trans. R. Soc. Lond. A* **1904**, *203* (359–371), 385–420.
- George, S. M.; DeSantolo, A. M.; Hall, R. B. Surface Diffusion of Hydrogen on Ni(100) Studied Using Laser-Induced Thermal Desorption. *Surface Science* **1985**, *159* (1), L425–L432.
- Haran, B. S.; Popov, B. N.; White, R. E. Determination of the Hydrogen Diffusion Coefficient in Metal Hydrides by Impedance Spectroscopy. *Journal of Power Sources* **1998**, *75* (1), 56–63.
- Inagaki, T.; Goudonnet, J. P.; Little, J. W.; Arakawa, E. T. Photoacoustic Study of Plasmon-Resonance Absorption in a Bigrating. *J. Opt. Soc. Am. B* **1985**, *2* (3), 433–439.
- Kaganovskii, Y.; Lipovskii, A.; Rosenbluh, M.; Zhurikhina, V. Formation of Nanoclusters through Silver Reduction in Glasses: The Model. *Journal of non-crystalline solids* **2007**, *353* (22–23), 2263–2271.
- Kholmanov, I. N.; Barborini, E.; Vinati, S.; Piseri, P.; Podestà, A.; Ducati, C.; Lenardi, C.; Milani, P. The Influence of the Precursor Clusters on the Structural and Morphological Evolution of Nanostructured TiO₂ under Thermal Annealing. *Nanotechnology* **2003**, *14* (11), 1168.
- Kim, T.; Lee, C.-H.; Joo, S.-W.; Lee, K. Kinetics of Gold Nanoparticle Aggregation: Experiments and Modeling. *Journal of Colloid and Interface Science* **2008**, *318* (2), 238–243.
- Korn, C.; Zamir, D. NMR Study of Hydrogen Diffusion in the Three Different Phases of the Titanium-Hydrogen System. *Journal of Physics and Chemistry of Solids* **1970**, *31* (3), 489–502.
- Kowalska, E.; Mahaney, O. O. P.; Abe, R.; Ohtani, B. Visible-Light-Induced Photocatalysis through Surface Plasmon Excitation of Gold on Titania Surfaces. *Phys. Chem. Chem. Phys.* **2010**, *12* (10), 2344–2355.
- Kreibig, U.; Vollmer, M. *Optical Properties of Metal Clusters*; Toennies, J. P., Gonser, U., Osgood, R. M., Panish, M. B., Sakaki, H., Lotsch, H. K. V., Series Eds.; Springer Series in Materials Science; Springer Berlin Heidelberg: Berlin, Heidelberg, 1995; Vol. 25.
- Lehmann, J.; Mersdorf, M.; Pfeiffer, W.; Thon, A.; Voll, S.; Gerber, G. Surface Plasmon Dynamics in Silver Nanoparticles Studied by Femtosecond Time-Resolved Photoemission. *Phys. Rev. Lett.* **2000**, *85* (14), 2921–2924.
- Lifshitz, I. M.; Slyozov, V. V. The Kinetics of Precipitation from Supersaturated Solid Solutions. *Journal of Physics and Chemistry of Solids* **1961**, *19* (1–2), 35–50.
- Luo, W.; Hu, W.; Xiao, S. Size Effect on the Thermodynamic Properties of Silver Nanoparticles. *J. Phys. Chem. C* **2008**, *112* (7), 2359–2369.
- Martínez, E. D.; Boissière, C.; Grosso, D.; Sanchez, C.; Troiani, H.; Soler-Illia, G. J. A. A. Confinement-Induced Growth of Au Nanoparticles Entrapped in Mesoporous TiO₂ Thin Films Evidenced by in Situ Thermo-Ellipsometry. *J. Phys. Chem. C* **2014**, *118* (24), 13137–13151.
- McBrayer, J. D.; Swanson, R. M.; Sigmon, T. W. Diffusion of Metals in Silicon Dioxide. *J. Electrochem. Soc.* **1986**, *133* (6), 1242–1246.
- Mie, G. Beiträge Zur Optik Trüber Medien, Speziell Kolloidaler Metallösungen. *Annalen der Physik* **1908**, *330*, 377–445.
- Miotello, A.; Marchi, G. D.; Mattei, G.; Mazzoldi, P.; Quaranta, A. Clustering of Silver Atoms in Hydrogenated Silver–sodium Exchanged Glasses. *Appl Phys A* **2000**, *70* (4), 415–419.
- Nadar, L.; Destouches, N.; Crespo-Monteiro, N.; Sayah, R.; Vocanson, F.; Reynaud, S.; Lefkir, Y.; Capoen, B. Multicolor Photochromism of Silver-Containing Mesoporous Films of Amorphous or Anatase TiO₂. *J Nanopart Res* **2013**, *15* (11), 1–10.

- Ocaña, M.; Garcia-Ramos, J. V.; Serna, C. J. Low-Temperature Nucleation of Rutile Observed by Raman Spectroscopy during Crystallization of TiO₂. *Journal of the American Ceramic Society* **1992**, 75 (7), 2010–2012.
- Ohko, Y.; Tatsuma, T.; Fujii, T.; Naoi, K.; Niwa, C.; Kubota, Y.; Fujishima, A. Multicolour Photochromism of TiO₂ Films Loaded with Silver Nanoparticles. *Nat Mater* **2003**, 2 (1), 29–31.
- Prudenziati, M.; Morten, B.; Gualtieri, A. F.; Leoni, M. Dissolution Kinetics and Diffusivity of Silver in Glassy Layers for Hybrid Microelectronics. *Journal of Materials Science: Materials in Electronics* **2004**, 15 (7), 447–453.
- Sakai, N.; Sasaki, T.; Matsubara, K.; Tatsuma, T. Layer-by-Layer Assembly of Gold Nanoparticles with Titania Nanosheets: Control of Plasmon Resonance and Photovoltaic Properties. *J. Mater. Chem.* **2010**, 20 (21), 4371–4378.
- Shang, L.; Chou, I.-M.; Lu, W.; Burruss, R. C.; Zhang, Y. Determination of Diffusion Coefficients of Hydrogen in Fused Silica between 296 and 523 K by Raman Spectroscopy and Application of Fused Silica Capillaries in Studying Redox Reactions. *Geochimica et Cosmochimica Acta* **2009**, 73 (18), 5435–5443.
- Sönnichsen, C.; Franzl, T.; Wilk, T.; von Plessen, G.; Feldmann, J.; Wilson, O.; Mulvaney, P. Drastic Reduction of Plasmon Damping in Gold Nanorods. *Phys. Rev. Lett.* **2002**, 88 (7), 77402.
- Sun, J.; Ma, D.; Zhang, H.; Liu, X.; Han, X.; Bao, X.; Weinberg, G.; Pfänder, N.; Su, D. Toward Monodispersed Silver Nanoparticles with Unusual Thermal Stability. *J. Am. Chem. Soc.* **2006**, 128 (49), 15756–15764.
- Tian, Y.; Tatsuma, T. Plasmon-Induced Photoelectrochemistry at Metal Nanoparticles Supported on Nanoporous TiO₂. *Chemical Communications* **2004**, No. 16, 1810.
- Tian, Y.; Tatsuma, T. Mechanisms and Applications of Plasmon-Induced Charge Separation at TiO₂ Films Loaded with Gold Nanoparticles. *J. Am. Chem. Soc.* **2005**, 127 (20), 7632–7637.
- Torresi, R. M.; Cámara, O. R.; De Pauli, C. P.; Giordano, M. C. Hydrogen Evolution Reaction on Anodic Titanium Oxide Films. *Electrochimica Acta* **1987**, 32 (9), 1291–1301.
- Valverde-Aguilar, G.; García-Macedo, J. A.; Rentería-Tapia, V.; Aguilar-Franco, M. Photoconductivity Studies on Amorphous and Crystalline TiO₂ Films Doped with Gold Nanoparticles. *Appl. Phys. A* **2011**, 103 (3), 659–663.
- von der Linde, D.; Sokolowski-Tinten, K.; Bialkowski, J. Laser–solid Interaction in the Femtosecond Time Regime. *Applied Surface Science* **1997**, 109–110, 1–10.
- von Goetz, N.; Lorenz, C.; Windler, L.; Nowack, B.; Heuberger, M.; Hungerbühler, K. Migration of Ag- and TiO₂-(Nano)particles from Textiles into Artificial Sweat under Physical Stress: Experiments and Exposure Modeling. *Environ. Sci. Technol.* **2013**, 47 (17), 9979–9987.
- Vykhodets, V. B.; Kurennykh, T. E.; Lakhtin, A. S.; Pastukhov, E. A.; Fishman, A. Y. Activation Energy of Hydrogen, Oxygen, and Nitrogen Diffusion in Metals. *Dokl Phys Chem* **2005**, 401 (4–6), 56–58.
- Wagner, C. Theorie Der Alterung von Niederschlägen Durch Umlösen (Ostwald-Reifung). *Zeitschrift für Elektrochemie, Berichte der Bunsengesellschaft für physikalische Chemie* **1961**, 65 (7–8), 581–591.
- White, T. P.; Catchpole, K. R. Plasmon-Enhanced Internal Photoemission for Photovoltaics: Theoretical Efficiency Limits. *Applied Physics Letters* **2012**, 101 (7), 73905.
- Zhou, W.; Li, T.; Wang, J.; Qu, Y.; Pan, K.; Xie, Y.; Tian, G.; Wang, L.; Ren, Z.; Jiang, B.; et al. Composites of Small Ag Clusters Confined in the Channels of Well-Ordered Mesoporous Anatase TiO₂ and Their Excellent Solar-Light-Driven Photocatalytic Performance. *Nano Res.* **2014**, 7 (5), 731–742.

Chapter IV. Growth kinetics above the threshold

At speed above the NP growth threshold discussed in the previous chapter, the kinetics of the NP thermal growth can also be significantly influenced by the scan speed. In this chapter, both experimental and numerical investigations of this growth kinetics were performed. According to the experimental observation of this chapter, the grown NP size changes in a non-monotonous ways with scan speed. It shows firstly an increase with scan speed and then a decrease at higher speeds. The laser-induced temperature rise always increases with scan speed. In order to properly interpret these phenomena, an improved numerical model with respect to the one presented in chapter III has been developed in this chapter. Two main features of the studied NP composite film are explicitly considered in this improved version: the poly-disperse distribution of NPs and the inter-particle coalescence phenomenon. In this chapter, theoretical simulations are also compared with experimentally measured Ag NPs size and laser-induced temperature rise. The latter shows that their variations with respect to the scan speed can be explained by a two-step activation of NP growth at two successive speeds. Influence of the scan duration at higher speeds where NP growth is completely activated is also discussed at the end of this chapter.

1. Experimental characterization of the NP growth

As the NP growth is assisted by a strong temperature rise, the NP growth is characterized through the grown NPs size distributions and the laser-induced thermal effects for a series of samples irradiated at different scan speeds.

1.1 Grown NP size

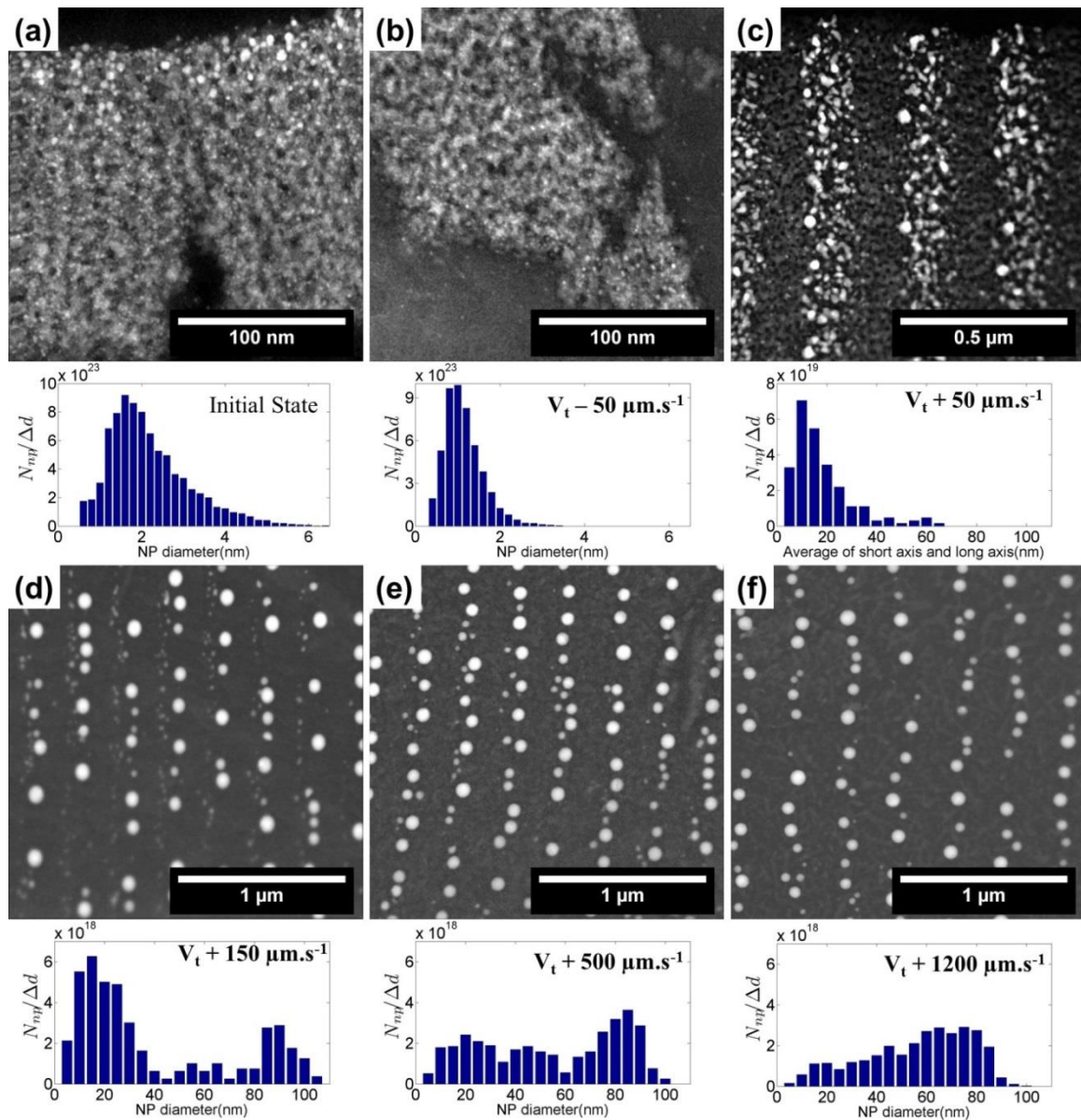


Figure IV.1. HAADF-STEM micrographs of the (a) initial sample S2 and samples exposed to the 488 nm CW laser beam with a scanning speed of (b) $V_t - 50 \mu\text{m.s}^{-1}$, (c) $V_t + 50 \mu\text{m.s}^{-1}$, (d) $V_t + 150 \mu\text{m.s}^{-1}$, (e) $V_t + 500 \mu\text{m.s}^{-1}$ and (f) $V_t + 1200 \mu\text{m.s}^{-1}$ where V_t is the speed threshold in this case: $300 \pm 50 \mu\text{m.s}^{-1}$. The size histogram at the bottom of each sub-figure is calculated from several HAADF-STEM images with an important quantity of NP.

Continuous-wave (CW) laser scans have been carried out on the initial sample S2, where the Ag impregnated TiO₂ matrix has been exposed to UV light (400 $\mu\text{W}\cdot\text{cm}^{-2}$ at 254 nm wavelength) for 30 min. This pre-treatment induces a slight increase of the size of initial Ag NPs ranging from 2 nm and 6 nm, as shown in figure IV.1.a. The NP growth has been performed under laser exposure at 488 nm with different scan speeds using fixed power (90 mW) and beam diameter (13 μm at $1/e^2$ intensity). Initial and laser processed samples were characterized by High Angular Annular Dark Field STEM (HAADF-STEM) imaging (figure IV.1) using a JEOL 2010F TEM. NP size distributions, shown at the bottom of HAADF STEM images, were calculated using the dedicated image processing algorithm, previously described in Chapter II and in the annex of this thesis. The vertical axis of the size histograms corresponds to $N_{np}/\Delta d$ in unit $\text{m}^{-3}\cdot\text{nm}^{-1}$ where N_{np} is the volume concentration of NPs in m^{-3} and Δd is the bar width in nm. In this way, the histogram height is independent of bar width and the total area of bars in one histogram represents the total NP volume concentration.

As observed in chapter III, for a fixed laser power and beam width, a speed threshold, noted as V_t , can be also identified here which separates two regimes where the NP growth or the NP shrinkage predominates respectively. In the present experiments, V_t experimentally locates at $300\pm 50 \mu\text{m}\cdot\text{s}^{-1}$. Below the threshold V_t (Figure IV.1.a-b) the size histogram narrows and shifts towards lower sizes. Above the threshold (Figure IV.1.c-f), interesting features are observed and detailed below.

HAADF STEM observations in Figure IV.1.c-f suggest that the grown NPs are self-organized in parallel lines. This phenomenon was reported in the previous work of our team [Destouches 2014] and results from optical interference phenomena that fall into place within the film due to the excitation of a guided mode within the TiO₂ film. This grating formation phenomenon will not be discussed in this chapter since we will only concentrate on the silver NP growth and not on its self-arrangement. Considering only the size variations, two regimes can be observed above V_t regarding the morphological features of the grown NPs. The first one, illustrated in figure IV.1.c, is located within a narrow speed range between V_t and $V_t+150 \mu\text{m}\cdot\text{s}^{-1}$. NPs grow in irregular aggregates with a high spatial density. Without knowing precisely the exact volume shape of each NP, the size distribution in this case is estimated by the average of the long axis and short axis of the aggregate top view. The NPs are grown to an average size between 10 nm and 15 nm, which is only about 10 times bigger than the initial average size. The second regime covers the scan speed range from $V_t+150 \mu\text{m}\cdot\text{s}^{-1}$ to about $V_t+1200 \mu\text{m}\cdot\text{s}^{-1}$. Above this speed range, the NP organization disappears and average size of NPs rapidly decreases to around 50 nm. In this speed range (between $V_t+150 \mu\text{m}\cdot\text{s}^{-1}$ and $V_t+1200 \mu\text{m}\cdot\text{s}^{-1}$), large spherical NPs with a lower density are produced (Figure IV.1.d-f). At speed $V_t+150 \mu\text{m}\cdot\text{s}^{-1}$, two classes of NPs whose mean sizes are respectively around 20 nm and 90 nm, emerge in the size histogram (Figure IV.1.d). At increasing speed (figure IV.1.d-f), the grown NPs distribution keep similar form and size

characteristics but the location of the two peaks in the size histograms get closer. At $V_t + 500 \mu\text{m}\cdot\text{s}^{-1}$, the shift to higher size of the small NPs corresponds to a diminution of the NP quantity at around 20 nm and an increase at around 45 nm. The same kind of right shift is more pronounced for $V_t + 1200 \mu\text{m}\cdot\text{s}^{-1}$ with most particles in the 60-80 nm range. HAADF-STEM images at these speeds (Figure IV.1 d-f) also confirm the progressive disappearance of small NPs and the emergence of medium size NPs. In the meanwhile, the mean value of the higher size peak is slightly shifted to lower size when scan speed increases.

1.2 Laser-induced temperature rise

As shown by chapter III, an important laser-induced thermal effect can be only observed above the speed threshold of NP growth. Further studies in this section indicate how this laser-induced temperature rise changes as a function of scan speed above the threshold. The estimation of the temperature can be performed both after and during the CW laser scan. In the first case, denoted by *post mortem* characterization, the growth NPs have already finished and temperature rise is estimated from the “traces” left by laser scans. In the second case, temperature rise is deduced from the signal recorded during the NP growth and this characterization is thus named as real-time *in situ* characterization.

1.2.1 *Post mortem* characterization

The temperature rise was firstly estimated by the crystal phase changes of the CW laser irradiated TiO_2 film. TiO_2 has three mains crystal phases: anatase, brookite and rutile. The transitions between these polymorphs take place at different temperature ranges and give thus a signature of the maximum laser-induced temperature rise that occur during laser processing. In this work, CW laser scans were performed upon initial sample S2 at a wavelength of 488 nm, as in the case of section 1.1, whereas the laser power and beam width were respectively changed to 210 mW and 18 μm . The NP growth phenomena shown in section 1.1 can be observed over a large parameter range. In particular a similar evolution of NP growth has been observed here: 1) The growth of NP into small irregular aggregates was observed at speed range between V_t and $V_t + 50 \mu\text{m}\cdot\text{s}^{-1}$. 2) From $V_t + 50 \mu\text{m}\cdot\text{s}^{-1}$ to $V_t + 1000 \mu\text{m}\cdot\text{s}^{-1}$, large spherical NPs were found. 3) Above $V_t + 1000 \mu\text{m}\cdot\text{s}^{-1}$, the self-organization of NPs disappeared. Moreover, the speed threshold of NP growth, V_t , was shifted to around $15 \pm 5 \mu\text{m}\cdot\text{s}^{-1}$ in the present study.

Raman spectrum

Post mortem Raman spectrums of the initial and laser irradiated samples at a series of scan speeds were performed by LabRAM ARAMIS Raman spectroscopy and are presented

in Figure IV.2. As the studied Ag:TiO₂ sample is photo-sensitive, the parameters of the laser probe exciting *post mortem* Raman signal should be carefully chosen to avoid any additionally modification on the Ag:TiO₂ composite. For this reason, the wavelength of the light probe was chosen at 633 nm, which is far from the wavelength used to grow the Ag NPs. Besides, the light intensity was also adjusted to a low level to avoid visible damage upon the sample surface.

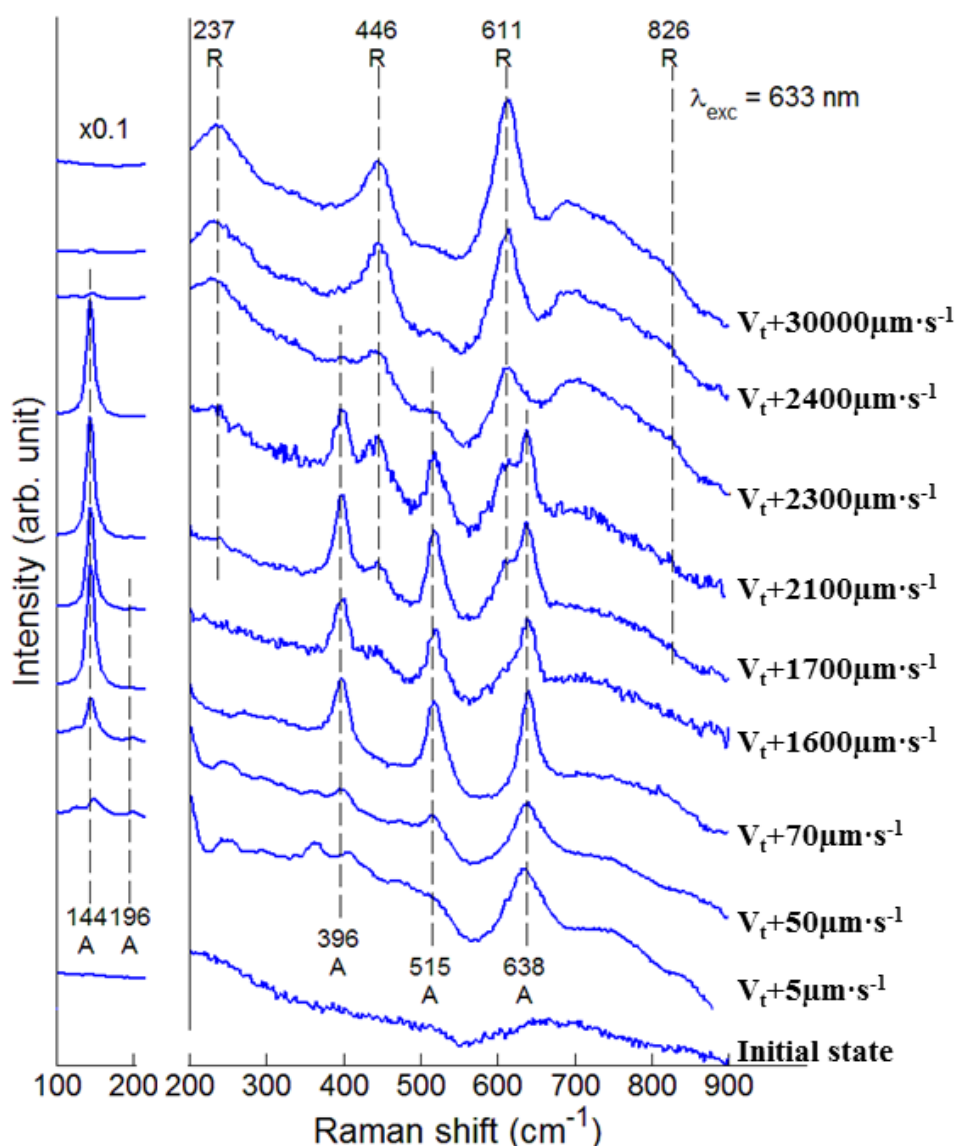


Figure IV.2 *Post mortem* Raman spectra of initial Ag:TiO₂ sample and of the CW laser irradiated sample for a series of speeds indicated on the graph. The excitation wavelength for Raman spectra is 633 nm. “A” and “R” respectively correspond to the active modes of TiO₂ anatase and rutile

Compared with the Raman spectrum of the initial amorphous TiO₂ film, several peaks can be observed on the Raman spectrum at speed $V_t + 5 \mu\text{m}\cdot\text{s}^{-1}$ (Figure IV.2). According to the literature [Chen 2007, Zhang 2000], some of these peaks, such as the ones at 196 cm⁻¹ and 638 cm⁻¹ may be attributed to the Anatase phase of TiO₂. However it is still difficult to

accurately identify the crystal phase of this sample. With an increase of speed until $V_t + 70 \mu\text{m}\cdot\text{s}^{-1}$, other active modes of TiO_2 anatase emerge at 144 cm^{-1} , 396 cm^{-1} and 515 cm^{-1} . The relative amplitudes of these signals also progressively increase with scan speed. A precise anatase phase can be firstly observed at speed $V_t + 70 \mu\text{m}\cdot\text{s}^{-1}$, where all the active modes of anatase can be clearly found in the spectrum. Similar anatase spectra were observed above this speed until around $V_t + 1600 \mu\text{m}\cdot\text{s}^{-1}$. At this last speed, another peak at 446 cm^{-1} appears on the spectrum. The latter can be assigned to the active mode of TiO_2 rutile [Ma 2007]. Above $V_t + 1600 \mu\text{m}\cdot\text{s}^{-1}$, other active modes of TiO_2 rutile at 237 cm^{-1} and 611 cm^{-1} progressively occur and coexist with the active modes of TiO_2 anatase, whose amplitudes gradually decrease with scan speed. This mixture of anatase and rutile coexist until $V_t + 2300 \mu\text{m}\cdot\text{s}^{-1}$. Above $V_t + 2300 \mu\text{m}\cdot\text{s}^{-1}$ and until $V_t + 30000 \mu\text{m}\cdot\text{s}^{-1}$, the highest speed can be performed by our experimental setup, only rutile phase can be observed.

According to the literature [Kholmanov 2003, Mossaddeq 2000, Yuan 1995, Ocana 1992], anatase and rutile phases are formed in different temperature ranges. With an increase of temperature, amorphous/anatase transition occurs firstly between 350°C and 400°C . The mixture of anatase and rutile usually emerges at higher temperature from 600°C . Above the range between 700°C and 900°C , only rutile phase exist.

In summary, the series of *post mortem* Raman spectrums suggests an increase of the maximum laser-induced temperature rise reached during the laser process with scan speed and this temperature rise can be as high as 900°C .

Electron microscopy images

Crystallization state at speeds below $V_t + 70 \mu\text{m}\cdot\text{s}^{-1}$ were not well clarified by the *post mortem* Raman spectrum. Further investigations have been carried out with Scanning Electron Microscopy (SEM) and Transmission Electron Microscopy (TEM), which show more details on the porosity of the laser processed TiO_2 films and the morphologies of TiO_2 crystals (Figure IV.3-4).

As explained at the beginning of section 1.2.1, between V_t and $V_t + 50 \mu\text{m}\cdot\text{s}^{-1}$, Ag NPs were grown into small irregular aggregates. SEM images (Figure IV.3.b) show that at these speeds, the TiO_2 film is still porous but the pore size and density is significantly reduced compared to the initial state (Figure IV.3.a). Further HR TEM measurements show the presence of small anatase crystals within these porous films. At speed $V_t + 50 \mu\text{m}\cdot\text{s}^{-1}$, pores were still visible upon the sample surface whereas Ag NPs are grown to about 100 nm and the density of the pores is significantly decreased (Figure IV.3.c). At $V_t + 70 \mu\text{m}\cdot\text{s}^{-1}$, where *post mortem* Raman spectrum clearly suggests the presence of TiO_2 anatase, the porosity of TiO_2 film totally disappears (Figure IV.3.d). Accordingly, at speed below $V_t + 70 \mu\text{m}\cdot\text{s}^{-1}$, the partial

crystallization of the TiO_2 film into anatase phase could be a possible explanation of the ambiguity of the *post mortem* Raman signals (Figure IV.2).

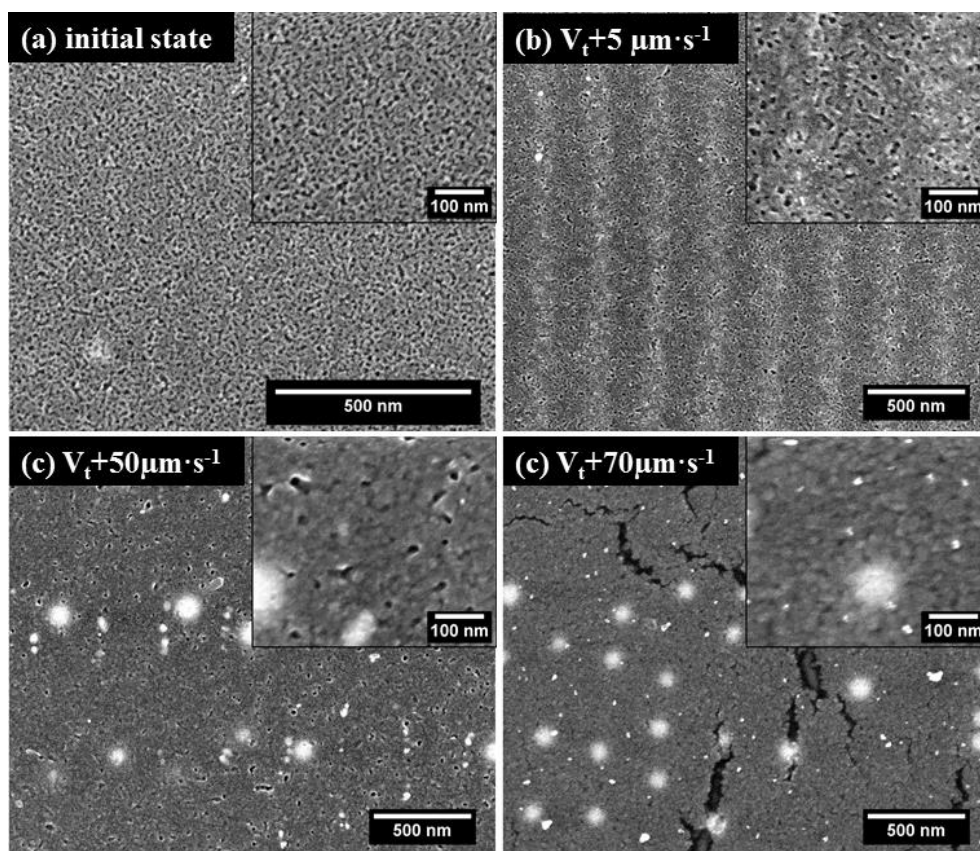


Figure IV.3. SEM images of initial Ag:TiO₂ sample S2 (a) together with the laser irradiated samples at speed $V_t + 5 \mu\text{m}\cdot\text{s}^{-1}$ (b), $V_t + 50 \mu\text{m}\cdot\text{s}^{-1}$ (c) and $V_t + 70 \mu\text{m}\cdot\text{s}^{-1}$ (d).

Above $V_t + 70 \mu\text{m}\cdot\text{s}^{-1}$, the morphologies of the anatase and rutile crystals were also studied. SEM images (Figure IV.4 c-f) of the laser irradiated samples at these higher speeds show two shapes of crystals. According to the diffraction pattern of the HR TEM measurement (Figure IV.4 a-b), the quasi-spherical (or rounded square) crystals correspond to the anatase phase and the rod-like crystals to the rutile phase. At the speed range where anatase phase is principally observed (Figure IV.4 c-d), the size of anatase crystals increases with the scan speed whereas the spatial density decreases. At $V_t + 1000 \mu\text{m}\cdot\text{s}^{-1}$ (Figure IV.4.d), rutile crystals begin to emerge in the SEM images even if no significant active modes have been observed in the *post mortem* Raman spectrum. Between $V_t + 2400 \mu\text{m}\cdot\text{s}^{-1}$ and $V_t + 30000 \mu\text{m}\cdot\text{s}^{-1}$, SEM images (Figure IV.4 e-f) suggest that length of rutile nanorods decreases with the scan speed, whereas their spatial density slightly increases.

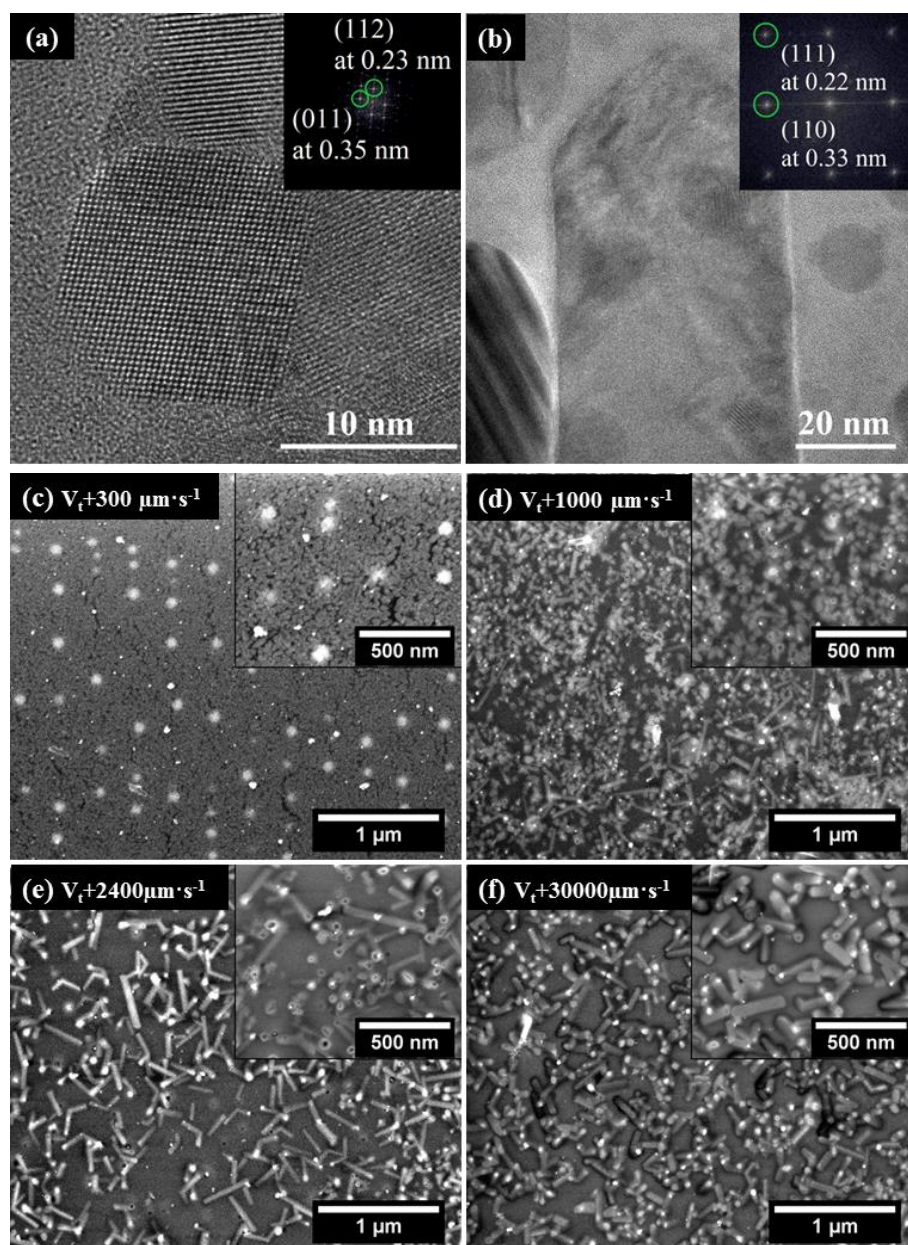


Figure IV.4. a-b: HR TEM images together with the corresponding diffraction pattern (inset) of anatase (a) and rutile (b) crystals obtained after CW laser irradiations. c-f: SEM images of laser irradiated samples at speed $V_t + 300 \mu\text{m}\cdot\text{s}^{-1}$ (c), $V_t + 1000 \mu\text{m}\cdot\text{s}^{-1}$ (d), $V_t + 2400 \mu\text{m}\cdot\text{s}^{-1}$ (e) and $V_t + 30000 \mu\text{m}\cdot\text{s}^{-1}$ (f).

In conclusion, partially crystallized anatase and partially collapsed TiO_2 films are observed at speed below $V_t + 70 \mu\text{m}\cdot\text{s}^{-1}$. Above this speed of $V_t + 70 \mu\text{m}\cdot\text{s}^{-1}$, TiO_2 films completely collapse and crystallize firstly into the anatase phase, which implies a temperature rise greater than 350-400°C. The anatase/rutile transition, corresponding to a temperature rise at around 600°C, begins at $V_t + 1000 \mu\text{m}\cdot\text{s}^{-1}$ and ends at $V_t + 2400 \mu\text{m}\cdot\text{s}^{-1}$. Above this speed range, pure rutile exists suggesting a temperature rise ranges from 700°C to 900°C. All the experimental characterizations prove a rise of temperature during

illumination with the laser scan speed, from less than 350°C, at speed just above the threshold, to higher temperatures probably at 900°C for faster speeds. Note that the glass transition temperature of the substrate supporting the film begins from 450°C. A layer of glass located just below the film is therefore expected to melt during the laser process, especially at speed above $V_t + 70 \mu\text{m}\cdot\text{s}^{-1}$.

1.2.2 Real-time *in situ* characterization

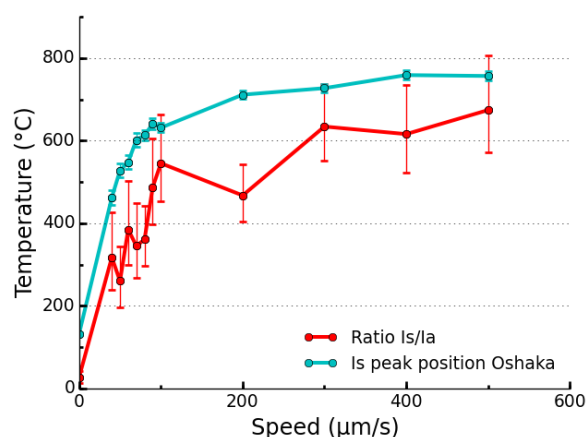


Figure IV.5 Laser-induced temperature rises at a series of speeds estimated by real-time *in situ* Raman spectroscopy. Red curve: temperature deduced from the intensity ratio between Stokes and anti-Stokes signals. Blue curve: temperature calculated according to the position shift of the anatase active mode at 144 cm^{-1} .

The increase in the temperature rise with scan speed has been confirmed by the changes in real-time *in situ* Raman signal (Raman spectroscopy: Renishaw Invia, translation stage: Jobin-Yvon T64000). In this case, the laser probe is the writing laser itself, sent on the initial sample S2. It creates the growth of Ag NPs, and is simultaneously used to record the Raman signal of the sample under evolution. Due to limitations of the experimental configuration, the probe laser was chosen at 533 nm and focalized by a 50x objective. In order to have a sufficient acquisition time, the scan speed was also limited to $500 \mu\text{m}\cdot\text{s}^{-1}$, below which only anatase crystals can be observed.

Temperature rises deduced from real-time *in situ* Raman signals are shown in figure IV.5. As explained in Chapter II, two methods were used to calculate the temperature rise: the intensity ratio of Stokes and anti-Stokes peaks at $\pm 144 \text{ cm}^{-1}$ (red curve) and the shift of active mode at 144 cm^{-1} (blue curve). The two curves suggest both a growth of the temperature rise with scan speed. The error bars in each curve only represent the uncertainty coming from numerical fitting of Raman peak (see Annex III). Another non-negligible uncertainty on these measurements results from the hypothesis made when calculating the temperature rise from the Raman peak characteristics extracted by curve fitting. It is difficult to quantitatively evaluate the latter by error bars. However their origin

and influence are discussed here. In the case of the estimation from the shift of active mode, uncertainty of numerical fitting is lower. However, the position of active mode could also be influenced by other factors than the temperature rise, such as the crystallographic defects, the presence of Ag NP or the amorphous fraction etc. [Kosacki 2002]. In this case, the uncertainty of the physical hypothesis made for temperature rise estimation could be much stronger than the one of curve fitting, even if the former is not considered in the error bars of the blue curve in figure IV.5. When estimating temperature rise by Stokes/anti-Stokes ratio, the uncertainty resulting from the method to compute the temperature rise is lower, whereas the one due to numerical fitting is stronger (Larger error bars for the red curve in figure IV.5), due to the complex mathematical expression yielding the temperature. Taking into account both uncertainties, the two curves appear to be quantitatively in good agreement with each other.

1.3 Evolution of the NP growth

According to the morphologies of Ag NPs and the observed temperature rise, 3 regimes can be successively found at speeds above the threshold of NP growth. Let's denote them here by R1, R2 and R3.

	Speed range		Final NP size	Thermal effect on TiO ₂ film
	P:90mW, ω :13 μ m Vt: $300 \pm 50 \mu\text{m}\cdot\text{s}^{-1}$ (Section 1.1)	P:210mW, ω : 18 μ m Vt: $15 \pm 5 \mu\text{m}\cdot\text{s}^{-1}$ (Section 1.2.1)		
R3	Above Vt+1200 $\mu\text{m}\cdot\text{s}^{-1}$	Above Vt+1000 $\mu\text{m}\cdot\text{s}^{-1}$	Quasi spherical NP around 50 nm. No organization	Complete crystallization in rutile
R2	[Vt+150, Vt+1200 $\mu\text{m}\cdot\text{s}^{-1}$]	[Vt+50, Vt+1000 $\mu\text{m}\cdot\text{s}^{-1}$]	Self-organized Spherical NP around 80 nm	Complete crystallization in anatase
R1	[Vt, Vt+150 $\mu\text{m}\cdot\text{s}^{-1}$]	[Vt, Vt+50 $\mu\text{m}\cdot\text{s}^{-1}$]	Self-organized Irregular aggregates around 20 nm	Partial collapse and crystallization in anatase
Shrinkage regime	Below Vt		Smaller than initial one	Same as initial one

Table IV.1. Experimentally observed laser-induced NP growth and thermal effect at different scan speeds reported in section 1.1 and 1.2.1. V_t is the speed threshold of NP growth. P and ω are respectively the laser power and beam width at $1/e^2$ intensity.

The first regime, R1, locates just above the speed threshold of growth, within a narrow speed range varying from $50 \mu\text{m}\cdot\text{s}^{-1}$ to $150 \mu\text{m}\cdot\text{s}^{-1}$, where the growth kinetic remains very low. Ag NPs are only grown to around 20 nm and the TiO₂ film is only partially crystallized and collapsed, which suggests a temperature rise around 350°C.

The second regime, R2, shows larger NPs than in R1. It begins from the end of R1, and ends at a speed of about $V_t + 1000 \mu\text{m}\cdot\text{s}^{-1}$. Ag NPs are grown into large spherical shape with a largest size around 80-100 nm and self-organized into parallel lines. The TiO_2 film is strongly crystallized in the anatase phase and collapsed, which suggests a temperature rise above 350°C but below 600°C . The temperature rise continues to increase with scan speed whereas the size of grown Ag NP decreases with speed.

The third regimes, R3, covers higher speeds than above. Laser-induced temperature rise can reach 900°C , as suggested by the emergence of the TiO_2 rutile phase. However, the size of Ag NPs is decreased to around 50 nm and the self-organization disappears.

2. Modeling with particle size distribution

In chapter III, a numerical model has been described which considered the physico-chemical reactions involved in the NP growth and successfully explained the threshold behavior of the NP growth as a tunable competition between the photo-oxidation and thermal growth of NPs. However, this former model only considers a monodisperse NP size distribution, which prevents from correct simulation of the NP size distribution as obtained experimentally. The improved model shown in this chapter explicitly takes into account poly-disperse NP size distributions and coalescence phenomena in order to properly describe changes in the NP size distribution during CW laser excitation.

2.1 State of the art

Population balance models are largely used to solve particle size distribution (PSD) problems involving particle sizes varying simultaneously with processes [Kumar 2008, Qamar 2009 and references therein]. PSD is usually described by its number density function $n(x, t)$ which corresponds to the quantity of NPs of volume x per unit volume at time t . One can yield the total NP volume concentration $N(t)$ by $N(t) = \int_0^\infty n(x, t) dx$. The general form of the Population Balance Equation (PBE) for a closed system where particles are well mixed can be formulated as: [Kumar 1997, Hounslow 1988]

$$\frac{\partial n(x, t)}{\partial t} = B(x, t) - D(x, t) - \frac{\partial G(x, t)n(x, t)}{\partial x} \quad (\text{IV.1})$$

where the temporal variation of the number density function $n(x, t)$ is given by the difference between the particle birth rate B and death rate D together with the influence

of the growth rate G calculated from Ostwald ripening mechanism when a monomer adds to a NP.

Both statistical and deterministic type methods can be used for solving this PBE. In statistical methods, the PBE is usually solved using the Monte Carlo technic [Smith 1998, Maisels 2004]: At each time step, one target particle is randomly chosen from the distribution and the particle growth event occurs only with a certain probability calculated according to its physical origin. The advantages of Monte Carlo methods are the possibility to track each particle with its spatial information and the simplicity of their numerical implementation. However, getting accurate results requires an important particle quantity to be considered, which may finally make such an approach highly time-consuming. Furthermore, statistical methods usually fail to converge to accurate results for long time scale processes, and including additional contributions (like chemical reactions) appears as hardly achievable.

In deterministic methods, the considered size range is usually discretized into adjacent sections, and PBEs are thus reformulated for each section to trace the particle distribution temporal evolution [Kumar 1997, Alexopoulos 2005, Kumar 2008, Qamar 2009]. The deterministic methods can be quite accurate for both particle distribution moments (1st and 2nd moments respectively correspond to the total and average volumes of particle distribution) and particle distribution shape. Moreover, thanks to the integro-differential form of the PBE, the deterministic method can be easily blended with other processes. Computing accuracy and time strongly depend on the chosen numerical techniques for solving the PBE. The numerical scheme needs therefore to be carefully chosen according to the simulated problem.

In our case, the silver NP growth process is very sharp in time and the number density function $n(x,t)$ can rapidly shift over several orders of magnitude, which requires choosing a robust and accurate simulation model. Moreover, chemical reactions such as silver ion reduction and NP photo-oxidation play a crucial role on the shape of the final NP size distribution and must be considered. For these reasons, we have chosen to implement a deterministic method with a “cell average” technique [Kumar 2008], which provides a good compromise between computation time and accuracy.

2.2 Developed numerical scheme

2.2.1 Nanoparticle coalescence

Nanoparticle coalescence has been observed in many metallic NP systems [Martinez 2015, Kim 2008, Ahn 1980]. In our work, the numerical approach used to treat the particle

coalescence is related to the “cell average” technique [Kumar 2008]. The considered nanoparticle volume range $[x_{\min}, x_{\max}]$ is discretized into M small adjacent sections, named by “cell”, where the i^{th} cell is limited by its lower and upper boundaries denoted by $x_{i-1/2}$ and $x_{i+1/2}$ as shown in figure IV.6.a. We have thus $x_{\min} = x_{1/2}$ and $x_{\max} = x_{M+1/2}$. In the current work, only coalescence of two particles is considered which creates both birth events at the newborn particles’ cell, and death events at the parent particles’ cells. A new population balance equation can then be rewritten for each cell:

$$\frac{dN_i}{dt} = B_i^{\text{tot}} - D_i^{\text{tot}}, i = 1, 2, 3, \dots, M \quad (\text{IV.2})$$

where N_i is the volume concentration of the nanoparticles within the i^{th} cell, B_i^{tot} and D_i^{tot} are respectively the total particle birth event rate and death event rate in the i^{th} cell.

In order to express B_i^{tot} and D_i^{tot} , one can assume that particles are only present at the center x_i of each cell, whose value is $x_i = (x_{i-1/2} + x_{i+1/2})/2$. According to Kumar et al. [Kumar 2008], the total birth events taken place within each cell during unit time can be calculated by:

$$B_i = \sum_{\substack{m \geq n \\ x_{i-1/2} \leq (x_m + x_n) \leq x_{i+1/2}}} (1 - \frac{1}{2} \delta_{m,n}) \beta_{m,n} N_m N_n \quad (\text{IV.3})$$

where $\beta_{m,n}$ is the coalescence kernel for a couple of particles of volumes x_m and x_n . $\delta_{m,n}$ is the Kronecker function. The mathematical form of $\beta_{m,n}$ depends on the physical origin of the NP coalescence and will be detailed later for the studied case. N_m is the volume concentration of particles of volume x_m . The term $\beta_{m,n} N_m N_n$ gives the coalescence rate per unit volume of the particle pair of volumes x_m and x_n . The sum operator takes over all particle pairs whose total volume is within the i^{th} cell range. From Eq.IV.3, the average volume v_i of these newborn particles in each cell can be deduced as:

$$v_i = \frac{\sum_{\substack{m \geq n \\ x_{i-1/2} \leq (x_m + x_n) \leq x_{i+1/2}}} (1 - \frac{1}{2} \delta_{m,n}) \beta_{m,n} N_m N_n (x_m + x_n)}{\sum_{\substack{m \geq n \\ x_{i-1/2} \leq (x_m + x_n) \leq x_{i+1/2}}} (1 - \frac{1}{2} \delta_{m,n}) \beta_{m,n} N_m N_n} \quad (\text{IV.4})$$

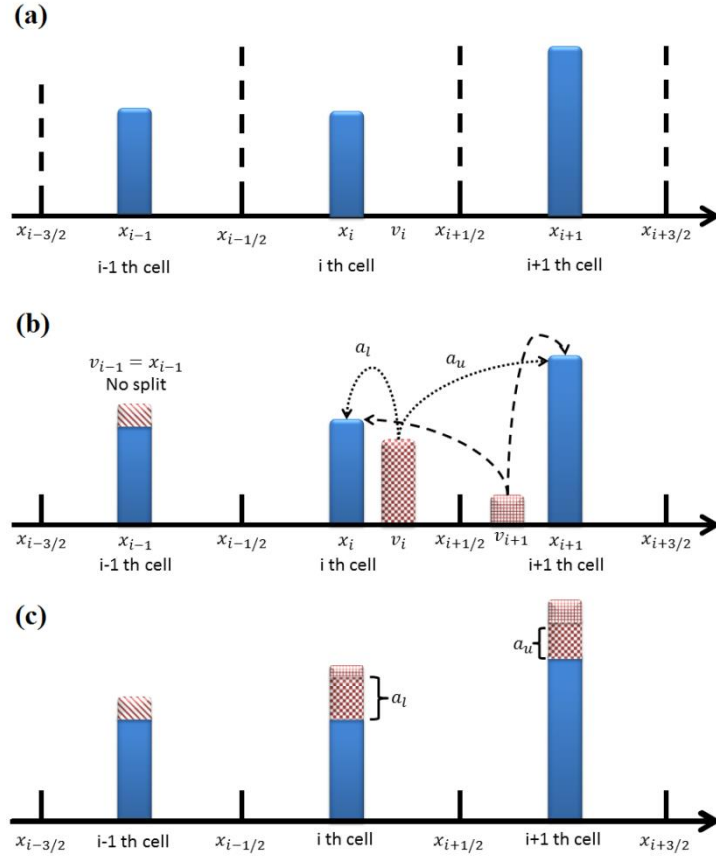


Figure IV.6. a: Discretization of considered particle volume range. b-c: Before (b) and after (c) split and reassignment of the newborn NPs (red bars) stemming from the coalescence process. Blue bars represent the current NP quantity at each cell center. Red bars correspond to newborn particles that are affected to the center of adjacent cells proportionally to the relative position of the newborn particle average volume between the neighboring cell centers.

If this average volume locates at a cell center, the whole quantity of the newborn particles in this cell can be assigned to it, *i.e.* the $(i-1)^{\text{th}}$ cell of figure IV.6.b-c. However, when the average volume locates between two neighboring centers, the newborn particles must be split into two parts and reassigned to the two closest centers. In the case of the i^{th} cell of figure IV.6.b-c, for an average volume of newborn particles that falls in the upper half part of the cell, let a_l and a_u be the fractions of the newborn particles to be reassigned to lower and upper closest centers x_i and x_{i+1} . In order to have quantity and volume conserved particle splitting processes, a_l and a_u must satisfy the conditions below:

$$a_u + a_l = B_i \quad (\text{IV.5})$$

$$a_u x_{i+1} + a_l x_i = B_i v_i \quad (\text{IV.6})$$

which give,

$$a_u = B_i \lambda_{i+1}^-(v_i) \quad (\text{IV.7})$$

$$a_l = B_i \lambda_i^+(v_i) \quad (IV.8)$$

with

$$\lambda_i^\pm(x) = \frac{x - x_{i\pm 1}}{x_i - x_{i\pm 1}} \quad (IV.9)$$

If the average volume falls in the lower half part of the cell (v_{i+1} of $(i+1)^{th}$ cell on figure IV.6.b-c), one has similarly: $a_u = B_{i+1} \lambda_{i+1}^-(v_{i+1})$ and $a_l = B_{i+1} \lambda_i^+(v_{i+1})$. So as in equations IV.7-IV.9, the index of B and v is the index of the cell where the newborn particles are created while the index of λ is this of the cell where the newborn particles are affected after splitting, and the sign “+” or “-” is respectively for “l” and “u”.

One cell may receive the birth contribution from both its lower and upper neighbors together with its own contribution. The total birth events term in one cell can be written as:

$$\begin{aligned} B_i^{tot} = & B_{i-1} \lambda_i^-(v_{i-1}) H(v_{i-1} - x_{i-1}) + B_i \lambda_i^-(v_i) H(x_i - v_i) \\ & + B_i \lambda_i^+(v_i) H(v_i - x_i) + B_{i+1} \lambda_i^+(v_{i+1}) H(x_{i+1} - v_{i+1}) \end{aligned} \quad (IV.10)$$

where $H(x)$ is the Heaviside step function whose value is zero for negative argument, one for positive argument and 0.5 for $H(0)$.

In each cell, the death event is only produced by the coalescence of its local particles with the particles in other cells and it takes the form:

$$D_i^{tot} = N_i \sum_{m=1}^M \beta_{m,i} N_m \quad (IV.11)$$

Substituting Eq.IV.10 and Eq.IV.11 in Eq.IV.2, the final set of PBEs for the coalescence process is given by

$$\begin{aligned} \frac{dN_i}{dt} = & B_{i-1} \lambda_i^-(v_{i-1}) H(v_{i-1} - x_{i-1}) + B_i \lambda_i^-(v_i) H(x_i - v_i) \\ & + B_i \lambda_i^+(v_i) H(v_i - x_i) + B_{i+1} \lambda_i^+(v_{i+1}) H(x_{i+1} - v_{i+1}) - N_i \sum_{m=1}^M \beta_{m,i} N_m \end{aligned} \quad \text{for } i=1,2,\dots,M \quad (IV.12)$$

The coalescence kernel $\beta_{m,n}$ is chosen here as a Brownian kernel, for the following two reasons. Firstly, the silver nanoparticle coalescence process is identified as a diffusion-controlled process and the Brownian kernel is generally accepted in this case [Schmitt 2000]. The reason for this is that the nanoparticle growth in our samples is assisted by a local heating up to 900°C due to the laser absorption by NPs, as shown in the experimental part of this chapter. At such temperatures, the sintering of a metal or semiconductor aggregate into a spherical form was reported to occur in nanosecond or even picosecond range [Egan 2004,

Lehtinen 2001]. Such times are shorter than the average particle collision time calculated in our case. Secondly, diffusion of bulk atoms and NP coalescence are activated only above the Tammann temperature [Sun 2006], which is usually the half of the melting point. In the case of metallic NPs, the melting point is found to depend on the particle size [Castro 1990]. The same dependence can be found by the analytical form of the NP Brownian diffusion coefficient D_{NP} , given by the Stokes-Einstein equation:

$$D_{NP} = \frac{k_B T}{6\pi\eta_v r_{np}} \quad (\text{IV.13})$$

where r_{np} is the radius of spherical particle, k_B the Boltzmann constant and T the absolute temperature. D_{NP} depends on the Arrhenius-type viscosity η_v , for Ag NP in TiO_2 matrix [Brancker 1950].

$$\eta_v = c \exp\left(\frac{E_v}{RT}\right) \quad (\text{IV.14})$$

With R the gas constant, E_v the activation energy, c is a constant pre-exponential factor. The analytical form of the Brownian kernel for particle pairs (m, n) can be written as: [Smith 1998]

$$\beta_{m,n} = 4\pi(D_{NP,m} + D_{NP,n})(r_m + r_n) = \frac{2k_B T}{3c} \exp\left(-\frac{E_v}{RT}\right)(r_m + r_n)\left(\frac{1}{r_m} + \frac{1}{r_n}\right) \quad (\text{IV.15})$$

where r_m and r_n are respectively the average radius of NPs in the m^{th} and n^{th} cell. Under the assumption of spherical NPs, NP radius r and volume x satisfy (Eq.IV.16).

$$x = \frac{4}{3}\pi r^3 \quad (\text{IV.16})$$

2.2.2 Nanoparticle growth by Ostwald ripening

In parallel with the NP coalescence, the NP size can also be modified by the absorption or the dissolution of monomers [Martinez 2015, Granqvist 1976], which are silver atoms (Ag^0) in our case. According to our previous work in chapter III, the quantity (noted Gwt) of Ag^0 absorbed by one NP of radius r per unit time under Ostwald Ripening process can be formulated as:

$$Gwt = 4\pi r^2 J_{\text{Ag}^0} \quad (\text{IV.17})$$

where J_{Ag^0} is the local flow of silver atoms from the external of NPs of radius r to their surface, whose analytical form can be written as:

$$J_{Ag0} = D_{Ag0} (C_{Ag0} - c_r) / r = D_0 \exp\left(-\frac{E_{Ag0}}{k_B T}\right) \frac{C_{Ag0} - c_r}{r} \quad (IV.18)$$

where D_{Ag0} is the temperature-dependent diffusion coefficient of silver atoms, C_{Ag0} is the Ag^0 concentration at macroscopic scale and c_r is the local silver atom concentration around one NP given by

$$c_r = S\left(1 + \frac{2\gamma\omega}{k_B T r}\right) \quad (IV.19)$$

with S the silver atom solubility, ω the atomic volume of silver and γ the Ag NP/ TiO_2 matrix interface tension.

According to the Ostwald Ripening theory [Lifshitz 1961], the growth of large NPs is based on the shrinkage of small NPs. For small enough NPs, J_{Ag0} can be negative and silver atoms flow out of NPs. In this case, NPs shrink and the global Ag^0 concentration increases. On the contrary, for large NPs, J_{Ag0} is positive and NPs grow by adsorbing silver atoms, which can come from small NPs.

Using the same volume based discretization as the previous “cell average” technique, the Ostwald ripening process at each cell center and cell boundary is given by

$$\left\langle \frac{dx_i}{dt} \right\rangle_{OR} = \omega \times Gwt_{x_i} = \omega 4\pi r_i^2 J_{Ag0}(r_i), \text{ for } i=1,2,\dots,M \quad (IV.20)$$

$$\left\langle \frac{dx_{i+1/2}}{dt} \right\rangle_{OR} = \omega \times Gwt_{x_{i+1/2}} = \omega 4\pi r_{i+1/2}^2 J_{Ag0}(r_{i+1/2}), \text{ for } i=0,1,2,\dots,M \quad (IV.21)$$

where r_i and $r_{i+1/2}$, deduced from x_i and $x_{i+1/2}$ by Eq.IV.16, are the radii of NPs located at the i^{th} cell center and its upper boundary, respectively. One can thus combine the Ostwald ripening process with the “cell average” NP coalescence scheme by solving simultaneously the ordinary differential equation (ODE) set Eq.IV.12, Eq.IV.20 and Eq.IV.21. This approach, named as “Lagrangian technique” by Kumar et al. [Kumar 2008], was evaluated as a computational costly strategy. Nevertheless, compared to other “efficient” techniques such as the “cell average” one for surface growth [Kumar 2008] and finite volume scheme [Qamar 2009], it is still the best method to combine these two processes thanks to its better precision for the stiff NP growth/shrinkage process which was observed previously in our samples [Liu 2015]. As well, the silver atom concentration variation due to Ostwald ripening can be finally formulated as :

$$\left\langle \frac{dC_{Ag0}}{dt} \right\rangle_{OR} = -\sum_{m=1}^M (Gwt_m \times N_m) = -\sum_{m=1}^M (4\pi r_m^2 J_{Ag0}(r_m) N_m) \quad (IV.22)$$

2.2.3 Nanoparticle photo-oxidation and silver ion reduction

Chemical reactions also control the growth of silver NPs. The latter oxidize and shrink under visible illumination due to the excitation of hot electrons through the LSPR and their transfer to the conduction band of TiO_2 through the Schottky junction formed at TiO_2/Ag interface [Clavero 2014, Yu 2006, Chen 2013]. The number of oxidized atoms per NP and per unit time, O_{xy} , can be written as:

$$O_{xy} = \eta_{ion} \frac{I \sigma_r}{h f_{inc}} \quad (\text{IV.23})$$

where I is the instantaneous laser intensity, σ_r is the absorption cross-section of silver NPs of radius r calculated using the Mie theory, h is the Planck constant and f_{inc} is the incident light frequency. The term $I \sigma_r / h f_{inc}$ gives the number of absorbed photons by a single NP of radius r per unit time and η_{ion} is the ionization quantum efficiency of silver NPs.

In a similar way as for Ostwald Ripening in equations IV.20, IV.21 and IV.22, one can rewrite here the variation rate of the NP volume at each cell center/boundary and the variation rate of the silver ion concentration due to photo-oxidation as

$$\left\langle \frac{dx_i}{dt} \right\rangle_{O_{xy}} = -\omega \times O_{xy_{x_i}} = -\omega \eta_{ion} \frac{I \sigma_{r_i}}{h f_{inc}}, i = 1, 2, \dots, M \quad (\text{IV.24})$$

$$\left\langle \frac{dx_{i+1/2}}{dt} \right\rangle_{O_{xy}} = -\omega \times O_{xy_{x_{i+1/2}}} = -\omega \eta_{ion} \frac{I \sigma_{r_{i+1/2}}}{h f_{inc}}, i = 0, 1, \dots, M \quad (\text{IV.25})$$

$$\left\langle \frac{dC_{Ag^+}}{dt} \right\rangle_{O_{xy}} = \sum_{m=1}^M (O_{xy_m} \times N_m) = \sum_{m=1}^M (N_m \omega \eta_{ion} \frac{I \sigma_{r_i}}{h f_{inc}}) \quad (\text{IV.26})$$

Reversely and simultaneously, silver ions present in the system can be reduced due to the laser induced heating. According to Kaganovskii's work [Kaganovskii 2007], the number of reduced atoms per unit volume per unit time is formulated as

$$\begin{aligned} \left\langle \frac{dC_{Ag^0}}{dt} \right\rangle_{red} &= -\left\langle \frac{dC_{Ag^+}}{dt} \right\rangle_{red} = p D_{red} C_{red} C_{Ag^+}^{2/3} \\ &= \exp\left(-\frac{E_p}{k_B T}\right) \cdot D_r \exp\left(-\frac{E_D}{k_B T}\right) C_{red} C_{Ag^+}^{2/3} \end{aligned} \quad (\text{IV.27})$$

which corresponds also to the quantity of lost silver ions, due to reduction.

In this equation, p and D_{red} are respectively the reduction probability and the reducing agent diffusion coefficient, which both follow an Arrhenius law. C_{red} is the concentration of the reducing agent and C_{Ag^+} the silver ion concentration. The reducing

agent is not clearly identified in our composite system. It may be H_2 in the atmosphere, TiO_2 itself at high temperature, or even chemical compounds from the glass substrate.

2.2.4 Final equation set

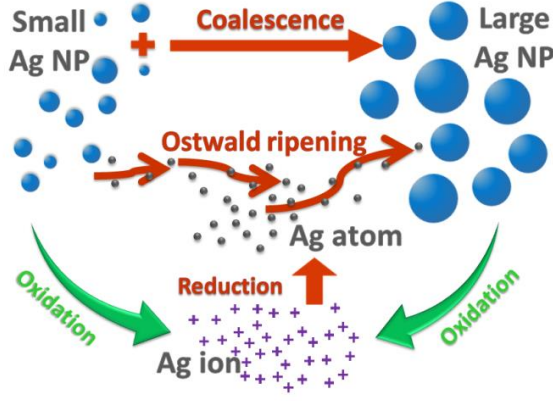


Figure IV.7. Sketch of matter flows between the different Ag species in the studied system. These flows are driven by physico-chemical processes which lead to the NP growth (red arrows) or shrinkage (green arrows).

At this stage, it is important to summarize the physico-chemical reactions and deduce the final ODE set to be solved. In our system, silver is present in three forms: silver ions (Ag^+), silver atoms (Ag^0) and silver NPs. The matter flows between these species are shown in figure IV.7. The photo-oxidation transfers silver from the NP form to the ionic form and leads to the shrinkage of NPs. This shrinkage process is controlled by the incident laser beam intensity. In the meanwhile, the reduction of silver ions provides firstly the source material for the NP growth, which is then produced by the double effect of Ostwald ripening and NP coalescence. This NP growth process is driven by the instantaneous local temperature in the system. According to Eq.22, Eq.26 and Eq.27, the variation rate of silver atom concentration and silver ion concentration can be written as:

$$\begin{aligned} \frac{dC_{Ag^0}}{dt} &= \left\langle \frac{dC_{Ag^0}}{dt} \right\rangle_{red} + \left\langle \frac{dC_{Ag^0}}{dt} \right\rangle_{OR} \\ &= pD_{red}C_{red}C_{Ag^+}^{2/3} - \sum_{m=1}^M (4\pi r_i^2 J_{Ag^0}(r_i) N_m) \end{aligned} \quad (IV.28)$$

$$\begin{aligned} \frac{dC_{Ag^+}}{dt} &= \left\langle \frac{dC_{Ag^+}}{dt} \right\rangle_{red} + \left\langle \frac{dC_{Ag^+}}{dt} \right\rangle_{oxy} \\ &= -pD_{red}C_{red}C_{Ag^+}^{2/3} + \sum_{m=1}^M (N_m \omega \eta_{ion} \frac{I \sigma_{ri}}{h\nu_{inc}}) \end{aligned} \quad (IV.29)$$

NP growth process is formulated by the “cell average” NP coalescence scheme in Eq.IV.12 together with the volume variation rate of each cell center and boundary in

Eq.IV.30-31, deduced from Eq.IV.20-21 and Eq.IV.24-25. In order to reduce the stiff level of the ODE system, one can also simulate the radius variation rate, under the assumption of spherical NPs, of the cell center/boundary, as given by Eq.IV.32-33 instead of Eq.IV.30-31.

$$\begin{aligned} \frac{dx_i}{dt} &= \left\langle \frac{dx_i}{dt} \right\rangle_{OR} + \left\langle \frac{dx_i}{dt} \right\rangle_{oxy} \\ &= \omega 4\pi r_i^2 J_{Ag^0}(r_i) - \omega \eta_{ion} \frac{I \sigma_{ri}}{h\nu_{inc}} \quad \text{for } i = 1, 2, \dots, M \end{aligned} \quad (IV.30)$$

$$\begin{aligned} \frac{dx_{i+1/2}}{dt} &= \left\langle \frac{dx_{i+1/2}}{dt} \right\rangle_{OR} + \left\langle \frac{dx_{i+1/2}}{dt} \right\rangle_{oxy} \\ &= \omega 4\pi r_{i+1/2}^2 J_{Ag^0}(r_{i+1/2}) - \omega \eta_{ion} \frac{I \sigma_{ri+1/2}}{h\nu_{inc}} \quad \text{for } i = 0, 1, \dots, M \end{aligned} \quad (IV.31)$$

$$\frac{dr_i}{dt} = \omega J_{Ag^0}(r_i) - \frac{\omega \eta_{ion}}{4\pi r_i^2} \frac{I \sigma_{ri}}{h\nu_{inc}}, \quad \text{for } i = 1, 2, \dots, M \quad (IV.32)$$

$$\frac{dr_{i+1/2}}{dt} = \omega J_{Ag^0}(r_{i+1/2}) - \frac{\omega \eta_{ion}}{4\pi r_{i+1/2}^2} \frac{I \sigma_{ri+1/2}}{h\nu_{inc}}, \quad \text{for } i = 0, 1, \dots, M \quad (IV.33)$$

Equations IV.12, IV.28, IV.29, IV.32 and IV.33 give the final ODE set of order $3M + 3$ for our NP growth problem.

2.2.5 Simulation parameters

The initial NP size distribution was reconstructed from the processing of tens of STEM-HAADF images acquired on initial samples (Figure IV.1.a). By fitting the experimental data (Figure IV.8.a), the initial NP volume concentration of each cell N_i^0 is expressed as

$$N_i^0 = \int_{r_{i-1/2}}^{r_{i+1/2}} \frac{N_0(2r - c_0)}{c_1^2} \exp\left(-\frac{2r - c_0}{c_1}\right) dr \quad (IV.34)$$

where $N_0 = 1.69 \times 10^{24} \text{ m}^{-3}$, $c_0 = 0.8 \text{ nm}$ and $c_1 = 0.75 \text{ nm}$. When $2r - c_0$ is negative, N_i^0 becomes negative and loses its physical meaning. In these cases, N_i^0 is replaced by zero. The initial Ag^0 concentration was chosen at $1.5 \times 10^{25} \text{ m}^{-3}$ so that the Ostwald ripening kinetic is almost zero for the initial NP size distribution without any light excitation. This means that the Ag^0 flow in Eq.IV.18 for a NP radius equal to the mean radius of the initial NP size distribution is almost zero. According to the Ag/Ti atom quantity ratio deduced from Energy Dispersive X-ray Spectroscopy (EDS) measurements on the Ag:TiO₂ sample and the Ti atom concentration estimated from the geometric features of the TiO₂ mesoporous matrix, the total silver concentration in the sample is estimated varying from $2 \times 10^{27} \text{ m}^{-3}$ to 2.8×10^{28} , which is in good agreement with the value estimated from HAADF STEM micrographics of

grown Ag NPs, as reported in Chapter III. Here, we chose the total silver concentration as $3 \times 10^{27} \text{ m}^{-3}$. Subtracting the silver atoms presented in NPs and in the form of Ag^0 from this total silver concentration, the silver ion concentration was estimated at around $2 \times 10^{27} \text{ m}^{-3}$ in this work.

As shown previously in Eq.15, Eq.18 and Eq.27, the NP growth is a temperature driven process. In this work, the local temperature rise is calculated upon a two layer structure which consists of a composite Ag:TiO₂ layer supported by a glass substrate, using the same thermal model discussed in Chapter III [Calder 1982]. Compared with the numerical model presented in Chapter III, separating the Ag:TiO₂ composite into two layers to approximate the polydispersity of NPs distribution is not necessary here as the latter is explicitly considered by the cell average technique. Moreover, computing reflectivity becomes difficult for a composite thin layer filled with a polydisperse size distribution. We then neglect the influence of reflectivity in this version for the sake of simplicity. During the simulation, the temperature is updated at each ODE solver time step, which depends on the absorption coefficient of the film α , calculated from the NP absorption cross-section σ_{ri} of each cell and the NP concentration N_i as

$$\alpha = \sum_{i=1}^M \sigma_{ri} N_i \quad (\text{IV.35})$$

Simulation parameters are presented in Table IV.2. Most of the other simulation parameters are chosen according to the work in the previous chapter, except the activation energy E_v and constant c in Eq.14 for the viscosity of silver NPs in TiO₂ matrix. To the best of our knowledge, few works have been reported on parameters E_v and c of similar Ag:TiO₂ systems. Martinez and co-workers [Martinez 2015] show that the growth kinetic energy of Au particles in TiO₂ matrix is 49 kJ.mol^{-1} within the temperature range where both Oswald ripening growth and coalescence may occur. This growth kinetic energy varies from 12 kJ.mol^{-1} to 120 kJ.mol^{-1} in the same Au:TiO₂ system under different atmosphere conditions [Yang 2009, Parker 2007]. In the case of Ag NP containing glass [Fluegel 2006], the activation energy of viscosity was reported around 86 kJ.mol^{-1} . As a result we consider the parameter range between 10 kJ/mol and 120 kJ/mol as reasonable for E_v in our simulations. c is considered as a proportionality coefficient to be fitted by comparison to experimental results.

At initial state, the studied volume range is discretized into 100 adjacent cells with cell boundaries given by a geometric law: $x_{i+1/2} = x_{\min} \times 2^{i/4}$ which is well adapted for the size distribution varying over several orders. x_{\min} is chosen as $6.5 \times 10^{-29} \text{ m}^3$ for an equivalent r_{\min} of 0.2 nm which corresponds to the size of one silver crystal cell. Shrinking below this volume, the NP is considered as a dead NP and its size cannot be modified anymore. An ODE

set of order 303 can be established by Eq.IV.12, Eq.IV.28, Eq.IV.29, Eq.IV.32 and Eq.IV.33. The numeric system is programmed using Python3 and the ODE set is solved by the ISODA stiff problem solver in SciPy open source package for the best compromise between calculation accuracy and duration. A typical simulation time for one laser scan is around 3 hours on the compute cluster of our laboratory (Intel Xeon E5-2680 @ 2.70GHz, 2 GB per cores).

η_{ion}	E_p eV	D_{red} m^2/s	E_D eV	D_{Ag0} m^2/s	E_{Ag0} eV	C_{red} m^{-3}	γ J/m^2	S m^{-3}	E_v $kJ \cdot mol^{-1}$	c $Pa \cdot s$
6×10^{-7} - 6×10^{-5}	0.3 - 0.4	1×10^{-10} - 1×10^{-15}	0.01 - 0.1	5×10^{-17} - 1×10^{-14}	0.5 - 1.5	1.5×10^{20} - 1.5×10^{21}	2	1×10^{24} - 1×10^{25}	10 - 120	5×10^{-5} - 5×10^{-7}

Table IV.2. Values of parameters used in simulation. The values of the diffusion coefficients of reducing agent D_{red} and silver atom D_{Ag0} are presented for the case of $T=500K$.

2.3 Validation of the model

In order to check the consistency of the elaborated model, theoretical simulations have been compared to experimental results of NP distributions shown in figure IV.1 of section 1.1. Simulated NP size histograms, shown in figure IV.8, have been performed with the same laser parameters as the experimental ones in section 1.1 and considering the initial NP size distribution given by Eq.IV.34 as shown by the red curve in figure IV.8.a. The simulation parameters used to calculate these results are presented in Table IV.3. These theoretical predictions give a speed threshold slightly shifted relative to the experimental one at around $250 \mu m \cdot s^{-1}$, *i.e.* a difference of $50 \mu m \cdot s^{-1}$. Nevertheless, the shape of the NP size distribution evolves in the same manner as the experimental one (Figure IV.8). The size distribution narrows and down-shifts below the threshold. At speed $V_t + 50 \mu m \cdot s^{-1}$ (figure IV.8.c), NPs grow to an average size of 10 nm, which is the same value than the experimental one. From $V_t + 150 \mu m \cdot s^{-1}$ (figure IV.8.d-f) histograms are characterized by two main peaks whose distance decreases when the speed increases, and whose positions are in the same size ranges as the experimental ones. Changes in the NP density are also very consistent with the experimental values as can be observed on the histograms.

Theoretical results are in good agreement with the experimental ones regarding the size ranges, the NP volume concentration and the presence of one or two populations in the NPs distributions. The model appears therefore quite reliable by taking into account the main mechanisms at the origin of the changes in the NP size. The non-perfect matching of the simulated and experimental histograms shape is likely to come from the model limitations and the statistics of the experimental histograms. Phase changes in the host matrix and collapse of the film porosity that occur during laser exposure are neglected. The latter will induce changes in the optical, thermal and chemical parameters of the $Ag:TiO_2$ composite during the laser process. However, all these parameters are kept constant during

simulations in order to maintain the simplicity of the model. Note that choosing different sets of parameters in a large reasonable range does not influence so much the evolution of the NP size histograms as a function of speed. We also make the approximation that NPs homogeneously and randomly distribute over the film without considering changes in the local NP density due to the self-organization. According to these approximations, the agreement between experimental and numerical results is really convincing.

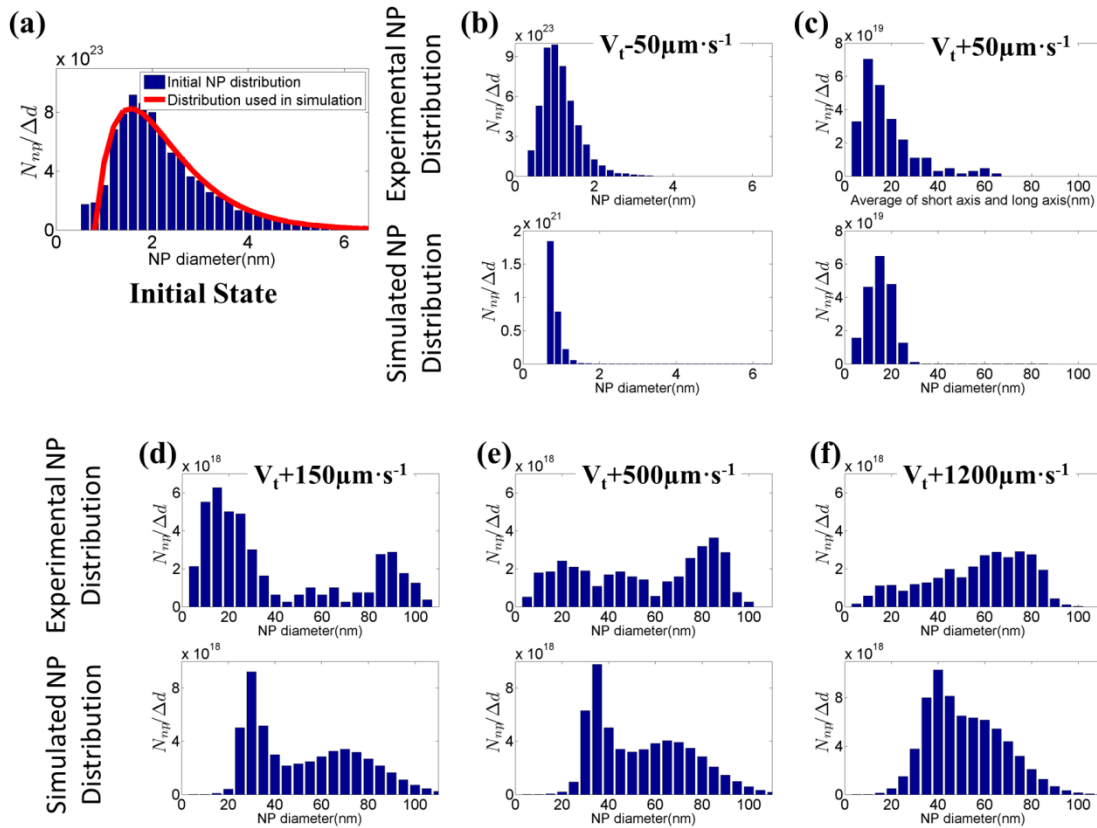


Figure IV.8. Experimental and simulated NP distributions after laser processing (b-f) when considering as starting point the fitted experimental size distribution reported in (a) . From (b) to (f), the scan speeds are respectively: $V_t - 50 \mu\text{m.s}^{-1}$, $V_t + 50 \mu\text{m.s}^{-1}$, $V_t + 150 \mu\text{m.s}^{-1}$, $V_t + 500 \mu\text{m.s}^{-1}$ and $V_t + 1200 \mu\text{m.s}^{-1}$. The speed threshold V_t for experimental results is $300 \pm 50 \mu\text{m.s}^{-1}$ and the one for simulated results is $250 \mu\text{m.s}^{-1}$.

η_{ion}	E_p eV	D_{red} m^2/s	E_D eV	D_{Ag0} m^2/s	E_{Ag0} eV	C_{red} m^{-3}	γ J/m^2	S m^{-3}	E_v $\text{kJ}\cdot\text{mol}^{-1}$	c $\text{Pa}\cdot\text{s}$
2.5×10^{-5}	0.4	1×10^{-10}	0.1	1×10^{-14}	1.5	1.36×10^{21}	2	1×10^{24}	40	5×10^{-5}

Table IV.3. Values of parameters used in simulations presented in figure IV.8. The values of the diffusion coefficients of reducing agent D_{red} and silver atom D_{Ag0} are presented for the case of $T=500\text{K}$.

Finally, in order to show that the growth kinetic is well governed by a combination of the described mechanisms, we have calculated what would happen if one of these mechanisms were removed. Figure IV.9 shows the best simulation results obtained by

neglecting the NP coalescence (Figure IV.9.a-c) or the Ostwald ripening growth (figure IV.9.d-f). Narrower histograms are found in all cases, with two close peaks when coalescence is neglected or a single peak when Ostwald ripening is neglected. The size range at low speed above the threshold is always larger than the experimental one whereas the size of large NPs at higher speed is always underestimated. The changes in the simulated NP density are also now significantly different from the experimental measurements

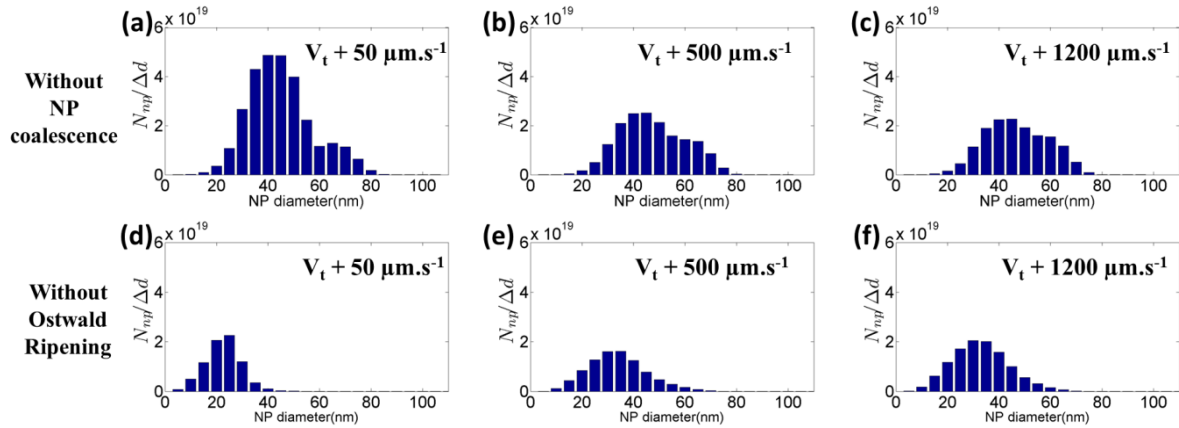


Figure IV.9. Simulated NP distribution without NP coalescence (a-c) or without Ostwald ripening (d-f) at different scanning speeds: $V_t + 50 \mu\text{m.s}^{-1}$ for (a) and (d), $V_t + 500 \mu\text{m.s}^{-1}$ for (b) and (e), $V_t + 1200 \mu\text{m.s}^{-1}$ for (c) and (f).

3. Origins of growth kinetic variation

Three different regimes, respectively named by R1, R2 and R3, have been identified in section 1.3 at speeds above the shrinkage regime. As shown in the section 1 of this chapter, the size of the Ag NP distribution and the laser-induced temperature rise has both different behaviors in these regimes. In order to explain the origin of these three regimes, simulations have been performed using the model of section 2 with the same parameters as the experimental ones described in section 1.2.1.

3.1 A two-step activation of growth

Compared with the model in Chapter III, the NP coalescence and the poly-disperse NP distribution have been explicitly considered here, which gives an improved understanding of the speed threshold discussed in Chapter III. As we will see from simulation results below, activation of NP growth is achieved in two steps.

3.1.1 Growth of the average size of the NP distribution

The competition between photo-oxidation and NP coalescence, tuned by the scan speed, produces the threshold above which the average size of NPs grows. This threshold, previously denoted by V_t in the section 1 of this chapter, separates the shrinkage regime and the R1 regime, where Ag NPs are grown in irregular aggregates at average size around 20 nm.

Simulated results at speeds both above and below V_t are shown in figure IV.10. 3D histograms in figure IV.10.a and d reveal the temporal evolutions of the Ag NP distribution. The bars of the same color in one line correspond to a 2D size histogram of NP distribution at a given time. A 3D histogram is then composed by a series of 2D histograms plotted for a fixed position on the Ag:TiO₂ sample at different times during laser scan, from the arrival (blue bars) to the departure (red bars) of laser beam. The heights of each 2D histogram are normalized in the way that the total volume of all the bars in one 2D histogram represents the instantaneous total volume fraction of Ag present in NPs distribution. At speed $V_t - 5 \mu\text{m}\cdot\text{s}^{-1}$ (Figure IV.10.a-c), the final average size of NP distribution is smaller than the initial one. The R1 type growth only occurs at speed above the threshold, *i.e.* $V_t + 5 \mu\text{m}\cdot\text{s}^{-1}$ where the final average NP size is larger than the initial one, although the total volume fraction of Ag in NPs has decreased compared to the initial one (figure IV.10.d-f). In these both cases, a significant growth of the NP size can be observed at the beginning of the laser scan before it comes back to a smaller size.

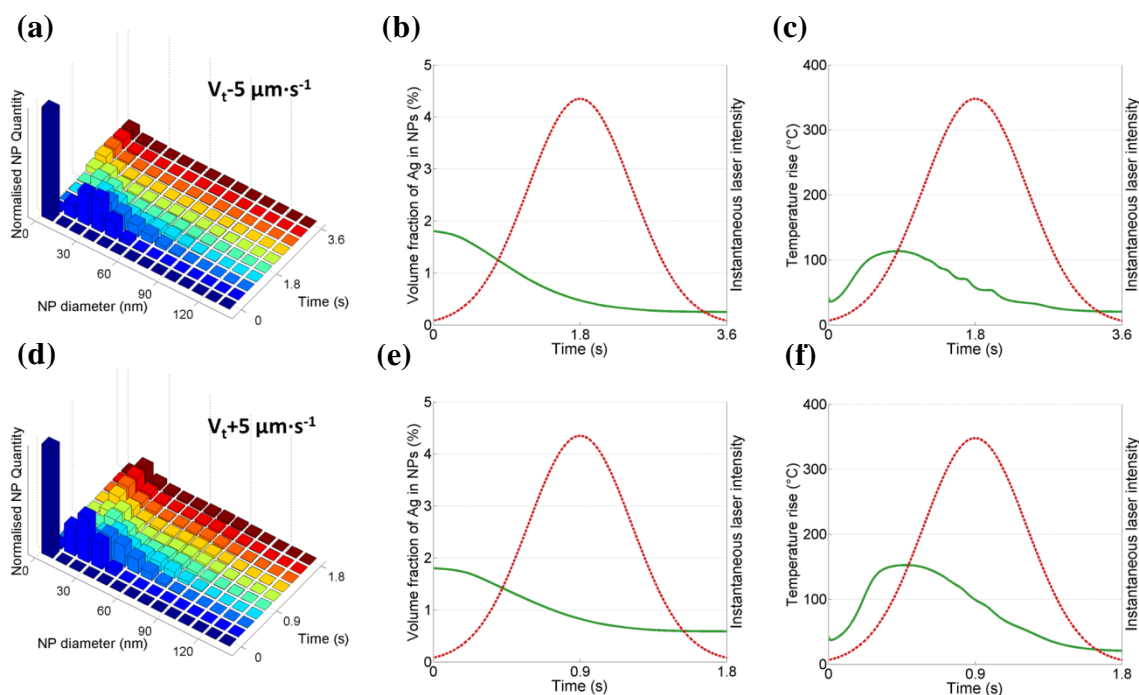


Figure IV.10. Temporal evolution of the size histogram of Ag NP distribution (a and d), the total volume fraction of Ag in NPs (green lines in b and e) and the laser-induced temperature rise (green lines in c and f) at speed both below ($V_t - 5 \mu\text{m}\cdot\text{s}^{-1}$, figure a-c) and above ($V_t + 5 \mu\text{m}\cdot\text{s}^{-1}$, figure d-f) the speed threshold of NP average size growth, denoted by V_t . Instantaneous laser intensity are plotted by red dotted lines.

The temporal evolutions of the total volume fraction of Ag in NPs (green curves) and instantaneous laser intensity (red dotted line) at a fixed position on the sample are shown in figure IV.10.b and e. The red curves in the same figures correspond to the temporal profiles of the instantaneous laser intensity. These figures reveal that at the both side of the threshold V_t , the total volume of Ag in NPs decreases during the laser scan. The photo-oxidation always outweighs the Ostwald ripening: the quantity of Ag atoms that are oxidized and dissolved from NP is greater than the one adsorbed on NPs. The temporal changes of the cell centers' position at speed $V_t - 5 \mu\text{m}\cdot\text{s}^{-1}$ (Figure IV.11) also confirms this conclusion. In figure IV.11, the positions of each cell used in the simulated model are plotted only if the volume concentration of NPs within this cell is more than $3 \times 10^{18} \text{ m}^{-3}$. One can notice that the entire NP distribution shrinks during laser scan. Larger NPs emerge progressively, which is a typical phenomenon of inter-particle coalescence. However, the size of the newborn NPs continues to decrease after their birth.

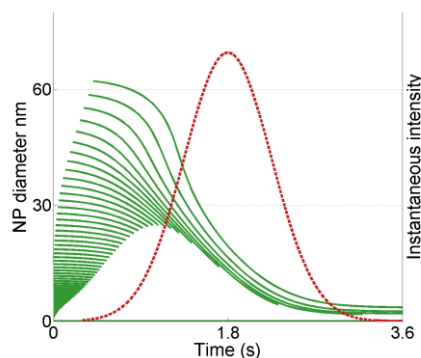


Figure IV.11 Temporal changes of the simulated NP cells' positions during laser scan at speed $V_t - 5 \mu\text{m}\cdot\text{s}^{-1}$. The curve of each is plotted only if volume concentration of NPs within this cell is more than $3 \times 10^{18} \text{ m}^{-3}$.

NP growth in R1 regime is thus only induced by the competition between photo-oxidation and NP coalescence tuned by the scan speed. NP coalescence occurs from the beginning of laser scans. If the scan duration is sufficiently long, all the NPs in the distribution, including the newborn ones from NP coalescence, can be sufficiently oxidized and the average size of final NP distribution becomes smaller than the initial one, like the case at speed $V_t - 5 \mu\text{m}\cdot\text{s}^{-1}$ (figure IV.10.a). When the scan speed increases, the duration of photo-oxidation is decreased. Larger NPs have more chance to "survive" from oxidation. Above a certain speed threshold, V_t , the average size of the survived NPs can eventually become larger than the initial one (Figure IV.10.d).

The increase in the laser-induced temperature rise with scan speed can also be explained in the same way. The temporal evolutions of the temperature rise are plotted as the green curves in figure IV.10.c and f. When the scan duration is shortened by scan speed, more Ag atoms remain in Ag NPs during laser scan and leads to a higher absorption of the Ag:TiO₂ composite film. For a given light power, the temperature rise increases with the

absorption of the sample. High temperature can thus be found with higher speed, *i.e.* shorter oxidation duration. Simulations also show that the maximum temperature rise never exceed 350°C (TiO₂ amorphous/anatase transition) in both the shrinkage and the R1 regime. This result is in good agreement with the experimentally observed partial crystallization and collapse of the mesoporous TiO₂. Physically, as NPs are absorbers of light, a local temperature rise more than 350°C can instantaneously occur around the grown NPs, which can explain the partial crystallization of TiO₂. However, this local thermal effect is not considered by the simulated temperature which only gives the averaged global temperature rise of the system at steady state after thermal diffusion from the NPs to the surrounding TiO₂ matrix.

3.1.2 Growth of the total volume fraction of Ag in NPs

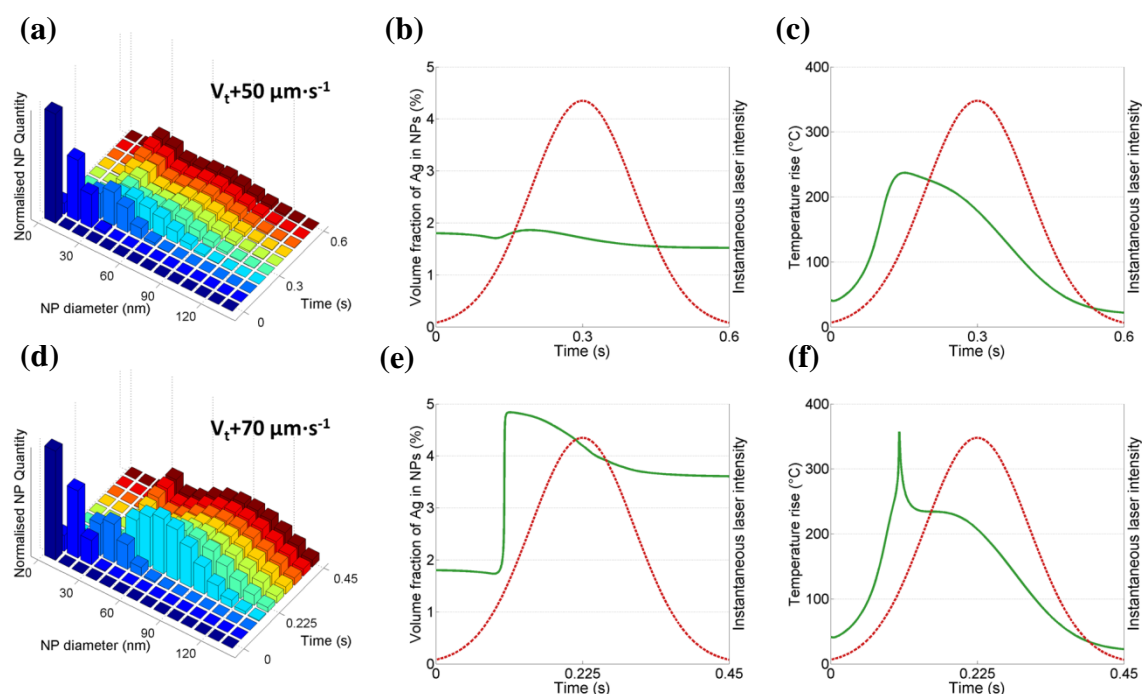


Figure IV.12. Temporal evolution of the size histogram of Ag NP distribution (a and d), the total volume fraction of Ag in NPs (green lines in b and e) and the laser-induced temperature rise (green lines in c and f) at the second speed threshold ($V_t + 50 \mu\text{m}\cdot\text{s}^{-1}$, figure a-c) and above ($V_t + 70 \mu\text{m}\cdot\text{s}^{-1}$, figure d-f). Above this second speed threshold, the total volume of Ag NP distribution increases after laser scan. Instantaneous laser intensity are plotted by red dotted lines.

The previous section shows that the temperature rise continues to increase with scan speed, even if the photo-oxidation predominates over the Ostwald ripening. Both NP coalescence and Ostwald ripening exponentially increase with temperature rise of the system (Eq.IV.15 and Eq.IV.18). At sufficiently high speeds, the increase of temperature rise should be able to activate the Ostwald ripening process, which could predominate over photo-oxidation, and lead to the growth of the total volume fraction of Ag in NPs.

Simulations confirm this trend above which both the average NP size and the total volume fraction of Ag in NPs increases after the laser scan.

At $V_t+50 \mu\text{m}\cdot\text{s}^{-1}$ (Figure.IV.12.a-c), the total volume fraction of Ag in NPs shortly increases during laser scan but ends up with a value slightly below the initial one. This implies that Ostwald ripening has temporarily outweighed photo-oxidation. Besides, compared with lower speeds (for instance $V_t+5 \mu\text{m}\cdot\text{s}^{-1}$ in figure.IV.10.d-f), thanks to a higher temperature rise achieved at this speed (Figure.IV.12.c), NPs become able to grow to about 100 nm (Figure.IV.12.a). Moreover, the maximum temperature at this speed is still below 350°C, which should not completely crystallized TiO_2 into anatase according to the analysis at the end of section 3.1.1. All these phenomena are in a good agreement with the experimental observations of the same scan speed ($V_t+50 \mu\text{m}\cdot\text{s}^{-1}$), that was previously shown in section 1.2.2.

At higher speed, $V_t+70 \mu\text{m}\cdot\text{s}^{-1}$, (figure IV.12.d-f), Ostwald ripening is activated until the end of laser scan. The final total volume fraction of Ag in NPs significantly increases compared with the initial one (Figure IV.12.d and e). The NP distribution grows both in average size and total volume. This double growth gives rise to a sharp peak on the temporal profile of temperature rise during the rising edge of Gaussian form laser intensity (Figure IV.12.f). The maximum temperature rise is above 350°C, which explains the complete crystallization and collapse of TiO_2 film observed experimentally in section 1.2.2 at the same scan speed.

We can thus conclude that the tunable competition between Ostwald ripening and photo-oxidation gives rise to another critical speed, above which the total volume fraction of Ag in NPs increases after the laser scan. The speed corresponds to the experimental observation at $V_t+50 \mu\text{m}\cdot\text{s}^{-1}$ in section 1.2.1, that separates regime R1 and regime R2.

3.2 Influence of scan duration at higher speeds

Experimental characterizations in section 1 showed that at higher speeds in R2 and R3 regimes, the size of Ag NPs in CW laser processed sample decreases with scan speed whereas the laser-induced temperature rise increases with scan speed.

The results of our simulations (Figure IV.13.a) confirm the experimentally observed increase of temperature rise with scan speed, as shown in section 1.2.1. According to the latter, TiO_2 anatase/rutile mixtures emerge from about $V_t+1000 \mu\text{m}\cdot\text{s}^{-1}$ and pure rutile phase occurs at speed above $V_t+2400 \mu\text{m}\cdot\text{s}^{-1}$, where the threshold of NP growth, V_t , is $15\pm5 \mu\text{m}\cdot\text{s}^{-1}$. Simulation results show that the maximum temperature achieved at such speeds are respectively around 600°C and 750°C, which are in a good agreement with the reported temperature ranges for these crystal phase transitions [Kholmanov 2003, Mossaddeq 2000,

Yuan et Tsujikawa 1995, Ocana 1992]. Besides, at the speed separating the R1 and R2 regimes, $V_t + 50 \mu\text{m}\cdot\text{s}^{-1}$, the increase in the maximum temperature rise has a greater slope than at other speeds. As seen in the section above, this behavior can be interpreted as resulting from the activation of both Ostwald ripening and NP coalescence leading to growth of both the average NPs size and the total volume fraction of Ag in NPs, which significantly increases the absorption of the NP composite film.

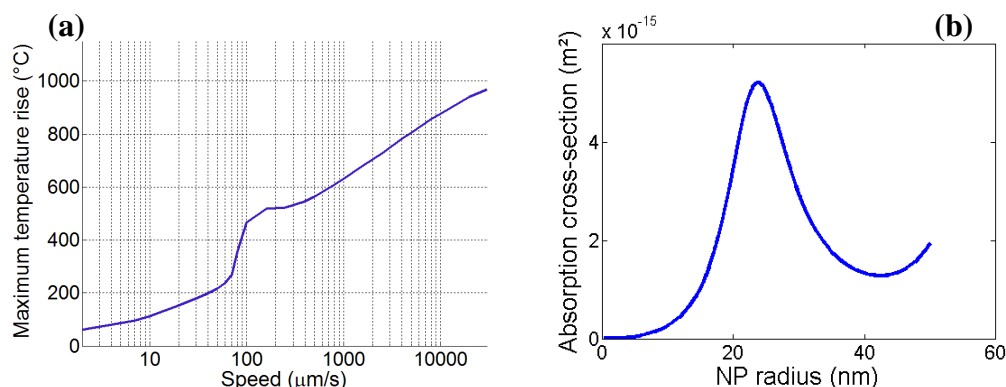


Figure IV.13. a: Evolution of simulated maximum temperature rise as a function of scan speed. b: Absorption cross-sections of spherical Ag NP within TiO_2 versus NP radius. The absorption cross-sections are calculated using Mie theory with an incident light at 488 nm.

The temporal profiles of average Ag NPs size during laser scans at transition speeds between R1 and R2 or between R2 and R3 regimes are also investigated by simulations (figure IV.14 b, e and h), which reveal a jump of the average size of Ag NPs at the rising edges of the Gaussian beam scan. This jump in the Ag NP size evolution has also been observed previously in chapter III and explained by a positive feedback loop established during the Ag NP growth. According to the Mie theory, the plasmon absorption of Ag NPs depends on the size of Ag NPs (Figure IV.13.b). In the studied case, the maximum absorption of NP is found at a radius around 22 nm, *i.e.* 44 nm in diameter. For this reason, below this size, the absorption of Ag NP can also be increased with NP thermal growth. Higher size means higher absorption and leads to higher temperature rise, which promotes the thermal growth of NPs. The absorption decreases with NPs size decrease above 44 nm, which breaks the positive feedback loop and the Ag NPs growth slows down after this point.

The maximum temperature rise depends both on the absorption of the sample and on the light intensity [Calder 1982]. It always occurs when the NP absorption is maximum, *i.e.* when the NP size is around 44 nm in average (Figure IV.14 c, f and i). The value of the maximum temperature rise is then defined by the instantaneous laser intensity during the size jump. When the scan speed increases, the temporal distance from the arrival of laser beam to this NP size jump is shortened. However, the duration of laser scan decreases more quickly than it. This jump thus occurs at a higher instantaneous laser intensity, which results

in a higher temperature at higher speed. As a result, the maximum temperature rise of laser scan always increases with the scan speed.

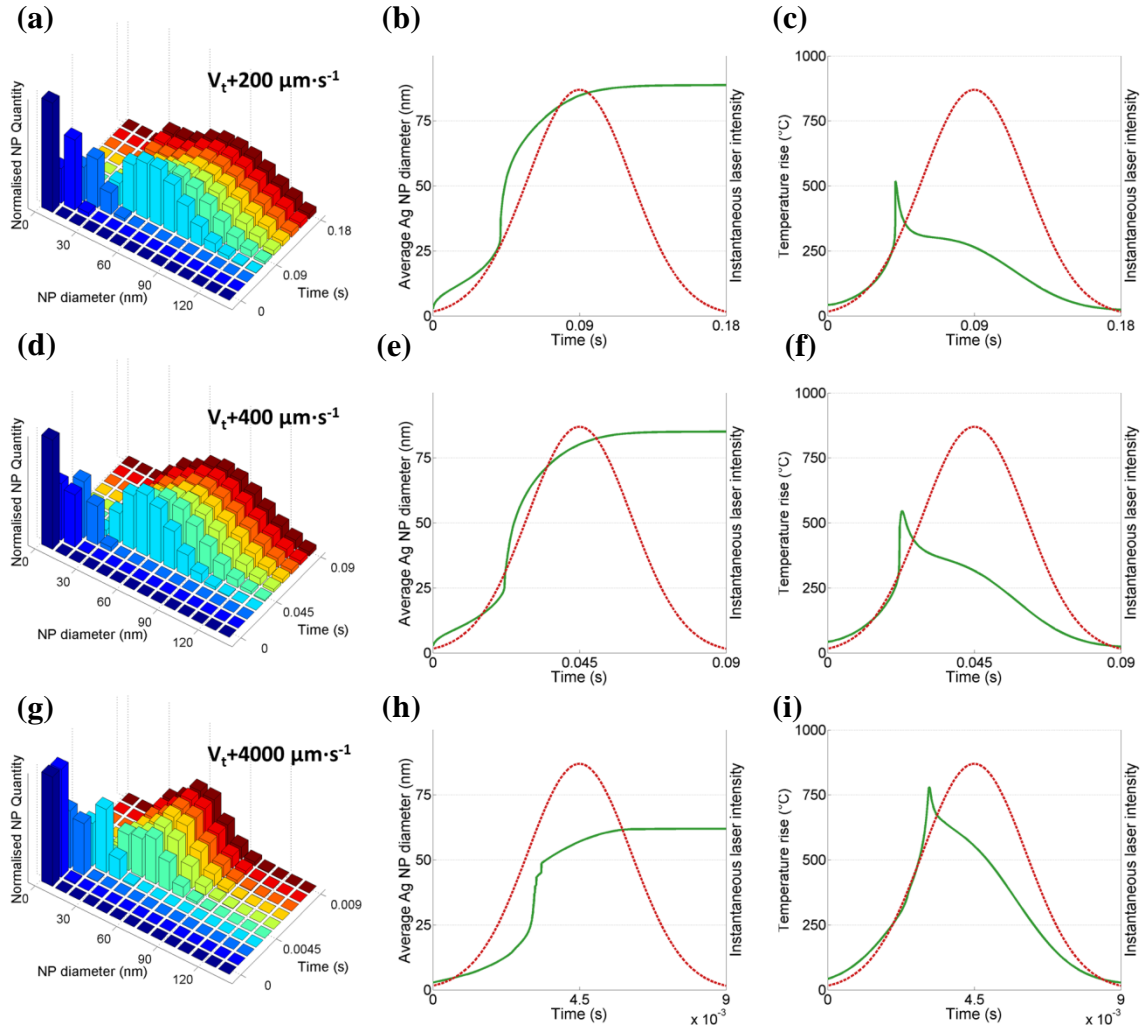


Figure IV.14. Temporal evolution of the size histogram of Ag NP distribution (a, d and g), the average size of Ag NP distribution (green lines in b, e and h) and the laser-induced temperature rise (green lines in c, f and i) at speeds $V_t + 200 \mu\text{m}\cdot\text{s}^{-1}$ (a-c), $V_t + 400 \mu\text{m}\cdot\text{s}^{-1}$ (d-f) and $V_t + 4000 \mu\text{m}\cdot\text{s}^{-1}$ (g-i). Instantaneous laser intensity are plotted by red dotted lines.

The decrease in the NP size can also be explained by the shortness of scan duration. In 3D histograms of figure IV.14, one find the same experimentally observed two peaks shape (see section 1.1) in NP size histograms of the simulation result at speed $V_t + 70 \mu\text{m}\cdot\text{s}^{-1}$ (figure IV.12.d). The two peaks emerge and separate from each other at the falling edge of the Gaussian laser beam, when the maximum temperature peak is already passed and only lower temperature rise occurs. The thermal growth rate becomes thus less important than in the rising edge of the Gaussian beam. Scan duration plays the dominant role. At speed $V_t + 200 \mu\text{m}\cdot\text{s}^{-1}$ (figure IV.14.a), the two peaks in size histograms have less time to fully separate from each other, when comparing with the case of $V_t + 70 \mu\text{m}\cdot\text{s}^{-1}$ in figure IV.12.d. When the speed is increased to $V_t + 400 \mu\text{m}\cdot\text{s}^{-1}$ (figure IV.14.d), the size histogram has even not time to separate in two. At higher speed, *i.e.* $V_t + 4000 \mu\text{m}\cdot\text{s}^{-1}$ (figure IV.14.h), the final size

of Ag NP converges at about 50 nm which corresponds to the end of the average size jump defined by the positive feedback loop explained above. The R3 regime, concluded at the end of section 1, can thus be established.

4. Conclusion

The growth of the CW laser induced Ag NPs is characterized and modeled as a function of the scan speed. Both the scan duration and the interactions between various physico-chemical processes involved during laser exposure play dominant roles in changing the grown NP size and the laser-induced thermal effect. The thermally activated growth mechanisms that occur either through the adsorption of silver atoms (Ostwald ripening and silver ion reduction) or the NP coalescence counterbalances the photo-oxidation leading to the decrease of NP size and absorption from the beginning of the laser scan. For a given couple of incident intensity and beam width, two different competitions between these processes can be tuned by the scan speed of the Gaussian laser beam. With an increase of scan speed, the NP coalescence outweighs firstly the photo-oxidation and results in a growth of NP into irregular shapes with an average size around 20 nm. A temperature rise less than 350°C is produced which partially crystallizes and collapses the mesoporous TiO₂ film. The Ostwald ripening growth is activated hereafter at higher speeds and leads to the simultaneous growth of the average size and the total volume of Ag in NPs. The latter creates much larger spherical NPs whose size reaches 100 nm within the TiO₂ film, which is completely crystallized by a higher temperature rise about 600°C. During the laser scan at these speeds, the average size of NPs increases principally through a jump from 20 nm to about 50 nm. This jump always occurs at the rising edge of the Gaussian laser beam and induces the maximum temperature rise during the scan. With an increase of the scan speed, the temporal position of this jump shifts to the beam center and increases the maximum temperature rise. During the falling edge of the laser scan, the growth rate becomes lower due to the decrease of light intensity and the smaller absorption of larger Ag NPs. The final NP size is then limited by the lack of time for growth at higher speeds.

The numerical model describing the Ag NP size variation has been improved so that the NP coalescence and the polydispersity of the NP distribution are explicitly taken into account. The main mechanisms at the origin of changes in the NP size have been formulated through an ODE set of four equations. Simulated results are in good agreement with experimental observations and reveal the significant influence of each involved process. Such a model can be applied to better predict and optimize the size evolution of metallic NPs in TiO₂ based systems used for photocatalysis and estimate changes in their efficiency. It is also a starting point to simulate self-organization mechanisms of metallic NPs upon laser

exposure. Furthermore, the numerical approach and physical formulation that have been presented for each involved physicochemical process give the possibility to apply or extend the NP growth model to other similar systems such as NPs in liquid solution or embedded NP in glass.

References

- Ahn, T.-M.; Tien, J. K.; Wynblatt, P. Coarsening Kinetics of Platinum Particles on Curved Oxide Substrates. *Journal of Catalysis* **1980**, *66* (2), 335–346.
- Alexopoulos, A. H.; Kiparissides, C. A. Part II: Dynamic Evolution of the Particle Size Distribution in Particulate Processes Undergoing Simultaneous Particle Nucleation, Growth and Aggregation. *Chemical Engineering Science* **2005**, *60* (15), 4157–4169.
- Brancker, A. V. Viscosity-Temperature Dependence. *Nature* **1950**, *166* (4230), 905–906.
- Calder, I. D.; Sue, R. Modeling of CW Laser Annealing of Multilayer Structures. *Journal of Applied Physics* **1982**, *53* (11), 7545–7550.
- Castro, T.; Reifengerger, R.; Choi, E.; Andres, R. P. Size-Dependent Melting Temperature of Individual Nanometer-Sized Metallic Clusters. *Phys. Rev. B* **1990**, *42* (13), 8548–8556.
- Chen, K.; Feng, X.; Hu, R.; Li, Y.; Xie, K.; Li, Y.; Gu, H. Effect of Ag Nanoparticle Size on the Photoelectrochemical Properties of Ag Decorated TiO₂ Nanotube Arrays. *Journal of Alloys and Compounds* **2013**, *554*, 72–79.
- Chen, X.; Mao, S. S. Titanium Dioxide Nanomaterials: Synthesis, Properties, Modifications, and Applications. *Chem. Rev.* **2007**, *107* (7), 2891–2959.
- Clavero, C. Plasmon-Induced Hot-Electron Generation at Nanoparticle/metal-Oxide Interfaces for Photovoltaic and Photocatalytic Devices. *Nat Photon* **2014**, *8* (2), 95–103.
- Destouches, N.; Crespo-Monteiro, N.; Vitrant, G.; Lefkir, Y.; Reynaud, S.; Epicier, T.; Liu, Y.; Vocanson, F.; Pigeon, F. Self-Organized Growth of Metallic Nanoparticles in a Thin Film under Homogeneous and Continuous-Wave Light Excitation. *J. Mater. Chem. C* **2014**, *2* (31), 6256–6263.
- Egan, G. C.; Sullivan, K. T.; LaGrange, T.; Reed, B. W.; Zachariah, M. R. In Situ Imaging of Ultra-Fast Loss of Nanostructure in Nanoparticle Aggregates. *Journal of Applied Physics* **2014**, *115* (8), 84903.
- Fluegel, A.; Varshneya, A. K.; Earl, D. A.; Seward, T. P.; Oksoy, D. Improved Composition-Property Relations in Silicate Glasses, Part I: Viscosity. In *Melt Chemistry, Relaxation, and Solidification Kinetics of Glasses*; Li, H., Ray, C. S., Strachan, D. M., Weber, R., Yue, Y., Eds.; John Wiley & Sons, Inc., 2006; pp 129–143.
- Granqvist, C. G.; Buhrman, R. A. Size Distributions for Supported Metal Catalysts: Coalescence Growth versus Ostwald Ripening. *Journal of Catalysis* **1976**, *42* (3), 477–479.
- Hounslow, M. J.; Ryall, R. L.; Marshall, V. R. A Discretized Population Balance for Nucleation, Growth, and Aggregation. *AIChE J.* **1988**, *34* (11), 1821–1832.
- Kaganovskii, Y.; Lipovskii, A.; Rosenbluh, M.; Zhurikhina, V. Formation of Nanoclusters through Silver Reduction in Glasses: The Model. *Journal of non-crystalline solids* **2007**, *353* (22–23), 2263–2271.

- Kholmanov, I. N.; Barborini, E.; Vinati, S.; Piseri, P.; Podestà, A.; Ducati, C.; Lenardi, C.; Milani, P. The Influence of the Precursor Clusters on the Structural and Morphological Evolution of Nanostructured TiO₂ under Thermal Annealing. *Nanotechnology* **2003**, *14* (11), 1168.
- Kim, T.; Lee, C.-H.; Joo, S.-W.; Lee, K. Kinetics of Gold Nanoparticle Aggregation: Experiments and Modeling. *Journal of Colloid and Interface Science* **2008**, *318* (2), 238–243.
- Kosacki, I.; Suzuki, T.; Anderson, H. U.; Colomban, P. Raman Scattering and Lattice Defects in Nanocrystalline CeO₂ Thin Films. *Solid State Ionics* **2002**, *149* (1–2), 99–105.
- Kumar, J.; Peglow, M.; Warnecke, G.; Heinrich, S. An Efficient Numerical Technique for Solving Population Balance Equation Involving Aggregation, Breakage, Growth and Nucleation. *Powder Technology* **2008**, *182* (1), 81–104.
- Kumar, S.; Ramkrishna, D. On the Solution of Population Balance Equations by discretization—III. Nucleation, Growth and Aggregation of Particles. *Chemical Engineering Science* **1997**, *52* (24), 4659–4679.
- Lehtinen, K. E. J.; Zachariah, M. R. Effect of Coalescence Energy Release on the Temporal Shape Evolution of Nanoparticles. *Phys. Rev. B* **2001**, *63* (20), 205402.
- Lifshitz, I. M.; Slyozov, V. V. The Kinetics of Precipitation from Supersaturated Solid Solutions. *Journal of Physics and Chemistry of Solids* **1961**, *19* (1–2), 35–50.
- Liu, Z.; Destouches, N.; Vitrant, G.; Lefkir, Y.; Epicier, T.; Vocanson, F.; Bakhti, S.; Fang, Y.; Bandyopadhyay, B.; Ahmed, M. Understanding the Growth Mechanisms of Ag Nanoparticles Controlled by Plasmon-Induced Charge Transfers in Ag-TiO₂ Films. *J. Phys. Chem. C* **2015**, *119* (17), 9496–9505.
- Ma, H. L.; Yang, J. Y.; Dai, Y.; Zhang, Y. B.; Lu, B.; Ma, G. H. Raman Study of Phase Transformation of TiO₂ Rutile Single Crystal Irradiated by Infrared Femtosecond Laser. *Applied Surface Science* **2007**, *253* (18), 7497–7500.
- Maisels, A.; Einar Kruis, F.; Fissan, H. Direct Simulation Monte Carlo for Simultaneous Nucleation, Coagulation, and Surface Growth in Dispersed Systems. *Chemical Engineering Science* **2004**, *59* (11), 2231–2239.
- Martínez, E. D.; Boissière, C.; Grosso, D.; Sanchez, C.; Troiani, H.; Soler-Illia, G. J. A. A. Confinement-Induced Growth of Au Nanoparticles Entrapped in Mesoporous TiO₂ Thin Films Evidenced by in Situ Thermo-Ellipsometry. *J. Phys. Chem. C* **2014**, *118* (24), 13137–13151.
- Mosaddeq-ur-Rahman, M.; Yu, G.; Soga, T.; Jimbo, T.; Ebisu, H.; Umeno, M. Refractive Index and Degree of Inhomogeneity of Nanocrystalline TiO₂ Thin Films: Effects of Substrate and Annealing Temperature. *Journal of Applied Physics* **2000**, *88* (8), 4634–4641.
- Ocaña, M.; Garcia-Ramos, J. V.; Serna, C. J. Low-Temperature Nucleation of Rutile Observed by Raman Spectroscopy during Crystallization of TiO₂. *Journal of the American Ceramic Society* **1992**, *75* (7), 2010–2012.
- Parker, S. C.; Campbell, C. T. Kinetic Model for Sintering of Supported Metal Particles with Improved Size-Dependent Energetics and Applications to Au on TiO₂ (110). *Phys. Rev. B* **2007**, *75* (3), 35430.
- Qamar, S.; Warnecke, G.; Elsner, M. P. On the Solution of Population Balances for Nucleation, Growth, Aggregation and Breakage Processes. *Chemical Engineering Science* **2009**, *64* (9), 2088–2095.
- Schmitt, A.; Odriozola, G.; Moncho-Jordá, A.; Callejas-Fernández, J.; Martínez-García, R.; Hidalgo-Álvarez, R. Multiple Contact Kernel for Diffusionlike Aggregation. *Phys. Rev. E* **2000**, *62* (6), 8335–8343.
- Smith, M.; Matsoukas, T. Constant-Number Monte Carlo Simulation of Population Balances. *Chemical Engineering Science* **1998**, *53* (9), 1777–1786.

Sun, J.; Ma, D.; Zhang, H.; Liu, X.; Han, X.; Bao, X.; Weinberg, G.; Pfänder, N.; Su, D. Toward Monodispersed Silver Nanoparticles with Unusual Thermal Stability. *J. Am. Chem. Soc.* **2006**, *128* (49), 15756–15764.

Yang, F.; Chen, M. S.; Goodman, D. W. Sintering of Au Particles Supported on TiO₂(110) during CO Oxidation. *J. Phys. Chem. C* **2009**, *113* (1), 254–260.

Yu, K.; Tian, Y.; Tatsuma, T. Size Effects of Gold Nanoparticles on Plasmon-Induced Photocurrents of Gold-TiO₂ Nanocomposites. *Phys Chem Chem Phys* **2006**, *8* (46), 5417–5420.

Yuan, J.; Tsujikawa, S. Characterization of Sol-Gel-Derived TiO₂ Coatings and Their Photoeffects on Copper Substrates. *J. Electrochem. Soc.* **1995**, *142* (10), 3444–3450.

Zhang, W. F.; He, Y. L.; Zhang, M. S.; Yin, Z.; Chen, Q. Raman Scattering Study on Anatase TiO₂ Nanocrystals. *J. Phys. D: Appl. Phys.* **2000**, *33* (8), 912.

Chapter V. Pulsed laser induced NP self-organization and anisotropic growth

In this chapter, we report on the generation of Ag nanostructures within Ag:TiO₂ composite films by femtosecond (fs) laser irradiations. Both self-organization and anisotropic growth of Ag NPs have been observed using a visible pulsed laser delivering ultra-short laser pulses of 350 fs at a frequency of 500 kHz and a wavelength of 515 nm. According to the volume and surface characterizations of the laser irradiated samples, the size and shape of the grown Ag NPs as well as the orientation and period of nanostructures are found to be strongly influenced by the laser fluence and scan speed. Laser induced periodic surface structures (LIPSS) are also found to simultaneously emerge on the film surface together with the growth of Ag nanostructures. However, the Ag nano-patterns are not necessarily correlated with LIPSS. Features of both can be tuned by varying laser exposure conditions. The laser processed samples exhibit different optical properties including excitation of guided modes, dichroic colors and diffractive colors on transparent support over large area. Thermal effects induced by fs laser are also compared with those characterized upon CW laser processes. This technique can lead to potential solutions in fields like active color displays, security, polarization imaging upon transparent and flexible support. This work was carried out in collaboration with the laser processing group of CSIC in Madrid, Spain.

1. Introduction

The growth behavior of Ag NPs in TiO₂ matrix driven by CW laser flux has been discussed in the previous chapters. This simple laser writing technique offers a new solution for organizing embedded Ag NPs along 1D grating with a sub-wavelength period over large areas. In the meanwhile, pulsed lasers have also been widely used during the past decades to control metallic NP features in composite materials. Unlike CW lasers, pulsed lasers allow confining optical energy into a short period of time down to the femtosecond (10^{-15} second) scale and lead to both interaction of highly intense light with composite matter and control of the transient response of NPs under photon excitation [Diels 1997]. The NP gratings resulting from light pulse-NP interactions are hence usually found to be tunable with various laser exposure parameters including temporal pulse length, optical fluence, repetition rate, beam shape, etc. Compared with classic top-down techniques for NPs synthesis, laser writing appears as a flexible and low-cost tool to tailor the spectral responses of metallic NP based materials over large areas to match specific applications, like multiplexed optical recording systems for high-density data storage [Chon 2007] or dichroic devices [Nicolas Filippin 2013] etc.

Shaping the optical response of NP composites can be based on modifications of the morphology of individual NPs. A pioneering work of this approach has been reported in 1999 [Kaempfe 1999] where high energetic femtosecond (fs) laser pulses were used to deform spherical Ag NPs embedded in glass into an anisotropic shape with uniform orientation to produce permanent dichroic optical responses of the glass sample. Hot electron emission, ion diffusion and electron-ion recombination at preferential direction induced by the highly intense laser pulse were considered to be at the origin of the NP reshaping. The shape of laser-deformed NPs hence strongly depends on the laser exposure parameters such as light polarization, pulse fluence and pulse number [Stalmashonak 2008]. Selective melting or fragmentation of metallic nanorods that is controlled by the wavelength of fs laser irradiations was also used to give rise to an overall anisotropy in a NP distribution initially randomly oriented [Chon 2007, Zijlstra 2009]. For laser pulses at picosecond (10^{-12} second) and nanosecond (10^{-9} second) ranges, growth of near-coalescence NPs via coarsening and agglomeration in preferential directions was widely used to change the optical response of nanocomposite systems [Nicolas Filippin 2013, Nouneh 2011]. At these pulse lengths, the laser-induced temperature rise becomes important thanks to the stationary thermal regimes usually established at a time scale of picosecond order [Von der Linde 1997]. In certain cases, this thermal effect also leads to the transformation of irregularly shaped NPs into spherical shape [Inasawa 2005, Resta 2006]. In order to achieve better control of the optical response of NP composites, researchers also tried to combine short laser pulses of different time lengths [Doster 2014] or different wavelengths [Stalmashonak 2009].

Another strategy for tailoring the optical response of a NP system is to arrange NPs into periodic grating-type structures. The optical response of such composite materials can be tuned both by varying features of the periodic structure and changing the morphology of individual NPs in these structures. Different implementation methods can be found in the literature. Several methods use pre-structured substrates as templates to restrain the generation of NPs at well-ordered positions. In this case, the NP structure can be formed by short laser pulses dewetting of a metallic thin film [Bris 2014, Oh 2013] on such templates. Instead of using templates, few works were reported on organization of NPs by pulse laser with DC electric field assistance [Yadavali 2014]. Other approaches use interference patterns raised from multi-beam irradiations to produce preferential growth of NPs at periodic positions [Kaneko 2003, Qu 2004, Smirnova 2009]. Another efficient way to generate interferograms is the use one single beam. The modulation of light intensity is then related either to interference of guided modes excited in a thin layer [Eurenius 2008], or interference between the incident wave and surface or scattered waves [Kaempfe 2001, Kiesow 2005, Loeschner 2010, Nakajima 2015]. The latter usually lead to Laser-Induced Periodic Surface Structures (LIPSS) that have been discovered already 50 years ago upon irradiation of materials including semiconductors [Birnbaum 1965], metals as well as dielectrics [Sipe 1983, van Driel 1982, and references therein] with pulsed lasers.

Pulsed laser is capable to produced diverse NP structures. Most of these structures are however formed at sample surfaces, especially when they are organized. These processes need to be complemented by a second step of cover layer deposition to protect NPs. Silver NPs, for instance is known to spontaneously oxide when exposed to air. Moreover, the growth of NPs usually relies on pre-deposited NPs or thin films which introduce complex preparations of initial samples before laser processing. The Ag:TiO₂ sample studied in the previous chapters is a good alternative since silver is initially loaded in the film by a simple impregnation of ionic solution and Ag NPs seeds grow spontaneously under ambient environment. Besides, CW laser experiments have proven the possibility of generating periodic NP structure by a simple single beam scan [Destouches, Crespo-Monteiro et al. 2014]. This gave us the motivation to exploit the interactions of pulsed laser irradiation on our Ag:TiO₂ composite.

The first pulsed laser experiments were performed through collaboration with the Laser Processing Group of Instituto de Optica, of Consejo Superior de Investigaciones Científicas (CSIC) in Madrid, Spain. In the present work, co-supervised by Dr. Jan Siegel of CSIC, we demonstrated that Ag NPs in TiO₂ matrix undergoes spectacular micro- and nano-structural modifications after raster scans of fs laser at 515 nm. Laser setup has been described in chapter II. The latter operates at 500 kHz delivering laser pulse of 300 fs. Raster laser scan is performed under normal incidence and at the focal plane of the laser beam, whose width is measured at about 35 μm . Each laser scan line was separated by 2 μm . Both

surface structure and volume structure were experimentally investigated using Atomic Force Microscope (AFM), Scanning Electron Microscope (SEM) and Transmission Electron Microscope (TEM) techniques. The possible origins of the embedded Ag NP structure and surface structures have been discussed. Thermal effects induced by the fs laser process are also compared with the case of a CW laser process. The latter is performed by compositional analysis of laser irradiated sample cross-sections using Electron Energy-Loss Spectroscopy (EELS). The advantage of the fs laser processes and possible applications of the fs laser-induced structures have also been pointed out at the end of this chapter.

2. Self-organization of NPs versus LIPSS formation

Self-organizations of silver NPs have been obtained with fs laser scans on the initial state S1 of the studied Ag:TiO₂ composite films using the setup described in section 2.2 of Chapter II. In this part, we show the surface and volume characterization these NP grating structures and give possible origins of their formations. The relations between the Ag NP self-organization and the LIPSS simultaneously formed by laser pulses will also be discussed.

2.1 Self-organization of NP related to the LIPSS formation

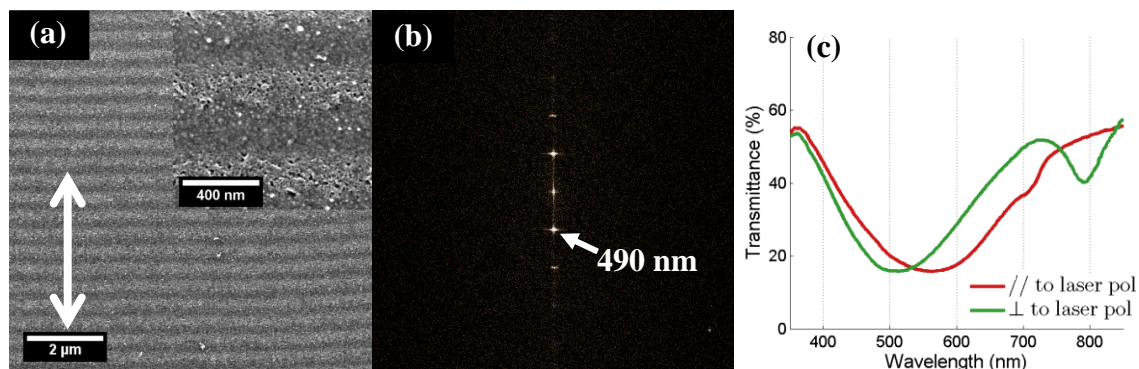


Figure V.1. a: SEM image of G1 at low and high (inset) magnification. The double-headed arrow indicates the incident laser polarization. b: 2D Fast-Fourier Transform (FFT) of subfigure a that shows a periodicity of 490 nm, near to incident wavelength (515 nm). c: Transmission spectrum of G1.

The first kind of NP self-organization, named G1, was obtained in a fluence range from 42 mJ·cm⁻² to 62 mJ·cm⁻² at scan speed varying from 50 mm·s⁻¹ to 120 mm·s⁻¹. SEM images of G1 (Figure V.1.a) show a periodic contrast on the surface, which is perpendicular to the incident laser polarization. The Fast Fourier Transform of the latter suggests a period around 490 nm (Figure V.1.c) that is similar to the incident laser wavelength (515 nm). We observe at higher magnification (Figure V.1.b) that this periodic contrast is at least caused by

a partial collapse (closure of pores on the top surface) of the initial mesostructure of TiO_2 in darker lines of SEM image. According to these SEM images, embedded Ag NPs also seem to grow within these darker lines. Anisotropic optical responses can be observed on this periodic structure (Figure V.1.c). We thus need further studies about the surface and volume structures of the films.

2.1.1 Surface structure

AFM images of G1 (Figure V.2.a) suggest that the periodic structure corresponds to a LIPSS. The LIPSS height is around 50 nm. The period and the orientation of the LIPSS in AFM images are all in good agreement with SEM measurements. The observed LIPSS in this case is a well-known structure usually named Low Spatial Frequency (LSF) LIPSS. As reported in the literature [Van Driel 1982, Sipe 1983, Bonse 2002, Ruiz de la Cruz 2014], this LSF LIPSS is usually formed with an orientation perpendicular to the incident laser polarization and has a period close to the incident wavelength. The origin of LSF LIPSS is generally accepted as the interference of the incident light and surface scattering light. In the case of G1, lines where the mesostructure has collapsed appear to correspond to the valleys of the LIPSS, which is later confirmed by its volume characterization.

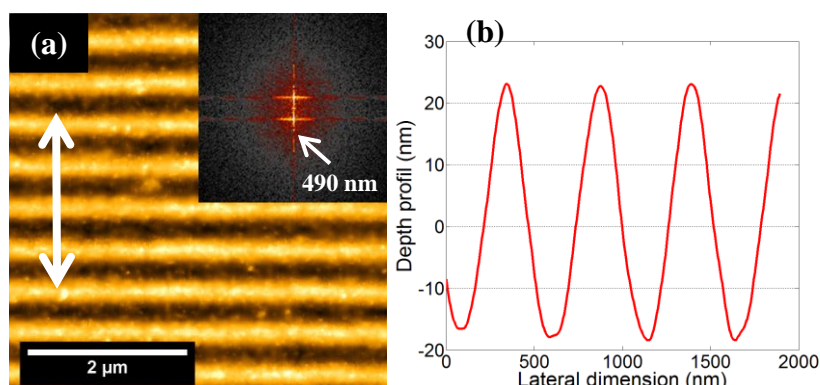


Figure V.2. a: AFM image and its FFT (inset) of G1. The double-headed arrow indicates the incident laser polarization. b: Depth profile of G1 along the laser polarization (perpendicular to LIPSS)

2.1.2 Volume structure

Embedded Ag NPs self-organized within the film are shown by the HAADF STEM images. Top views of G1 samples suggest a growth of Ag NPs from about 1.5 nm to about 20 nm in lines where the TiO_2 mesostructure has collapsed (Figure V.3.a). Further in-depth information about G1 is given by HAADF STEM characterizations of a FIB cross section (Figure V.3.b-d). The latter is extracted perpendicular to the LIPSS orientation, so that the sinusoidal topography that was previously shown on AFM image can also be found here. The position of the grown Ag NPs can be clearly determined at the valley of the LIPSS. One can

now conclude that the parallel mesoporous lines correspond to the ridges of the LIPSS and the collapsed lines are the valleys where Ag NPs grow near to TiO_2 top surface during laser irradiation. One can deduce that anisotropic optical response of G1 also comes from Ag NP gratings.

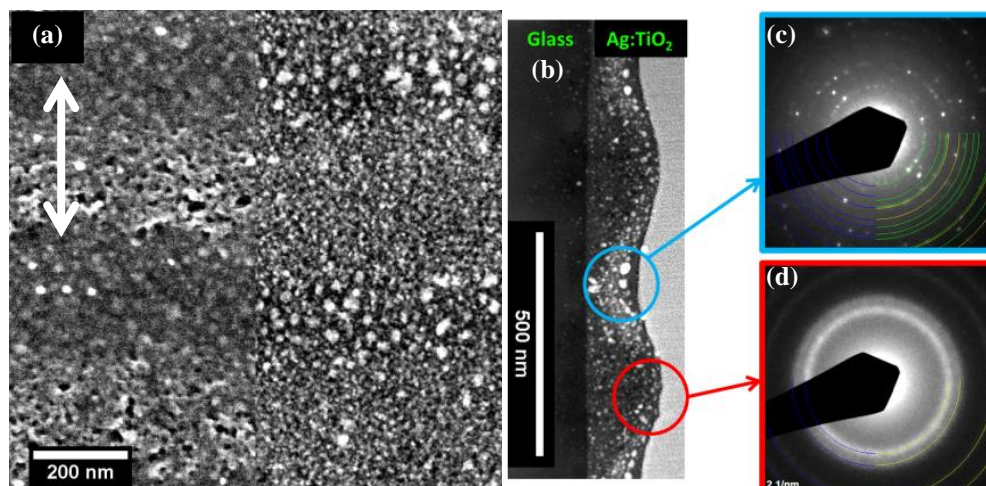


Figure V.3. a. Top view SEM (left) and HAADF STEM (right) images of G1. The double-headed arrow indicates the incident laser polarization. b. HAADF STEM image of film cross-section cut perpendicular to LIPSS. c-d: diffraction patterns of the blue (c) and red (d) circle zones in b. Concentrated rings or diffraction spots locating in different rings can be observed on c and d. Blue curves in c and d indicate observed rings, whose radius correspond to the positions of diffraction spots of silver (yellow curves) or TiO_2 (green curves).

2.1.3 Crystallization state

In order to investigate the crystallization state of the initial amorphous TiO_2 after laser irradiation, TEM diffraction patterns were recorded within valleys (figure V.3.c) and ridges (figure V.3.d) of LIPSSs. Below ridges (figure V.3.d), no significant diffraction spots are observed except four concentrated rings (labelled by blue curves). The radii of the latter all correspond to the positions of the weak diffraction of small Ag NPs (yellow curve) that were already present in the initial sample. However, numerous diffraction spots corresponding to either silver (yellow curve) or TiO_2 (green curve) can be found below the valleys of LIPSS. This suggests that TiO_2 remains amorphous and mesoporous within the ridges and that only the valleys of LIPSS are filled with nanocrystals of TiO_2 and grown Ag NP.

The nature of crystals present in the valleys can also be identified from diffraction patterns as being mainly fcc Ag and anatase TiO_2 . We however also used the 4D STEM imaging technique [Ophus 2014] to recover an accurate map of the different kinds of nanocrystals present within the nanostructured film. The 4D STEM image acquisition and the corresponding analysis were performed by Thierry EPICIER from MATEIS laboratory in Lyon. Figure V.4 shows the crystallographic analysis as permitted by the 4D STEM procedure

developed by Gatan. When recording a conventional STEM image, a nano-diffraction pattern is recorded at each probe position, enabling to reconstruct a crystalline phase map by applying adequate filters in the Fourier space (diffraction space). Experiments were performed on a FEI-Titan ETEM microscope operated at 300 kV. A nano-probe imaging mode was used where the probe size was estimated to about 1 nm and the incident beam half-convergence to 0.3 mrad.

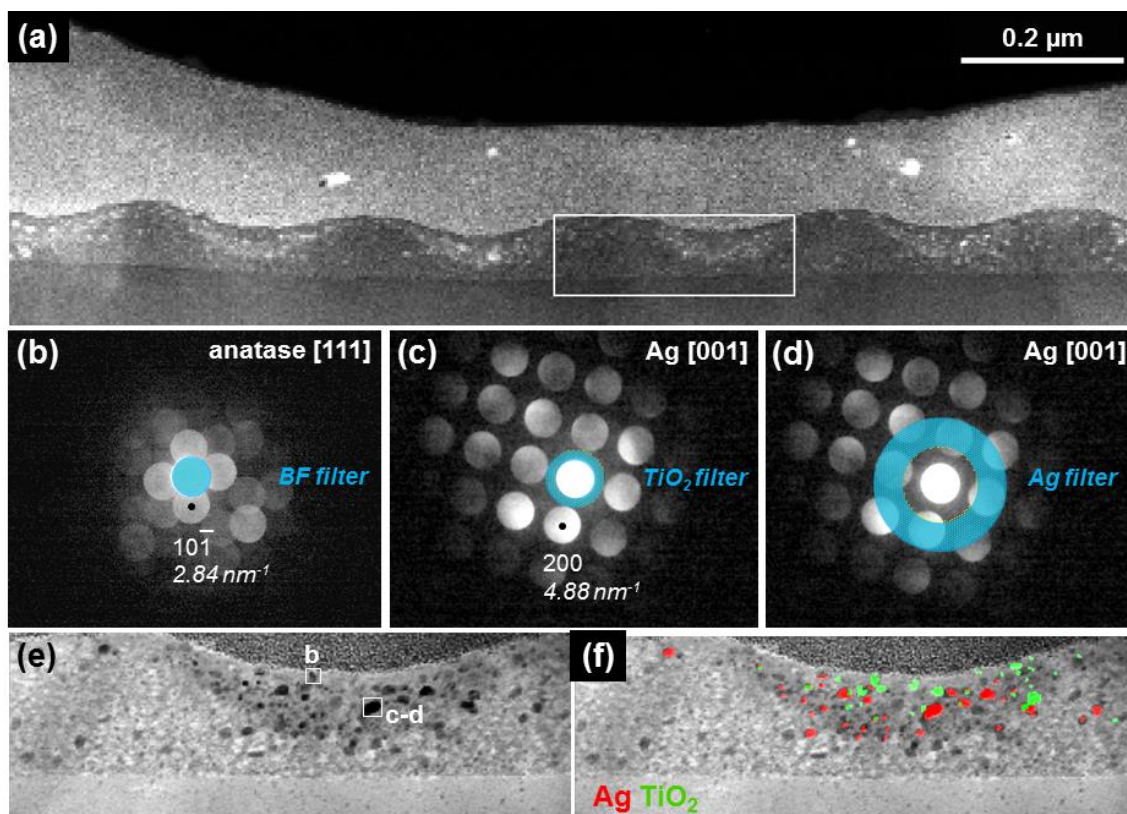


Figure V.4. Crystallographic mapping of the G1 cross-section (FIB section, FEI-Titan ETEM 300 kV). a: Low magnification HAADF-STEM image showing the LIPSS and the working area (white frame) studied in “4D-STEM” in b to d; b-d: Typical nano-diffraction patterns recorded at positions marked in e; according to the filters indicated by the blue dashed areas, the transmitted intensity in each pixel can be reconstructed to give the complete 300 x 100 pixels maps shown in sub-figure e (reconstructed bright field image where dark areas are diffracting crystalline regions) and in sub-figure f (where the red and green pixels correspond respectively to Ag and TiO₂ crystalline phases reconstructed by the bandpass filters in c and d).

According to the fact that all possible crystalline TiO₂ phases (brookite, anatase or rutile) have significantly larger lattice parameters than the fcc lattice of silver, a very narrow pass-band filter positioned close to the central beam as shown in figure V.4.c will exclude any reflection from the silver lattice and will then easily image the TiO₂ phases without contribution from the metallic phase. Similarly to the way to reconstruct TiO₂, Ag NPs can be selected by applying a different bandpass filter passing higher frequencies (Figure V.4.c). Reconstructed TiO₂ crystals and Ag NPs were then labelled by different colors in figure V.4.f. In this figure, TiO₂ is crystallized in nanocrystals but only around the grown Ag NP. According to the literature, the lowest temperature at room conditions to form TiO₂ crystal is about

350-400°C. One can thus conclude that a strong temperature rise occurs during the growth process of Ag NPs and that this strong heating remains confined on a distance smaller than the period of the periodic nanostructure.

2.1.4 Origin of NP self-organization

According to the previous surface and volume characterizations, the self-organized Ag nanostructures appear to be strongly correlated with the LSF LIPSS at TiO₂ top surface. The origin of the LSF LIPSS is generally described as the interference of the incident light with a surface electromagnetic field scattered by the roughness of the sample surface [Van Driel 1982, Sipe 1983, Bonse 2002]. This interference gives rise to a modulated light intensity which finally induces a periodic local modification (often ablation) of the sample surface.

In the present case, Ag NPs exhibit a strong thermally-induced growth during the visible fs laser exposure, as observed with CW lasers [Destouches, Crespo-Monteiro et al. 2014, Liu 2015]. According to the previous conclusion in Chapter III and IV, we know from the modeling and analysis of the light induced physico-chemical mechanisms that occur in such systems that Ag NPs only grow when the temperature is sufficiently high; otherwise they oxidize upon visible light and decrease in size. We thus propose the following explanation for the formation of G1. If we assume the commonly admitted model for the LSF LIPSS formation, interference creates firstly a periodic light intensity near the top surface of the sample where the absorption of visible light is homogeneous. At the positions where local light intensity is enhanced, a stronger temperature rise is expected and activates the growth process of Ag NP such as the reduction of Ag⁺, Ostwald Ripening and Ag NP coalescence shown in the previous chapters. However, at the positions where local light intensity is attenuated, only lower temperature rise can be achieved and Ag NP size remains the same or may even decreased by visible light. Once this modulated growth of Ag NP occurs, the larger Ag NPs can increase the local absorption of the film and lead to a modulated film absorption. The latter enhances again the modulation of the temperature rise induced by the interference model of light intensity. A positive feedback loop can be formed which promotes in continuous the thermal growth of Ag NP in periodic lines. The periodic temperature rise also crystallizes TiO₂ and makes the mesoporosity collapsed which forms the LIPSS structure at TiO₂ surface. The modulation of light intensity locates at the top surface of TiO₂ which explains also the growth of Ag NP close to the top surface of TiO₂. We can note that this spontaneous structuring is initiated at a visible wavelength absorbed by Ag NPs, thus it is most probably a one photon process and happens for relatively low laser fluence. Without the presence of silver, no LIPSS structures can be formed on the TiO₂ layer at this fluence range.

2.2 NP self-organization perpendicular to LIPSS

Compared with G1, at slower scan speed, typically ranging from $5 \text{ mm} \cdot \text{s}^{-1}$ to $40 \text{ mm} \cdot \text{s}^{-1}$ and in a narrower fluence range from $46 \text{ mJ} \cdot \text{cm}^{-2}$ to $54 \text{ mJ} \cdot \text{cm}^{-2}$, one obtains a different kind of NP self-organized structure named G2 here. The top view SEM image of G2 (Figure V.5.a) suggests a 2D periodicity of the sample, as confirmed by its FFT (Figure V.5.b). Transmission spectrum (Figure V.5.c) shows that G2 also exhibits an anisotropic optical response.

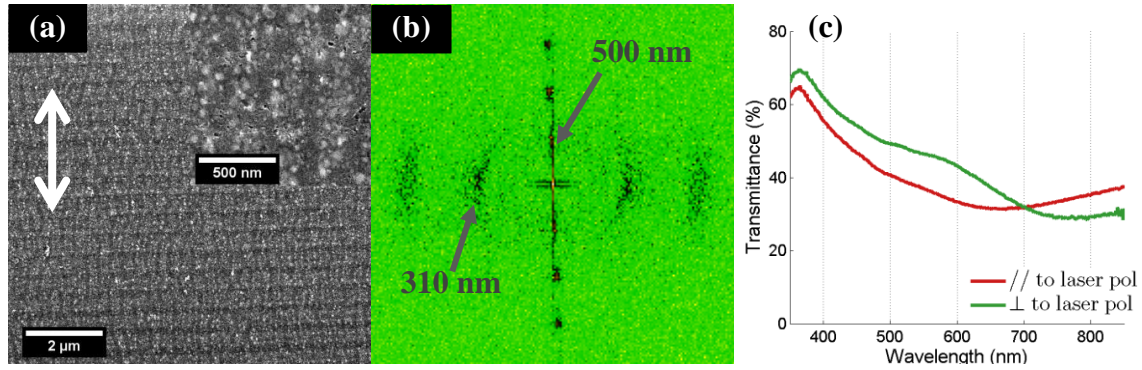


Figure V.5 a: SEM image of G2 top view at low and high (inset) magnification. The laser polarization is indicated by the double-headed arrow. b: FFT of SEM image in a, which reveals a 2D periodicity. c: Transmission spectrum of G2.

2.2.1 Surface structure

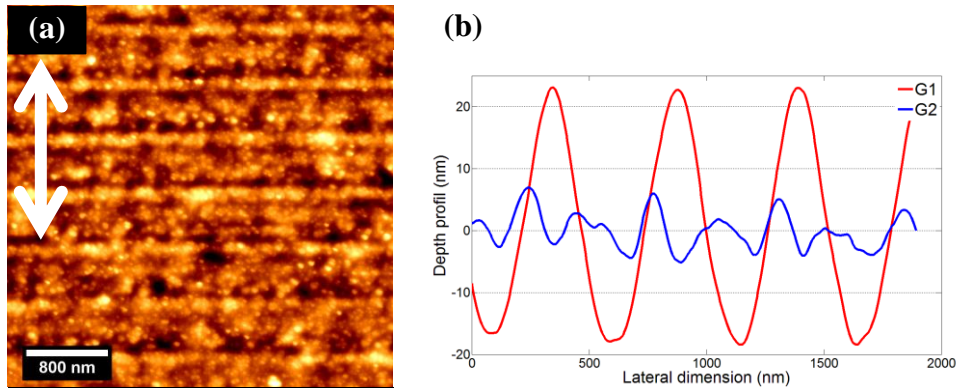


Figure V.6. a: AFM image of G2. The double-headed arrow indicates the incident light polarization. b: depth profile of G1 and G2 along laser polarization.

The periodic structure that perpendicular to laser polarization in the SEM image of G2 (Figure V.5.a) appears to correspond to a LIPSS with a period of 500 nm. More details of the surface topography of G2 are shown by its AFM image (Figure V.6.a). Within each period of 500 nm, one finds a narrow and about 10 nm high ridge and a broad protuberance. The broad protuberance is less regular and less pronounced than the narrow ridge, but splits a 500 nm period in two parts (Figure V.6.b). The periodicity of the ridge/protuberance structure can be thus interpreted as a coarse modulation with period 500 nm, close to λ the

incident wavelength, and a fine modulation close to $\lambda/2$. Due to the lack of homogeneity, the fine modulation is far from a perfect sinusoid. The overall amplitude of the LIPSS in G2 is much smaller than on G1. Finally we notice that no line oriented parallel to the laser polarization is observed in this surface topography.

The LIPSS of G2 is usually known as High Spatial Frequency (HSF) LIPSS in the literature [Bonse 2012, Harzic 2011, Yao 2012, Hou 2011, Ruiz de la Cruz 2014]. The period of the HSF LIPSS is much smaller than the incident laser wavelength. The mechanism of HSF LIPSS formation is still a very open question. Possible explanations including self-organization through relaxation of a perturbed surface [Costache 2003], second-harmonic generation (SHG) upon target surface [Borowiec 2003, Dufft 2009], excitation of Surface Plasmon Polaritons (SPP) or of a guided mode [Martsinovskii 2008, Miyaji 2008], and Coulomb explosion [Dong 2004] have been proposed by different authors. The HSF LIPSS of G2 are formed in a similar fluence range but at lower scan speed than on G1 where only LSF LIPSS were observed. One possible explanation of the fine modulation in G2 might be the splitting of the LSF LIPSS into two parts. Recent works [Yao 2012, Hou 2011, Ruiz de la Cruz 2014] show that a new light amplification within each period of the LSF LIPSS can be formed by the previously formed LSF LIPSS itself and additional light pulses. In the case of metal material, this new light amplification can split the ridge of LSF LIPSS in two parts and gives rise to this HSF LIPSS. In the studied case, the excitation of LSPR on Ag NP and the generation of hot electrons can also transform the composite sample into a metal-like state [Martsinovskii 2008]. Meanwhile, we notice that multi-photon excitation has also been used to explain the formation of HSF LIPSS [Das 2009] at much higher fluence than the one use for G2. However, the local field enhancement induced by the LSPR of Ag NP could also activate the multi-photon excitation of TiO_2 , which has a strong absorption at 262 nm, *i.e.* close to the half incident wavelength. The validity of these hypotheses still requires a detailed theoretical analysis and more experimental studies.

2.2.2 Volume structure

Top view SEM pictures of G2 (Figure V.5.a) indicate the presence of a periodic component parallel to laser polarization with a period of 310 nm, which is not observed in its surface topography. HAADF STEM measurements (Figure V.7.a) show that it corresponds to the embedded grating lines of Ag NPs having irregular shapes and size principally varying from 60 nm to 80 nm. Much smaller NPs are also observed and Ag NPs look randomly distributed within lines whose width is about a half period.

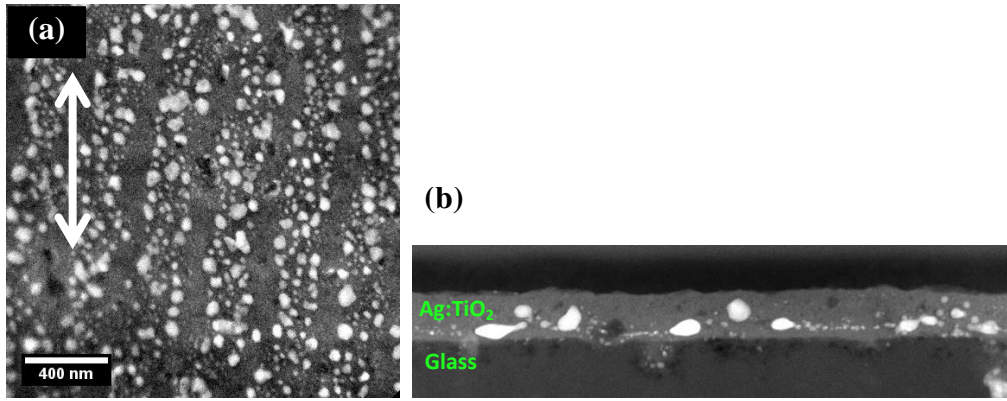


Figure V.7 a: HAADF STEM of G2 top view. The excitation laser polarization is indicated by the double-headed arrow. b: HAADF STEM of G2 cross-section cut perpendicular to the Ag NP self-organized lines.

A depth cross-section of G2 was also measured perpendicular to the Ag NP lines (Figure V.7.b). Different from G1, the Ag NPs in G2 are more likely to grow at the bottom of the TiO_2 layer, instead of close to the top surface. The cross-section view reveals an oblate shape for most of Ag NPs and confirms the presence of small Ag NPs between the lines of large NPs.

2.2.3 Origin of NP self-organization

The period, orientation and depth of Ag NP lines in the TiO_2 layer are all different from LIPSS features. These characterizations suggest that the Ag NP self-organization and LIPSS could be produced by different mechanisms. Similar pulse laser induced metallic NP self-organizations that are parallel to laser polarization have also been reported in the literature [Kaempfe 2001, Loeschner 2010, Eurenus 2008] even if they are all based on pre-deposited NPs. In these works, NP gratings were considered to be at the origin of the dichroic responses of these composites. In the case of G2, the dichroic response is certainly related to NP grating lines (Figure V.5.c). However, the contribution of the low amplitude LIPSS to the dichroism is unclear.

The Ag NP self-organization in G2 goes with a growth of these NPs. Its structure is more similar to the CW laser induced NP self-organization structure shown in the previous chapter of this thesis. According to a previous explanation of our team [Destouches, Crespo-Monteiro et al. 2014], the self-organization of Ag NPs should result from the interference of the incident light with a guided mode excited within the TiO_2 thin layer. The modulated light intensity gives rise to the periodic growth of Ag NPs, which in turn enhances again the amplitude of the guided mode and the contrast of the interference pattern that promotes the organized growth. The period of laser induced NP self-organization is therefore expected to be equal to λ/n_{eff} . n_{eff} is the effective index of the guided mode which is greater than the

substrate refractive index (glass, ~ 1.35) and smaller than the film index (~ 1.7). The latter yields a NPs grating period between 300 nm and 380 nm. Under nanosecond laser pulses, 1D organization of pre-deposited Ag NPs was explained by a waveguide mode excited within a Si_3N_4 thin layer that supports Ag NP [Eurenius 2008]. Excitation of waveguide modes within a thin layer into the depth of a Silicon wafer was also reported under femtosecond laser irradiations [Martsinovskii 2008]. The latter gives rise to a modulation of optical intensity and a formation LIPSS parallel to laser polarization. However, an exhaustive explanation of Ag NP self-organization of G2 still needs further investigations.

		G1	G2
Laser parameters	Fluence	42-62 $\text{mJ}\cdot\text{cm}^{-2}$	46-54 $\text{mJ}\cdot\text{cm}^{-2}$
	Scan speed	50-120 $\text{mm}\cdot\text{s}^{-1}$	5-40 $\text{mm}\cdot\text{s}^{-1}$
	Pulse nb per area *	2-5 μm^{-2}	6.25-50 μm^{-2}
	Pulse nb at a fixed point **	1900-4800	6000-48000
LIPSS	Period	~ 490 nm (close to λ)	Coarse: ~ 510 nm (close to λ) Fine: ~ 250 nm (close to $\lambda/2$)
	Orientation	$\perp \vec{E}$	$\perp \vec{E}$
Ag NP self-organization	Period	~ 490 nm (close to λ)	~ 310 nm
	Orientation	$\perp \vec{E}$	$\parallel \vec{E}$
	Depth position in TiO_2 thin layer	Close to top surface	Close to bottom
Possible origins of NP self-organization		Correlated with LIPSS	Independent with LIPSS

Table V.1. Comparison of self-organization features in G1 and G2. λ and \vec{E} are respectively the wavelength and polarization of incident pulsed laser operated at 515 kHz with a pulse duration of 300 fs. The beam width at focus plane is measured at about $35\mu\text{m}$. * Total number of pulses per unit area calculated by f_{rep}/dv , where f_{rep} is the repetition rate of laser, d the distance between two successive laser scan lines ($2\mu\text{m}$), v the scan speed. ** Average number of pulses arriving at a given point in the irradiated region defined by $f_{\text{rep}}A_{\text{beam}}/dv$, where A_{beam} is the area of beam cross-section at focal plane.

One can conclude for sure that the mechanisms giving rise to the self-organization of the Ag NP in G1 and G2 are different. A short comparison of G1 and G2 is given in Table V.1

3. NP growth in anisotropic shape

Spatially homogeneous growth of Ag NPs exhibiting a dichroic optical behavior has also been observed with slower speeds and fluences lower than those of the above mentioned G1 and G2. Surface and volume characterizations have been performed to study the size and shape of the grown Ag NP. Laser processed TiO₂ state has also been investigated.

3.1 Anisotropic Ag NPs in surface structured TiO₂ Layer

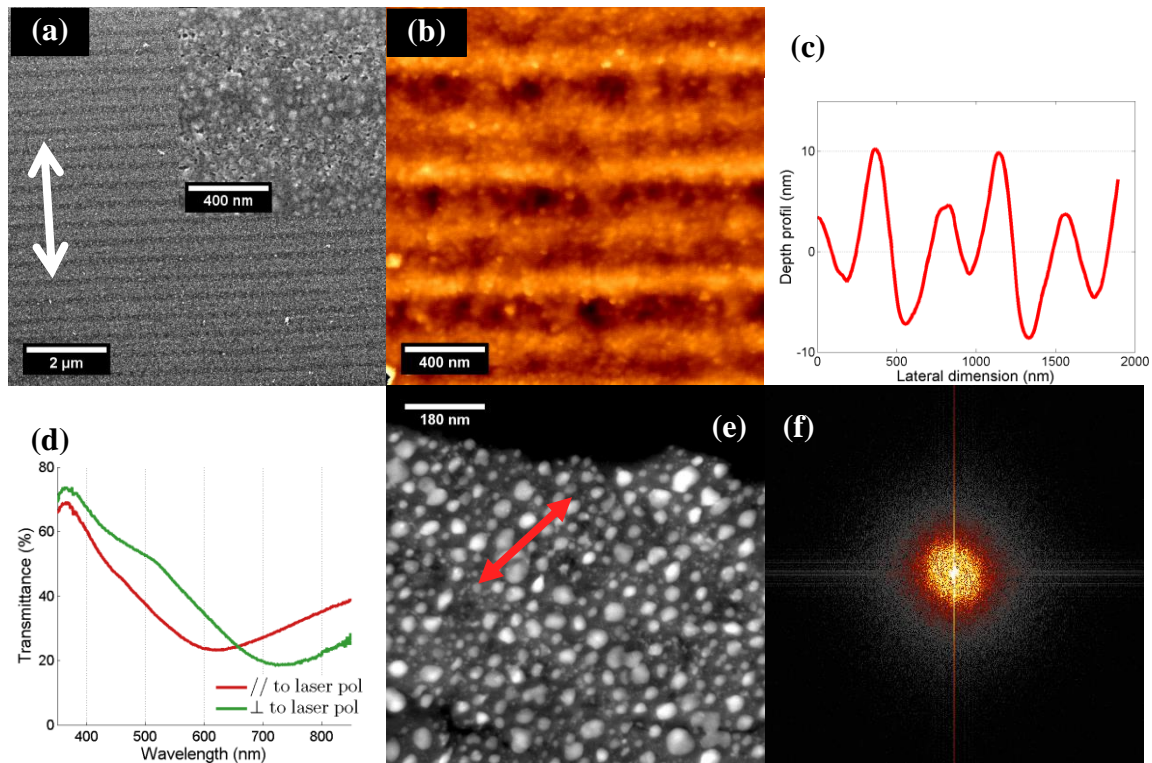


Figure V.8. a-b: SEM (a) and AFM (b) images of G3. The double-headed arrow indicates the polarization of incident laser and works for both images. c: The depth profile of LIPSS in G3 along laser polarization. d: Transmission spectrum of G3. e-f: Top view HAADF STEM image (e) of G3 and its FFT (f). The laser polarization is unknown due to the sample technique used for the preparation of TEM samples. The red arrow in e gives the averaged long axis of NPs estimated by the FFT in f.

Compared with G2, the femtosecond laser irradiated sample named G3 is obtained with lower fluence, ranging from $37 \text{ mJ}\cdot\text{cm}^{-2}$ to $46 \text{ mJ}\cdot\text{cm}^{-2}$, and similar speed, ranging from $5 \text{ mm}\cdot\text{s}^{-1}$ to $30 \text{ mm}\cdot\text{s}^{-1}$. Similar to G2, G3 also exhibits anisotropic optical responses as shown by changes in its transmission spectrum for cross polarizations (Figure V.8.d). Top view SEM images of G3 (Figure V.8.a) show a 1D periodic contrast oriented perpendicular to the laser polarization with a period of about 500 nm. The latter is confirmed to a surface modulation by AFM characterizations (Figure V.8.b), which also suggest a fine modulation of this periodic pattern with features finally repeating each 250 nm (close to $\lambda/2$). This fine structuring is much more regular than in the case of G2 (Figure V.6). Two ridges of about equal width but

slight different amplitudes are formed close to each other in one period of the coarse modulation. The global amplitude of LIPSS in G3 and G2 is about the same, and varies from 15 nm to 20 nm.

Unlike what was observed on G2, STEM micrographs (Figure V.8.e) of G3 show a homogeneous growth of Ag NPs in the irradiated sample with an average size estimated at around 50 nm. The grown Ag NPs locate closely to each other and their shapes are irregular but almost circular. However, FFT of STEM micrograph (Figure V.8.d) suggests an elliptical distribution of spatial frequencies, which implies the presence of ellipsoidal Ag NPs oriented along one direction. This direction can be deduced by the short axis of the elliptical distribution in frequency space, as shown by the red arrow of figure V.8.e. Actually, one does find several NPs or aggregates of near-coalescence NPs elongated in the direction given by this red arrow. As the measured specimen is prepared by manually scraping the film, it is impossible to know the relative orientation of the laser polarization with the long axis of Ag NPs in Figure V.8.e. According to previous works of NP reshaping by pulse laser [Kaempfe 1999, Baraldi 2013, Doster 2014, Stalmashonak 2008], a reasonable estimation of the laser polarization should be the direction in which NPs are elongated (red arrow in Figure V.8.e). In these works, dichroic behaviors of the NP composite are directly linked to the anisotropic shape of NPs. Such an explanation of dichroism is also valid in the case of G3, even if the contribution of LIPSS is no clear with present characterizations. A possible origin of the Ag NP growth in anisotropic shape will be discussed in part 3.3.

3.2 Anisotropic Ag NPs in mesoporous TiO_2 Layer

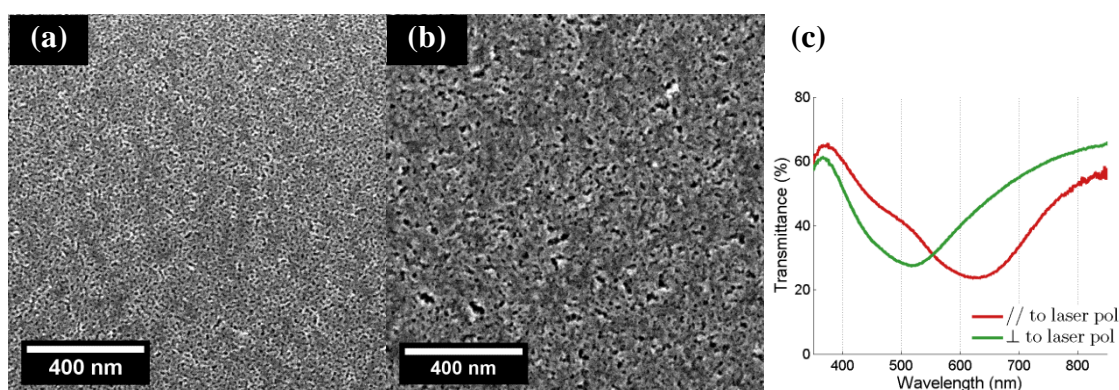


Figure V.9. a: SEM images of Ag:TiO₂ (initial state S1) before laser irradiation. b-c: SEM image and transmission spectrum of G4.

Another type of laser-induced structure, named as G4, is achieved using the same scan speed range but at lower fluence (ranging from 29 mJ·cm⁻² to 37 mJ·cm⁻²) than G3. A significant difference of G4 compared with the other laser-irradiated samples is that both Ag NPs and LIPSS on TiO₂ are not visible on the SEM images of the sample (Figure V.9.b).

However, the G4 sample still exhibits a plasmon absorption at visible wavelength, as well as a strong dichroism, as shown in figure V.9.c.

The TiO_2 thin layer of G4 is still completely mesoporous but the pore size and density has been slightly changed relative to the initial state (Figure V.9.a-b). Both SEM and AFM characterizations (Figure V.10.a) show the absence of any surface modulation on G4. The volume structure characterization of G4 has thus been performed with the help of HAADF-STEM measurements. The latter (Figure V.10.b) shows that small Ag NPs of size varying from 5 to 15 nm are formed within the TiO_2 matrix. As the specimens for HAADF-STEM measurement are prepared by manual cut in random direction (more detail in Chapter II), it is impossible to know the position and the orientation of the each specimen within the laser irradiated region. The visualization of these Ag NPs can be either under top view or cross-sectional view. For this reason, it is difficult to give the exact shape of these Ag NPs under view, even if most of the NPs shown by HAADF-STEM micrographs have an anisotropic shape. However, in any case, no organization of Ag NPs can be found in HAADF-STEM micrographs. The anisotropic growth of Ag NPs becomes the only possibility to interpret the dichroism of G4.

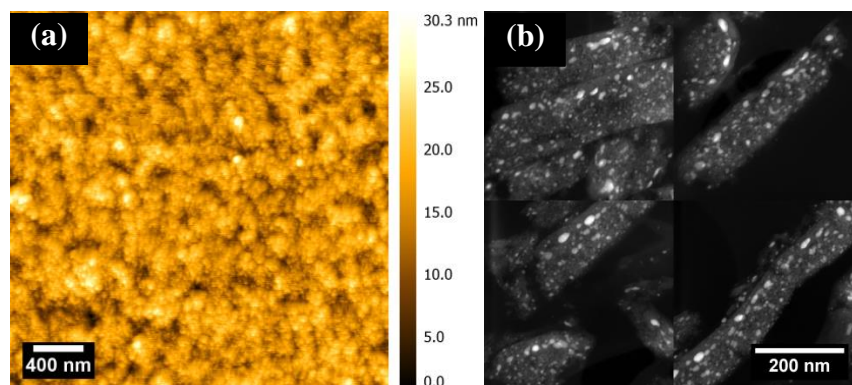


Figure V.10 a: AFM image of G4. b: HAADF-STEM images of small specimen of G4 prepared by a manual cut technique. The precise position and orientation of these specimens in the laser irradiated region is unknown.

3.3 Possible origin of NP anisotropic growth

Stalmashonak et al. [Stalmashonak 2008] explains the anisotropic reshaping of pre-deposited NP in soda-lime glass under fs laser illumination by three successive steps in the time scale. Firstly, once a laser pulse arrives on the composite, Surface Plasmon Resonance (SPR) enhances the electronic temperature and stimulates the hot electrons emission from Ag NPs preferentially at the two poles given by the laser polarization [Kelly 2003]. These hot electrons are then trapped by the host matrix close to the poles of the ionized particles. Secondly, after a few picoseconds, the electronic heat is transferred into the lattice of the Ag NP [Bigot 2000] via electron-phonon coupling. As a result, the lattice temperature of Ag NPs

increases, which enhances the diffusion of the Ag ions formed in the first step around the NPs in random directions. Thirdly, after few more picoseconds, the thermal flow leaves the NP and transfers into the matrix in its immediate vicinity. This enhances the recombination of Ag ions with the trapped electrons closed to the poles into Ag atoms. The latter can either diffuse back to the NP forming an anisotropic shape or precipitate at the poles of NP.

As discussed in chapter III and IV, the small Ag NPs present in the initial state of the studied Ag:TiO₂ composite can grow through silver ion reduction, Ostwald ripening and particle coalescence which are activated by temperature rise. In the case of G3 and G4, these growth processes are also expected in both the second and the third steps of Stalmashonaks' model. Under successive pulses, an accumulated temperature rise can be achieved which induces the reduction of Ag⁺ ions, furnished by both the initial Ag:TiO₂ composite and the photo-ionization process. At the poles of Ag NP, more Ag⁺ ions are expected to be reduced, as the generated hot-electrons increase the reduction of ions in the regions where they are located. Together with the Ostwald Ripening and particle coalescence process, Ag NPs are then grown in anisotropic shape or coalescence along laser polarization.

4. Optical properties of fs laser irradiated Ag:TiO₂ and their potential applications

4.1 Guided mode excitation

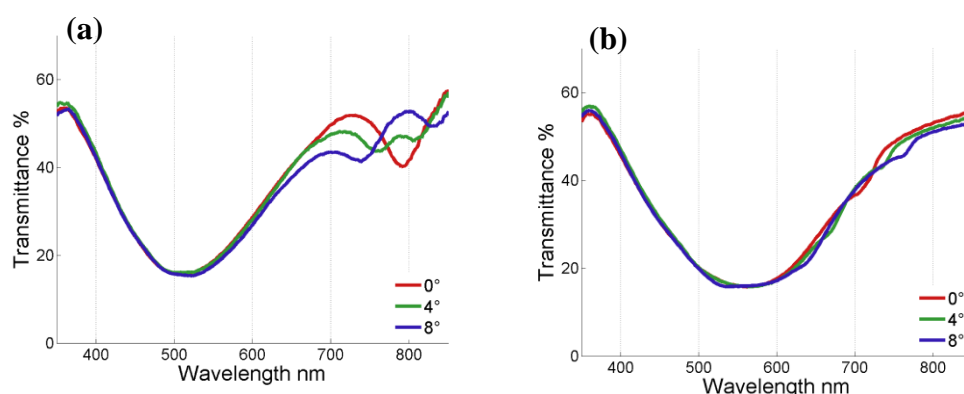


Figure V.11 Transmission spectrum of G1 under different incident angles with polarization of light probe is parallel (a, TE mode) and perpendicular (b, TM mode) to the LIPSS of G1. The sample is rotated around the axis defined by the orientation of LIPSS and 0° corresponds to normal incidence.

Transmission spectrum of G1 is plotted in Figure V.11. It exhibits the signature of both NPs plasmonic absorption and excitation of guided modes, when using a linearly

polarized light probe either parallel (TE mode, figure V.11.a) or perpendicular (TM mode, figure V.11.b) to LIPSS. In the case of TE mode, two transmission dips can be observed in the transmission spectrum recorded under normal incidence (Figure V.11.a). Under oblique incidences (when rotating the sample around an axis parallel to the LIPSS), the first broad dip, covering from 400nm to 600nm, is invariant but the second narrow dip, which locates around 790 nm under normal incidence, begins to split into two transmission dips. This split, considered as the signature of a guided mode excitation around 790nm, can be explained as wavelength shift of the forward and backward guided modes under oblique incidence.

$$n_{eff} = \pm n' \sin(\theta) + \frac{\lambda^{\pm}}{\Lambda_{gra}} \quad (V.1)$$

Guided modes propagate in the film and are excited by the LIPSS grating coupler. The coupling equation is given in Eq.V.1, where n_{eff} , is the effective propagation index of the guided mode, λ^{\pm} is wavelength of the forward (sign “-”) and backward (sign “+”) guided modes. θ is the incidence angle. Λ_{gra} is the NP grating period and n' is the refraction index of the environment where light is coming from, which is air in the case of G1, *i.e.* $n'=1$. Forward and backward propagating guided modes can be excited. n_{eff} depends on the geometric features of the planar waveguide, including refractive indices and thicknesses of different thin layers. It is difficult to calculate an accurate value for n_{eff} in a composite material like G1. However, the value of n_{eff} can be found when looking at the case of normal incidence where the term $n' \sin(\theta)$ cancels. Eq.V.1 can be then rewritten as $n_{eff} = \frac{\lambda}{\Lambda_{gra}}$, where forward and backward guided wavelengths are the same and equals to 790nm. Since Λ_{gra} is known to be equal to 500 nm approximately as given from AFM and SEM characterizations, it is possible to deduce n_{eff} (at this wavelength). Numerical application gives an effective propagation index of the guided mode around $n_{eff} = 1.58$. Then, the forward and backward guided wavelength can be estimated by:

$$\lambda^{\pm} = (1.58 \mp \sin(\theta)) * \Lambda_{gra} \quad (V.2)$$

Numerical application of Eq.V.2 gives the wavelengths at which the forward and backward propagating guided modes are excited under oblique incidence.

	Forward mode	Backward mode
4°	755nm	824nm
8°	720nm	860nm

Table V.2 Forward and backward guided wavelengths of G1 under oblique incidences calculated by Eq.V.2 with an effective refractive index estimated from the guided wavelength under normal incidence.

We notice from Table.V.2 that numerical results are close to the transmission dips observed in the measured spectrum (Figure V.11.a). The latter can come from the fact that the effective propagation index is a function of wavelength whose value can be different when guided wavelengths are shifted in tilted configurations. Another origin can be the act that the resonance position is shifted from the location of the minimum of transmission. This shift of the resonance position can originate from the presence of losses in the system and from the hybridization of the plasmon and guided resonance modes [Alam 2014]. Hybridization is clearer at TM mode where the spectral position of the guided mode also completely falls into the broad plasmon absorption band. Hybridization can also be noticed when comparing spectra measured at TE and TM modes where both the dips corresponding to plasmon absorption and guided mode are shifted. The same case has also been observed in our previous work [Destouches, Crespo-Monteiro et al. 2014]. Considering these conditions, the theoretically predicted forward and backward guided wavelengths are still in good agreements with the measured spectrum.

4.2 Diffractive and dichroic color upon transparent support

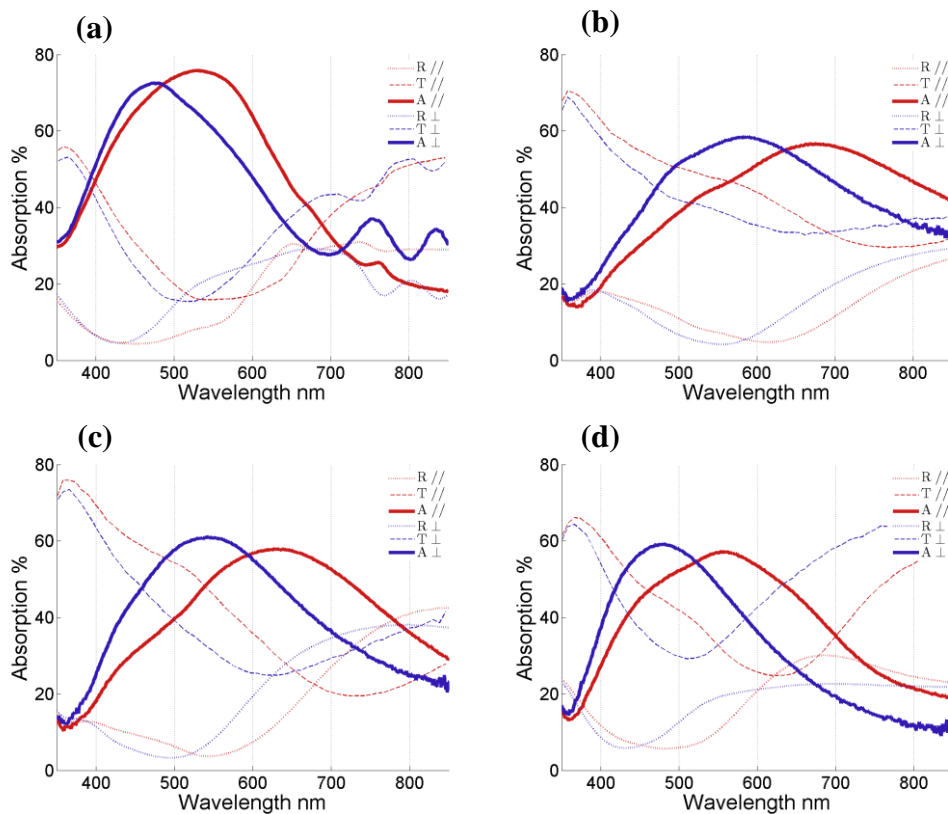


Figure V.12. Optical spectra of fs laser irradiated zones (G1 - G4) under oblique incidence at 8° . a: G1, $42 \text{ mJ}\cdot\text{cm}^{-2}$, $100 \text{ mm}\cdot\text{s}^{-1}$. b: G2, $50 \text{ mJ}\cdot\text{cm}^{-2}$, $10 \text{ mm}\cdot\text{s}^{-1}$. c: G3, $42 \text{ mJ}\cdot\text{cm}^{-2}$, $10 \text{ mm}\cdot\text{s}^{-1}$. d: G4, $33 \text{ mJ}\cdot\text{cm}^{-2}$, $10 \text{ mm}\cdot\text{s}^{-1}$. The absorption spectrum is deduced from the corresponding reflectance and transmittance by neglecting the scattering light.

The laser irradiated Ag:TiO₂ samples exhibit different colors in reflection and transmission, due to an important absorption of visible light by the grown Ag NPs. These colors both in reflection and transmission are also dichroic, principally because of the LIPSS, the self-organization or the anisotropic shape of Ag NPs in one orientation. Figure.V.12 shows the optical spectra of zones of G1 to G4 and the experimental parameters used to produce each zone are reminded in the figure caption. Considering the small size of Ag NPs, scattering light can be neglected. Absorption spectra (A) can be deduced by $A = 1 - R - T$, where R and T are respectively the reflectance and transmittance under oblique incident at 8°. In the four studied cases, the positions of the main absorption maxima of each polarization are principally defined by the size distribution and the shape of Ag NPs. However, the exact form of the absorption peak should also be modified by the organizations of the Ag NPs in the case of G1 and G2 [Destouches, Martinez et al. 2014, Fort 2003]. Particularly, the LIPSS play also important role on the dichroic behavior of G1 through the excitation of the guided mode which hybrids with the plasmon absorption of Ag NPs. As explained in the section above, such hybridization of modes gives rise to polarization-depended optical responses.

Experimentally, the structure parameters of the composite sample that get rise to the dichroic color can be tuned by varying the laser irradiation conditions. Within the entire value range of laser fluence and scan speed for G1-G4, one can thus obtain a dichroic color palette covering a large color gamut upon the fs laser irradiated Ag:TiO₂, as shown in Figure V.13.a. By combining these dichroic colors, one can fabricate the color patterns whose form varies with polarization. Figure V.13.b shows a simple example: the same 9 color squares gives a vertical orange line in one polarization but a red cross with the horizontal polarization. This technique leads to innovative solutions in fields like active color displays, security, polarization imaging.

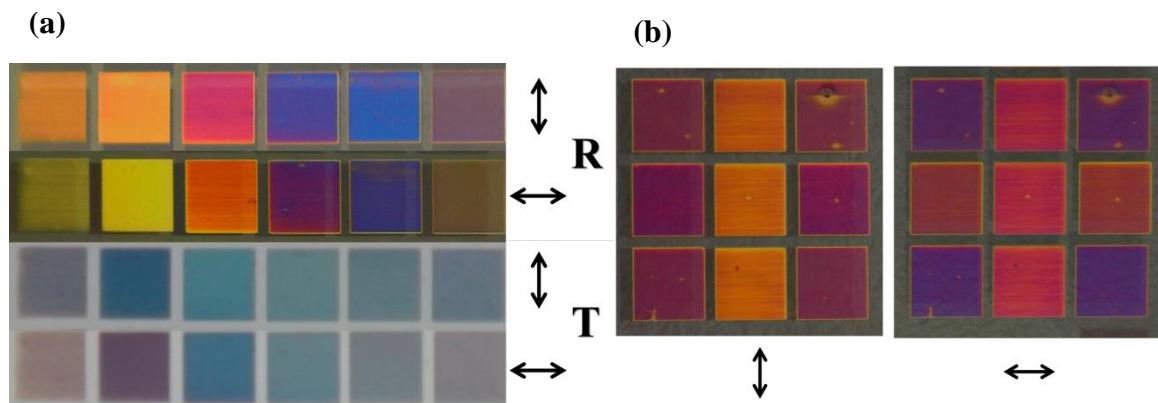


Figure V.13. a: fs laser induced dichroic color palette in specular reflection and transmission. In specular reflection (R) and transmission (T), different colors can be observed at polarization parallel (\parallel) and perpendicular (\perp) to the polarization of the fs laser that induces the color. b: A simple example of color pattern whose form varies with polarization. The light polarization used for observation is shown by the double-headed arrow below each figure

Besides, the LIPSS and Ag NP grating of G1 also form a diffraction grating which gives strong diffractive colors upon the transparent TiO_2 surface. An example of this diffraction grating written at a fluence of $42 \text{ mJ}\cdot\text{cm}^{-2}$ and a scan speed of $100 \text{ mm}\cdot\text{s}^{-1}$, is shown in Figure V.14. The diffraction efficiency of the structure is characterized by the fraction of light power diffracted to the +1 order in reflection compared to the incident power. This value is quantified at 8% for a probe light at 405nm wavelength. However, as the initial Ag: TiO_2 sample is transparent, this diffraction efficiency is still very high, which is also confirmed by the significant diffractive color pattern in figure V.14.a. The laser processing speed for this structure can reach up to $0.25 \text{ mm}^2\cdot\text{s}^{-1}$. This technique gives potential solution for diffraction grating at a high speed over a large area.

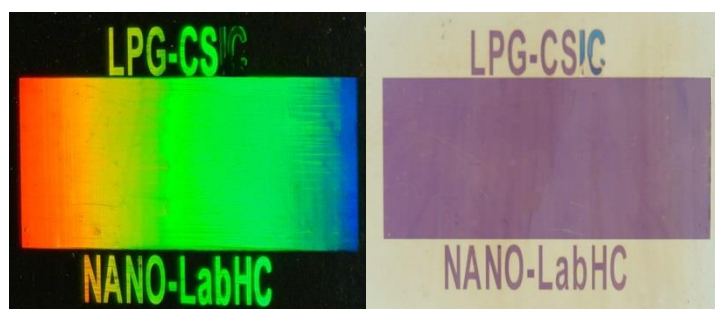


Figure V.14: Color photograph in diffraction (a) and transmission (b) of a LIPSS and Ag NP self-organization based diffraction grating written in a transparent Ag: TiO_2 thin layer. The size of the rectangular is $1\text{cm}\times 2\text{cm}$.

5. Thermal effect of fs and CW laser processes

In the previous chapter, laser induced growth and self-organization of Ag NP have been found to strongly depend on the temperature rise that occur during laser exposure. In the case of CW laser, Ag NP structures formed with a temperature rise that can reach more than $700\text{-}900^\circ\text{C}$ as evidenced by the rutile phase formed after laser exposure. The mesostructure of TiO_2 also completely collapses during CW laser exposure. However, the fs laser irradiated zones are still partially (G1-3) or completely (G4) mesoporous, which suggests a lower temperature rise during the formation of Ag NP structures.

Scanning TEM (STEM) micrographs and electron energy loss spectroscopy (EELS) analysis of sample cross-sections prepared by focused ion beam (FIB) also give interesting additional information about the in depth structure of the self-organized structure produced by CW laser (488 nm , 120 mW) and fs laser (G2: 515 nm , $50 \text{ mJ}\cdot\text{cm}^{-2}$). In the case of CW laser (Figure V.15.a-b), Ag NPs are large and spherical and they are located below a film composed by TiO_2 nanocrystals (Figure V.15.b). The latter is actually immersed in a Si-based amorphous phase. A new amorphous layer, about $100\text{-}150 \text{ nm}$ thick, including both Ti from the initial

film and Si from the glass substrate appears below the crystalized TiO_2 films (Figure V.15.b). A Ti:Si ratio of 3:2 is estimated from EELS data. This layer is on the top part of the glass substrate. All this analysis suggests that an important temperature rise is achieved during laser exposure which melts a thin layer of glass and enhances the diffusion of TiO_2 and glass between each other. The high temperature rise in the case of CW laser exposure is considered as a drawback since it affects the integrity of the supporting material and prohibits the ability to producing self-organized structures on soft and flexible substrates that have low thermal resistance, like plastic and paper ones.

However, in the case of fs laser (Figure V.15.c-d), self-organization of Ag NP can be obtained without altering the top surface of glass substrate. Oblate Ag NPs are located in the TiO_2 films where its boundary with the glass substrate can be clearly observed both in the HAADF STEM image (Figure V.15.c) and the corresponding EELS measurement (Figure V.15. d). Absence of the intermediate layer mixing Ti and Si indicate that the thermal effect is much lower than with the use of a CW laser. G2 structure (Figure V.15.c-d) is produced using the highest fluence and highest number of accumulated laser pulses (see Table V.1). The thermal effect is expected to be lower in other fs laser processed structures presented in this work. In the case of G1, TiO_2 is only crystalized around the Ag NPs as shown by the 4D-STEM characterization in figure V.4, which proves also that the thermal effect is confined around Ag NPs. Such difference in thermal effects induced at pulsed and CW regimes has been theoretically interpreted by Baffou et Rigneault [Baffou 2011]. They demonstrated that relying on the brief duration of pulse energy, pulsed laser induced temperature rise on a metallic NP is both sharper in spatial distribution and shorter in temporal evolution compared with CW illumination. The latter enters a steady state of the temperature rise which presents in permanent and extends heating to alter the whole medium.

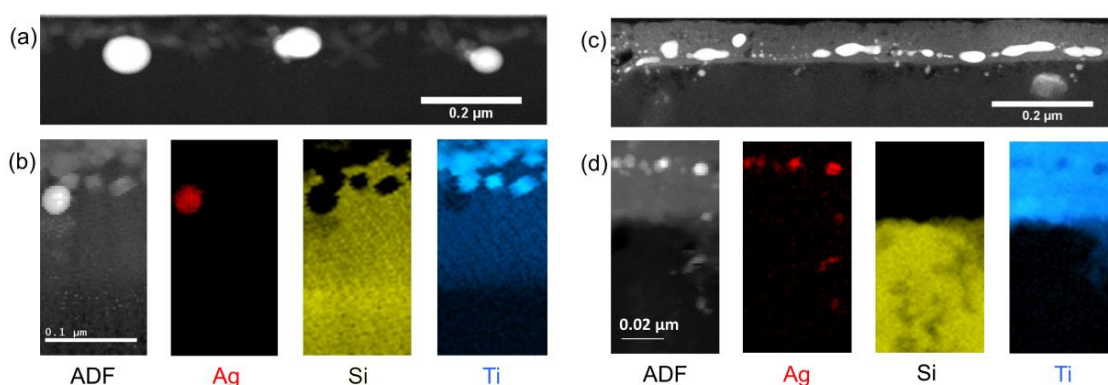


Figure V.15: HAADF-STEM micrographs (FEI-TITAN ETEM, 300 kV) (a, c) and STEM-EELS maps (b, d) of sample cross-sections processed with a CW laser (a-b) or fs laser pulses (c-d).

6. Conclusion

This chapter reports the self-organization and the anisotropic growth of Ag NPs induced by a fs laser scanning the Ag:TiO₂ composite thin layer. At relatively higher fluence and scan speed, Ag NPs can grow and organize in 1D periodic structure at sub-wavelength period within the TiO₂ matrix. Both HSF LIPSS and LSF LIPSS can be simultaneously formed upon the composite layer surface through the periodic collapse of the mesostructure. But the origin of Ag NP self-organization can be either correlated or independent to the LIPSS. Ag NP self-organizations that are perpendicular or parallel to the LIPSS are both observed. At lower fluence and scan speed, only the anisotropic growth of Ag NP over the entire irradiated sample is found. Laser fluence is found as a crucial parameter which defines the size of the grown Ag NPs and the morphological state of the TiO₂. At the lowest fluence used in this study (around 30 mJ·cm⁻²), Ag NPs are grown into an anisotropic shape with smaller sizes around 15 nm in a completely porous TiO₂ matrix without any surface modulation. Using higher fluence, large NPs around 50 nm can be generated within a periodic collapsed TiO₂. The latter corresponds to a LIPSS on TiO₂ surface. The presence of LIPSS has clearly no influence on the growth of Ag NPs. In both cases, Ag NPs are homogeneously and randomly distributed within the film, whether LIPSS is observed or not.

The fs laser induced Ag NP structures exhibit various interesting optical effects, including excitation of a guided mode within the host TiO₂ matrix, strong diffractive color and shining dichroic color in both reflection and transmission upon a transparent supporting material. Compared with techniques in literature that tailoring optical responses of NP composite by pulsed laser, the reported approach does not need pre-deposition of NP or thin metallic film and is able to extend these optical properties over large area, using a single laser beam pass. These lead to innovative solutions in fields like active color displays, security, polarization imaging. Furthermore, we have experimentally shown that unlike the case of CW laser processing, fs laser process is able to produce Ag NP structures with a much less important thermal effect without altering the substrate material. It gives a potential solution to transfer these optical properties upon a soft and flexible supports which have low thermal resistance.

References

- Alam, M. Z.; Aitchison, J. S.; Mojahedi, M. A Marriage of Convenience: Hybridization of Surface Plasmon and Dielectric Waveguide Modes. *Laser & Photonics Reviews* **2014**, 8 (3), 394–408.
- Baffou, G.; Rigneault, H. Femtosecond-Pulsed Optical Heating of Gold Nanoparticles. *Phys. Rev. B* **2011**, 84 (3), 35415.

- Baraldi, G.; Gonzalo, J.; Solis, J.; Siegel, J. Reorganizing and Shaping of Embedded near-Coalescence Silver Nanoparticles with off-Resonance Femtosecond Laser Pulses. *Nanotechnology* **2013**, *24* (25), 255301.
- Bigot, J.-Y.; Halté, V.; Merle, J.-C.; Daunois, A. Electron Dynamics in Metallic Nanoparticles. *Chemical Physics* **2000**, *251* (1–3), 181–203.
- Birnbaum, M. Semiconductor Surface Damage Produced by Ruby Lasers. *Journal of Applied Physics* **1965**, *36* (11), 3688–3689.
- Bonse, J.; Baudach, S.; Krüger, J.; Kautek, W.; Lenzner, M. Femtosecond Laser Ablation of Silicon–modification Thresholds and Morphology. *Appl Phys A* **2002**, *74* (1), 19–25.
- Bonse, J.; Krüger, J.; Höhm, S.; Rosenfeld, A. Femtosecond Laser-Induced Periodic Surface Structures. *Journal of Laser Applications* **2012**, *24* (4), 42006.
- Borowiec, A.; Haugen, H. K. Subwavelength Ripple Formation on the Surfaces of Compound Semiconductors Irradiated with Femtosecond Laser Pulses. *Applied Physics Letters* **2003**, *82* (25), 4462–4464.
- Bris, A. L.; Maloum, F.; Teisseire, J.; Sorin, F. Self-Organized Ordered Silver Nanoparticle Arrays Obtained by Solid State Dewetting. *Applied Physics Letters* **2014**, *105* (20), 203102.
- Chon, J. W. M.; Bullen, C.; Zijlstra, P.; Gu, M. Spectral Encoding on Gold Nanorods Doped in a Silica Sol–Gel Matrix and Its Application to High-Density Optical Data Storage. *Adv. Funct. Mater.* **2007**, *17* (6), 875–880.
- Costache, F.; Henyk, M.; Reif, J. Surface Patterning on Insulators upon Femtosecond Laser Ablation. *Applied Surface Science* **2003**, *208–209*, 486–491.
- Das, S. K.; Dufft, D.; Rosenfeld, A.; Bonse, J.; Bock, M.; Grunwald, R. Femtosecond-Laser-Induced Quasiperiodic Nanostructures on TiO₂ Surfaces. *Journal of Applied Physics* **2009**, *105* (8), 84912.
- Destouches, N.; Crespo-Monteiro, N.; Vitrant, G.; Lefkir, Y.; Reynaud, S.; Epicier, T.; Liu, Y.; Vocanson, F.; Pigeon, F. Self-Organized Growth of Metallic Nanoparticles in a Thin Film under Homogeneous and Continuous-Wave Light Excitation. *J. Mater. Chem. C* **2014**, *2* (31), 6256–6263.
- Destouches, N.; Martínez-García, J.; Hébert, M.; Crespo-Monteiro, N.; Vitrant, G.; Liu, Z.; Trémeau, A.; Vocanson, F.; Pigeon, F.; Reynaud, S.; et al. Dichroic Colored Luster of Laser-Induced Silver Nanoparticle Gratings Buried in Dense Inorganic Films. *J. Opt. Soc. Am. B* **2014**, *31* (11), C1–C7.
- Diels, J.-C.; Rudolph, W.; Miller, R., Steven A. Ultrashort Laser Pulse Phenomena. *Opt. Eng* **1997**, *36* (8), 2362–2362.
- Dong, Y.; Molian, P. Coulomb Explosion-Induced Formation of Highly Oriented Nanoparticles on Thin Films of 3C–SiC by the Femtosecond Pulsed Laser. *Applied Physics Letters* **2004**, *84* (1), 10–12.
- Doster, J.; Baraldi, G.; Gonzalo, J.; Solis, J.; Hernandez-Rueda, J.; Siegel, J. Tailoring the Surface Plasmon Resonance of Embedded Silver Nanoparticles by Combining Nano- and Femtosecond Laser Pulses. *Applied Physics Letters* **2014**, *104* (15), 153106.
- Dufft, D.; Rosenfeld, A.; Das, S. K.; Grunwald, R.; Bonse, J. Femtosecond Laser-Induced Periodic Surface Structures Revisited: A Comparative Study on ZnO. *Journal of Applied Physics* **2009**, *105* (3), 34908.
- Eurenius, L.; Hägglund, C.; Olsson, E.; Kasemo, B.; Chakarov, D. Grating Formation by Metal-Nanoparticle-Mediated Coupling of Light into Waveguided Modes. *Nat Photon* **2008**, *2* (6), 360–364.
- Fort, E.; Ricolleau, C.; Sau-Pueyo, J. Dichroic Thin Films of Silver Nanoparticle Chain Arrays on Facetted Alumina Templates. *Nano Lett.* **2003**, *3* (1), 65–67.
- Harzic, R. L.; Dörr, D.; Sauer, D.; Stracke, F.; Zimmermann, H. Generation of High Spatial Frequency Ripples on Silicon under Ultrashort Laser Pulses Irradiation. *Applied Physics Letters* **2011**, *98* (21), 211905.

- Hou, S.; Huo, Y.; Xiong, P.; Zhang, Y.; Zhang, S.; Jia, T.; Sun, Z.; Jianrong Qiu; Xu, Z. Formation of Long- and Short-Periodic Nanoripples on Stainless Steel Irradiated by Femtosecond Laser Pulses. *J. Phys. D: Appl. Phys.* **2011**, *44* (50), 505401.
- Inasawa, S.; Sugiyama, M.; Yamaguchi, Y. Laser-Induced Shape Transformation of Gold Nanoparticles below the Melting Point: The Effect of Surface Melting. *J. Phys. Chem. B* **2005**, *109* (8), 3104–3111.
- Kaempfe, M.; Graener, H.; Kiesow, A.; Heilmann, A. Formation of Metal Particle Nanowires Induced by Ultrashort Laser Pulses. *Applied Physics Letters* **2001**, *79* (12), 1876–1878.
- Kaempfe, M.; Rainer, T.; Berg, K.-J.; Seifert, G.; Graener, H. Ultrashort Laser Pulse Induced Deformation of Silver Nanoparticles in Glass. *Applied Physics Letters* **1999**, *74* (9), 1200–1202.
- Kaneko, K.; Sun, H.-B.; Duan, X.-M.; Kawata, S. Two-Photon Photoreduction of Metallic Nanoparticle Gratings in a Polymer Matrix. *Applied Physics Letters* **2003**, *83* (7), 1426–1428.
- Kelly, K. L.; Coronado, E.; Zhao, L. L.; Schatz, G. C. The Optical Properties of Metal Nanoparticles: The Influence of Size, Shape, and Dielectric Environment. *J. Phys. Chem. B* **2003**, *107* (3), 668–677.
- Kiesow, A.; Strohark, S.; Löschner, K.; Heilmann, A.; Podlipensky, A.; Abdolvand, A.; Seifert, G. Generation of Wavelength-Dependent, Periodic Line Pattern in Metal Nanoparticle-Containing Polymer Films by Femtosecond Laser Irradiation. *Applied Physics Letters* **2005**, *86* (15), 153111.
- Lamprecht, B.; Schider, G.; Lechner, R. T.; Ditlbacher, H.; Krenn, J. R.; Leitner, A.; Aussenegg, F. R. Metal Nanoparticle Gratings: Influence of Dipolar Particle Interaction on the Plasmon Resonance. *Phys. Rev. Lett.* **2000**, *84* (20), 4721–4724.
- Liu, Z.; Destouches, N.; Vitrant, G.; Lefkir, Y.; Epicier, T.; Vocanson, F.; Bakhti, S.; Fang, Y.; Bandyopadhyay, B.; Ahmed, M. Understanding the Growth Mechanisms of Ag Nanoparticles Controlled by Plasmon-Induced Charge Transfers in Ag-TiO₂ Films. *J. Phys. Chem. C* **2015**, *119* (17), 9496–9505.
- Loeschner, K.; Seifert, G.; Heilmann, A. Self-Organized, Gratinglike Nanostructures in Polymer Films with Embedded Metal Nanoparticles Induced by Femtosecond Laser Irradiation. *Journal of Applied Physics* **2010**, *108* (7), 73114.
- Martsinovskii, G. A.; Shandybina, G. D.; Smirnov, D. S.; Zaboltnov, S. V.; Golovan', L. A.; Timoshenko, V. Y.; Kashkarov, P. K. Ultrashort Excitations of Surface Polaritons and Waveguide Modes in Semiconductors. *Opt. Spectrosc.* **2008**, *105* (1), 67–72.
- Miyaji, G.; Miyazaki, K. Origin of Periodicity in Nanostructuring on Thin Film Surfaces Ablated with Femtosecond Laser Pulses. *Optics Express* **2008**, *16* (20), 16265.
- Nakajima, Y.; Nedyalkov, N.; Takami, A.; Terakawa, M. Formation of Periodic Metal Nanowire Grating on Silica Substrate by Femtosecond Laser Irradiation. *Appl. Phys. A* **2015**, *119* (4), 1215–1221.
- Nicolas Filippin, A.; Borrás, A.; Rico, V. J.; Frutos, F.; González-Elipé, A. R. Laser Induced Enhancement of Dichroism in Supported Silver Nanoparticles Deposited by Evaporation at Glancing Angles. *Nanotechnology* **2013**, *24* (4), 45301.
- Nouneh, K.; Oyama, M.; Lakshminarayana, G.; Kityk, I. V.; Wojciechowski, A.; Ozga, K. Kinetics of Picosecond Laser Treatment of Silver Nanoparticles on ITO Substrate. *Journal of Alloys and Compounds* **2011**, *509* (40), 9663.
- Oh, Y.-J.; Kim, J.-H.; Thompson, C. V.; Ross, C. A. Templated Assembly of Co–Pt Nanoparticles via Thermal and Laser-Induced Dewetting of Bilayer Metal Films. *Nanoscale* **2013**, *5* (1), 401–407.
- Ophus, C.; Ercius, P.; Sarahan, M.; Czarnik, C.; Ciston, J. Recording and Using 4D-STEM Datasets in Materials Science. *Microscopy and Microanalysis* **2014**, *20* (Supplement S3), 62–63.

- Qu, S.; Qiu, J.; Zhao, C.; Jiang, X.; Zeng, H.; Zhu, C.; Hirao, K. Metal Nanoparticle Precipitation in Periodic Arrays in Au₂O-Doped Glass by Two Interfered Femtosecond Laser Pulses. *Applied Physics Letters* **2004**, *84* (12), 2046–2048.
- Rechberger, W.; Hohenau, A.; Leitner, A.; Krenn, J. R.; Lamprecht, B.; Aussenegg, F. R. Optical Properties of Two Interacting Gold Nanoparticles. *Optics Communications* **2003**, *220* (1–3), 137–141.
- Resta, V.; Siegel, J.; Bonse, J.; Gonzalo, J.; Afonso, C. N.; Piscopiello, E.; Tenedeloo, G. V. Sharpening the Shape Distribution of Gold Nanoparticles by Laser Irradiation. *Journal of Applied Physics* **2006**, *100* (8), 84311.
- Ruiz de la Cruz, A.; Lahoz, R.; Siegel, J.; de la Fuente, G. F.; Solis, J. High Speed Inscription of Uniform, Large-Area Laser-Induced Periodic Surface Structures in Cr Films Using a High Repetition Rate Fs Laser. *Opt. Lett.* **2014**, *39* (8), 2491–2494.
- Sipe, J. E.; Young, J. F.; Preston, J. S.; van Driel, H. M. Laser-Induced Periodic Surface Structure. I. Theory. *Phys. Rev. B* **1983**, *27* (2), 1141–1154.
- Smirnova, T. N.; Kokhtych, L. M.; Kutsenko, A. S.; Sakhno, O. V.; Stumpe, J. The Fabrication of Periodic Polymer/silver Nanoparticle Structures: In Situ Reduction of Silver Nanoparticles from Precursor Spatially Distributed in Polymer Using Holographic Exposure. *Nanotechnology* **2009**, *20* (40), 405301.
- Stalmashonak, A.; Podlipensky, A.; Seifert, G.; Graener, H. Intensity-Driven, Laser Induced Transformation of Ag Nanospheres to Anisotropic Shapes. *Appl. Phys. B* **2008**, *94* (3), 459–465.
- Stalmashonak, A.; Seifert, G.; Graener, H. Spectral Range Extension of Laser-Induced Dichroism in Composite Glass with Silver Nanoparticles. *J. Opt. A: Pure Appl. Opt.* **2009**, *11* (6), 65001.
- van Driel, H. M.; Sipe, J. E.; Young, J. F. Laser-Induced Periodic Surface Structure on Solids: A Universal Phenomenon. *Phys. Rev. Lett.* **1982**, *49* (26), 1955–1958.
- von der Linde, D.; Sokolowski-Tinten, K.; Bialkowski, J. Laser–solid Interaction in the Femtosecond Time Regime. *Applied Surface Science* **1997**, *109–110*, 1–10.
- Yadavali, S.; Sachan, R.; Dyck, O.; Kalyanaraman, R. DC Electric Field Induced Phase Array Self-Assembly of Au Nanoparticles. *Nanotechnology* **2014**, *25* (46), 465301.
- Yao, J.-W.; Zhang, C.-Y.; Liu, H.-Y.; Dai, Q.-F.; Wu, L.-J.; Lan, S.; Gopal, A. V.; Trofimov, V. A.; Lysak, T. M. High Spatial Frequency Periodic Structures Induced on Metal Surface by Femtosecond Laser Pulses. *Optics Express* **2012**, *20* (2), 905.
- Zijlstra, P.; Chon, J. W. M.; Gu, M. Five-Dimensional Optical Recording Mediated by Surface Plasmons in Gold Nanorods. *Nature* **2009**, *459* (7245), 410–413.

General conclusion

In this work, we have characterized and modeled the main physicochemical mechanisms that lead to the growth and shrinkage of Ag NPs in TiO_2 matrices loaded with Ag^+ , Ag^0 and Ag NPs, when exposed to visible CW laser under conditions that lead to self-organization phenomena (even though we did not take the latter into account). Moreover, we demonstrated how high repetition rate femtosecond laser emitting in the visible range can be used to create various Ag NP structures either self-organized or anisotropically reshaped in a given direction, on the same composite system.

The threshold behavior of the Ag NP growth under CW laser scan has been studied experimentally and interpreted by multiphysics modeling. For sufficiently high incident laser intensity, the LSPR of Ag NPs generates two opposite effects, photo-oxidation that leads to the NP shrinkage, and plasmon-absorption induced thermal effect that leads to NPs growth which counterbalances shrinkage. Oxidation is proportional to the number of photons absorbed by silver NPs due to their LSPR. On the contrary, the growth of silver NPs and silver ion reductions, are all promoted by the plasmon-induced temperature rise and varies in an exponential way with the laser intensity. The relative importance of both processes can be tuned by the laser exposure conditions: thermal growth processes can only overweight the photo-oxidation with a combination of sufficiently high light intensity and large size of Ag NPs. Under Gaussian laser scans, this competition explains why NPs growth only occurs above a speed threshold and NP shrinkage is observed at lower speed. At the beginning of a Gaussian laser scan, oxidation always predominates over growth processes and NPs shrink firstly. At low speed below the speed threshold, the long duration of oxidation can significantly decrease the size of Ag NPs and prohibits the plasmon absorption and thermal growth. The final NP size is smaller than the initial one after the beam passage and TiO_2 matrix remains mesoporous and amorphous. Thermal growth can only be activated above the speed threshold. The final Ag NPs size becomes much larger than the initial one and induces a bright shining color on the TiO_2 surface.

This work gives also a detailed understanding of the variations of grown Ag NPs size and thermal effects at speeds above the threshold. The thermal growth of Ag NPs is produced either through the NP coalescence or the adsorption of silver atoms (Ostwald ripening and silver ion reduction). The former only results in the growth of the average NP size, while the latter leads to a global growth of both the average size and the total Ag atom quantity in the NPs. Above the speed threshold, the two processes successively predominate

over photo-oxidation at different speeds. This gives rise to two speed ranges above the threshold. Firstly, within a narrow speed range just above the threshold, only NP coalescence can predominate over oxidation. The final size of Ag NPs is increased to about 20 nm with an irregular shape. The thermal effect at these speeds is still moderate, and just partially collapses and crystallizes TiO_2 matrix. Secondly, at speed higher than the first speed range, the two growth processes predominate over the oxidation, the growth of both NP average size and total atom quantity in NP distributions results in much larger (about 100 nm) spherical NPs after the laser scan. A strong temperature rise can also be stimulated, which crystallizes and completely collapses the TiO_2 film. In this second speed range, the growth of NPs occurs within duration of microsecond order, in which the maximum temperature rise of the film is also reached. With an increase of scan speed, the spatial distance between the beam center and the location where the Ag NP growth becomes very fast decreases and leads to stronger thermal effects at higher speeds (maximum film absorption reached at higher laser intensity). This thermal effect can then reach more than 800°C and is able to induce a crystallization of TiO_2 into the rutile phase. It can also significantly alter the top surface of glass substrate.

Multi-physics models have been developed in this thesis to describe and study the temporal size variation of the Ag NP distribution under laser irradiations. The models take into account the collective contribution of various physicochemical processes that are Ostwald ripening, NP coalescence, NP photo-oxidation and silver ion reduction through an Ordinary Differential Equations (ODEs) set. Physical processes such as the absorption of silver NP through LSPR, thermal effects, silver ion and atom diffusion were also included in the model. The NP distribution can be treated either under monodisperse approximation, or with a polydisperse NP distribution to follow more accurately the behavior of the composite system, but leading to a more complicated numerical scheme. Solutions of the ODEs set were carried out considering a CW laser emitting in the visible range and scanning the sample surface. Simulations are found in good agreement with experimental observations and reveal the significant influence of each involved processes. The variations of the theoretically predicted speed threshold as a function of experimental conditions, such as beam width, beam power and initial NP size are also in line with experimental results. Considering the size distribution of nanoparticles gives access to realistic results that make the description of the system evolution quite reliable. Such a model can be applied to better predict the size evolution of metallic NPs in TiO_2 based systems used for photocatalysis and estimate changes in their efficiency. It is also a starting point to simulate self-organization mechanisms of metallic NPs upon laser exposure.

Finally, the thesis reports the self-organization and the anisotropic growth of Ag NPs on the same $\text{Ag}:\text{TiO}_2$ composite films induced by femtosecond (fs) laser irradiations. At relatively higher fluence and scan speed, Ag NPs grow and organize in 1D periodic structures

with sub-wavelength periods within the TiO_2 matrix. Both High Spatial Frequency (HSF) and Low Spatial Frequency (LSF) Laser Induced Periodic Surface Structures (LIPSS) can be simultaneously formed upon the composite layer surface through the periodic collapse of the mesostructure. However, the origin of the Ag NP self-organization can be either correlated or independent with the LIPSS. Ag NPs self-organizations perpendicular or parallel to the LIPSS were both observed. At lower fluence and scan speed, only the anisotropic growth of Ag NP over the entire irradiated sample was observed. Laser fluence has been found to be a crucial parameter which defines the size and shape of the Ag NPs in this regime, and also influences the final state of the host matrix. The fs laser induced Ag NP structures exhibit various interesting optical effects, including excitation of guided modes within the host TiO_2 matrix, strong diffractive colors and shining dichroic colors in both reflection and transmission upon a transparent supporting material.

Furthermore, the thesis demonstrates that thermal effects that occur during the formation of Ag NP structures can be significantly reduced by fs laser processing. In this case, the TiO_2 matrix is only crystallized around the grown Ag NP and is still partially mesoporous after laser exposure. It gives a potential solution to transfer these optical properties upon a soft and flexible support without altering the latter by the high temperature rise induced by laser. These optical properties, produced by a single laser beam pass, lead to innovative solutions in fields like active color displays, security, polarization imaging.

Perspectives

The motivations of scientific research never fade at the end of a thesis contract. The encouraging results of this work bring useful perspectives for both theoretical modeling and laser experimentations, which have already more or less begun to integrate in the research activities of the group coordinating this thesis.

Modeling of NP growth – Towards a Monte-Carlo approach

Theoretical description of the NP growth under CW laser exposures through solving of differential system is of good success. Now, a new aim of the group is to consider the spatial distribution of NPs during the growth process. Tracking the spatial positions of each NP during laser irradiation can provide an improved understanding of the 1D self-organization process and the recently discovered 2D organization that are initiated by complex optical interference of a single incident light within the TiO_2 thin layer [Destouches 2014, Baraldi 2016 submitted]. By combining with the electromagnetic models developed by the group [Bakhti 2016], this new model could also help to predict and optimize the color properties of the laser processed $\text{Ag}:\text{TiO}_2$ composite.

The spatial information of NPs can be taken into account using a statistical approach, for example Monte-Carlo techniques [Liffman 1992, Smith 1998, Maisels 2004, Zhao 2006]. For a finite particle population within a closed system, Monte-Carlo techniques work in a straightforward way by explicitly tracking the information of each considered particle, such as size, shape and spatial position. The processes leading to variations in the NP size, like coalescence, Ostwald ripening or oxidation, are treated as events. Each event for a target NP is then characterized by its reaction rate in the system, which is also named the “probability” of the event. The temporal evolution of the system is performed at discretized time steps. At each time step, one event can act on a NP only if a stochastic condition is met. Instead of choosing in a deterministic manner the event and the target NP as the one giving the highest probability, random variables are generated according the probability distribution of all the events to find a target event and its target NP. This technique only ensures that the most probable event and NP have the highest chance to take place. Due to this stochastic behavior of Monte-Carlo methods, two simulations applied on the same initial NP system will not necessarily give identical results.

Using stochastic processes, Monte-Carlo approaches describe the statistical characteristics of the system. However, it can only converge accurately with the result of analytic models on condition that an important population of NPs is simulated. For this reason, more than thousands of NPs are usually simultaneously tracked during a simulation and several techniques should be implemented to avoid the drop of the NP quantity. “Constant number” method [Smith 1998] keeps the NP quantity always constant. When an event modifies the NP quantity, *i.e.* coalescence, the simulated volume is adjusted according to the volume concentration of NP. In the case of “constant volume” methods [Maisels 2004, Liffman 1992], the quantity of NPs is periodically regulated. The list of NPs is copied to double the simulated volume and the NP population once the latter drops to its half. The length of one time step can be calculated either in an “event-driven” way or in a “time-driven” way. In time-driven methods [Liffman 1992, Zhao 2006], the time step is fixed constant, and during this time every event is stochastically evaluated and has a chance to take place. However, in order to guarantee the accuracy of simulations, the constant time step is chosen to be smaller than the inverse of the highest event rate of the system so that at most one event may take place during one time step. This process results in a lot of “empty” time steps, during which no event has a chance to acts on the NP distribution, and decreases significantly the efficiency of this approach. An improved version can be achieved using event-driven methods [Smith 1998, Maisels 2004]. In this case, the time step is chosen as the inverse of the average rate of all the events on each NP. In one time step, there is always one event that happens on a target NP (or NP pair in the case of coalescence), which increases the computational efficiency of the model.

A first Monte-Carlo test of the studied Ag NP growth phenomenon has been performed before the end of this thesis, using a constant volume and event-driven scheme [Maisels 2004] and event rates which were easily deduced from Eq. 15, 18, 23, 27 in Chapter IV. However, the simulation processes have strongly suffered from long computation time, in both cases of NP shrinkage at low scan speed and NP growth at higher speeds. Until the time of writing this section, simulations have been executed during more than 50 days on computational servers (Intel Xeon E5-2680 @ 2.70GHz, 2 GB per cores) but none of them has reached the end. In the corresponding cases of deterministic method, the simulation duration is usually around 3 hours on the same server. Monte-Carlo technique becomes very time consuming when used with an important NP population to increase the accuracy of the results. The computational complexity of event probabilities can reach the order of N^2 , where N is the quantity of simulated NPs, for example in the case of coalescence. Compared with the deterministic method developed in Chapter IV, which only considers 100 pivot points at one time, Monte-Carlo method tracks more than thousands of particles and significantly multiplies the quantity of numerical computations. Furthermore, in the case of deterministic method, the time step that solves the ODEs system is automatically adjusted by the standard solvers so that the event rates are recomputed only if they have significantly

changed by the evolution of the system. However, in Monte-Carlo approach, all the event rates should be updated once a single event takes place, even if this event has negligible influence on the whole event rates. A typical example can be the lost or attraction of one atom on a 10 nm Ag NP, which significantly changes neither the size of this NP nor event rates relied on the latter.

This problem can be solved in several ways. Firstly, most of the Monte-Carlo techniques are coupled with parallel programming techniques nowadays, as the computations of event rates are fully independent tasks which can be efficiently parallelized on multicore servers or Graphics Processing Units (GPU). Examples of parallelized Monte-Carlo schemes for population balance problems can be also found in literature [Wei 2014, Xu 2015]. Secondly, one can apply an optimized mechanism that avoids useless updates of event rates at each time step. The size variations of Ag NP are driven by their plasmon absorption and the temperature rise induced by the latter. An efficient model may only recalculate the event rates once an important variation of these two factors is observed.

Laser experimentation - Better control of thermal effect

Laser-induced Ag NP self-organized structures exhibit dichroic colors, which can produce innovative solutions for applications in domains like color design, polarization imaging, and security etc. However, transferring this technique to flexible substrates like paper or glass is limited by the strong thermal effect induced by CW laser processing that alters the substrate.

Chapter V has experimentally illustrated that pulsed laser is able to decrease the plasmon-induced temperature rise and confine the latter around grown Ag NPs. In several experimental conditions, this temperature rise is expected to be less than the thermal resistance of the flexible support used in other works of the group [Tricot 2014]. Several tests of fs laser inscription on plastic supported composite systems have already been performed under the framework of an industrial collaboration, which is giving encouraging results.

References

Bakhti, S.; Baraldi, G.; Liu, Z.; Destouches, N. Fano Resonance in Self-Organized Embedded Metallic Nanoparticle Gratings and Application as Optical Security Features. In *International Conference on Metamaterials, Photonic Crystals and Plasmonics (META'16)*; Malaga, Spain, 2016.

Destouches, N.; Crespo-Monteiro, N.; Vitrant, G.; Lefkir, Y.; Reynaud, S.; Epicier, T.; Liu, Y.; Vocanson, F.; Pigeon, F. Self-Organized Growth of Metallic Nanoparticles in a Thin Film under Homogeneous and Continuous-Wave Light Excitation. *J. Mater. Chem. C* **2014**, *2* (31), 6256–6263.

Liffman, K. A Direct Simulation Monte-Carlo Method for Cluster Coagulation. *Journal of Computational Physics* **1992**, *100* (1), 116–127.

Maisels, A.; Einar Kruis, F.; Fissan, H. Direct Simulation Monte Carlo for Simultaneous Nucleation, Coagulation, and Surface Growth in Dispersed Systems. *Chemical Engineering Science* **2004**, *59* (11), 2231–2239.

Smith, M.; Matsoukas, T. Constant-Number Monte Carlo Simulation of Population Balances. *Chemical Engineering Science* **1998**, *53* (9), 1777–1786.

Tricot, F.; Vocanson, F.; Chaussy, D.; Beneventi, D.; Reynaud, S.; Lefkir, Y.; Destouches, N. Photochromic Ag:TiO₂ Thin Films on PET Substrate. *RSC Adv.* **2014**, *4* (106), 61305–61312.

Wei, J. Comparison of Computational Efficiency of Inverse and Acceptance –rejection Scheme by Monte Carlo Methods for Particle Coagulation on CPU and GPU. *Powder Technology* **2014**, *268*, 420–423.

Xu, Z.; Zhao, H.; Zheng, C. Accelerating Population Balance-Monte Carlo Simulation for Coagulation Dynamics from the Markov Jump Model, Stochastic Algorithm and GPU Parallel Computing. *Journal of Computational Physics* **2015**, *281*, 844–863.

Zhao, H.; Maisels, A.; Matsoukas, T.; Zheng, C. Analysis of Four Monte Carlo Methods for the Solution of Population Balances in Dispersed Systems. *Powder Technology* **2007**, *173* (1), 38–50.

Zhao, H.; Zheng, C. Monte Carlo Simulation for Simultaneous Particle Coagulation and Deposition. *SCI CHINA SER E* **2006**, *49* (2), 222–237.

Annex I. Segmentation of Ag NPs in heterogeneous matrix

The following segmentation and filtering methods aim to extract automatically the mean diameter of thousands of NPs of a given chemical composition embedded in a heterogeneous matrix from processed HAADF STEM images. In the case of mesoporous Ag:TiO₂ samples (Figure.A-I.1), silver NPs correspond to brighter regions owing to their much higher atomic density than the titania regions; their intensity can vary strongly from one part of the image to another; also, their contrast with respect to the background appears to vary significantly along the contour of a single NP, which often leads to non-homogeneous or even non-closed NP contours. If the watershed transform is a largely used method in the literature to detect NPs in images [Thiedmann 2012, Leary 2012, Park 2013], it appears inoperative in our images because it relies on a closed contour detection of target objects as calculated by an edge detection operator. The following algorithm has therefore been implemented to identify NPs within the mesoporous matrix.

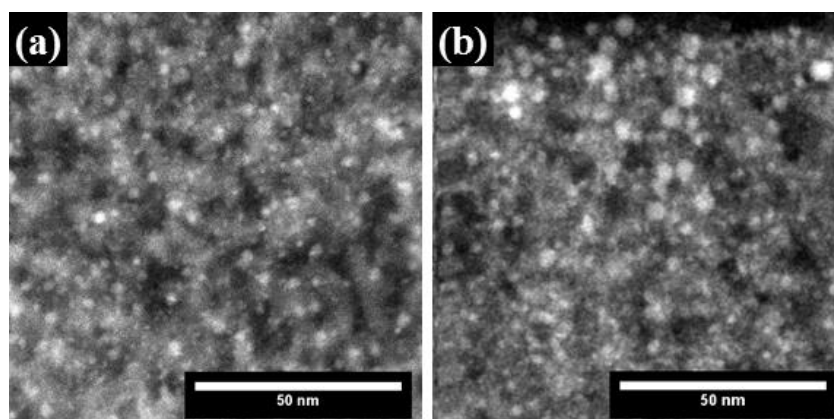


Figure A-I.1. HAADF STEM images of initial Ag:TiO₂ samples at states S1 (a) and S2 (b) defined in Chapter II. All micrographs show different Ag NP size distributions over a non-uniform background.

1. NP segmentation method

In order to illustrate the developed NP segmentation method, we use one image of initial sample S1 as the original image for image processing (Fig. A-I.1). A Gaussian filter with a standard deviation of 2 pixels is applied to the whole image to reduce the Gaussian white noise produced by the camera (Figure.A-I.2.a). A two-step method is then applied on the filtered image. First, the position of the NPs center is detected using extended-maxima transform [Soille 2004] (Figure.A-I.2.b). Ag NPs exhibit higher HAADF intensity, which corresponds to regional maxima or to convex regions if we use the vocabulary of image

morphology. The extended-maxima transform only keeps the convex regions whose height is higher than a threshold value. The latter is manually fixed to the minimum height of convex regions observed in an image, in order to detect the largest possible number of candidate zones for NPs. Consequently, at this stage, the selected convex regions are not well-defined and may include noise or TiO_2 regions. In a second step, each candidate NP is more carefully segmented by a threshold defined by its local morphology. Around each saved center position, we select a subimage centered on this position (Figure.A-I.2.c) on which a reconstruction by dilatation from the center is applied [Soille 2004]. This morphological image processing replaces the nearest convex regions around the center position by local minima without modifying the intensity of other pixels (Figure.A-I.2.d). The highest value of these detected local minima (that are shown in Figure.A-I.2.e) is then chosen to be the intensity level at which the NP contour is defined. A subimage showing only the NP is finally calculated by a simple thresholding (Figure.A-I.2.f) and the whole segmented image is reconstructed by repeating the process for all center positions detected in the first step.

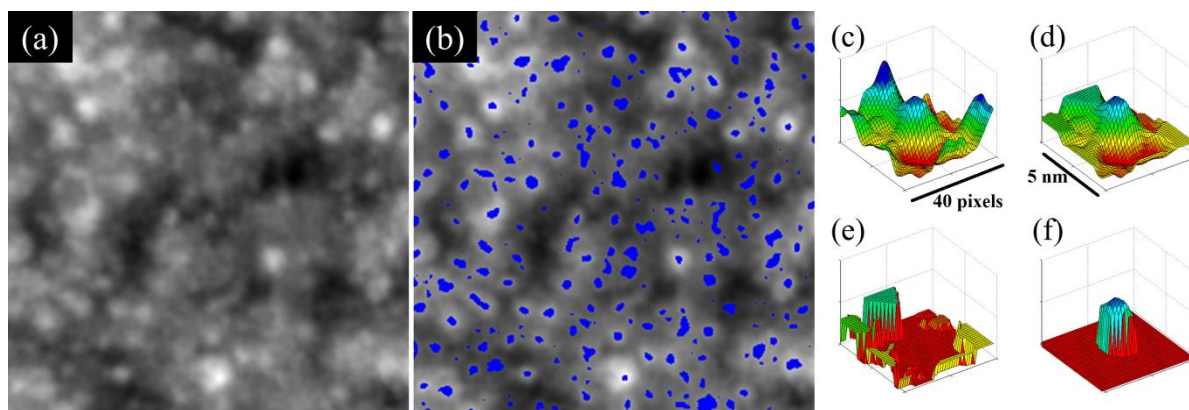


Figure A-I.2. Intermediate steps of the NP segmentation program. a): Initial image denoised by Gaussian filter. b): Candidate regions (in blue) marking the center of NPs found by extended-maxima transform. c-f) : Convex regions reconstruction. c): Initial morphology of a subimage centered on a potential NP. d): After reconstructing by morphological dilatation operator. e): Local minima values around the subimage center. f): NP segmented by thresholding at the maximum value in e.

2. Filtering segmented NPs from quantitative analysis of the HAADF STEM signal

Among segmented candidate NPs, some may correspond to heterogeneities of the background and must be discarded from statistical analysis to avoid introducing too much distortion in histograms. Developing predictive models for the study of the laser-induced growth of Ag NPs in TiO_2 films indeed requires a high accuracy on the measurement of the Ag NPs size histograms. We therefore apply a method firstly developed by M. M. J. Treacy and S. B. Rice [Treacy 1989] to select only NPs that are expected to be Ag. This method is based on the quantitative analysis of the HAADF signal. As proposed by previous works in

literature [Treacy 1989, Epicier 2012], in the case of crystalline spherical particles as are Ag NPs in our samples, the HAADF STEM intensity integrated over a whole NP once any background has been subtracted, I_{NP} , is given by:

$$I_{NP}^{1/3} = \left(\frac{k \rho_{Ag} Z_{Ag}^{\alpha} \pi}{6} \right)^{1/3} D \quad (\text{A-I.1})$$

where Z_{Ag} and ρ_{Ag} have been defined above. Considering the NPs found on the segmented images, D is the diameter of the equivalent circle with the same area than the segmented particle. Such an equation states that the cubic root of the total intensity of a NP, of given nature and crystal phase, varies linearly with its diameter D . All Ag NPs must therefore draw a line in the $(I_{NP}^{1/3}, D)$ plane, whose slope is characteristic of fcc Ag nanocrystals. In this work, I_{NP} , which is the sum of pixels of one particle, must be corrected to remove the TiO_2 background that superimposes to the NP. Here, the background intensity is defined as the average intensity of pixels of the inner and outer contours of the NP and is subtracted to each pixel of the NP before summing. Here, the inner contours are defined as the boundary pixels within the segmented regions and the outer contours are the adjacent pixel at outside of the inner contour. Note that if the background intensity is adequately removed, the linear regression fitting the dots resulting from the characterization of all NPs of a sample must pass through zero.

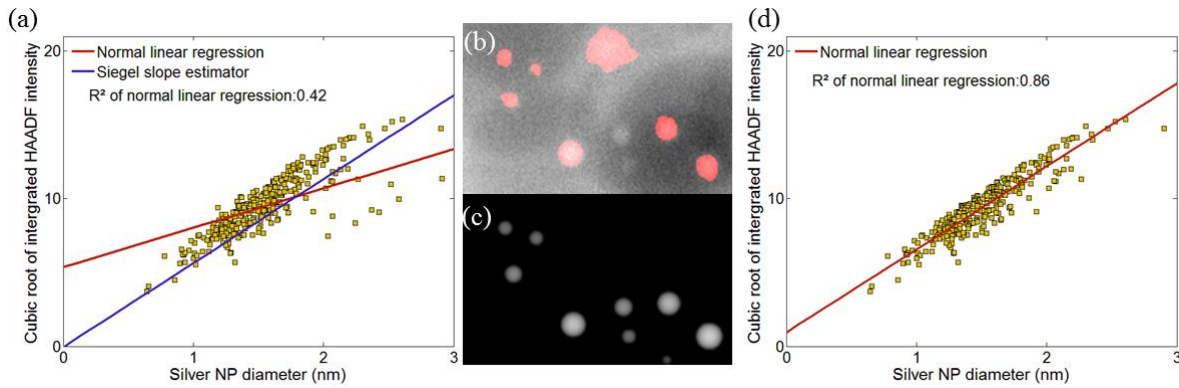


Figure A-I.3 Effect of filtering by quantitative analysis of the HAADF STEM signal on segmented images. a: Quantitative analysis of simulated images of S1 before any filtering. b: Zoom on a segmented region including missed NPs (NPs present in c) and not underlined in b, detected silver NPs (highlighted in red) and an outlier corresponding to a dot far from the Siegel slope estimator in graph a. c: Initial simulated silver NPs in the same segmented region as in b without displaying any background. d). Final quantitative analysis of the segmented region after filtering the non-silver regions.

The outlier of this line can be then considered as false segmentations of the image processing algorithm. Here, we used a realistic synthesized images (see Annex II) of S1 to give a better interpretation of these outliers. Figure A-I.3.a shows how the cubic root of I_{NP} , for the segmented NPs, is distributed as a function of their equivalent diameter D in one synthesized image. The distribution can be fitted using a normal linear regression, where

many dots look far from the straight line and are not expected to correspond to spherical Ag NPs. In figure A-I.3.b, we show a small region of the initial synthesized image in which the automatically segmented NPs have been highlighted in red. For comparison, figure A-I.3.c shows the Ag NPs that had been introduced in this region of the synthesized image, without displaying any background. One can observe that six Ag NPs are properly located in this region, three Ag NPs are missing in the segmented image and an additional candidate particle, which corresponds to a large TiO_2 heterogeneity, has been detected as a NP. The influence of the former is discussed in Annex II. The latter corresponds to a dot far from the averaged straight line and will be removed from the segmented image after filtering by the quantitative analysis method.

In presence of numerous outliers (non-Ag NPs or non-spherical Ag NP) in the dot distribution, the classical linear regression may be false (Figure A-I.3.a). It appears then helpful to use a robust slope estimator, such as the Siegel variation [Siegel 1982] of the Theil-Sen slope estimator, to get rid of these outliers (Figure A-I.3.d). In Siegel estimator, the final slope of the linear regression is given by the most repeated median value of slopes estimated from each couple of points using $(y_j - y_i)/(x_j - x_i)$, where (x_m, y_m) corresponds to the coordinates of point m. The outliers are removed iteratively: the farthest point from the line estimated by Siegel estimator is removed and the classical linear regression estimated slope is calculated again. When all the outliers are removed, the linear regression can finally give a similar slope as the Siegel estimator. The iteration is stopped once this condition is established. The filtering can remove the non-spherical Ag NPs, but the small population of non-spherical Ag NPs within in the image gives only negligible influence on the statistical characteristic of the NP distribution. This filtering also improves the coefficient of determination R^2 of the linear regression. An example of automatically segmented NPs in a real image after quantitative analysis filtering of non-silver NP are shown in the figure below.

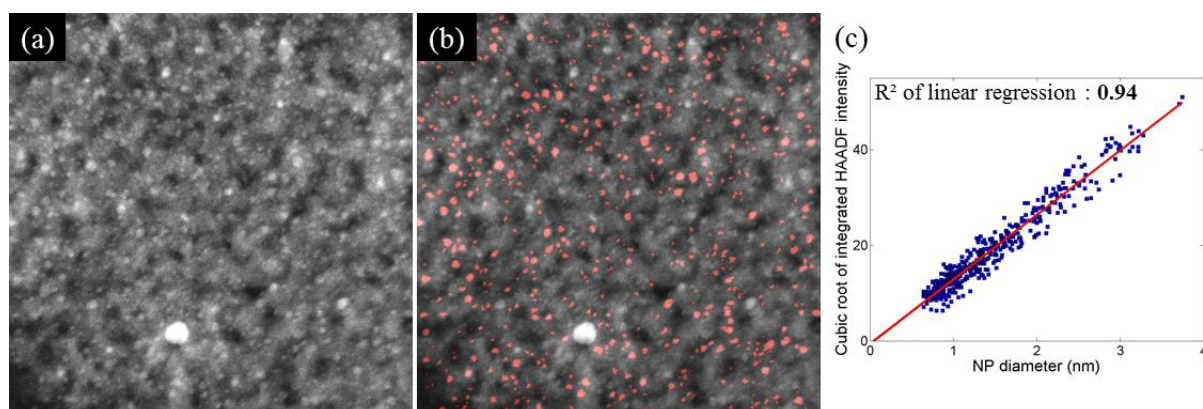


Figure A-I.4. Same figure as Figure II.9. a. STEM-HAADF image of initial state Ag:TiO₂ sample. b. Candidate Ag NP zone detected by automatic image processing method and quantitative analysis (red zones). c: Quantitative analysis of the segmented regions shown in subfigure b.

The final size of NPs D_{NP} is corrected to take into account the widening of the measured NPs due to the probe size D_{Pr} :

$$D_{NP} = \sqrt{D_0^2 - D_{Pr}^2} \quad (\text{A-I.2})$$

where D_0 is the apparent NP size deduced from image processing.

References

- Epicier, T.; Sato, K.; Tournus, F.; Konno, T. Chemical Composition Dispersion in Bi-Metallic Nanoparticles: Semi-Automated Analysis Using HAADF-STEM. *J Nanopart Res* **2012**, *14* (9), 1–10.
- Leary, R.; Saghi, Z.; Armbrüster, M.; Wowsnick, G.; Schlögl, R.; Thomas, J. M.; Midgley, P. A. Quantitative High-Angle Annular Dark-Field Scanning Transmission Electron Microscope (HAADF-STEM) Tomography and High-Resolution Electron Microscopy of Unsupported Intermetallic GaPd₂ Catalysts. *J. Phys. Chem. C* **2012**, *116* (24), 13343–13352.
- Park, C.; Huang, J. Z.; Ji, J. X.; Ding, Y. Segmentation, Inference and Classification of Partially Overlapping Nanoparticles. *IEEE Transactions on Pattern Analysis and Machine Intelligence* **2013**, *35* (3), 1–1.
- Siegel, A. F. Robust Regression Using Repeated Medians. *Biometrika* **1982**, *69* (1), 242–244.
- Soille, P. *Morphological Image Analysis*; Springer Berlin Heidelberg: Berlin, Heidelberg, 2004.
- Thiedmann, R.; Spettil, A.; Stenzel, O.; Zeibig, T.; Hindson, J. C.; Saghi, Z.; Greenham, N. C.; Midgley, P. A.; Schmidt, V. NETWORKS OF NANOPARTICLES IN ORGANIC – INORGANIC COMPOSITES: ALGORITHMIC EXTRACTION AND STATISTICAL ANALYSIS. *Image Analysis & Stereology* **2012**, *31* (1), 27–42.
- Treacy, M. M. J.; Rice, S. B. Catalyst Particle Sizes from Rutherford Scattered Intensities. *Journal of Microscopy* **1989**, *156* (2), 211–234.

Annex II. Evaluation the robustness of the image processing technique and HAADF STEM images synthesis

This annex shows how to evaluate the reliability of the NP segmentation method described in Annex I through the analysis of numerically synthesized images. The latter are based on the simulation of HAADF STEM projections of a 3D volume of the studied Ag:TiO₂ sample. The results obtained with synthesized images also allow inferring empirical rules to determine imaging parameters that ensure a good reliability of histograms.

1. HAADF STEM image synthesis of Ag:TiO₂ composite

Simulating the STEM HAADF intensity I in each pixel of an image is achieved according to the usual description of the incoherent scattering in HAADF which predicts [Treacy 1989, Epicier 2012], that

$$I = k \sum_i n_i Z_i^\alpha \quad (\text{A-II.1})$$

where n_i is the number of atoms of nature i probed by the electron beam, Z_i their atomic number, α is a coefficient estimated to be close to 2 for high angle detectors [Jesson 1995], and k a constant that depends on the experimental TEM imaging conditions, such as the dwell time or magnification, and does not depend on the ambient noise. It has no significant influence on the result of image processing since all treatments consist in analyzing the relative intensities of the different phases. It has been fixed to 0.04 in the simulated images, which is the mean value determined from the normalization of our real HAADF STEM micrographs.

To simulate the volume probed by the electron beam, which gives rise to the intensity of each pixel, we have to consider the thickness of the films, estimated to about 80 nm according to the method of preparation. Then, these 80 nm-thick films were filled with atomic densities corresponding to the three phases considered: TiO₂, pores and Ag NPs. For the TiO₂ matrix, we used Ti and O atomic densities from anatase, *i.e.* $\rho_{\text{Ti}} = 4 \text{ atoms}\cdot\text{nm}^{-3}$ and $\rho_{\text{O}} = 8 \text{ atoms}\cdot\text{nm}^{-3}$, with respective atomic numbers $Z_{\text{Ti}} = 22$ and $Z_{\text{O}} = 8$. The pores were kept empty, and the silver NPs filled with a Ag atomic density of $\rho_{\text{Ag}} = 59 \text{ atoms}\cdot\text{nm}^{-3}$ (4 atoms in a fcc cell with a parameter equal to 0.409 nm) and $Z_{\text{Ag}} = 47$. Realistic NP and pore size distributions were used to synthesize realistic HAADF STEM images with similar features to those of S1 and S3 samples described previously (samples with the smallest Ag NPs). The

pore size distribution (Figure A-II.1.b) was deduced from SEM images (Figure A-II.1.a, SE mode) of the TiO_2 films, where pores appear as darker regions. The latter were detected by an extended-minima transform [Soille, 2004] of the SEM image, which segments the regional minima (dark region) whose depth is higher than a certain threshold. The pores appeared to be randomly and homogeneously distributed; they were however not really spherical: their circularity ($4\pi A/P^2$, where A and P are respectively the area and perimeter of pores) varies in a broad range in 2D images, as shown in Figure A-II.1.b. For the sake of simplicity, we have nevertheless considered spherical pores with a Gaussian-shape size distribution fitted from the experimental histogram of Figure A-II.1.b, and centered at 4 nm (pore radius) with a standard deviation of 1.4 nm. The surface density of pores was also estimated and extended to a volume density by assuming that the mean distance in depth between pores equals the pore average diameter of 8 nm. We then get a volume density of about $4 \times 10^5 \mu\text{m}^{-3}$.

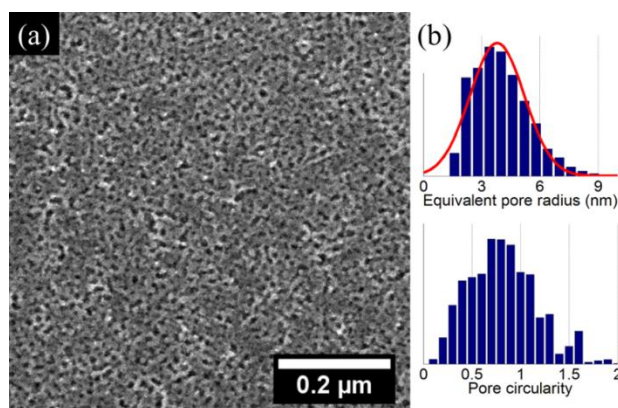


Figure A-II.1. a): SEM image of a mesoporous film of amorphous TiO_2 . b): Normalized histograms of equivalent pore radius and pore circularity.

Silver-NP size distributions were estimated from the processing of experimental HAADF STEM images using the method described in the next section. Simulated samples corresponding to S1 are called SS1. They have a NP size distribution centered at 1.4 nm with a standard deviation of 0.45 nm and the NP density was estimated to $1.6 \times 10^6 \mu\text{m}^{-3}$. In the case of S3, simulated samples are noted SS3 and have a silver NP distribution centered at 0.5 nm with a standard deviation of 0.40 nm and a density of $1.0 \times 10^6 \mu\text{m}^{-3}$. The type of NP size distribution is approximated to a Gaussian form in order to keep the simplicity of the simulation. The mean values and the standard deviations mentioned above were calculated from the raw distribution of the real sample. The shape of simulated silver NPs is also chosen to be spherical to simplify simulations, a very reasonable assumption in this case.

Finally, a Gaussian filter with a diameter (at $1/e^2$) of 0.5 nm is applied to simulated images to take into account the influence of the electron probe size; no beam spreading was accounted across the sample thickness. A Gaussian noise is also added to the image, the intensity of which was estimated from experimental measurements. It is calculated from a homogeneous region of HAADF STEM images located outside of the mesoporous film,

typically on the carbon film of TEM grids. The noise variance was estimated at 0.0016 for an image intensity normalized between 0 and 1.

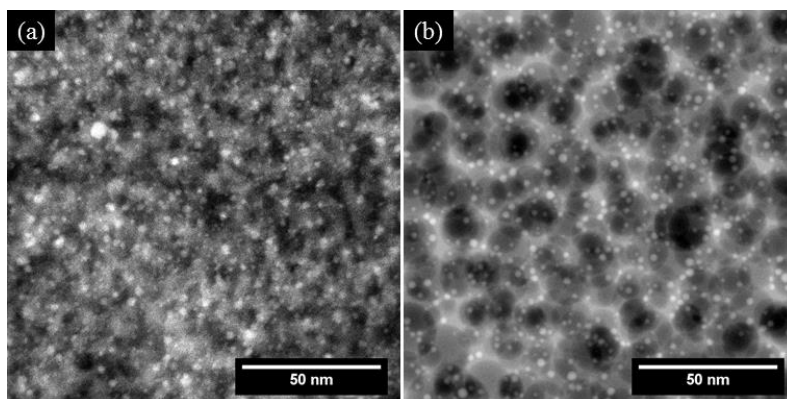


Figure A-II.2. a): STEM HAADF image of sample S1 at x600k magnification. b): Synthesized image using the same image magnification and a similar NP size distribution. A value of 1.8 has been used for the parameter α in Eq. A-II.1.

Figure A-II.2 shows a STEM HAADF micrograph of sample S1 (Figure A-II.2.a) together with a simulated image SS1 using the same NP size distribution as in sample S1 (Figure A-II.2.b). As stated previously, the contrast of Ag NPs strongly varies in the image, and even along the contour of one NP; furthermore, it can be seen that the background and silver NPs in different areas can have the same intensity level.

2. Reliability of the NP segmentation technique at different image magnifications

Synthesized images (Figure A-II.2.b) show sometimes that Ag NPs can completely disappear depending on their size and location in the heterogeneous film. Obviously, these hidden NPs could not be retrieved by image processing. But such realistic synthesized images will allow us to estimate the errors done on the calculated histograms by the method proposed in Annex I and to predict better the imaging conditions, for example the most suitable magnification. Segmented results strongly depend on the image magnification. Increasing the magnification gives access to more details with a higher spatial resolution but decreases the number of measured NPs, which reduces the accuracy of statistical measurements using a given number of images.

Figure A-II.3.a-c give the size histograms of simulated and segmented NPs for synthesized image of initial sample S1 at three different magnifications. At x200k magnification (Figure A-II.3.a), the pixel size is 0.42 nm and most of NPs are missing in the reconstructed histogram after image processing due to a lack of image resolution. On the other side, using x1.5M magnification (Figure A-II.3.c) gives only access to a small number of NPs and to a poor statistics. In this case, missing particles can significantly affect the

histogram shape and especially the standard deviation of results. Better results are obtained at an intermediate magnification, x600k, where missing NPs do not significantly distort the histogram shape, nor its position. Figures A-II.3.d compares the average value and the standard deviation of size histograms deduced from initial distributions and segmented images as a function of image magnification. It gives the range of magnifications leading to a minimum error on the measured histograms (compared to the simulated ones). Note that choosing the lower magnification in this range limits the number of HAADF STEM images to acquire and to process. x600k is therefore a good choice for characterizing NP distribution of the studied initial Ag:TiO₂ samples.

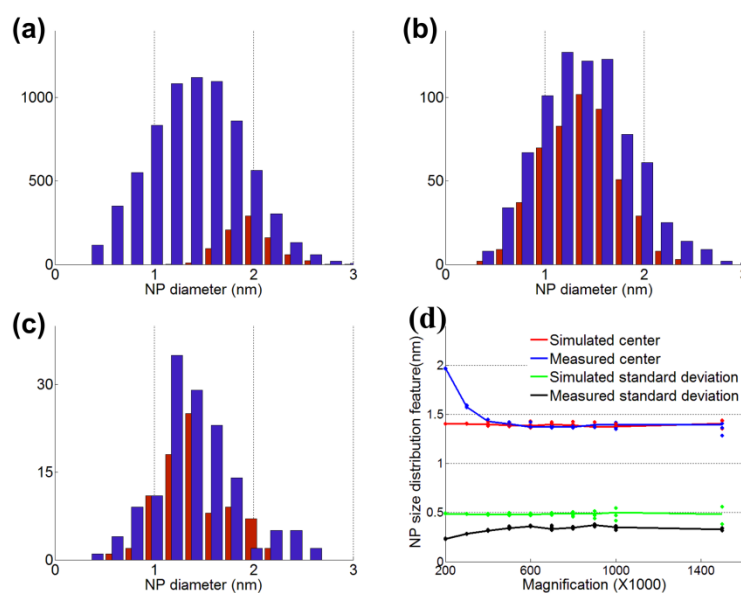


Figure A-II.3. a-c: Simulated initial size histograms of Ag NPs (blue) used to synthesize S1 samples at different magnifications (a): x200k, b): x600k, c): x1.5M) and NP size histograms deduced from the segmented images after filtering by quantitative analysis (red). d: Centers and standard deviations of the simulated and segmented NP size distributions for different magnifications.

References

- Epicier, T.; Sato, K.; Tournus, F.; Konno, T. Chemical Composition Dispersion in Bi-Metallic Nanoparticles: Semi-Automated Analysis Using HAADF-STEM. *J Nanopart Res* **2012**, *14* (9), 1–10.
- Jesson, D. E.; Pennycook, S. J. Incoherent Imaging of Crystals Using Thermally Scattered Electrons. *Proceedings of the Royal Society of London A: Mathematical, Physical and Engineering Sciences* **1995**, *449* (1936), 273–293.
- Soille, P. *Morphological Image Analysis*; Springer Berlin Heidelberg: Berlin, Heidelberg, 2004.
- Treacy, M. M. J.; Rice, S. B. Catalyst Particle Sizes from Rutherford Scattered Intensities. *Journal of Microscopy* **1989**, *156* (2), 211–234.

Annex III. Curve fitting of real-time *in situ* raw Raman spectra

1. Preprocessing of raw spectra

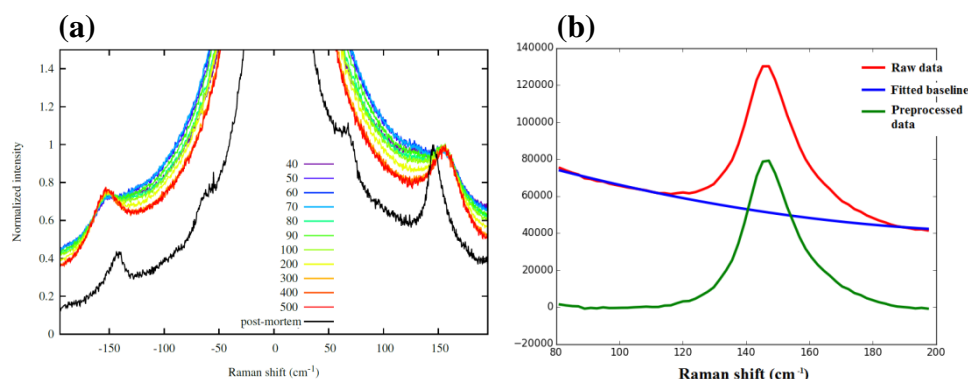


Figure A-III.1. a: Raw Raman spectra measured by the real-time *in situ* setup shown in Chapter II. b: Removing the influence of the baseline of a raw Stokes spectrum by polynomial fitting.

A rapid decrease of raw Raman intensity from the center (0 cm^{-1} , *i.e.* incident wavelength) of the raw spectra can be observed in figure A-III.1.a. The Raman intensity at around $\pm 144 \text{ cm}^{-1}$ is given both by the contribution of the TiO_2 anatase characteristic peak and this baseline. Modeling of the baseline is performed by a polynomial fitting of degree 2 using raw data at two separated value ranges surrounding the $\pm 144 \text{ cm}^{-1}$ peaks. In this work, these ranges were chosen at $[\pm 95 \text{ cm}^{-1}, \pm 105 \text{ cm}^{-1}]$ and $[\pm 185 \text{ cm}^{-1}, \pm 198 \text{ cm}^{-1}]$ for Stokes (sign +) and anti-Stokes (sign -). Figure A-III.1.b shows an example of baseline fitting in a Stokes spectrum. The red curve corresponds to the raw spectrum and the blue curve is the baseline deduced from polynomial fitting. The intensity peak corresponding to TiO_2 anatase can then be obtained by a simple subtraction between the raw data and the fitted baseline.

2. Curve fitting of Raman peaks

2.1. Models of spectral line shape

The shape of Raman peaks, also known under the name of “line shape”, can be modified by numerous factors such as the nature of the measured sample, experimental conditions, physical origins of the line etc. Different curve functions can be used to fit Raman peaks including Gaussian, Lorentzian, Gaussian-Lorentzian and Voigt. Mathematical formulas

of these curves are well-known. However, it is worth to precise the morphological meaning of parameters involved in their mathematical expressions.

Gaussian (G) and Lorentzian (L) are two basic profiles. Their mathematic expressions can be respectively written as:

$$G = A \exp(-p^2 \ln 2) \quad (\text{A-III.1})$$

$$L = \frac{A}{1+p^2} \quad (\text{A-III.2})$$

A is the amplitude of the profile. p is a subsidiary variable:

$$p = \frac{x_{\max} - x}{w/2} \quad (\text{A-III.3})$$

where x_{\max} is the position of the maximum value, *i.e.* peak center, x the variable giving the spatial position. w is the width of the peak measured at the half of the maximum intensity (the full width at half maximum, shortened to FWHM). A comparison of the centered Gaussian and Lorentzian profiles of unit amplitude and FWHM of 2 (figure A-III.2.a) shows the shape difference of these single peak functions.

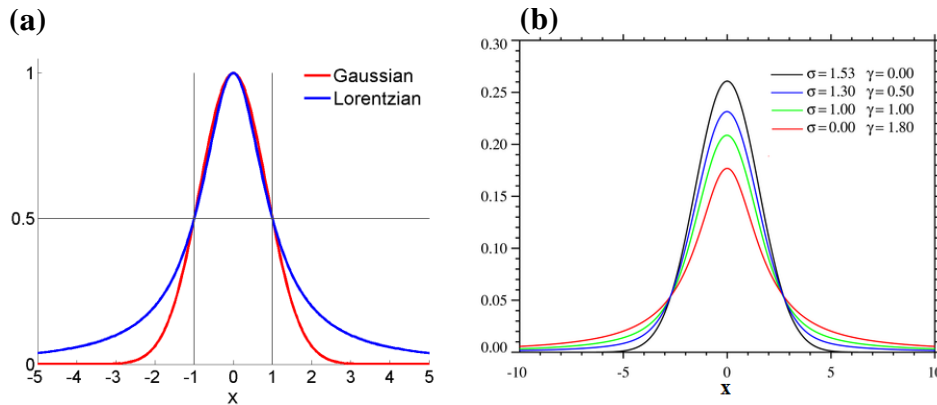


Figure A-III.2 a: Gaussian (red curve) and Lorentzian (blue curve) profiles of same amplitude ($A = 1$), FWHM ($w = 2$) and maximum value position ($x_{\max} = 0$). b: Comparison of centered Voigt profiles computed by different combinations of Gaussians and Lorentzians together with two extreme cases: pure Gaussian ($\gamma = 0$, black curve) and pure Lorentzian ($\sigma = 0$, red curve). The FWHM of each Voigt profile is close to 3.6.

Combining both Gaussian and Lorentzian gives rise to Gaussian-Lorentzian (GL) function and Voigt function. Gaussian-Lorentzian function can be simply expressed as the sum of Gaussian and Lorentzian:

$$GL = \alpha G + (1 - \alpha) L \quad (\text{A-III.4})$$

where G and L is respectively the Gaussian and the Lorentzian of same amplitude, FWHM and maximum value position, as defined in Eq. A-III.1 and Eq. A-III.2. α is the percentage of the Gaussian profile in GL, which adjusts the peak shape.

Voigt function is able to adjust more precisely the peak shape as shown in figure A-III.2.b. It is defined by the convolution of Gaussian and Lorentzian functions which can have different FWHMs:

$$V(x; \sigma, \gamma) = \int_{-\infty}^{\infty} G_v(x'; \sigma) L_v(x - x'; \gamma) dx' \quad (\text{A-III.5})$$

with:

$$G_v(x; \sigma) = \frac{\exp(-x^2/(2\sigma^2))}{\sigma\sqrt{2\pi}} \quad (\text{A-III.6})$$

$$L_v(x; \gamma) = \frac{\gamma}{\pi(x^2 + \gamma^2)} \quad (\text{A-III.7})$$

σ and γ are parameters that define the width of Gaussian and Lorentzian profiles, respectively. The relation between the FWHM (w) of Eq.A-III.3 and σ , γ can be given as:

$$w_G = 2\sigma\sqrt{2\ln 2} \quad (\text{A-III.8})$$

$$w_L = 2\gamma \quad (\text{A-III.9})$$

where w_G and w_L are FWHMs of Gaussian and Lorentzian. The FWHM of Voigt can be then written as:

$$w_V \approx 0.5346w_L + \sqrt{0.2166w_L^2 + w_G^2} \quad (\text{A-III.10})$$

Numerically, instead of performing the convolution, Voigt functions can be programmed by the Faddeeva (Fad) function which is usually predefined in commonly used scientific computing libraries:

$$V(x; \sigma, \gamma) = \frac{\text{Re}[Fad(z)]}{\sigma\sqrt{2\pi}} \quad (\text{A-III.11})$$

with

$$z = \frac{x_{max} - x + i\gamma}{\sigma\sqrt{2}} \quad (\text{A-III.12})$$

The maximum value of Voigt function V_{max} occurs at $x = x_{max}$. In order to explicitly define the amplitude (A) of Voigt function, we then rewrite Eq. A-III.11 as:

$$V(x; \sigma, \gamma) = \frac{A}{V_{max}} \frac{\text{Re}[Fad(z)]}{\sigma\sqrt{2\pi}} \quad (\text{A-III.13})$$

2.2. Curve fitting and error evaluation

In order to perform a curve fitting with the four line shape functions presented above, we can consider here a general expression of line shape function as $\vec{y} = f_{ls}(\vec{x}; x_{max}, \vec{w}, A)$ where the line shape function f_{ls} use a series of discrete value \vec{x} in wavenumber to yield the corresponding Raman peak intensity \vec{y} . The peak shape is then defined by the maximum value of the peak (A), its position x_{max} and FWHM \vec{w} , which is a scalar value in the case of Gaussian, Lorentzian, Gaussian-Lorentzian and a two element vector in the case of Voigt to represent the Gaussian and Lorentzian portion. Curve fitting can then be performed by the non-linear least square approach: For a given line shape function, find an optimal (x_{max}, \vec{w}, A) set that has the minimum difference between \vec{y} and the measured Raman peak. Such a technique has already been integrated in different scientific computation libraries as routine which also gives the relative errors of the optimized (x_{max}, \vec{w}, A) set. The latter helps to evaluate the uncertainty of the calculated temperatures induced by the numerical fitting process, as shown by error bars in figure IV.5 of this thesis. We have presented in chapter II that calculation of temperature rise can rely on either the Stokes/anti-Stokes ratio or the peak shift at 144 cm^{-1} . We can write a general expression of temperature rise with the error induced by numerical fitting as:

$$T = f_T(m \pm \Delta m) \quad (\text{A-III.14})$$

where f_T is one of the two methods above that compute the temperature rise, m the peak characteristic extracted from curve fitting and Δm the relative error of curve fitting. In the case that temperature rise is calculated by the Stokes/anti-Stokes ratio, *i.e.* $m = I_s/I_{as}$, Δm should be written as $(I_s \Delta I_{as} + I_{as} \Delta I_s)/I_{as}^2$, where ΔI_s and ΔI_{as} are respectively the relative error of Stokes intensity I_s and anti-Stokes intensity I_{as} .

Raman peak can also be fitted by a polynomial function. However, polynomial fitting suffers from the Runge's phenomenon represented by a strong oscillation at the edges of the fitting interval. We then just use the fitted value around the peak center, so only the maximum peak intensity and its position can be deduced from this technique.

3. Temperature rise estimations by different numerical processes

Growth of temperature rise with an increase of scan speed can be observed using different fitting models described above.

When the temperature rise is estimated by the Stokes/anti-Stokes ratio (Figure A-III.3. a-c), the intensity of Raman peak can be expressed either by the maximum value (Figure A-III.3.a) or the integrated intensity over an interval of maximum value positions $\pm 5 \text{ cm}^{-1}$ and

$\pm 10 \text{ cm}^{-1}$ (Figure A-III.3.b-c). Fitting with Voigt function can always give a similar temperature rise whatever the type of intensity used. This probably relies on the flexibility of Voigt profile that is able to precisely fit both the maximum value and the lateral shape of the peak. For other profiles, integrating over a larger interval can compensate the error of fitted maximum peak values. For this reason, temperature rises estimated by different line shape models converge when using integrated intensity over maximum value position $\pm 10 \text{ cm}^{-1}$. However, a quantitative estimation of the relative error in integrated intensity is more complex. We then chose the maximum peak value fitted by Voigt profile to compute temperature rise.

When the temperature rise is estimated by peak shift, all the four line shapes give quasi-identical temperature rises, except that polynomial fitting is not able to give accurate estimation of peak characteristic. To be coherent with the previous case, we still chose Voigt function to fit the position of peak maximum value.

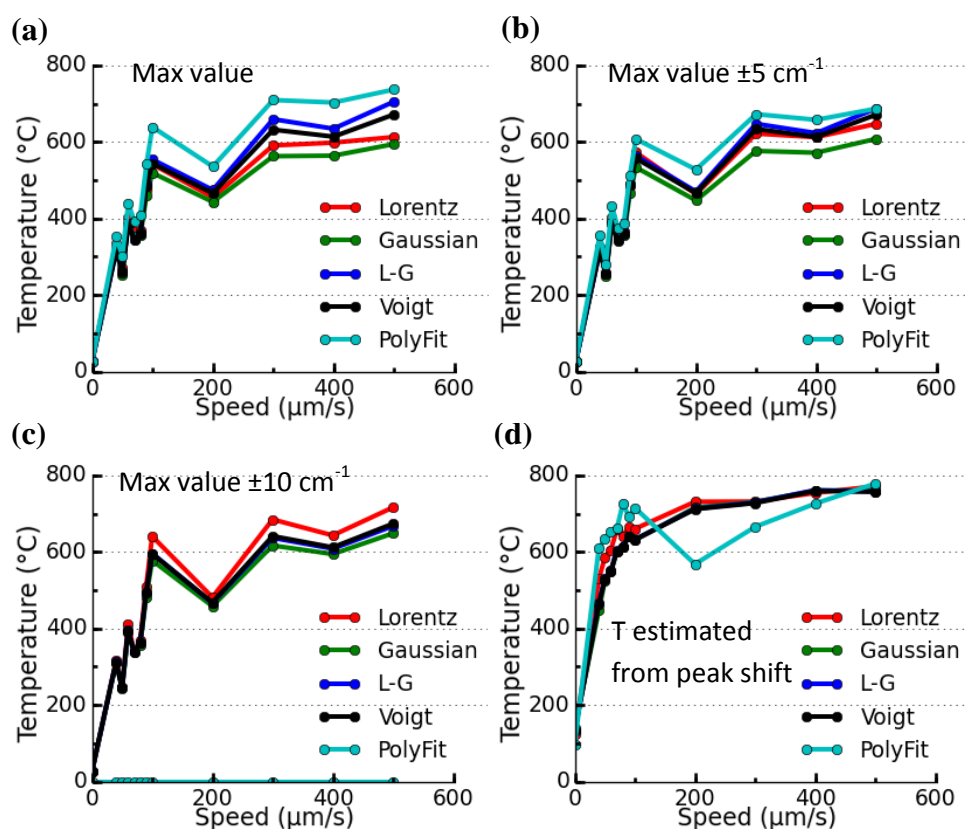


Figure A-III.3. a-c: Temperature rise estimated from the Stokes/anti-Stokes intensity ratio where the intensity of Raman peak respectively corresponds to the maximum value of the peak (a), and an integrated intensity over an interval of maximum value position $\pm 5 \text{ cm}^{-1}$ (b) and $\pm 10 \text{ cm}^{-1}$ (c). d: The temperature rise estimated by Raman peak shift.

Scientific productions in relation with the thesis

Articles in international journals:

- Z. Liu, G. Vitrant, Y. Lefkir, S. Bakhti, N. Destouches, "Laser induced mechanisms controlling the size distribution of metallic nanoparticles", *Phys. Chem. Chem. Phys.* **2016**, 18 (35), 24600–24609.
- Z. Liu, N. Destouches, G. Vitrant, Y. Lefkir, T. Epicier, F. Vocanson, S. Bakhti, Y. Fang, B. Bandyopadhyay, M. Ahmed, "Understanding the Growth Mechanisms of Ag Nanoparticles Controlled by Plasmon-Induced Charge Transfers in Ag-TiO₂ Films". *J. Phys. Chem. C* **2015**, 119 (17), 9496–9505.
- N. Destouches, J. Martínez-García, M. Hébert, N. Crespo-Monteiro, G. Vitrant, Z. Liu, A. Trémeau, F. Vocanson, F. Pigeon, S. Reynaud, "Dichroic Colored Luster of Laser-Induced Silver Nanoparticle Gratings Buried in Dense Inorganic Films". *J. Opt. Soc. Am. B* **2014**, 31 (11), C1–C7.
- N. Destouches, G. Vitrant, N. Crespo-Monteiro, Z. Liu, Y. Lefkir, F. Vocanson, T. Epicier, " Laser-induced periodic nanoparticle patterns," *Proceedings of SPIE Vol. 8969*, **2014**, Article Number: 89690G.
- Z. Liu, T. Epicier, Y. Lefkir, G. Vitrant, N. Destouches, "HAADF-STEM Characterization and Simulation of Nanoparticle Distributions in an Inhomogeneous Matrix", *Submitted to J. Microsc.*
- G. Baraldi, S. Bakhti, Z. Liu, S. Reynaud, Y. Lefkir, F. Vocanson, N. Destouches, "Polarization-driven self-organization of silver nanoparticles in 1D and 2D subwavelength gratings for plasmonic photocatalysis", *submitted to Nanotechnology*
- 2 other articles in preparation

International conferences:

- N. Destouches, G. Vitrant, N. Crespo-Monteiro, Z. Liu, Y. Lefkir, F. Vocanson, "Self-organization of metal nanoparticles in a waveguide under free-space light excitation", *ISN2A, 1st International Symposium on Nanoparticles/Nanomaterials and Applications*, 20th-22nd January **2014**, Lisbon, Portugal.
- N. Destouches, G. Vitrant, N. Crespo-Monteiro, Z. Liu, Y. Lefkir, F. Vocanson, T. Epicier, "Laser-induced periodic nanoparticle patterns", *SPIE Photonics West, Lasers and Applications in Science and Engineering*, SPIE proceeding 8969-14, 1-6 février **2014**, San Francisco, USA.
- N. Destouches, G. Vitrant, N. Crespo-Monteiro, Z. Liu, Y. Lefkir, F. Vocanson, M. Hébert, A. Trémeau, F. Pigeon "When light plays with metal nanoparticles in optical waveguides and creates spontaneously active color filters", *HPLA/BEP (International High Power Laser Ablation and Beamed Energy Propulsion)*, 21-25 April **2014**, Santa Fe, USA. (invited conference)
- Z. Liu, N. Destouches, G. Vitrant, Y. Lefkir, T. Epicier, F. Vocanson and S. Bakhti, "How oxidation and growth of silver nanoparticles compete in TiO₂ films when exposed to a moving visible laser", *2nd International Workshop on Metallic Nano-Objects (MNO 2014)*, 13-14 November **2014**, Lille, France.

- N. Destouches, Z. Liu, G. Vitrant, Y. Lefkir, and S. Reynaud , “Waveguiding Metallic Photonic Crystals Produced by Plasmon-driven Self-organization”, *PIERS 2015*, 06-09 July, **2015**, Prague, Czech Republic.
- N. Destouches, Z. Liu, G. Vitrant, Y. Lefkir, F. Vocanson, “Tuning the photochemistry of silver nanoparticles in TiO₂ with a gaussian-shape laser”, *European Materials research society (E-MRS) 2015 Spring Meeting*, May 11 – 15, **2015**, Lille, France.
- Z. Liu, J. Siegel, M. Garcia-Lechuga, J. Solis, G. Vitrant, S. Reynaud, Y. Lefkir, N. Destouches, "Laser-induced periodic surface structures and embedded metallic nanoparticle gratings", *European Materials research society (E-MRS) 2016 spring meeting*, 2-6 May **2016**, Lille, France.
- Z. Liu, J. Siegel, M. Garcia-Lechuga, J. Solis, G. Vitrant, S. Reynaud, Y. Lefkir, N. Destouches, “Laser-induced periodic surface structures and embedded metallic nanoparticle gratings”, *17th International Symposium on Laser Precision Microfabrication (LPM 2016)*, May 23-27, **2016**, Xi'an, China.
- S. Bakhti, G. Baraldi, Z. Liu, N. Destouches, "Fano resonance in self-organized embedded metallic nanoparticle gratings and application as optical security features", *International Conference on Metamaterials, Photonic Crystals and Plasmonics (META'16)*, July 25-28, **2016**, Malaga, Espagne.
- Z. Liu, G. Vitrant, L. Saviot, M. Marco-De-Lucas, T. Epicier, M. Bugnet, Y. Lefkir, S. Reynaud, J. Siegel, M. Garcia-Lechuga, J. Solis, N. Destouches, "Temperature rise during laser-induced self-organization of nanoparticle gratings revealed by Raman microspectroscopy and electron microscopy", *European Microscopy Congress (EMC)*, August 28 – September 2, **2016**, Lyon, France.

National conferences:

- N. Destouches, Z. Liu, G. Vitrant, Y. Lefkir, T. Epicier, N. Crespo-Monteiro, F. Vocanson, D. K. Diop, L. Simonot, D. Babonneau, « Mécanismes et conditions d'auto-organisation de nanoparticules métalliques sous excitation plasmonique », *GDR NACRE*, 28-30 september **2015**, Oleron, France.
- Z. Liu, N. Destouches, G. Vitrant, Y. Lefkir, T. Epicier, « Nanosources de chaleur photo-induites dont la température diminue avec le temps d'exposition », *GDR NACRE*, 28-30 september **2015**, Oleron, France.
- Z. Liu, T. Epicier, Y. Lefkir, G. Vitrant, N. Destouches. « Automatic reconstruction of Nanoparticle Size Distribution assisted by STEM-HAADF imaging ». *Colloque SEMPA 2016*, March 16-18, **2016**, Saint Etienne, France.

Abstract

This doctoral thesis focuses on the study of laser-induced self-organization of Ag nanoparticles (NPs) in TiO_2 thin layers. This laser technique was recently developed to provide original printing solutions for applications like active color displays, security, or polarization imaging. Here, we investigate experimentally and theoretically the different mechanisms involved in the NPs formation for a better control of their morphology and organization. In the case of continuous-wave (cw) laser, our experimental results prove that the speed at which the laser scans the sample surface is a crucial parameter to control the NP size and the laser-induced temperature rise. Ag NPs shrink at low scan speed, whereas growth governed by a thermal effect only occurs above a speed threshold. Above this threshold, the size of grown Ag NPs changes in a non-monotonous way with scan speed, whereas laser-induced temperature rise increases with speed. In order to explain these counter-intuitive behaviors, several numerical models have been developed to simulate changes in the size distribution of Ag NPs induced by visible light. Simulation results are in good agreement with experimental observations and reveal the origin of the observed phenomena by collective interactions of various physico-chemical processes involved in the variation of NPs size. Finally, this thesis demonstrates that self-organization of NPs at sub-wavelength scale on large areas can also be performed with femtosecond (fs) laser pulses. Oriented anisotropic growth of NPs has also been observed using a proper selection of laser irradiation parameters. Compared with the cw laser induced structures, fs pulses offer better control of the thermal effect and NP size, which opens the way to transfer these technologies on plastic or paper substrates.

Résumé

La présente thèse porte sur l'étude de l'auto-organisation induite par laser de nanoparticules (NPs) d'argent dans des couches minces de TiO_2 . Cette technique laser a été récemment mise au point pour fournir des solutions d'impression originales pour des applications comme l'imagerie polarimétrique, la sécurité ou le design. Ici, nous étudions expérimentalement et théoriquement les différents mécanismes impliqués dans la formation des NPs pour un meilleur contrôle de leur morphologie et de leur organisation. Dans le cas de lasers continus, nos résultats expérimentaux prouvent que la vitesse à laquelle le faisceau laser balaye la surface de l'échantillon est un paramètre crucial pour le contrôle de la taille finale des NPs, et de l'élévation de température induite dans la couche par le laser. La taille des NPs d'argent diminue aux basses vitesses d'écriture, alors que leur croissance est activée par effet thermique et apparaît uniquement au-dessus d'un seuil de vitesse. La taille finale des NPs varie dans ce cas de façon non-monotone avec la vitesse de balayage alors que la hausse de température ne cesse de croître. Afin d'expliquer ces phénomènes contre-intuitifs, plusieurs modèles numériques ont été développés qui permettent de simuler la variation de la taille des NPs sous insolation laser dans le domaine spectral du visible. Les résultats théoriques concordent bien avec les observations expérimentales et révèlent que l'origine de ces phénomènes résulte d'interactions complexes entre les différents processus physico-chimiques impliqués dans la formation des NPs. Finalement, cette thèse démontre que l'auto-organisation des NPs à l'échelle sub-longueur d'onde peut être aussi réalisée avec des impulsions laser femto-secondes (fs), et une croissance anisotrope des NPs a été également observée pour une gamme particulière de paramètres laser. La comparaison avec les structures de NPs produites par lasers continus suggère que les impulsions laser fs offrent une meilleure maîtrise des effets thermiques et de la taille des NPs. L'usage de laser fs offre ainsi une nouvelle approche pour transférer ces technologies sur des supports souples comme les papiers ou les plastiques.